

VOLUME 77

JUNE 21, 1973

NUMBER 13

JPCHAX

THE JOURNAL OF

PHYSICAL
CHEMISTRY

PUBLISHED BIWEEKLY BY THE AMERICAN CHEMICAL SOCIETY

THE JOURNAL OF PHYSICAL CHEMISTRY

BRYCE CRAWFORD, Jr., *Editor*

STEPHEN PRAGER, *Associate Editor*

ROBERT W. CARR, Jr., **FREDERIC A. VAN-CATLEDGE**, *Assistant Editors*

EDITORIAL BOARD: A. O. ALLEN (1970-1974), C. A. ANGELL (1973-1977), J. R. BOLTON (1971-1975), F. S. DAINTON (1972-1976), M. FIXMAN (1970-1974), H. S. FRANK (1970-1974), R. R. HENTZ (1972-1976), J. R. HUIZENGA (1969-1973), W. J. KAUZMANN (1969-1973), R. L. KAY (1972-1976), W. R. KRIGBAUM (1969-1973), W. J. MOORE (1969-1973), R. M. NOYES (1973-1977), J. A. POPLE (1971-1975), B. S. RABINOVITCH (1971-1975), H. REISS (1970-1974), S. A. RICE (1969-1975), F. S. ROWLAND (1973-1977), R. L. SCOTT (1973-1977), W. A. ZISMAN (1972-1976)

AMERICAN CHEMICAL SOCIETY, 1155 Sixteenth St., N.W., Washington, D. C. 20036

Books and Journals Division

JOHN K CRUM *Director*

RUTH REYNARD *Assistant to the Director*

CHARLES R. BERTSCH *Head, Editorial Processing Department*

D. H. MICHAEL BOWEN *Head, Journals Department*

BACIL GUILLEY *Head, Graphics and Production Department*

SELDON W. TERRANT *Head, Research and Development Department*

©Copyright, 1973, by the American Chemical Society. Published biweekly by the American Chemical Society at 20th and Northampton Sts., Easton, Pa. 18042. Second-class postage paid at Washington, D. C., and at additional mailing offices.

All manuscripts should be sent to *The Journal of Physical Chemistry*, Department of Chemistry, University of Minnesota, Minneapolis, Minn. 55455.

Additions and Corrections are published once yearly in the final issue. See Volume 76, Number 26 for the proper form.

Extensive or unusual alterations in an article after it has been set in type are made at the author's expense, and it is understood that by requesting such alterations the author agrees to defray the cost thereof.

The American Chemical Society and the Editor of *The Journal of Physical Chemistry* assume no responsibility for the statements and opinions advanced by contributors.

Correspondence regarding accepted copy, proofs, and reprints should be directed to Editorial Processing Department, American Chemical Society, 20th and Northampton Sts., Easton, Pa. 18042. Head: CHARLES R. BERTSCH. Assistant Editor: EDWARD A. BORGER. Editorial Assistant: JOSEPH E. YURVATI.

Advertising Office: Centcom, Ltd., 142 East Avenue, Norwalk, Conn. 06851.

Business and Subscription Information

Send all new and renewal subscriptions *with payment to* Office of the Controller, 1155 16th Street, N.W., Washington, D. C. 20036. Subscriptions should be renewed promptly to avoid a break in your series. All correspondence and telephone calls regarding changes of

address, claims for missing issues, subscription service, the status of records, and accounts should be directed to Manager, Membership and Subscription Services, American Chemical Society, P.O. Box 3337, Columbus, Ohio 43210. Telephone (614) 421-7230.

On changes of address, include both old and new addresses with ZIP code numbers, accompanied by mailing label from a recent issue. Allow four weeks for change to become effective.

Claims for missing numbers will not be allowed (1) if loss was due to failure of notice of change in address to be received before the date specified, (2) if received more than sixty days from date of issue plus time normally required for postal delivery of journal and claim, or (3) if the reason for the claim is "issue missing from files."

Subscription rates (1973): members of the American Chemical Society, \$20.00 for 1 year; to nonmembers, \$60.00 for 1 year. Those interested in becoming members should write to the Admissions Department, American Chemical Society, 1155 Sixteenth St., N.W., Washington, D. C. 20036. Postage to Canada and countries in the Pan-American Union, \$5.00; all other countries, \$6.00. Single copies for current year: \$3.00. Rates for back issues from Volume 56 to date are available from the Special Issues Sales Department, 1155 Sixteenth St., N.W., Washington, D. C. 20036.

Subscriptions to this and the other ACS periodical publications are available on microfilm. Supplementary material not printed in this journal is now available in microfiche form on a current subscription basis. For information on microfilm or microfiche subscriptions, write Special Issues Sales Department at the address above.

THE JOURNAL OF
PHYSICAL CHEMISTRY

Volume 77, Number 13 June 21, 1973

JPCA_x 77(13) 1601-1724 (1973)

Mecharistic Structure of the Water-Gas Shift Reaction in the Vicinity of Chemical Equilibrium Shoichi Oki and Reiji Mezaki*	1601 ■
Electron Spin Resonance Study of Oxygen Species Adsorbed on γ -Irradiated Zeolites Jacques C. Vedrine* and Claude Naccache	1606
Relation between an Excited State Geometry Change and the Solvent Dependence of 9-Methyl Anthroate Fluorescence T. C. Werner* and Ronald M. Hoffman	1611
Luminescence Emission and Excitation Spectra of Benzene and Alkane Thin Films under Slow Electron Impact at 77°K Kenzo Hiraoka and William H. Hamill*	1616
Flash Photolysis of Phenylglycine in Aqueous Solutions L. J. Mittal, J. P. Mittal, and E. Hayon*	1620
Kinetics of OH ⁻ and H ⁺ Reactions of Pyrimidines and Purines by Pulse Radiolysis C. L. Greenstock,* P. C. Shragge, and J. W. Hunt	1624
Electron Spin Resonance Study of the Reaction of Hydroxyl Radicals with Pyrrole, Imidazole, and Related Compounds A. Samuni and P. Neta*	1629
Electron Spin Resonance Studies of Spin-Labeled Polymers. III. The Molecular Weight Dependence of Segmental Rotational Correlation Times of Polystyrene in Dilute Solution A. T. Bullock,* G. G. Cameron, and P. M. Smith	1635
Matrix Infrared Spectrum and Evidence for Photoisomerism of Li ⁺ (ON) ⁻ . Infrared Spectrum of Li ⁺ (ON) ²⁻ -Li ⁺ David E. Tevault and Lester Andrews*	1640
Matrix Reactions of Sodium, Potassium, Rubidium, and Cesium Atoms with Nitric Oxide. Infrared Spectra of the M ⁺ (NO) ⁻ Species David E. Tevault and Lester Andrews*	1646
Infrared Spectra of the Ammonia-Hydrochloric Acid Complex in Solid Nitrogen Bruce S. Ault and George C. Pimentel*	1649
Optical Activity of Oriented Helices. Quadrupole Contributions Joseph Snir and John Schellman*	1653
Energy Parameters and Charge-Transfer Spectra of the Complexes of Bromine with Substituted Pyridines P. Huyskens,* J. D'Hondt, F. Govaerts, and Th. Zeegers-Huyskens	1662
Vibrational Transitions in Atom + Diatomic Systems. Use of the Lennard-Jones Potential Hyung Kyu Shin	1666
SCF-MO Calculations of Spectra of Ketyl Radicals and Radical Anions of Uracil and Cytosine Alec Grimison and Manfred K. Eberhardt*	1673
Potentials of Glass Membranes in Molten Binary Nitrates T. J. van Reenen* and W. J. de Wet	1676
Heats of Mixing of Globular Molecules Differing in Size D. D. Deshpande and D. Patterson*	1679
Ligand Field Theory of Metal Sandwich Complexes. Axial Field Spin-Orbit Perturbation Calculations for d ¹ (d ⁹), d ² (d ⁸), and d ³ (d ⁷) Configurations Keith D. Warren	1681 ■
Revised Group Additivity Parameters for the Enthalpies of Formation of Oxygen-Containing Organic Compounds H. K. Eigenmann, D. M. Golden,* and S. W. Benson	1687 ■

Film Bursting. V. The Effect of Various Atmospheres and the Anomaly of Newton Black Films Karol J. Mysels* and B. R. Vijayendran	1692
Polymorphism in the Solid Solutions, Potassium Chloride-Sodium Chloride and Rubidium Chloride-Potassium Chloride, at High Pressure Lin-gun Liu,* William A. Bassett, and Maria S. Liu	1695
Thermodynamic Properties of the Reciprocal System ($K^+, Ag^+ NO_3^-, SO_4^{2-}$) from Its Phase Diagram M. L. Saboungi, C. Vallet,* and Y. Doucet	1699
Kinetics and Mechanism of the Reaction between Hydroxyapatite and Fluoride in Aqueous Acidic Media Zao-Shon Liang and William I. Higuchi*	1704
Effect of the Dielectric Constant on the Reactivity of the Solvated Electron F. Barat, L. Gilles, B. Hickel,* and B. Lesigne	1711
An Electron Paramagnetic Resonance Study of π System Interaction in Dithiin Derivatives Dolan H. Eargle, Jr.,* and Maria de Conceicao Ramos de Carvalho	1716
Influence of Annealing on the Catalytic Activity of Cold-Worked Metals for the Decomposition of Formic Acid Shozo Kishimoto	1719
Electron Transfer Interactions between Superoxide Ion and Organic Compounds R. Poupko and I. Rosenthal*	1722

■ Supplementary material for this paper is available separately, in photocopy or microfiche form. Ordering information is given in the paper.

* In papers with more than one author, the asterisk indicates the name of the author to whom inquiries about the paper should be addressed.

AUTHOR INDEX

Andrews, L., 1640, 1646	Eberhardt, M. K., 1673	Lesigne, B., 1711	Saboungi, M. L., 1699
Ault, B. S., 1649	Eigenmann, H. K., 1687	Liang, Z.-S., 1704	Samuni, A., 1629
		Liu, L., 1695	Schellman, J., 1653
Barat, F., 1711	Gilles, L., 1711	Liu, M. S., 1695	Shin, H. K., 1666
Bassett, W. A., 1695	Golden, D. M., 1687	Mezaki, R., 1601	Shragge, P. C., 1624
Benson, S. W., 1687	Govaerts, F., 1662	Mittal, J. P., 1620	Smith, P. M., 1635
Bullock, A. T., 1635	Greenstock, C. L., 1624	Mittal, L. J., 1620	Snir, J., 1653
	Grimison, A., 1673	Mysels, K. J., 1692	
Cameron, G. G., 1635	Hamill, W. H., 1616	Naccache, C., 1606	Tevault, D. E., 1640, 1646
de Carvalho, M. d. C. R.,	Hayon, E., 1620	Neta, P., 1629	Vallet, C., 1699
1716	Hickel, B., 1711	Oki, S., 1601	van Reenen, T. J., 1676
Deshpande, D. D., 1679	Higuchi, W. I., 1704	Patterson, D., 1679	Vedrine, J. C., 1606
de Wet, W. J., 1676	Hiraoka, K., 1616	Pimentel, G. C., 1649	Vijayendran, B. R., 1692
D'Hondt, J., 1662	Hoffman, R. M., 1611	Poupko, R., 1722	Warren, K. D., 1681
Doucet, Y., 1699	Hunt, J. W., 1624	Rosenthal, I., 1722	Werner, T. C., 1611
	Huyskens, P., 1662		
Eargle, D. H., Jr., 1716	Kishimoto, S., 1719		Zeegers-Huyskens, T., 1662

NOTICE TO AUTHORS

I. General Considerations

The Journal of Physical Chemistry is devoted to reporting both experimental and theoretical research dealing with fundamental aspects of physical chemistry. Space limitations necessitate giving preference to research articles dealing with previously unanswered basic questions in physical chemistry. Acceptable topics are those of general interest to physical chemists, especially work involving new concepts, techniques, and interpretations. Research that may lead to reexaminations of generally accepted views is, of course, welcome.

Authors reporting data should include an interpretation of the data and its relevance to the theories of the properties of matter. However, the discussion should be concise and to the point and excessive speculation is to be discouraged. Papers reporting redeterminations of existing data will be acceptable only if there is reasonable justification for repetition: for example, if the more recent or more accurate data lead to new questions or to a reexamination of well known theories. Manuscripts that are essentially applications of chemical data or reviews of the literature are, in general, not suitable for publication in *The Journal of Physical Chemistry*. Detailed comparisons of methods of data analysis will be considered only if the paper also contains original data, or if such comparison leads to a genesis of new ideas.

Authors should include an introductory statement outlining the scientific rationale for the research. The statement should clearly specify the questions for which answers are sought and the connection of the present work with previous work in the field. All manuscripts are subject to critical review. It is to be understood that the final decision relating to a manuscript's suitability rests solely with the editors.

Symposium papers are sometimes published as a group, but only after special arrangement with the editor.

Authors' attention is called to the "Handbook for Authors," available from the Special Issues Sales Department, American Chemical Society, 1155 Sixteenth St., N.W., Washington, D. C. 20036, in which pertinent material is to be found.

II. Types of Manuscripts

The Journal of Physical Chemistry publishes two types of manuscripts: *Articles* and *Communications*.

A. *Articles* should cover their subjects with thoroughness, clarity, and completeness. However, authors should also strive to make their *Articles* as concise as possible, avoiding unnecessary historical background. Abstracts to *Articles* should be brief—300 words is a maximum—and should serve to summarize the significant data and conclusions. The abstract should convey the essence of the *Article* to the reader.

B. *Communications* are of two types, *Letters* and *Comments*. Both types are restricted to three-quarters of a page (750 words or the equivalent) including tables, figures, and text, and both types of *Communications* are subject to critical review, but special efforts will be made to expedite publication.

Letters should report preliminary results whose immediate availability to the scientific community is deemed important, and whose topic is timely enough to justify the double publication that usually results from the publication of a *Letter*.

Comments include significant remarks on the work of others. The editors will generally permit the authors of the work being discussed to reply.

The category of *Notes* has been discontinued since the handling of such manuscripts was precisely the same as that of *Articles* save for the requirement of an Abstract, and since even a short *Article* will need an Abstract ultimately, it seems as well to ask the author to provide this. Short *Articles* will of course continue to be welcome contributions.

III. Introduction

All manuscripts submitted should contain brief introductory remarks describing the purpose of the work and giving sufficient background material to allow the reader to appreciate the state-of-knowledge at the time when the work was done. The introductory remarks in an *Article* should constitute the first section of the paper and should be labeled accordingly. In *Communications*, the introductory material should not be in such a separate section. To judge the appropriateness of the manuscript for *The Journal of Physical Chemistry*, the editors will place considerable weight on the author's intentions as stated in the Introduction.

IV. Functions of Reviewers

The editors request the scientific advice of reviewers who are active in the area of research covered by the manuscript. The reviewers act only in an advisory capacity and the final decision concerning a manuscript is the responsibility of the editors. The reviewers are asked to comment not only on the scientific content, but also on the manuscript's suitability for *The Journal of Physical Chemistry*. With respect to *Communications*, the reviewers are asked to comment specifically on the urgency of publication. Authors are encouraged to suggest, when submitting a manuscript, names of scientists who could give a disinterested and informed and helpful evaluation of the work. All reviews are anonymous and the reviewing process is most effective if reviewers do not reveal their identities to the authors. An exception arises in connection with a manuscript submitted for publication in the form of a comment on the work of another author. Under such circumstances the first author will, in general, be allowed to review the communication and to write a rebuttal, if he so chooses. The rebuttal and the original communication may be published together in the same issue of the journal. Revised manuscripts are generally sent back to the original reviewers, who are asked to comment on the revisions. If only minor revisions are involved, the editors examine the revised manuscript in light of the recommendations of the reviewers without seeking further opinions. For the convenience of reviewers, authors are advised to indicate clearly, either in the manu-

script or in a covering letter, the specific revisions that have been made.

V. Submission of Manuscripts

All manuscripts must be submitted in triplicate to expedite handling. Manuscripts must be typewritten, double-spaced copy, on $8\frac{1}{2} \times 11$ in. paper. Legal sized paper is not acceptable. Authors should be certain that copies of the manuscript are clearly reproduced and readable. Authors submitting figures must include the original drawings or photographs thereof, plus three xerographic copies for review purposes. These reproductions of the figures should be on $8\frac{1}{2} \times 11$ in. paper. Graphs must be in black ink on white or blue paper. Figures and tables should be held to a minimum consistent with adequate presentation of information. All original data which the author deems pertinent must be submitted along with the manuscript. For example, a paper reporting a crystal structure should include structure factor tables for use by the reviewers.

All references and explanatory notes, formerly set up as footnotes on individual pages, are now grouped at the end of the article in a section called "References and Notes." They should be numbered consecutively in the order in which they are first mentioned in the text, and the complete list of notes and literature citations should appear at the end of the manuscript. Nomenclature should conform to that used in *Chemical Abstracts* and mathematical characters should be underlined for italics, Greek letters should be annotated, and subscripts and superscripts clearly marked.

Papers should not depend for their usefulness on unpublished material, and excessive reference to material in press is discouraged. References not readily available (*e.g.*, private technical reports, preprints, or articles in press) that are necessary for a complete review of the paper must be included with the manuscript for use by the reviewers.

VI. Revised Manuscripts

A manuscript sent back to an author for revision should be returned to the editor within 6 months; otherwise it will be considered withdrawn and treated as a new manuscript when and if it is returned. Revised manuscripts returned to the editor must be submitted in triplicate and all changes should be made by typewriter. Unless the changes are very minor, all pages affected by revision must be re-typed. If revisions are so extensive that a new typescript of the manuscript is necessary, it is requested that a copy of the original manuscript be submitted along with the revised one.

VII. Supplementary Material

From time to time manuscripts involve extensive tables, graphs, spectra, mathematical material, or other "supplementary material" which, though of value to the specialized reader who needs all the data or all the detail, does not help and often hinders the effective presentation of the work being reported. The American Chemical Society has instituted a policy of including such supplementary material in the *microfilm* editions of its journals, which are available in many scholarly libraries; in addition, interested readers will be able to obtain the microfilm material directly at

nominal cost. Authors are encouraged to make use of this resource, in the interests of shorter articles (which mean more rapid publication) and clearer, more readable presentation.

Supplementary material for inclusion in the microfilm edition should accompany a manuscript at the time of its original submission to an editor. It should be clipped together and attached at the end of the manuscript, along with a slip of paper clearly indicating that the material is "supplementary material for the microfilm edition." A paragraph should appear at the end of the paper indicating the nature of the supplementary material and the means by which the interested reader might be able to obtain copies of the data without use of the microfilm edition itself. The following is an example.

Supplementary Material Available. A listing of structure factor amplitudes will appear following these pages in the microfilm edition of this volume of the journal. Photocopies of the supplementary material from this paper only or microfiche (105×148 mm, $20\times$ reduction, negatives) containing all of the supplementary material for the papers in this issue may be obtained from the Journals Department, American Chemical Society, 1155 16th St., N.W., Washington, D. C. 20036. Remit check or money order for \$0.00 for photocopy or \$2.00 for microfiche, referring to code number JPC-00-0000.

The amount of money to be indicated in the blanks will be filled in by the Editorial Office at Easton, Pa., after the acceptance of an article.

VIII. Proofs and Reprints

Galley proofs, original manuscript, cut copy, and reprint order form are sent by the printer directly to the author who submitted the manuscript. The attention of the authors is directed to the instructions which accompany the proof, especially the requirement that all corrections, revisions, and additions be entered on the proof and not on the manuscript. Proofs should be checked against the manuscript (in particular all tables, equations, and formulas, since this is not done by the editor) and returned as soon as possible. No paper is released for printing until the author's proof has been received. Alterations in an article after it has been set in type are made at the author's expense, and it is understood that by entering such alterations on proofs the author agrees to defray the cost thereof. The filled-out reprint form must be returned with the proof, and if a price quotation is required by the author's organization a request for it should accompany the proof. Since reprinting is generally done from the journal press forms, all orders must be filed before press time. None can be accepted later, unless a previous request has been made to hold the type. Reprint shipments are made a month or more after publication, and bills are issued by the printer subsequent to shipment. Neither the editors nor the Washington office keeps any supply of reprints. Therefore, only the authors can be expected to meet requests for single copies of papers.

A page charge is assessed to cover in part the cost of publication. Although payment is expected, it is not a condition for publication. Articles are accepted or rejected only on the basis of merit, and the editor's decision to publish the paper is made before the charge is assessed. The charge per journal page is \$50.

THE JOURNAL OF PHYSICAL CHEMISTRY

Registered in U. S. Patent Office © Copyright, 1973, by the American Chemical Society

VOLUME 77, NUMBER 13 JUNE 21, 1973

Mechanistic Structure of the Water-Gas Shift Reaction in the Vicinity of Chemical Equilibrium

Shoichi Oki

Department of Chemistry, Utsunomiya University, Utsunomiya, Tochigi, Japan

and Reiji Mezaki*

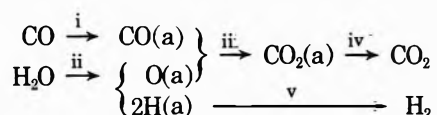
Department of Chemical Engineering, New York University, Bronx, New York 10453 (Received October 26, 1972)

The mechanistic study of the water-gas shift reaction over an iron oxide catalyst was made utilizing the isotopic exchange reaction of oxygen-18. Reaction temperatures ranged from 400 to 450° and the total pressure of the reaction system was 80 mm. The forward and backward rates of the rate-determining steps of the reaction, that is, $\text{CO} \rightleftharpoons \text{CO(a)}$ (step i) and $2\text{H(a)} \rightleftharpoons \text{H}_2$ (step v) were computed and compared. The comparison indicated that the order of magnitude of the forward rate of step i is comparable with that of the forward rate of step v and that in the early stage of the reaction, step v would govern the overall rate, whereas step i becomes the governing step as the reaction progresses to approach the chemical equilibrium. The results are in good agreement with those of earlier investigations.

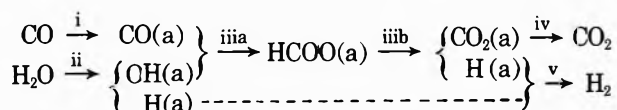
Introduction

The mechanistic study of the water-gas shift reaction has been greatly advanced by the use of isotopic tracers.¹⁻⁵ In the study the stoichiometric number concept introduced by Horiuti⁶ has been intensively used for the determination of rate-controlling step or steps in various reaction mechanisms proposed. Recently Oki and Kaneko¹⁻⁵ have employed three different isotopic tracers including deuterium, carbon-14, and oxygen-18 to obtain more definitive conclusions concerning rate-controlling steps as well as reaction mechanisms of the water-gas shift reaction over an iron oxide catalyst. Their experimental results indicated that reaction mechanisms I and II are most plausible and that steps i and v of these mechanisms appear to be rate controlling.

Mechanism I



Mechanism II



More recently Mezaki and Oki⁷ reanalyzed the rate data gathered in the experiment^{4,5} with oxygen-18 and found that for the experimental conditions employed the nature of the rate-controlling step slowly changes from step v dominance to steps i and v dominance as the experimental conditions approach chemical equilibrium. In this investigation only the ratio of the forward and backward rates of step i were computed for various experimental conditions to find the relative importance of step i to the overall reaction. It was not yet known how the forward and backward rates of steps i and v change as the reaction conditions approach chemical equilibrium.

The present study thus aims to calculate the forward and backward rates of steps i and v employing experimental data obtained with oxygen-18 and to examine whether these rates decrease or increase with change in experimental conditions, in particular with decrease in the overall

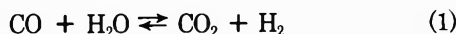
- (1) Y. Kaneko and S. Oki, *J. Res. Inst. Catal., Hokkaido Univ.*, **13**, 55 (1965).
- (2) Y. Kaneko and S. Oki, *J. Res. Inst. Catal., Hokkaido Univ.*, **13**, 169 (1965).
- (3) Y. Kaneko and S. Oki, *J. Res. Inst. Catal., Hokkaido Univ.*, **15**, 185 (1967).
- (4) S. Oki, Y. Kaneko, Y. Arai, and M. Shimada, *Shokubai*, **11**, 184 (1969).
- (5) S. Oki, J. Happel, M. A. Hnatow, and Y. Kaneko, *Proc. Int. Congr. Catal., 5th*, 1972, in press.
- (6) J. Horiuti and M. Ikushima, *Proc. Imp. Acad. Jap.*, **15**, 39 (1939).
- (7) R. Mezaki and S. Oki, *J. Catal.*, in press.

rate of the water-gas shift reaction. It was hoped that the above investigation would provide a much clearer insight into the change of rate-controlling step or steps of the reaction if that change occurs when the reaction conditions pass from one extreme to another.

Mathematical Analysis

In this section we developed mathematical expressions by which the forward and backward rates of oxygen paths of mechanisms I and II are calculated.

The overall reaction of the water-gas shift reaction is given by the equation



Consider a closed circulating reaction system in which a gaseous mixture consisting of carbon monoxide, water vapor, carbon dioxide, and hydrogen is circulating through an iron oxide catalyst bed. When mechanism I is assumed, the following relationships exist for the oxygen paths i, ii, iii, and iv of mechanism I.

$$t_{\text{CO}} = -\frac{d(n_{\text{CO}}Z_{\text{CO}})}{dt} = Z_{\text{CO}}v_{+i} - Z_{\text{CO(a)}}v_{-i} \quad (2)$$

$$= Z_{\text{CO(a)}}v_{+iii} - Z_{\text{CO}_2\text{(a)}}v_{-iii} \quad (3)$$

$$t_{\text{H}_2\text{O}} = -\frac{d(n_{\text{H}_2\text{O}}Z_{\text{H}_2\text{O}})}{dt} = Z_{\text{H}_2\text{O}}v_{+ii} - Z_{\text{O(a)}}v_{-ii} \quad (4)$$

$$= Z_{\text{O(a)}}v_{+iii} - Z_{\text{CO}_2\text{(a)}}v_{-iii} \quad (5)$$

$$t_{\text{CO}_2} = \frac{d(n_{\text{CO}_2}Z_{\text{CO}_2})}{dt} = Z_{\text{CO}_2\text{(a)}}v_{+iv} - Z_{\text{CO}_2}v_{-iv} \quad (6)$$

where $v_{\pm i}$ denotes the forward and backward rates of step i and n_i is the number of moles of the i component in the reaction system. Note that Z_i is the atomic fraction of oxygen-18 in i component and that $Z_{i(a)}$ is the atomic fraction of oxygen-18 in the i species adsorbed on the catalyst surface.

Solving for $Z_{\text{CO(a)}}$ and $Z_{\text{CO}_2\text{(a)}}$ in eq 2 and 6, respectively, and substituting the resulting solutions in eq 3, we obtain

$$t_{\text{CO}} = \frac{v_{+iii}}{v_{-i}}(Z_{\text{CO}}v_{+i} - t_{\text{CO}}) - \frac{v_{-iii}}{v_{+iv}}(Z_{\text{CO}_2}v_{-iv} + t_{\text{CO}_2}) \quad (7)$$

For an oxygen exchange path which includes steps i, iii, and iv, we define

$$V = V_{+i,iii,iv} - V_{-i,iii,iv} \quad (8)$$

where V denotes the overall rate of the water-gas shift reaction and $V_{+i,iii,iv}$ and $V_{-i,iii,iv}$ are, respectively, the forward and the backward rate of the oxygen exchange path.

Using Csuhá's definitions⁸ of $V_{+i,iii,iv}$ and $V_{-i,iii,iv}$ and combining eq 7 and 8, we get

$$\frac{v_{+i}v_{+iii}v_{+iv}}{v_{-i}v_{-iii}v_{-iv}} = \left\{ \frac{1}{t_{\text{CO}} - VZ_{\text{CO}}} (t_{\text{CO}} - VZ_{\text{CO}_2}) + \left(\frac{v_{+iv}}{v_{-iv}} - 1 \right) (t_{\text{CO}} - t_{\text{CO}_2}) \right\} \quad (9)$$

A detailed derivation of eq 9 is presented elsewhere.⁵

The results of the earlier investigations^{4,5} which were obtained under exactly the same reaction conditions as those employed in this work showed that the forward and backward rates of steps ii, iii, and iv are extremely high compared to those of steps i and v. On this ground it is assumed that the following relationship also holds for our case, that is

$$v_{+iii}/v_{-iii} \cong 1 \quad \text{and} \quad v_{+iv}/v_{-iv} \cong 1 \quad (10)$$

Hence eq 9 reduces to

$$\frac{v_{+i}}{v_{-i}} = \frac{t_{\text{CO}} - VZ_{\text{CO}_2}}{t_{\text{CO}} - VZ_{\text{CO}}} \quad (11)$$

The overall reaction rate V of eq 11 can be obtained from

$$V = -dn_{\text{CO}}/dt \quad (12)$$

Combination of eq 2, 11, and 12 gives

$$\frac{v_{+i}}{v_{-i}} = 1 - (Z_{\text{CO}_2} - Z_{\text{CO}}) \left(\frac{dn_{\text{CO}}}{dt} / n_{\text{CO}} \frac{dZ_{\text{CO}}}{dt} \right) \quad (13)$$

For the direct use of experimental data the following equation may be more advantageously employed

$$\frac{v_{+i}}{v_{-i}} = 1 - (Z_{\text{CO}_2} - Z_{\text{CO}}) \left(\frac{dp_{\text{CO}}}{dt} / p_{\text{CO}} \frac{dZ_{\text{CO}}}{dt} \right) \quad (14)$$

where p_{CO} denotes the partial pressure of carbon monoxide in the system.

The overall net reaction rate V is also given in terms of v_{+i} and v_{-i} , that is

$$V = -dp_{\text{CO}}/dt = v_{+i} - v_{-i} \quad (15)$$

Note that eq 14 and 15 may be solved simultaneously to give the values of v_{+i} and v_{-i} for various experimental conditions.

When steps i and v are rate controlling, the chemical affinity of the water-gas shift reaction, $-\Delta G$, may be expressed by the following relationships

$$-\Delta G = RT \ln \left\{ \frac{p_{\text{CO}}p_{\text{H}_2\text{O}}}{p_{\text{H}_2}p_{\text{CO}_2}} K_p \right\} \quad (16)$$

and

$$\Delta G = RT \left\{ \ln \left(\frac{v_{+i}}{v_{-i}} \right) + \ln \left(\frac{v_{+v}}{v_{-v}} \right) \right\} \quad (17)$$

in which K_p is the thermodynamic equilibrium constant of the reaction, T is the reaction temperature, and p_i is the partial pressure of gaseous component i. Thus the values of v_{+v} and v_{-v} can be readily obtained if those of v_{+i} and v_{-i} are available.

Experimental Section

Heavy water containing 10.9% ¹⁸O was purchased from the Research and Development Ltd., Rehovoth, Israel, and was used without further purification. Carbon monoxide was prepared by dehydration of formic acid and purified by passing it through a liquid nitrogen trap. Carbon dioxide was formed by decomposition of sodium bicarbonate and purified by vacuum distillation. Hydrogen gas was supplied by Takayama Shoji Co. For purification the hydrogen gas was passed through a silica gel column, a liquid nitrogen trap, a palladium thimble which was kept at 380°, and a liquid nitrogen trap. All the gases fed into the reaction system were analyzed by a mass spectrometer and the analysis indicated that the concentrations of all the gases were higher than 99.99%.

An iron oxide catalyst was donated by Mitsubishi Kasei Co., Ltd. The catalyst was crushed and screened to about 12 mesh. The amount of the catalyst used was 0.5 g. On pretreatment of the catalyst iron oxide in the form of Fe₂O₃ was reduced to Fe₃O₄. Prior to the experiments, the catalyst was bathed with a gaseous mixture of carbon

(8) R. S. Csuhá and J. Happel, *AIChE J.*, **17**, 927 (1971).

monoxide, water vapor containing oxygen-18, hydrogen, and carbon dioxide, for approximately 100 hr at 500°. After each experiment, the reaction system was evacuated at the temperature of that experiment.

The reaction temperature ranged from 400 to 450°. For all experiments the feed contained carbon monoxide, water vapor, carbon dioxide, and hydrogen. The partial pressures of these component gases were varied widely.

In absence of the catalyst a series of experiments was made by employing the same experimental conditions as those used for experiments in the presence of the catalyst. Results of these blank experiments showed that no oxygen exchange nor water-gas shift reaction occurred to any measurable extent. Thus it was established that all measurable conversions of these reactions were due to the iron oxide catalyst.

A detailed description of the experimental apparatus and the procedure utilized in this study was presented elsewhere.² A closed-recycling type reactor was used. The entire apparatus was made of Pyrex glass because our experiments showed that oxygen exchange between the wall of apparatus and oxygen-containing gases was minimized when Pyrex glass was utilized.

Gas samples were drawn into gas sampling bulbs at specified time intervals. The atomic fractions of oxygen-18 in carbon monoxide and carbon dioxide were determined by a Hitachi mass spectrometer, RMS-3B type, with a constant electron accelerating voltage of 80 V.

Preliminary experiments were performed to determine the effect of gas flow rate on reaction rate. Using 0.5 g of the iron oxide catalyst, the reaction rates were measured for various flow rates of gas mixture at temperatures between 400 and 450° and at a total pressure of 80 mm. The mixture initially contained equal portions of carbon monoxide, carbon dioxide, hydrogen, and water vapor. The result of these preliminary experiments indicated that mass flow rates greater than 1.5 g/min of catalyst had no appreciable effect on the reaction rate. Consequently, this flow rate was employed in the present study. By using the method of Yang and Hougen⁹ we calculated the partial pressure drops of the reactants and the products between the gas stream and exterior surface of the catalyst particle for the highest possible reaction rate. It was determined that the drops do not exceed 0.2% of their ambient values. Concerning diffusion inside the catalyst, calculations¹⁰ showed that the value of the effectiveness factor was essentially unity even at the highest reaction rate. In light of these experimental and computational results it was considered that the gaseous diffusion inside and outside the catalyst has no effect on the reaction rate for the experimental conditions of this study.

Results

Table I¹¹ shows the experimental data used for the computation of the forward and backward rates of step i, step v, and the rate of the overall reaction. These rates were calculated by a procedure detailed in a previous section.

Figure 1 presents, as an example, the rates of run 1. Similar results were obtained for other sets of experimental data. As can be seen from the figure, the forward and backward rates of step i decrease rather monotonously and the difference of these two rates, that is, the net overall rate diminishes continuously as the reaction conditions approach the chemical equilibrium. Whereas the forward and backward rates of step v seem to increase as the

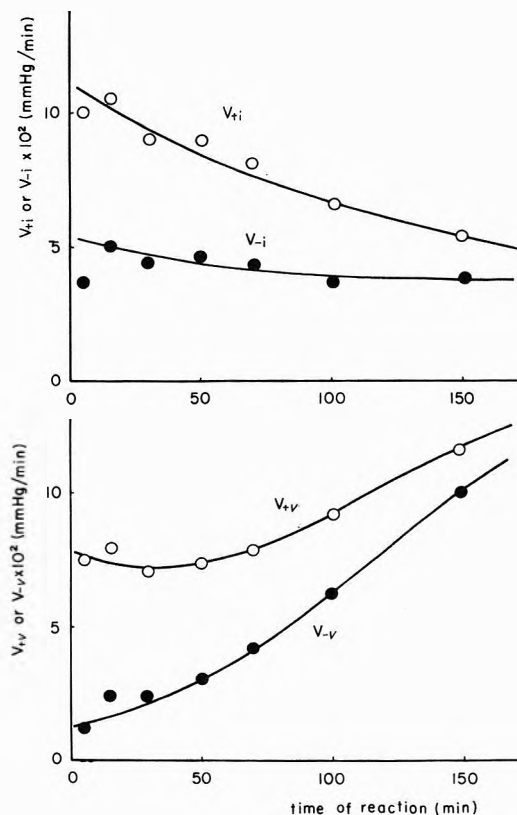


Figure 1. The forward and backward rates of step i and step v (run 1, reaction temperature 400°).

water-gas shift reaction proceeds. The difference of these two rates of step v is also reduced steadily, indicating that the rate of increase of the backward rate of step v is higher compared to that of the forward rate. This difference, needless to say, ultimately vanishes when the reaction reaches chemical equilibrium. It should be noted that the forward rate of step v goes through the minimum value to approach equilibrium conditions.

In Figure 2 the forward reaction rates of run 1 are compared. The comparison indicates that at the beginning of the reaction the forward rate of step i is higher than that of step v. As the reaction progresses toward equilibrium, however, the magnitudes of these rates were reversed.

Figure 3 shows relationships between the forward rates of step i and the partial pressure of carbon monoxide for various reaction temperatures. In Figure 4 the dependence of the forward rate of step v on the partial pressures of water vapor is presented. We examine these figures more fully in Discussion section.

Discussion

It can be seen from Table I that for all the runs Z_{CO} increases gradually with reaction time elapsed, whereas the maximum Z_{CO_2} occurs within the first 30 min of reaction time. This experimental result may provide evidence to support the adequacy of reaction mechanisms of the

- (9) K. H. Yang and O. A. Hougen, *Chem. Eng. Progr.*, **46**, 146 (1950).
 (10) C. N. Satterfield, "Mass Transfer in Heterogeneous Catalysis," M.I.T. Press, Cambridge, Mass., 1970.
 (11) Table I will appear following these pages in the microfilm edition of this volume of the journal. Single copies may be obtained from the Business Operations Office, Books and Journals Division, American Chemical Society, 1155 Sixteenth St., N.W., Washington, D. C. 20036. Remit check or money order for \$3.00 for photocopy or \$2.00 for microfiche, referring to code number JPC-73-1601.

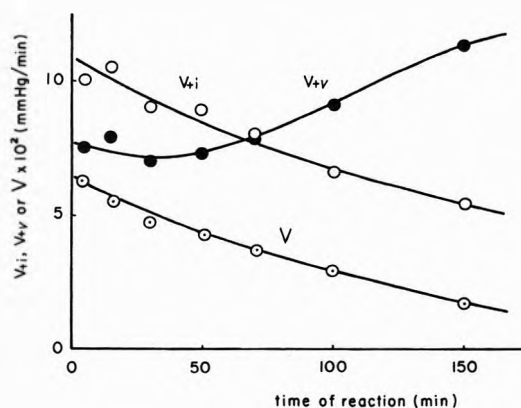


Figure 2. A comparison of the forward rates of step i, step v, and the overall reaction (run 1, reaction temperature 400°).

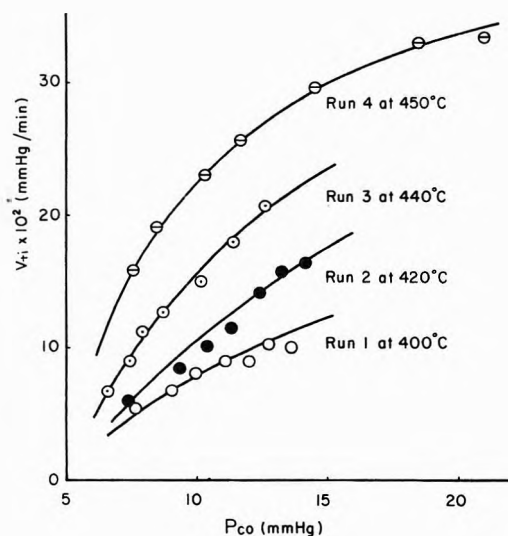


Figure 3. Relationships between the forward rates of step i and the partial pressures of carbon monoxide.

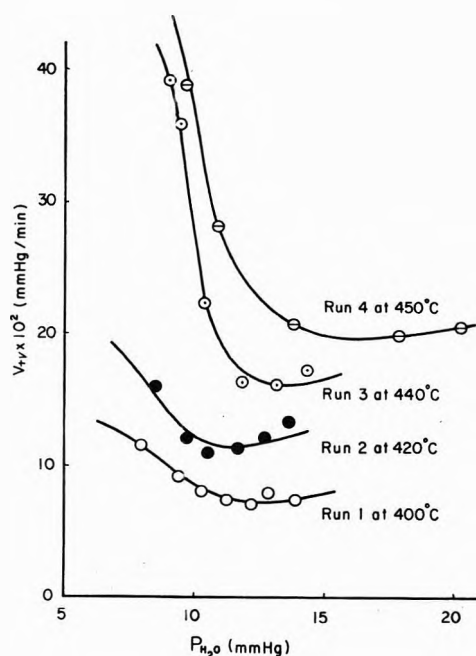


Figure 4. Relationships between the forward rates of step v and the partial pressures of water vapor.

water-gas shift reaction, which were proposed in an earlier section of this article. That is, water vapor containing oxygen-18 is readily transferred into carbon dioxide because the rates of steps ii, iii, and iv are quite high. During this period of reaction Z_{CO_2} increases sharply with reaction time. The accumulation of oxygen-18 in the carbon dioxide increases the reverse transfer rates of oxygen-18 via steps i-iv. In particular, a noticeable amount of oxygen-18 is transferred to carbon monoxide by way of step i, the rate of which is considered to be low in the fore-mentioned mechanisms. This balance between the forward and reverse transfer rates of oxygen-18 seems to explain the occurrence of the maximum Z_{CO_2} during the course of the reaction.

It is evident from eq 13 and 14 that experimental measurements of Z_{CO} and Z_{CO_2} have a profound effect on the estimates of v_{+i} , v_{-i} , v_{+v} , and v_{-v} . It is also evident from the derivation of eq 2-14 that the relationship of eq 14 is dependent upon the reaction mechanism of the reaction. In the case where the oxygen reaction occurs through a scheme or schemes other than those included in mechanism I or II, the results obtained here would become equivocal. For this reason, a comprehensive study was made on isotopic oxygen exchange reaction which may possess significant bearing on the present investigation. Several investigators^{12,13} reported that the isotopic oxygen exchange occurs between oxygen in reactant gases and the lattice oxygen of the catalyst. In order to determine the extent of the isotopic oxygen exchange reaction, about 20 mm of water vapor which contained 10.9% of oxygen-18 was allowed to contact the iron oxide catalyst at temperatures between 400 and 450° to attain equilibrium of the exchange reaction. A similar experiment was made by using carbon dioxide containing oxygen-18. Note that the amount of oxygen-18 employed was the same as that used for the rate study. These experimental studies showed that the amount of oxygen of the iron oxide catalyst which was replaced with gaseous oxygen-18 was about 10^{19} atoms. In the rate study approximately 2×10^{22} oxygen-18 atoms were introduced to the reaction system. Assuming that carbon dioxide, carbon monoxide, and water vapor, respectively, exchange their oxygen-18 with the lattice oxygen atoms of the catalyst in proportion to the partial pressures of oxygen-18 carrying carbon dioxide, carbon monoxide, and water vapor, it was determined that the errors in Z_{CO_2} and Z_{CO} due to this isotopic oxygen exchange were less than 0.1% under the present experimental conditions. Temkin¹⁴ and Glavachek¹⁵ reported that a Rideal-Eley type mechanism can best describe the rate data of the water-gas shift reaction, obtained using an iron-chromium catalyst. However, the results of previous investigations^{1-5,7,16} with deuterium, oxygen-18, and carbon-14 entirely ruled out this reaction mechanism. It may also be conceivable that the isotopic oxygen exchange takes place by homogeneous reactions. A case of interest is represented by $H_2O + CO_2 \rightleftharpoons H_2CO_3$ equilibrium. The compound H_2CO_3 exists only in the liquid phase. Thus it seems improbable that the compound is formed at temperatures as high as those employed in this investigation.

(12) O. V. Krylov, Z. A. Markova, I. I. Tretyakov, and E. A. Fokina, *Kinet. Katal.*, 6, 128 (1965).

(13) C. Wagner, *Advan. Catal.*, 21, (1970).

(14) G. G. Shchibrya, N. M. Morozov, and M. I. Temkin, *Kinet. Katal.*, 6, 1057 (1965).

(15) V. Glavachek, M. Marek, and M. Korzhinkova, *Kinet. Katal.*, 9, 1107 (1968).

(16) S. Oki and R. Mezaki, *J. Phys. Chem.*, 77, 447 (1973).

On the basis of the above discussion the experimental measurements of Z_{CO_2} and Z_{CO} shows reasonably accurate values of exchanged oxygen-18 by the operation of mechanism I or II during the course of the water-gas shift reaction.

The foregoing results present various interesting features of the rate-determining steps of the water-gas shift reaction. First, as shown in Figure 2, the order of magnitude of the forward rate of step i is comparable with that of the forward rate of step v. This is true even if the experimental conditions, in particular, the partial pressures of component gases, vary rather widely. The result would justify that of an earlier mechanistic study^{5,16} in which Oki and coworkers proposed that both step i and step v are rate determining. Second, for the reaction conditions employed in this study (approximately equal portions of carbon monoxide, water vapor, carbon dioxide, and hydrogen were introduced in the closed reaction system) the rate of step i is higher than that of step v in the early stage of the reaction and the rate of step v increases rapidly, yielding a higher rate compared to the forward rate of step i as experimental conditions approach equilibrium. This implies that during the earlier stage of the reaction, in which the partial pressure of carbon monoxide is relatively high, step v would control the overall rate and that step i becomes governing as the reaction proceeds toward equilibrium. The result partially supports that of a more recent investigation,⁷ in which Mezaki and Oki found that the rate-determining step of the water-gas shift reaction gradually changes from dominance of step v to dominance of step v and step i.

In these earlier studies^{5,7} the rate-determining step or steps of the reaction were pinpointed from the free energy change associated with the individual elementary step or from the apparent stoichiometric number observed by the experiments. In the present study we computed the forward and backward rates of step i and step v to examine the relative contribution of each step to the overall rate. The calculation of the forward and backwards rates, obviously, provides a much clearer view for the change of rate-determining step, if it occurs. It must be pointed out that the information which has been accumulated so far concerning the rate-determining step of the water-gas shift reaction is quite consistent. For example, as can be seen from Figure 2, there exists a set of experimental conditions wherein the forward rates of step i and step v coincide. For these particular conditions the free energy changes of step i and step v are equal (see ref 5 and 7) and, moreover, the apparent stoichiometric number observed should be 2 (see ref 5 and 7).

At this point one may wonder in what manner the for-

ward and backward rates attain equilibrium. Unfortunately the data gathered in the present study may not be sufficient to precisely predict the behavior of these rates in the immediate vicinity of equilibrium. However, the forward rate of step i would continuously decrease up to equilibrium, whereas the forward rate of step v would level off somewhere to reach the equilibrium point.

As will be discussed below, the forward and backward rates of step i and step v depend strongly on the partial pressures of the gaseous components. Thus the above pattern of the forward and backward rates would completely change when different experimental conditions are used. From the reaction scheme presented in a preceding section, the forward and backward rates of step i and step v may be written as

$$v_{+i} = k_{+i}p_{CO}(1 - \theta) \quad (18)$$

$$v_{-i} = k_{-i}\theta_{CO} \quad (19)$$

$$v_{+v} = k_{+v}(\theta_H)^2 \quad (20)$$

$$v_{-v} = k_{-v}p_{H_2}(1 - \theta) \quad (21)$$

where k_{+s} and k_{-s} are, respectively, the rate constants of the forward and backward rates of step s, θ is the fraction of total active site occupied by gaseous species, and θ_i is the fraction of active site occupied by species i.

As shown in Figures 3 and 4 the linear relationships are not obtained for the forward rates of step i and step v. Furthermore, the calculated backward rate of step i decreases with increase in the partial pressure of carbon dioxide. In the light of these experimental findings, apparently the forward and backward rates of step i and step v cannot be described by simple Langmuir-type adsorption models. More elaborate models should be used for adequate representation of experimental data. Presumably the concentration of adsorbed gaseous species as well as the total concentration of empty adsorption sites undergo some change in the course of the reaction. It may be conceivable that the fraction of adsorption sites occupied by atomic hydrogen, θ_H , increases with increase in the hydrogen partial pressure to produce a more reduced state of the catalyst surface. Because of this state of the surface carbon monoxide molecules adsorbed on the surface may be competitively desorbed from the surface to decrease the backward rate of step i (see eq 19).

Further experimentation is vitally needed to explore the true conditions of the catalyst surface and to analyze more rigorously the results obtained in this investigation. However, the above assumption about the surface would be sufficient to provide a qualitative explanation of our experimental results.

Electron Spin Resonance Study of Oxygen Species Adsorbed on γ -Irradiated Zeolites

Jacques C. Vedrine* and Claude Naccache

Institut de Recherches sur la Catalyse, C.N.R.S., 69100 Villeurbanne, France (Received October 24, 1972)

Publication costs assisted by Institut de Recherches sur la Catalyse, C.N.R.S.

Molecular oxygen instantaneously reacts at 77 K with V centers created by γ irradiation of hydrogen faujasite and mordenite type zeolites. The paramagnetic oxygen species have been found to be unstable and the V centers to be restored by outgassing at room temperature. The esr spectra are characterized by two signals with the following parameters: for HY zeolite, $g_{zz} \approx 2.032$, $g_{yy} \approx 2.0015$, and $g_{xx} = 1.9995$ and $g_{zz} \approx 2.022$, $g_{yy} \approx 2.0015$, and $g_{xx} = 1.9975$; for HZ zeolite, $g_{yy} \approx 2.0005$ and $g_{xx} = 1.9985$ and $g_{yy} \approx 2.0005$ and $g_{xx} \approx 1.9965$. Using ^{17}O -enriched oxygen, only g_{yy} could be resolved into two components, $c_{yy}^A = 84.5$ and $c_{yy}^B = 64.2$ Oe, for both samples while the other components were shown to be small and unresolved. The oxygen species have been identified with peroxy radicals weakly bonded to O atoms of the zeolite lattice.

Introduction

Electron spin resonance (esr) studies of the adsorption of oxygen onto oxide surfaces have received considerable attention recently. Different charged oxygen species such as O_2^- ,¹⁻⁴ O_2^+ ,⁵ O^- ,^{6,7} and O_3^- ⁶⁻⁸ have been postulated. Generally, indirect methods based upon analysis of the g tensor values were used, although comparing such values is not itself a reliable method of identifying paramagnetic species. However, experiments using isotopic labeling (^{17}O isotope, $I = \frac{5}{2}$) should aid the identification of the oxygen species considerably. In fact, hyperfine interactions are a rich source of information on the chemical nature and the electronic structure of the radical. Moreover, Tench and other authors, using ^{17}O -enriched oxygen, have shown that O_2^- radicals were produced by action of oxygen on MgO ,⁹ ZnO ,¹⁰ TiO_2 ,¹¹ and SnO_2 .¹² More recently, the ^{17}O isotope was used for the study of O^- ¹³ and O_3^- ^{14,15} species adsorbed on MgO .

Particular attention has recently been paid on zeolites because of their use as catalysts and as crystal hosts. On the basis of g tensor values O_2^- radicals have been postulated to exist on irradiated Na Y¹⁶ and decationated Y¹⁷ zeolites. This assignment has been derived from theoretical relationships given by Kanzig and Cohen¹⁸ and has been based essentially upon the largest value of the g tensor.² However, as shown in ref 19, changes in coordination index of a surface atom and changes in the ionic character of the O_2^- -surface cation bond^{20,21} may lead to important shifts in the g values.

In the present work we have exploited the available hyperfine structure by conducting experiments with ^{17}O -enriched oxygen, in order to obtain a more direct identification of the paramagnetic oxygen species. This study was conducted on decationated faujasite and H mordenite. From esr parameters measurements, the spreading of the unpaired electron over the entire radical molecule could be established.

Experimental Section

Decationated faujasite (denoted HY zeolite) was obtained from the corresponding NH_4^+ form. The NH_4^+ Y samples, prepared by exchanging Na^+ ions of a Na-Y

Linde zeolite in a conventional way, were placed into esr quartz tubes. They were first degassed at 400° for several hours, then heated in an oxygen atmosphere at 400° to remove hydrocarbons, and finally outgassed under vacuum (10^{-5} Torr) overnight. The H mordenite, (denoted HZ zeolite) was supplied by Norton on a hydrogen form and was heat treated as above.

The γ irradiation was performed at 77 K in a ^{60}Co cell for doses of about 5 Mrads. Esr spectra were recorded at 77 K with E₃ or V 4502 Varian spectrometers, using either X-band ($\nu_e = 9.4$ GHz) or Q-band ($\nu_e = 34.5$ GHz) accessories. The values of the g -tensor components were measured by using a dual cavity and a DPPH sample ($g = 2.0036$) in the X band and by using the H atoms hyperfine lines of the zeolite ($g = 2.00248$) including a second order correction²² in the Q band.

In the experiments, 62% ^{17}O -enriched oxygen or pure $^{16}\text{O}_2$ gas was used. Mass spectrography measurements in-

- (1) J. H. Lunsford and J. P. Jayne, *J. Chem. Phys.*, **44**, 1487 (1966).
- (2) J. Vedrine, G. Dalmai, and B. Imelik, *Proc. Colloq. AMPERE*, **15**, 304 (1969).
- (3) M. Che, C. Naccache, and B. Imelik, *J. Chim. Phys.*, **65**, 1301 (1968).
- (4) V. A. Shvets, M. E. Sarichev, and V. B. Kazansky, *J. Catal.*, **11**, 378 (1968).
- (5) R. D. Iyengar, M. Codell, J. S. Karra, and J. Turkevich, *J. Amer. Chem. Soc.*, **88**, 5055 (1966).
- (6) W. B. Williamson, J. H. Lunsford, and C. Naccache, *Chem. Phys. Lett.*, **9**, 33 (1971).
- (7) A. J. Tench and T. Lawson, *Chem. Phys. Lett.*, **7**, 459 (1970).
- (8) C. Naccache, *Chem. Phys. Lett.*, **11**, 323 (1971).
- (9) A. J. Tench and P. Holroyd, *Chem. Commun.*, 471 (1968).
- (10) A. J. Tench and T. Lawson, *Chem. Phys. Lett.*, **8**, 177 (1971).
- (11) C. Naccache, P. Meriaudeau, M. Che, and A. J. Tench, *Trans. Faraday Soc.*, **67**, 506 (1971).
- (12) P. Meriaudeau, C. Naccache, and A. J. Tench, *J. Catal.*, **21**, 208 (1971).
- (13) N.-B. Wong and J. H. Lunsford, *J. Chem. Phys.*, **55**, 3007 (1971).
- (14) A. J. Tench, *J. Chem. Soc., Faraday Trans. 1*, **68**, 1181 (1972).
- (15) N.-B. Wong and J. H. Lunsford, *J. Chem. Phys.*, **56**, 2664 (1972).
- (16) P. H. Kasai, *J. Chem. Phys.*, **43**, 3322 (1965).
- (17) K. M. Wang and J. H. Lunsford, *J. Phys. Chem.*, **73**, 2069 (1969); **74**, 1512 (1970).
- (18) W. Kanzig and M. H. Cohen, *Phys. Rev. Lett.*, **3**, 509 (1959).
- (19) E. G. Derouane and V. Indovina, *Chem. Phys. Lett.*, **14**, 455 (1972).
- (20) H. R. Zeller and W. Kanzig, *Helv. Phys. Acta*, **40**, 845 (1967).
- (21) R. T. Shuey and H. R. Zeller, *Helv. Phys. Acta*, **40**, 873 (1967).
- (22) A. Abou-Kais, J. C. Vedrine, J. Massardier, G. Dalmai-Imelik, and B. Imelik, *C. R. Acad. Sci. Ser. C*, **272**, 883 (1971).

indicated the ¹⁷O-enriched oxygen to be composed of approximately 15% ¹³/₁₈O₂, 35% ¹⁷O₂, and 50% ¹⁶/₁₈O¹⁷O. The oxygen was introduced at 77 K after irradiation unless otherwise stated.

Results

When decationated H-Y and H-Z zeolite samples were γ irradiated at 77 K under vacuum mainly V centers were formed. The esr spectra were primarily composed of a broad line ($g_{\parallel} \approx 2.046$, $g_{\perp} \approx 1.995$, and $g_{av} = 2.012$) upon which a six-line hyperfine structure was superimposed ($a^{Al} \approx 7.5$ Oe) (Figure 1). These signals may be attributed to an electron hole localized in a p orbital of an oxygen atom which bonds either to an aluminum and silicon atom (V centers denoted V₁), or to two silicon atoms (denoted V₂).²³

The two previous V centers disappeared instantaneously after the samples were exposed to oxygen and new esr signals were obtained. Their spectra are characterized by the following g values: $g_{zz} \approx 2.032$, $g_{yy} \approx 2.0015$, $g_{xx} = 1.9995$ and $g_{zz} \approx 2.022$, $g_{yy} \approx 2.0015$, $g_{xx} = 1.9975$ corresponding respectively to the V₁ and V₂ centers of the HY zeolite; $g_{yy} \approx 2.0005$, $g_{xx} = 1.9985$ and $g_{yy} \approx 2.0005$, $g_{xx} = 1.9965$ in the case of the HZ samples. In the two latter signals the g_{zz} value could not be determined.

In all of these experiments we did not observe the hyperfine structure due to the interaction of the unpaired electron of the oxygen species with surface aluminum atoms as in ref 17. This is in agreement with the adsorption of oxygen molecules on lattice oxygen atoms which possess an unpaired electron (V centers).

When irradiation was carried out in the presence of oxygen, approximately ten times more paramagnetic oxygen species than previously were formed and their esr parameters are similar. They probably characterize oxygen molecules adsorbed on the same type of sites.

When the samples were warmed up and outgassed at room temperature for a few minutes, the oxygen species signals disappeared and the underlying V center signals reappeared. Thus, oxygen species seem to be only weakly adsorbed at the surface.

The adsorption of ¹⁷O-enriched oxygen on HY and HZ zeolites γ irradiated under vacuum gave a more complex esr spectrum than experiments performed with ¹⁶O₂ (see Figure 2). The spectra given in Figures 3 and 4 were obtained when irradiation was carried out in the presence of about 0.1 Torr of ¹⁷O-enriched oxygen to obtain a high spin concentration (10²⁰ spins/g) and consequently a better signal/noise ratio. When ¹⁷O-enriched oxygen was adsorbed on samples irradiated under vacuum, we did not observe any change in the hyperfine line positions with respect to Figures 3 and 4.

The hyperfine patterns in Figures 3 and 4 consisted of two sets of six hyperfine lines centered about the g_{yy} value. The hyperfine splittings (hfs) values for the two sets (denoted A and B) were equal to 84.5 and 64.2 Oe, respectively. These two sextets were the dominant feature of the spectra but several additional hyperfine lines of low intensity were also observed in the spectra. It is interesting to remark that the splittings between consecutive hyperfine lines of each sextet are about equal whatever be the M_I values and that the center of the hyperfine patterns for each value of $|M_I|$ are the same in both the X and Q bands. In other words, no second-order corrections must be included. Consequently the correction for the y axis, known to be equal to

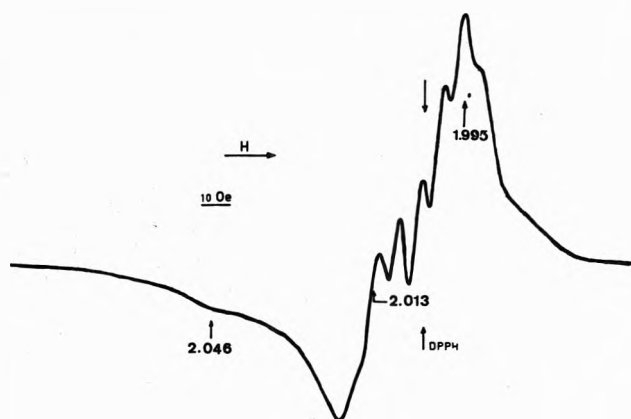


Figure 1. ESR X-band spectrum of HZ zeolite γ -irradiated under vacuum at 77 K.

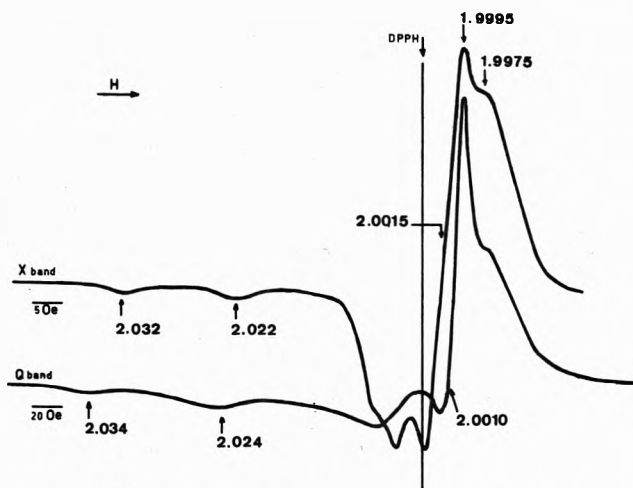


Figure 2. ESR X- and Q-band spectra of HY zeolite samples γ -irradiated in the presence of ¹⁶O₂ (0.1 Torr) at 77 K.

$$\frac{c_{zz}^2 + c_{xx}^2}{2} \frac{1}{2H_0} \left[\frac{35}{4} - M_I^2 \right]$$

is negligible, *i.e.*, c_{zz} and c_{xx} are small compared to c_{yy} . This was confirmed by the fact that the hyperfine structure corresponding to the g_{xx} and g_{zz} values are not resolved in the spectra.

When ¹⁷O-enriched oxygen was adsorbed on HZ zeolites, the hyperfine esr structure was similar to that observed in HY zeolites. It consisted of two sextets centered about $g_{yy} = 2.0005$ with $c_{yy}^A = 84.5$ and $c_{yy}^B = 64.2$ Oe.

Analysis of the ESR Spectra. The signal of Figure 2 was observed only after oxygen adsorption, with the hyperfine lines appearing when ¹⁷O-enriched oxygen was used. Consequently, one can conclude that the signals are due to paramagnetic oxygen species. Upon adsorption of O₂ on the zeolites, species such as O⁻, O₂⁺, O₂⁻, O₃⁻, or peroxy radicals might be formed.

Although the formation of two distinct O⁻ radicals characterized by different hfs constants could explain the two sets of six lines, one can rule out this assignment because the additional hyperfine lines shown in Figures 3 and 4 would not be explained, and also on the basis of theoretical and experimental grounds ($g_{\parallel} < g_{\perp}$ for O⁻ adsorbed on MgO⁶).

(23) A. Abou-Kais, J. C. Vedrine, J. Massardier, G. Dalmay-Imelik, and B. Imelik, submitted for publication in *J. Phys. Chem.*

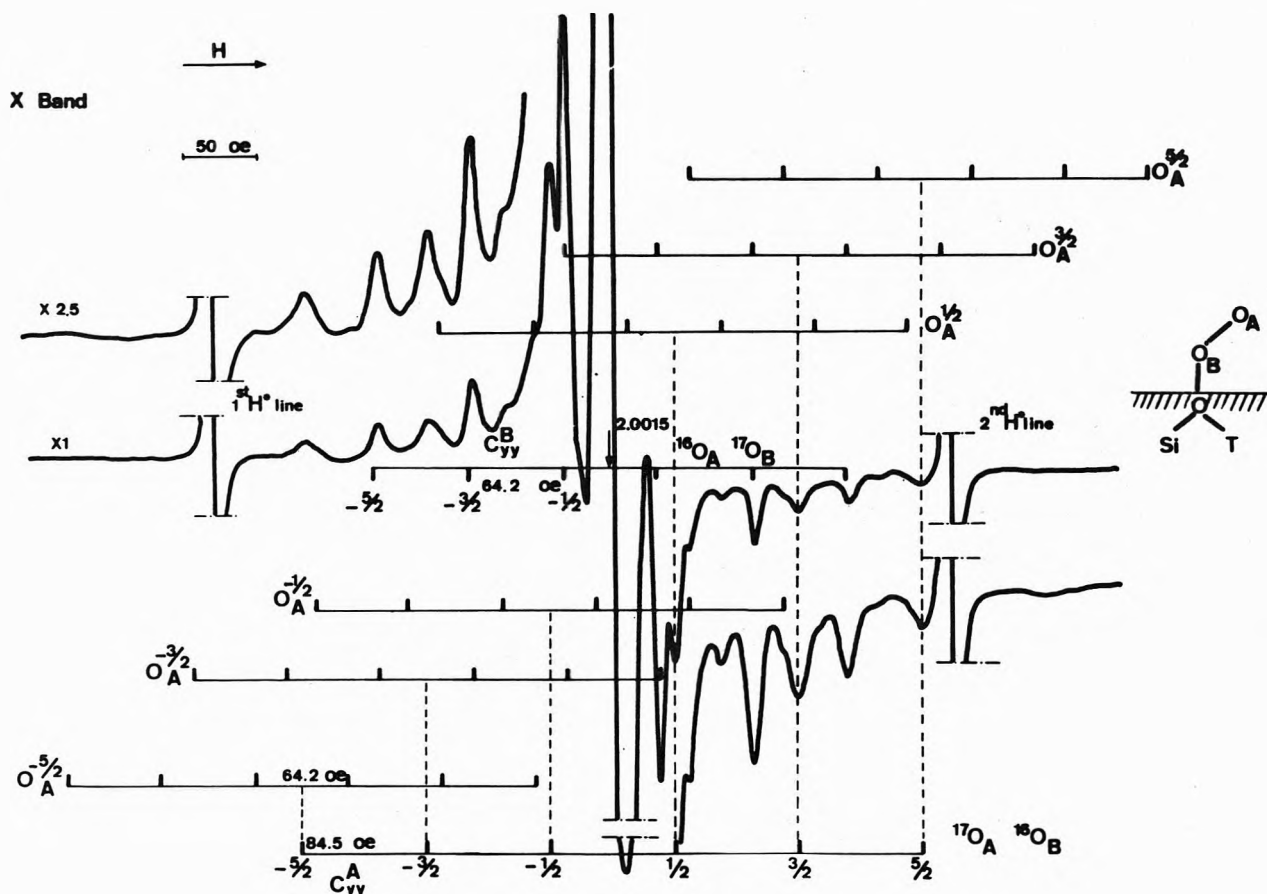


Figure 3. X-Band spectrum of HY zeolite irradiated in the presence of ^{17}O -enriched oxygen ($p \approx 0.1$ Torr) at 77 K. T represents either Si or Al atom.

The adsorption of oxygen molecules on V centers, which are electron holes, seems to favor an O_2^+ radical assignment. However, the isoelectronic NO radical is known to have g values less than g_e and $g_{\parallel} < g_{\perp}$ in contrast with our data.²⁴ Moreover, we have shown²⁵ that CO molecules, which have approximately the same ionization potential, do not form CO^+ radicals in the same conditions, but only under irradiation.

The formation of O_2^- radicals, ionically bonded to surface cations may also be considered, but note the following points.

(i) From the theoretical expressions derived by Kanzig and Cohen, one can expect $g_{zz} \gg g_{yy} > g_{xx} \approx g_e$, while the present spectra show two g values (g_{yy} and g_{xx}) close to the free electron g value (g_e).

(ii) Experiments using ^{17}O -enriched oxygen have shown that ionically bonded O_2^- radical has two equivalent oxygen atoms; *i.e.*, the unpaired electron is equally localized on the two oxygen nuclei.⁹⁻¹² Consequently, one should have a six-line pattern corresponding to ^{16}O - $^{17}\text{O}^-$ radical and an 11-line pattern corresponding to ^{17}O - $^{17}\text{O}^-$ radical. Analysis of Figures 3 and 4 indicates that the experimental spectra can be fitted if one assumes that the unpaired electron interacts differently with the two oxygen nuclei. As a matter of fact, the additional lines in the spectra can be interpreted as due to the splitting of each hyperfine line of the sextet A into six lines corresponding to the sextet B splittings. This assignment may give $6 \times 6 = 36$ lines as shown in the stick diagrams, but only the more intense ones could be clearly observed, namely those corresponding to the $M_I = \pm 1/2$ of the sextets A and B. In other

words, one can conclude that the unpaired electron is unequally spread over two oxygen nuclei.²⁶

(iii) It may also be possible that within the zeolite structure strong electrical fields change the spreading of the spin density over the radical and consequently the hfs splittings. Such an influence has been reported for Cl_2^- ions adsorbed on HY and HZ zeolites;²⁷ namely, the spin density on both nuclei is different for the HZ sample in contrast with the HY sample. It was then suggested that the Cl-Cl bond is parallel to the surface, the electrical field being perpendicular to this direction in HY zeolite and along the internuclear axis in HZ zeolite. As we have previously shown, we did not observe any change in the

(24) J. H. Lunsford, *J. Chem. Phys.*, **46**, 4347 (1967).

(25) J. C. Vedrine and C. Naccache, *Chem. Phys. Lett.*, **18**, 190 (1973).

(26) In the case of liquid phase or isotropic hf couplings, the 36 lines are expected to have an equal intensity. However, it is known that each hyperfine component of a powder spectrum is an envelope of individual lines, which correspond to all the random orientations between the principal axis of the species and the continuous magnetic field one. In the case of anisotropy, the resonant field of the individual lines is orientation dependent. If two of the hyperfine components are small as in oxygen species ($C_{yy} = 84.5$ Oe; $C_{xx} \approx C_{zz} \approx 0$), the position of the x and z component lines will be close to the g_{xx} and g_{zz} magnetic field positions, whereas the y position will be shifted from the magnetic field value corresponding to g_{yy} to a value proportional to $M_I C_{yy}$. Moreover, each of the $2I + 1$ hf components has an equal intensity but each spectrum is spread in the magnetic field range between $M_I C_{yy}$ and 0. Consequently, when the $|M_I|$ value increases, the overall intensity of the component being taken constant, the height of the corresponding yy line sharply decreases. Therefore, the components corresponding to small values of $|M_I|$ will primarily be observable, compared to higher values ones.

(27) J. A. R. Coope, C. L. Gardner, C. A. McDowell, and A. I. Pelman, *Mol. Phys.*, **21**, 1405 (1971).

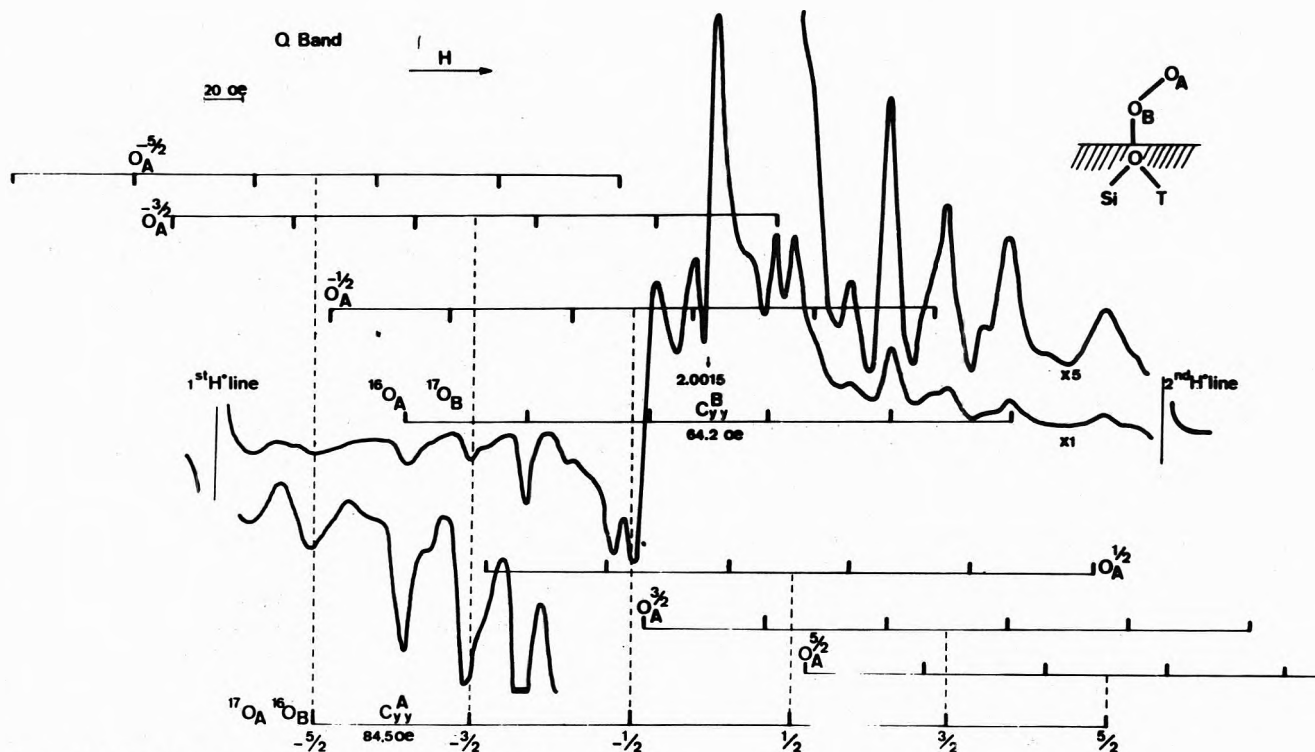


Figure 4. Q-Band spectrum of the same sample as in Figure 3.

hfs constant values of ¹⁷O between HY and HZ samples. One has only observed a small shift in the g_{xx} and g_{yy} values, which is probably due to the differences in electrical fields between the two samples.

One may also consider ionically bonded O₃⁻ species. However, the g values we have observed are very different compared to those found for O₃⁻ on MgO⁶⁻⁸ and the above analysis of the additional lines indicates that the unpaired electron is mainly localized on two oxygen nuclei. It is noteworthy that (i) V centers on zeolites may be considered as O⁻ ions in an ionic model and (ii) the hfs constant values c_{yy} for the two ¹⁷O nuclei, equal to 84.5 and 64.2 Oe, respectively, are very close to two of the three values obtained for O₃⁻ on MgO (82, 65, and 26 Oe). Moreover, such an ozonide ion has been postulated by Tench,¹⁴ when molecular oxygen is reacting with surface V centers induced by neutron irradiation of MgO.

One question arises as to whether these two splitting constants, 84.5 and 64.2 Oe, refer to two nonequivalent oxygen nuclei (A and B in Figures 3 and 4) in the same O₂ species or to equivalent oxygen nuclei of two O₂ species in two different sites as one should expect from the two sets of g values. These two possibilities may be distinguished from a detailed analysis of the ¹⁷O-¹⁷O spectrum lines as shown in ref 28. However, the broadening or narrowing of the corresponding ¹⁷O-¹⁷O lines toward the center of the spectrum, mentioned in ref 28, is not applicable in the case of zeolites, because (i) the ¹⁷O-¹⁷O lines are poorly resolved and their line widths are not measurable and (ii) it is only valid in the liquid phase or for isotropic hf couplings since the lines of the sextet have an equal intensity, whereas in polycrystalline samples line height for each M_I component greatly depends on the M_I value.²⁶

In the case of two oxygen species with an equal coupling of the unpaired electron on both nuclei, one may expect for each species a sextet and an eleven-line spectrum centered upon the field corresponding to g_{yy} . One can see in

Figures 3 and 4 that the additional lines do not fit such an assignment but that if one takes into account the influence of the value of M_I on the line intensities, they may rather correspond to an unequal coupling of the electron with the two nuclei as indicated above.

Our results may also be discussed in terms of peroxy radicals in which oxygen nuclei are nonequivalent. However, the g_{iso} values found in alkylperoxy radicals (≈ 2.015 ²⁹) and in HO₂[•] (≈ 2.013 - 2.016 ³⁰) are much larger than those obtained for HY and HZ zeolites or FO₂[•] radicals (2.0038³¹).

Hyperfine Structure Analysis and Molecular Orbital Coefficients. As previously stated, the spectra shown in Figures 3 and 4 were interpreted assuming that the radicals contain two nonequivalent oxygen atoms. The two hyperfine tensors, corresponding to the A and B couplings, can be separated into isotropic and anisotropic terms as

$$\begin{pmatrix} c_{xx} & & \\ & c_{yy} & \\ & & c_{zz} \end{pmatrix} = \begin{pmatrix} a_{iso} & & \\ & a_{iso} & \\ & & a_{iso} \end{pmatrix} + \begin{pmatrix} b_{xx} & & \\ & b_{yy} & \\ & & b_{zz} \end{pmatrix}$$

The values of the c_{xx} and c_{zz} hfs components were shown to be negligible and in the first approximation were assumed to be equal to zero, since they are small and their signs are unknown. One has $a_{iso} = -28.2$ Oe, $b_{xx} = b_{zz} = 23.2$ Oe, and $b_{yy} = -56.3$ Oe for the A coupling (γ_n is known to be negative) and $a_{iso} = -21.4$ Oe, $b_{xx} = b_{zz} = 21.4$ Oe and $b_{yy} = -42.8$ Oe for the B coupling, so the two dipolar tensors, A and B, are axially symmetric. The dipolar interaction, given by $b_{jj} = b_{dip} (3 \cos^2 \theta_{jj} - 1)$, where θ_{jj} is the angle between the jj axis and the yy axis, varies from $b_{||} = 2b_{dip}$ to $b_{\perp} = -b_{dip}$. The isotropic a_{iso}

(28) M. Che and A. J. Tench, *Chem. Phys. Lett.*, **18**, 199 (1973).

(29) R. W. Fessenden and R. H. Schuler, *J. Chem. Phys.*, **39**, 2147 (1963).

(30) E. Saito and B. H. J. Bielsky, *J. Amer. Chem. Soc.*, **83**, 4467 (1961).

(31) R. W. Fessenden and R. H. Schuler, *J. Chem. Phys.*, **44**, 434, (1966).

and anisotropic b_{dip} constants equal $a_{iso} = A_0 C_{2s}^2$ and $b_{dip} = B_0 C_{2p}^2$ where C_{2s}^2 and C_{2p}^2 are the spin densities of the unpaired electron in the 2s and 2p orbitals of the oxygen atom and A_0 and B_0 hf constants for pure 2s and 2p orbitals. For lack of better sources the values of A_0 and B_0 are usually taken from SCF calculations performed on the free oxygen atom. The A_0 and B_0 values recently published by Morton, Rowland, and Whiffen (MRW) and Hurd and Coddling (HC) have been summarized by Ayscough.³² One has $B_0 = 51.5$ (and 59.9 Oe) and $A_0 = 1655$ (and 1890 Oe). The values in parentheses correspond to HC's calculations, the others to MRW. Taking the experimental values of a_{iso} and b_{dip} and the above A_0 and B_0 values, one can determine the spin density of the unpaired electron on the orbitals 2s and 2p of the two oxygen nuclei. One has respectively 0.017 (0.015) and 0.547 (0.417) for nucleus A and 0.013 (0.011) and 0.415 (0.357) for nucleus B. Consequently, the spin densities are about 0.56 (0.49) on nucleus A and 0.43 (0.37) on nucleus B and the total spin density on the density on the oxygen radical is 0.99 (0.86).

Discussion

On the basis of g factor and hfs component values, none of the assignments recently published on oxygen species could fit the spectra observed for the zeolites. The adsorption of oxygen such as envisaged here may be tentatively explained as follows.

The oxygen molecule is paramagnetic since it possesses two unpaired electrons localized in its two orthogonal 2p Π_g^* molecular orbitals. When exposing the zeolite to oxygen, one of these unpaired electrons may couple the unpaired electron of a V center, with the remaining unpaired electron giving rise to the esr signal. Unfortunately, it is difficult to determine from a powder spectrum the orientation of the principal axes of the g -factor and hfs tensors with respect to the molecular axes. However, in the above model the axis perpendicular to the molecular plane of the V-O₂ species is expected to correspond to the higher electron spin density and to be very ineffective in admixing excited states with the ground state,³³ *i.e.*, to correspond to the largest c value and smallest $|g-g_e|$ shift. Consequently, the yy axis can be assigned to this orientation, since symmetry requires this axis to be the principal axis of both g and c tensors as observed. No assumption could reasonably be made for the other axes. However, an influence of strong electrical fields may change the spin

density distribution of a V— $\begin{array}{c} \text{O} \\ | \\ \text{O} \end{array}$ species. In such a case

one should also expect a change in the spin density distribution between V₁— $\begin{array}{c} \text{O} \\ | \\ \text{O} \end{array}$ and V₂— $\begin{array}{c} \text{O} \\ | \\ \text{O} \end{array}$, which was not

observed. Consequently, it is considered here that the nonlinear V-O-O radical, which would also account for the nonaxial symmetry and the unequal coupling of the unpaired electron with the two oxygen nuclei.

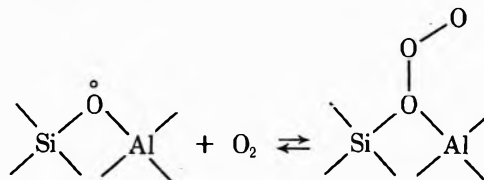
For alkylperoxy radicals it has been shown that the two oxygen nuclei are not equivalent and it has been possible to assign³⁴ the two hyperfine isotropic constants to the terminal (21.8 Oe) and inner (16.4 Oe) oxygen nuclei. With respect to our data, it seems reasonable to follow the same assignment as indicated in the Figures 3 and 4.

We did not observe any change in the hfs splittings and in the relative intensities of the lines corresponding to the ¹⁷O and ¹⁶O components when the irradiation was carried out either in the presence of ¹⁷O enriched oxygen or under vacuum, the oxygen being introduced afterward. Moreover, we did not observe any change in the spectrum shape and in the intensity when the samples were warmed up and γ irradiated several times, so it appears that no isotopic exchange had occurred between lattice oxygen atoms and molecular oxygen ones, even under irradiation.

Conclusion

A paramagnetic oxygen species has been identified on HY and HZ zeolites. The molecular oxygen has been found to react instantaneously at 77 K with V centers, which were induced by γ irradiation and were identified with electron holes in a filled p orbital of lattice oxygen atoms. The g factor and hfs values are unusual and have been interpreted in terms of peroxy-like radicals.

The reaction mechanism proposed corresponds to the coupling of one of the two unpaired electrons of the molecular oxygen with the unpaired electron of the V center according to the scheme



The reversibility is obtained by pumping off the oxygen at room temperature. Isotopic exchange between lattice oxygen and the atoms of oxygen molecules has not been observed to occur, even under γ irradiation.

From the point of view of catalysis, these results are important, since they suggest that oxygen molecules are weakly adsorbed on the zeolite in such a way that the electron density distribution is slightly modified. Consequently, adsorbed oxygen molecules may be active in oxidation reactions and should be considered in writing mechanisms.

Acknowledgment. We are indebted to Dr. G. Dalmaïmelik for her interest throughout the course of this work. The technical assistance of M. G. Wicker is gratefully acknowledged. We also thank Drs. M. Che and A. J. Tench for very valuable suggestions.

(32) P. B. Ayscough, "ESR in Chemistry," Methuen, London, 1967, Appendix III.

(33) F. J. Adrian, *J. Chem. Phys.*, **46**, 1543 (1967).

(34) K. Adamic, K. U. Ingold, and J. R. Morton, *J. Amer. Chem. Soc.*, **92**, 922 (1970).

Relation between an Excited State Geometry Change and the Solvent Dependence of 9-Methyl Anthroate Fluorescence¹

T. C. Werner* and Ronald M. Hoffman

Department of Chemistry, Union College, Schenectady, New York 12308 (Received November 7, 1972)

Publication costs assisted by the Petroleum Research Fund

The interaction between the carboxyl group and the anthracene ring in the excited state results in solvent-dependent fluorescence properties for 9-methyl anthroate. From the increase in Stokes shift in aprotic solvents of increasing polarity, the excited singlet state dipole moment is about 4.5D larger than the ground-state value. The Stokes shifts in protic solvents are significantly greater than those in polar aprotic solvents. This is indicative of a large hydrogen bond contribution to solvation of the excited state. The fluorescence quantum yield (ϕ_f) of 9-methyl anthroate in nonpolar solvents is greater than that of anthracene. For the former compound, it is suggested that the excited singlet lies at a position which is intermediate between the first and second triplets. Intersystem crossing to either triplet is thereby inhibited and ϕ_f increases. In solvents of increasing polarity, the ϕ_f of 9-methyl anthroate decreases. This quenching effect is greatest in protic solvents. From fluorescence lifetime and ϕ_f data, the protic solvent quenching is primarily due to increased rates of radiationless decay. A solvent-induced increase in the rate of internal conversion is the likely mode for nonradiative decay in protic solvents.

Introduction

The absorption and fluorescence spectra of anthracene have considerable vibrational structure and show a classic mirror image relationship. When a carboxyl group is substituted at the 9 position of anthracene, the absorption spectrum retains its anthracene-like structure while the fluorescence spectrum becomes diffuse and highly Stokes shifted.^{2a} These observations are attributed to differences in the ground and excited singlet state molecular geometries.^{2a}

The carboxyl group substitution also effects other fluorescence properties of the parent hydrocarbon. In benzonitrile, the fluorescence quantum yield (ϕ_f) for 9-methyl anthroate (9-COOMe) is about twice as large as the relatively solvent independent ϕ_f of anthracene.^{2a} This is in contrast to the observation that carboxyl substitution generally inhibits fluorescence.^{2b} The values of ϕ_f and the fluorescence lifetime (τ_f) for 9-COOMe in ethanol are only about one-third of their respective values in benzonitrile.^{2a} In addition, there is a significant difference in the wavelength maximum of fluorescence for 9-COOMe in the two solvents.^{2a} These data suggest that the fluorescence behavior of 9-COOMe is strongly solvent dependent.

We report here an investigation of the solvent dependence of 9-COOMe fluorescence. From the solvent dependence of the fluorescence maximum, it can be shown that the excited singlet state is considerably more polar than the ground state. From the solvent dependence of ϕ_f and τ_f , the radiative and the sum of the radiationless rate constants can be calculated. Using these data, it is possible to comment on the modes of solvent-induced quenching.

Experimental Section

Acetonitrile, benzonitrile, 2-propanol, *p*-dioxane, 2,2,2-trifluoroethanol, acetone, ether, methyl formate, and *N,N*-dimethylformamide were Matheson Coleman and Bell Spectroquality solvents. Benzene and methanol were

Fisher Scientific Spectroanalyzed solvents. Absolute ethanol from U. S. Industrial Chemicals was used. Deuterium oxide (99.8% minimum isotopic purity) was from Diaprep Incorporated, Atlanta, Ga.

9-Methyl anthroate was prepared from 9-anthric acid as described previously.⁵

Absorption spectra were recorded on a Cary Model 14 spectrophotometer.

Fluorescence spectra were recorded on a Perkin-Elmer Hitachi-MPF-2A spectrofluorometer which was uncorrected for spectral response. Correction factors for the xenon source-excitation monochromator system were obtained with a rhodamine B quantum counter as described by Chen.⁴ The response of the emission monochromator-detector side was corrected by comparing the uncorrected emission spectra of 9-methyl anthroate in cyclohexane and in ethanol with spectra obtained on a corrected spectral instrument at the Perkin-Elmer Corp., Norwalk, Conn. From the ratio of uncorrected to corrected response at a given wavelength, a sensitivity curve was generated from 380 to 580 nm. Uncorrected emission spectra were computer corrected by multiplication of the fluorescence intensity at a given wavelength by the sensitivity factor at that wavelength.

Fluorescence quantum yield (ϕ_f) determinations were made using the following equation where *r* and *u* stand for reference and unknown, respectively

$$\phi_u = \phi_r \frac{n_u^2 A_r F_u}{n_r^2 A_u F_r}$$

where *n* is the solvent refractive index, *A* is the solution absorbance at the exciting wavelength (<0.02, 1-cm cells), and *F* is the area under the corrected emission spectrum ob-

- (1) Presented at the 165th National Meeting of the American Chemical Society, Dallas, Tex., April 1973.
- (2) (a) T. C. Werner and D. M. Hercules, *J. Phys. Chem.*, **73**, 2005 (1969); (b) R. T. Williams and J. Bridges, *J. Clin. Path.*, **17**, 371 (1964).
- (3) J. A. Moore and D. E. Reed, *Org. Syn.*, **41**, 16 (1961).
- (4) R. F. Chen, *Anal. Biochem.*, **20**, 339 (1967).

tained by the cut and weigh technique. The quantum yield reference was 9-methyl anthroate in ethanol ($\phi_f = 0.18$, ref 2a). Solutions with $\phi_f > 0.20$ were deoxygenated by five-six freeze-pump-thaw cycles and sealed in cells under vacuum before fluorescence was measured. For smaller quantum yields, the short fluorescent lifetimes precluded significant oxygen quenching. All reported ϕ_f values are the average of at least three independent determinations.

Fluorescence lifetimes were obtained with the Ortec nanosecond decay time fluorescence system. This instrument employs the monophoton technique.⁵ The decay curves were deconvoluted and analyzed using the method of moments⁶ in conjunction with an IBM computer. The best fit of the data was obtained by assumption of a single component decay. Solutions with lifetimes >4 nsec were deoxygenated and sealed as noted above.

Results

Table I summarizes the spectral data, Stokes shifts ($\bar{\nu}_a - \bar{\nu}_f$), fluorescence quantum yields (ϕ_f), and some fluorescence lifetimes (τ_f) for 9-COOMe in 28 solvents and solvent mixtures.

The absorption spectra of the methyl ester have anthracene-like structure^{2a} while the fluorescence spectra are broad, diffuse bands with slight structure being apparent only in cyclohexane. Due to the nature of the spectra, the 0-0 fluorescence band cannot be ascertained and the fluorescence maxima are reported in Table I. The Stokes shifts ($\bar{\nu}_a - \bar{\nu}_f$) listed in Table I are from the 0-0 absorption band to the fluorescence maximum.

As solvent polarity increases, as measured by Kosower Z values,⁷ the Stokes shifts also generally increased. This trend is clearly indicated by the plot of $\bar{\nu}_a - \bar{\nu}_f$ vs. Z in Figure 1. Since the positions of the absorption bands are relatively solvent independent (Table I), the increase in $\bar{\nu}_a - \bar{\nu}_f$ with increasing Z primarily reflects a shift of the fluorescence maximum toward lower energies with increasing solvent polarity.

In nonpolar and in some of the polar aprotic solvents, the ϕ_f of 9-COOMe is considerably greater than the relatively solvent independent ϕ_f of unsubstituted anthracene (0.28-0.36, ref 8 and 9). Like the fluorescence maximum, the ϕ_f value is also solvent dependent. The plot of ϕ_f vs. Z in Figure 2 shows that ϕ_f generally decreases as solvent polarity increases. The relative effects of the various solvents on the radiative (k_f) and nonradiative ($k_{ic} + k_{ix}$) rate constants can be ascertained from the ϕ_f and τ_f data in Table I using the equations

$$k_f = \phi_f / \tau_f \quad (k_f = \text{fluorescence rate constant})$$

$$(k_{ic} + k_{ix}) = (k_f / \phi_f) - k_f$$

$$(k_{ic} = \text{internal conversion rate constant})$$

$$(k_{ix} = \text{intersystem crossing rate constant})$$

Values of k_f and ($k_{ic} + k_{ix}$) for ten representative solvents are listed in Table II.

The solvents in Table II can be grouped into three categories based on their ability to affect the rate constants. For the first three solvents, where $\phi_f > 0.60$, there is no significant variation in either k_f or ($k_{ic} + k_{ix}$). In the second three solvents, ϕ_f decreases from 0.55 to 0.32. This decrease in ϕ_f is the result of decreasing values of k_f and increasing values of ($k_{ic} + k_{ix}$). Note, however, that the absolute change in either set of rate constants is less than twofold, except for acetonitrile. The last four solvents are

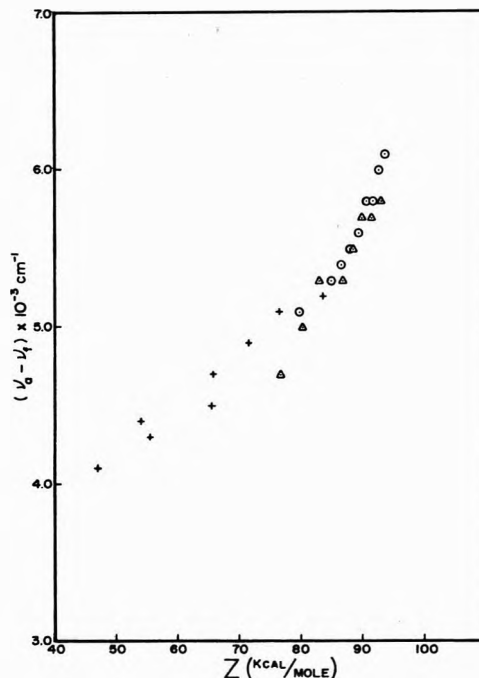


Figure 1. The Stokes shift of 9-COOMe fluorescence as a function of Kosower Z value: O, ethanol-water mixtures; Δ , dioxane-water mixtures; +, pure organic solvents.

protic solvents for which $\phi_f < 0.20$. The rate constant data for these solvents are subject to greater error because of uncertainty in the very short τ_f 's. Despite this fact, the trends in the rate constants are quite clear. The variation in k_f for these solvents is less than a factor of 2. In addition, the k_f values for the protic solvents are not markedly different than the k_f values for the aprotic solvents. However, the ($k_{ic} + k_{ix}$) values for the protic solvents are greater than the values in the aprotic solvents by a factor of 2-25. Thus the greatly reduced ϕ_f 's found in protic solvents are mostly the result of more efficient nonradiative processes in these solvents.

The ratio of the intensities of 9-COOMe fluorescence in 90% water-10% dioxane and 90% deuterium oxide-10% dioxane was measured by comparing the areas of the fluorescence spectra in the two solvents. In this manner, the ϕ_f value is found to be 14% greater in the latter solvent mixture.

Discussion

I. Solvent Dependence of the Fluorescence Maximum.

In the ground state of 9-COOMe, the planes of the carboxyl group and anthracene ring are nearly perpendicular.¹⁰ This accounts for the lack of significant carboxyl group perturbation on the anthracene-like absorption spectrum of 9-COOMe. In the lowest excited singlet state, the carboxyl group and ring approach coplanarity. The diffuse and highly Stokes shifted fluorescence spectrum is suggested to be partly a result of charge transfer interaction between the carboxyl group and ring in this configura-

(5) W. R. Ware, "Creation and Detection of the Excited State," A. Lamola, Ed., Marcel Dekker, New York, N. Y., 1971.

(6) I. Isenberg and R. Dyson, *Biophys. J.*, **9**, 1337 (1969).

(7) E. Kosower, *J. Amer. Chem. Soc.*, **80**, 3253 (1958).

(8) W. H. Melhuish, *J. Phys. Chem.*, **65**, 229 (1961).

(9) R. S. Becker in "Theory and Interpretation of Fluorescence and Phosphorescence," Wiley-Interscience, New York, N. Y., 1969, Chapter 11.

(10) R. O. C. Norman and P. D. Ralph, *J. Chem. Soc.*, 2221 (1961).

TABLE I: Spectral Data for 9-COOMe in Various Organic Solvents and Solvent Mixtures

Solvent	Z ^a	φ _f ^e	$\bar{\nu}_a \times 10^{-4} \text{ cm}^{-1}$ ^c	$\bar{\nu}_f \times 10^{-4} \text{ cm}^{-1}$ ^d	$(\bar{\nu}_a - \bar{\nu}_f) \times 10^{-3} \text{ cm}^{-1}$	τ _f , nsec
Ethanol (10%)	93.6	0.02	2.62	2.01	6.1	
Ethanol (20%)	92.6	0.03	2.62	2.02	6.0	
Ethanol (30%)	91.6	0.04	2.62	2.04	5.8	
Ethanol (40%)	90.5	0.06	2.62	2.04	5.8	
Ethanol (50%)	89.2	0.08	2.62	2.06	5.6	1.9 ± 1
Ethanol (60%)	87.9	0.09	2.62	2.07	5.5	
Ethanol (70%)	86.4	0.11	2.62	2.08	5.4	
Ethanol (80%)	84.8	0.13	2.62	2.09	5.3	
Ethanol (90%)	82.5	0.15	2.62	2.08	5.4	
Ethanol (100%)	79.6	0.18	2.62	2.11	5.1	4.1 ± 1
Dioxane (10%)	93.0	0.02	2.61	2.03	5.8	
Dioxane (20%)	91.4	0.03	2.61	2.04	5.7	
Dioxane (30%)	89.9	0.04	2.61	2.04	5.7	
Dioxane (40%)	88.4	0.07	2.61	2.06	5.5	
Dioxane (50%)	86.7	0.10	2.61	2.08	5.3	1.3 ± 1
Dioxane (60%)	85.0	0.14	2.61	2.08	5.3	
Dioxane (70%)	82.8	0.16	2.61	2.08	5.3	
Dioxane (80%)	80.2	0.22	2.61	2.11	5.0	
Dioxane (90%)	76.7	0.29	2.61	2.14	4.7	
Dioxane (100%)	55.4 ^b	0.55	2.61	2.18	4.3	14.4 ± 0.5
Methanol	83.6	0.11	2.62	2.10	5.2	1.7 ± 1
Trifluoroethanol		0.02	2.64	2.05	5.9	
2-Propanol	76.3	0.24	2.62	2.11	5.1	
Acetonitrile	71.3	0.32	2.62	2.13	4.9	8.1 ± 0.5
Benzonitrile	65.5	0.65	2.59	2.14	4.5	12.7 ± 0.5
Acetone	65.7	0.44	2.62	2.15	4.7	12.9 ± 0.5
Benzene	54	0.64	2.61	2.17	4.4	14.1 ± 0.5
Cyclohexane	47 ^b	0.68	2.62	2.21	4.1	13.1 ± 0.5

^a See ref 7. ^b Estimated from E_T values. See ref 7. ^c 0-0 absorption band. ^d Fluorescence maximum. ^e ±10% accuracy.

ration.^{2a} Hence the excited singlet is expected to be more polar than the ground state and should exhibit the greater solvent dependence. This is confirmed by the plot in Figure 1.

The magnitude of the excited state charge transfer interaction can be evaluated from the solvent dependence of the Stokes shift. Several workers have proposed theoretical treatments for the solvent dependence of fluorescence.¹¹⁻¹³ When the solute-solvent interaction is primarily of a dipole-dipole nature, eq 1 is obtained,¹⁴ where

$$\bar{\nu}_a - \bar{\nu}_f \approx \frac{2}{hc_0} \left(\frac{\epsilon - 1}{2\epsilon + 1} - \frac{n^2 - 1}{2n^2 + 1} \right) \times \left(\frac{(\mu_e - \mu_g)^2}{a^3} \right) + \text{constant} \quad (1)$$

the terms are defined as follows: $\bar{\nu}_a - \bar{\nu}_f$ is the Stokes shift as defined previously (see Results), h is Planck's constant, c_0 is the speed of light in a vacuum, ϵ is the solvent dielectric constant, n is the solvent refractive index, μ_e is the dipole moment of the lowest excited singlet of 9-COOMe, μ_g is the ground-state dipole moment of 9-COOMe, and a is the Onsager cavity radius for 9-COOMe. If a known, $\mu_e - \mu_g$ can be evaluated from the slope of a plot of $\bar{\nu}_a - \bar{\nu}_f$ vs. the refractive index-dielectric constant term.

The a parameter can be estimated from the size of the molecule. From X-ray diffraction studies on anthracene¹⁵ and Fisher-Hershfield-Taylor models of 9-COOMe the a value is taken to be 5 Å.

A plot of eq 1 is shown in Figure 3 for 9-COOMe in several solvents. The line is drawn through the circled points

which represent data from *polar aprotic* solvents. From the slope, the value of $\mu_e - \mu_g$ is 4.5D. The accuracy of this value is uncertain since it depends critically on the Onsager cavity radius. However, even with a possible error of ±50%, as previously estimated,¹⁴ the $\mu_e - \mu_g$ value is indicative of a rather polar excited state. By comparison, Mataga, *et al.*, have found $\mu_e - \mu_g$ to be 0.5-1.0D for β-naphthyl methyl ether and α,β-naphthols¹¹ while Seliskar and Brand found $\mu_e - \mu_g$ to be 9D for 2-amino-6-naphthalenesulfonate.¹⁴

The increased dipole moment of the excited state is consistent with two other observations. Werner has studied the temperature dependence for the fluorescence spectra of the *tert*-butyl ester of 9-anthracic acid in ethanol-methanol (1:5).¹⁶ He has estimated the solvent relaxation energy to be ca. 1500 cm⁻¹ which is characteristic of excited states with a charge-transfer component. Recently, Schulman and Pace have shown that the 9-anthracic acid acidium cation becomes more basic in the excited state.¹⁷ The lowest anthracene excited state (¹La) is polarized parallel to the short axis. A migration of electron density on excitation from the ring to the carboxyl group

(11) N. Mataga, Y. Kaifu, and M. Koizumi, *Bull. Chem. Soc. Jap.*, **29**, 465 (1956).

(12) E. Lippert, *Z. Naturforsch. A*, **10**, 541 (1959).

(13) E. McRae, *J. Phys. Chem.*, **61**, 252 (1957).

(14) C. Seliskar and L. Brand, *J. Amer. Chem. Soc.*, **93**, 5414 (1971).

(15) J. M. Robertson in "Determination of Organic Structures by Physical Methods," E. Braude and F. Nachod, Ed., Academic Press, New York, N. Y., 1955.

(16) T. C. Werner, Ph.D. Thesis, M.I.T., 1969.

(17) S. Shulman and I. Pace, *J. Phys. Chem.*, **76**, 1946 (1972).

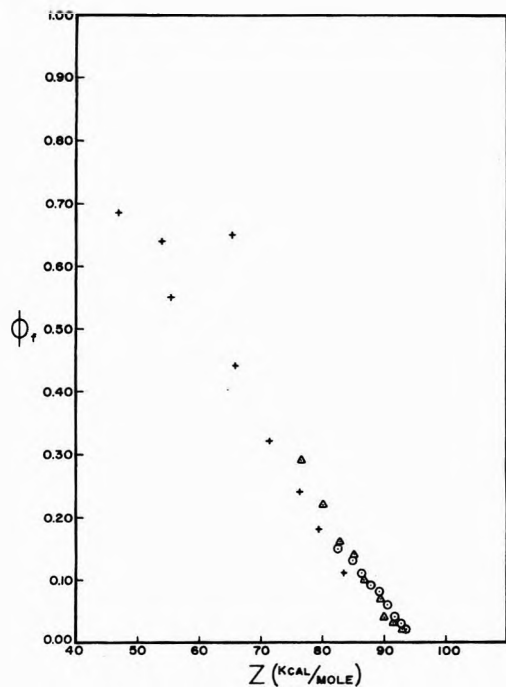


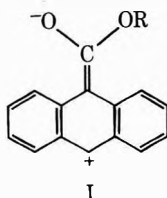
Figure 2. The quantum yield of 9-COOme fluorescence as a function of Kosower Z value: O, ethanol-water mixtures; ▲, dioxane-water mixtures; +, pure organic solvents.

TABLE II: Values of the Radiative ($S_1 \rightarrow S_0$) and the Sum of the Radiationless Rate Constants ($S_1 \rightsquigarrow T_1$, $S_1 \rightsquigarrow S_0$) and Estimated Singlet-Triplet (S_1-T_1) Split for 9-COOme in Several Solvents

Solvent	ϕ_f	$k_f \times 10^{-7}$ sec $^{-1}$	$(k_{ix} + k_{ic})$ $\times 10^{-7}$ sec $^{-1}$	$\Delta E(S_1-T_1)$, ^d cm $^{-1}$
Cyclohexane	0.68	5.2 ^a	2.4 ^a	7400
Benzonitrile	0.65	5.1 ^a	2.7 ^a	6700
Benzene	0.64	4.5 ^a	2.5 ^a	7000
Dioxane	0.55	3.8 ^a	3.1 ^a	7100
Acetone	0.44	3.4 ^a	4.3 ^a	6800
Acetonitrile	0.32	3.9 ^a	8.4 ^a	6600
Ethanol	0.18	4.4 ^b	18.7 ^b	6400
Methanol	0.11	6.5 ^c	52.6 ^c	6300
Dioxane (50%)	0.10	7.7 ^c	69.3 ^c	6100
Ethanol (50%)	0.08	4.2 ^c	48.3 ^c	5900

^a $\pm 15\%$. ^b $\pm 25\%$. ^c $\pm 50\%$. ^d S_1 is fluorescence maximum, T_1 is assumed to be 14,700 cm $^{-1}$ which is the T_1 energy for anthracene.

produces an excited-state resonance contribution shown as



I. Hence protonation of the carbonyl type oxygen should be facilitated in the excited state.

Besides the data from polar aprotic solvents, several points are included in Figure 3 from dioxane-water mixtures. It is readily apparent that these points (triangular in shape) significantly deviate from the line through the polar aprotic solvent data. Similar deviations are ob-

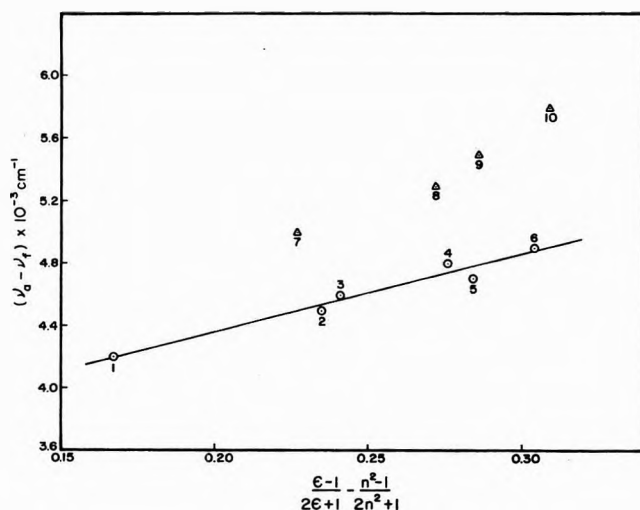


Figure 3. The Stokes shift of 9-COOme fluorescence as a function of solvent polarity parameters. The numbers refer to the following solvents: 1 = ethyl ether; 2 = benzonitrile; 3 = methyl formate; 4 = *N,N*-dimethylformamide; 5 = acetone; 6 = acetonitrile; 7 = 80% dioxane-20% water; 8 = 60% dioxane-40% water; 9 = 40% dioxane-60% water; 10 = 20% dioxane-80% water.

served for all the data taken in protic solvents. This means, that in protic solvents besides the dipolar effects, significant hydrogen bonding interaction must contribute to the Stokes shift. Referring again to structure I, it is apparent that a stronger hydrogen bond would be formed between solvent and the coplanar excited state than between solvent and the perpendicular ground state.

II. *Solvent Dependence of ϕ_f* . The large increase in ϕ_f for 9-COOme in *nonpolar solvents* relative to ϕ_f for anthracene is an anomaly. Generally, meta-directing substituents tend to inhibit the fluorescence of the parent hydrocarbon.^{2b}

One possible source for the enhanced ϕ_f of 9-COOme could arise from the relative energies in the singlet and triplet manifolds. For anthracene, the first (T_1) and second (T_2) triplet levels are located at 14,700 and 26,050 cm $^{-1}$, respectively.⁹ Since the lowest excited singlet (S_1) is only 650 cm $^{-1}$ above T_2 favorable Franck-Condon factors enable the intersystem crossing process ($S_1 \rightsquigarrow T_2$) to compete quite well with fluorescence.⁹ Internal conversion ($S_1 \rightsquigarrow S_0$) is negligible for anthracene.⁹

Attempts to locate the triplet levels of 9-COOme by phosphorescence and triplet-triplet absorption have been unsuccessful.¹⁸ However, since triplet states are generally less affected by charge-transfer effects than excited singlet states,¹⁹ it is expected that the shift in the energies of T_1 and T_2 for 9-COOme relative to those of anthracene would be smaller than the shift of S_1 . From the fluorescence maxima, S_1 of 9-COOme is ca. 3000 cm $^{-1}$ lower in energy than S_1 of anthracene. Assuming the shift in T_2 to be considerably less than this, S_1 may now be as much as 2000 cm $^{-1}$ below T_2 . Thus crossing to T_2 from S_1 might now require an appreciable activation energy. At the same time, S_1 would still be quite a bit higher than T_1 so that the $S_1 \rightsquigarrow T_1$ process would still be inefficient due to unfavorable Franck-Condon factors. Hence, for 9-COOme, intersystem crossing might compete less effectively with flu-

(18) W. Hardy and D. M. Hercules, private communication.

(19) E. Vander Donckt and G. Porter, *Trans. Faraday Soc.*, **64**, 3218 (1968).

orescence than it does in the case of anthracene. The result would be a larger ϕ_f for the former. Cowan and Schmiegel have suggested a similar ordering of the electronic energy levels for 9-anthroic acid.²⁰

Another factor which might affect the intersystem crossing rate is possible geometry differences between S_1 and the triplet states. If charge-transfer effects are smaller in T_1 and T_2 than in S_1 , it is possible that the triplet levels maintain the ground-state geometry. The vibrational overlap factors which control the radiationless transition $S_1 \rightsquigarrow T$ might be unusually small even if the energy of S_1 is closer to that of T_1 or T_2 than anticipated above. Lim, *et al.*,²¹ have previously suggested the existence of such "geometry factors."

It is apparent from Table II that the Z dependent solvent quenching of 9-COOMe fluorescence is greatest in solvents or solvent mixtures which have hydrogen bond donor capabilities. The quenching in these protic solvents is primarily a result of increased nonradiative decay rates. In addition, the magnitude of $(k_{ix} + k_{ic})$ is greater for methanol and the water-containing solvents than for ethanol which is consistent with the expected hydrogen bond donor abilities.

In the absence of data on the 9-COOMe triplet, it is impossible to determine the relative contributions of k_{ix} and k_{ic} to the quenching process. However, it is possible to make some comment on possible quenching pathways.

The shift in the fluorescence maximum of 9-COOMe over the range of solvents used (see Table I) is *ca.* 2000 cm^{-1} . If the shift in T_1 is considerably less than this, $\Delta E(S_1-T_1)$ should decrease as the energy of the fluorescence maximum decreases. Seliskar and Brand showed that such a situation leads to fluorescence quenching through enhanced rates of intersystem crossing ($S_1 \rightsquigarrow T_1$) for amino-6-naphthalenesulfonate derivatives.¹⁴ Table II lists estimates of $\Delta E(S_1-T_1)$ for 9-COOMe in several solvents assuming the T_1 energy to be the same as that of anthracene (14,700 cm^{-1}). Although $\Delta E(S_1-T_1)$ does decrease as ϕ_f decreases in protic solvents, the minimum value of $\Delta E(S_1-T_1)$ is far too large to produce significant Franck-Condon integrals between S_1 and T_1 . Also the difference in $\Delta E(S_1-T_1)$ between protic and aprotic solvents is too small to account for the differences in ϕ_f between these solvents. If this mechanism is operative for 9-COOMe, there should be a triplet level at *ca.* 20,000 cm^{-1} . This would mean either a very large blue shift of T_1 relative to anthracene or a highly red-shifted T_2 which is less solvent dependent than S_1 . Either case is unlikely and thus an enhanced k_{ix} *via* this mechanism is improbable.

From the variation in $(\bar{\nu}_a - \bar{\nu}_f)$ between protic and aprotic solvents, it was implied that the 9-COOMe excited state possesses some of the resonance character of structure I. It seems likely that the hydrogen bond formed between the carbonyl-type oxygen in the ester excited state and a protic solvent would be intimately involved in the solvent-induced quenching. In support of this, the intensity of 9-COOMe fluorescence is 14% greater in 90% D_2O -10% dioxane than in 90% H_2O -10% dioxane. The hydrogen bond may provide strong coupling between the excited solute and solvent with the result being an enhanced internal conversion rate and subsequent loss of excitation energy to the vibrational modes of the environment. Forster has previously suggested such a mechanism to account for a deuterium effect on *N,N*-dimethyl-1-amino-5-naphthalenesulfonate fluorescence.²² In addition, enhanced internal conversion rates could account for the failure to observe the 9-COOMe triplets by flash or phosphorescence in protic solvents.¹⁸

In aprotic solvents (Table II), a decreasing radiative rate constant also contributes to the observed quenching. The variation in k_f for these solvents is attributed to the dependence of k_f on the square of the refractive index.²³ The variation in $(k_{ix} + k_{ic})$ for these solvents is most likely due to an enhanced k_{ic} resulting from the greater solute-solvent interaction as solvent polarity increases.

It should be pointed out that the benzonitrile data represent an exception to the ϕ_f polarity dependence. Based on Z values, the ϕ_f in benzonitrile should be closer to that of acetone. Apparently the coupling between benzonitrile and excited 9-COOMe which leads to increased k_{ic} values is smaller than solvent polarity would reflect.

Acknowledgments. Acknowledgment is made to the donors of the Petroleum Research Fund, administered by the American Chemical Society, for support of this research.

The authors would also like to thank the following: Drs. Renata Cathou and James Bunting of Tufts Medical School for the use of their Ortec fluorescence lifetime equipment and for their aid in the analysis of the data, Mr. Tom Porro of the Perkin-Elmer Corporation for supplying the corrected spectral data necessary for the generation of our spectral sensitivity curve, and Professor Peter Frosch of Union College for helpful discussions.

(20) D. Cowan and W. Schmiegel, *J. Amer. Chem. Soc.*, **94**, 6779 (1972).

(21) E. Lim, J. Laposa, and J. Yu, *J. Mol. Spectrosc.*, **19**, 412 (1966).

(22) Th. Forster and K. Rokos, *Chem. Phys. Lett.*, **1**, 279 (1967).

(23) S. J. Strickler and R. A. Berg, *J. Chem. Phys.*, **37**, 814 (1962).

Luminescence Emission and Excitation Spectra of Benzene and Alkane Thin Films under Slow Electron Impact at 77°K

Kenzo Hiraoka and William H. Hamill*

Department of Chemistry and the Radiation Laboratory,¹ University of Notre Dame, Notre Dame, Indiana 46556
(Received March 12, 1973)

Publication costs assisted by the U. S. Atomic Energy Commission

Luminescence bands of thin-film benzene at 77°K, excited by slow electron impact, are attributed to fluorescence of the monomer at 275 nm, of benzene excimer at 315 nm, of an unknown at 390 nm, and possibly to the phosphorescence of biphenyl at 430–530 nm. Alkane emissions appear at 250, 290, 340, and ~500 nm for neopentane; at 220, 325, and 480 nm for 3-methylpentane; at 200, 280, 365, and 510 nm for *n*-hexane; at 200, 280, 370, and 480 nm for cyclohexane; and at 200, 290, 375, and 510 nm for *n*-nonane. Luminescence excitation spectra by slow electron impact have been measured. For alkanes the 200–250-nm fluorescence bands onset at ~8 eV, the 340–375-nm and the 480–530-nm bands have the same onset for each alkane at ~14 eV. The 280–290-nm bands were too weak for excitation measurements. The ~290-nm band could not be detected for 3-methylpentane, nor was the 430-nm recombination luminescence observed.

Introduction

Liquid alkanes fluoresce under uv excitation in the range 200–245 nm.² Under slow electron impact at 77°K, cyclohexane and *n*-hexane show both 200-nm fluorescence and additional luminescence bands at ~360 and ~490 nm.³ Continued investigation⁴ of solid alkanes provides more reliable detail in their characteristic electron energy loss spectra than could be achieved previously.⁵ It was also possible to improve the measurement of weak luminescence and excitation spectra from thin-film alkanes at 77°K under slow electron impact. The alkanes chosen were neopentane, 3-methylpentane, *n*-hexane, cyclohexane, and *n*-nonane. Benzene has also been examined under the same conditions.

Experimental Section

The experimental procedures have been described.^{3,6} Films were ~10² Å thick. The electron current to the film was ~10⁻⁹ A for measurements of characteristic losses, ~10⁻⁷ A for luminescence emission spectra, and ~5 × 10⁻⁸ A for luminescence excitation spectra. A high-intensity monochromator was used for measuring emission spectra and narrow bandpass filters were used for excitation spectra of alkanes with λ_{max} (and half-widths) at 334.5(7), 350.5(10), 360(11), and 505(11) nm. There was insufficient signal to measure excitation spectra at 280–290 nm.

Photomultiplier pulse counting was used for all measurements. The excitation spectra are presented at dL/dV_i vs. eV_i where L is the luminescence intensity and eV_i is the incident electron energy. Characteristic electron energy loss spectra are presented as dI_t/dV_i vs. eV_i where I_t is the current transmitted by the film. The first peak in each of these spectra⁴ (not shown here) defines the nominal zero of energy.

Results

The emission spectra of thin-film alkanes at 77°K and at several incident electron energies appear in Figure 1 for neopentane, in Figure 2 for 3-methylpentane, in Figure 3 for *n*-hexane, in Figure 4 for cyclohexane, in Figure 5 for *n*-nonane, and in Figure 6 for benzene. In all instances the

spectra were measured at intervals of 10 nm. The data points are shown for benzene in Figure 6 to indicate the precision of the measurements. The electron impact excitation spectra of those emissions which provided sufficient signal are presented in the same order in Figures 7–12.

The luminescence emission spectra of the alkanes in Figures 1–5 are similar and follow a common pattern of four resolved bands. The position of the highest energy band is strongly red shifted by branching, as in 3-methylpentane, and clearly is the same as the uv-excited fluorescence.² The weak band at ~290 nm is unresolved for 3-methylpentane and it is not shifted by carbon number or branching for other molecular species. The next band has its highest energy in the branched alkanes and may be red shifted with increasing carbon number.

For the lowest energy band of neopentane and *n*-nonane the value of λ_{max} shifts with the excitation energy. For 3-methylpentane at 24-eV excitation there is also an unresolved shoulder at ~430 nm. These facts, as well as the considerable band width, indicate no less than two components of the lowest energy band.

Discussion

The values of λ_{max} for recombination luminescence of 3-methylpentane and 2-methylpentane glasses at 77°K are both ~420 nm but the bands span 400 to 500 nm. For isopentane recombination luminescence, λ_{max} is ~490 nm for the glass and ~405 nm for the crystal, but with complete overlap.⁷ All of these emissions may contribute weakly to the alkane luminescence at ~400 nm observed here. The phase effect reported for isopentane may be a consequence of shifting the intensity from one of these common low-energy emissions to the other. None of the

- (1) The Radiation Laboratory of the University of Notre Dame is operated under contract with the U. S. Atomic Energy Commission. This is AEC Document No. COO-38-878.
- (2) F. Hirayama and S. Lipsky, *Chem. Phys. Lett.*, **5**, 296 (1970).
- (3) P. B. Merkel and W. H. Hamill, *J. Chem. Phys.*, **54**, 1695 (1971).
- (4) K. Hiraoka and W. H. Hamill, *J. Chem. Phys.*, submitted for publication.
- (5) D. Lewis, P. B. Merkel and W. H. Hamill, *J. Chem. Phys.*, **52**, 1733 (1970).
- (6) K. Hiraoka and W. H. Hamill, *J. Chem. Phys.*, **57**, 3870 (1972).
- (7) O. Jannssen and K. Funabashi, *J. Chem. Phys.*, **46**, 101 (1967).

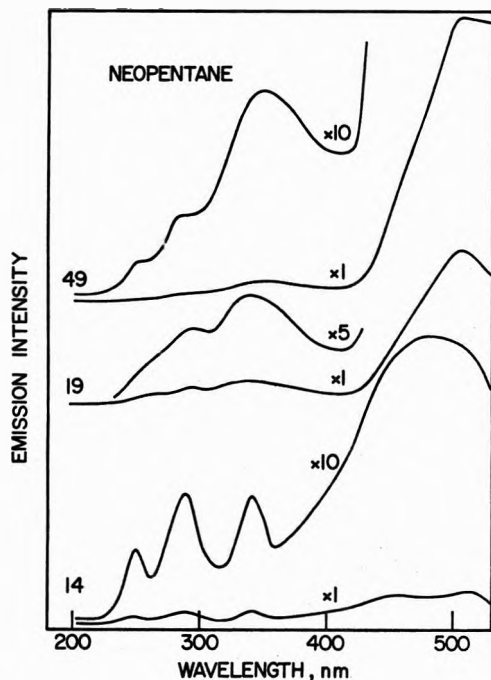


Figure 1. Emission spectra for thin-film neopentane at 77°K under slow electron impact at 14, 19, and 49 eV.

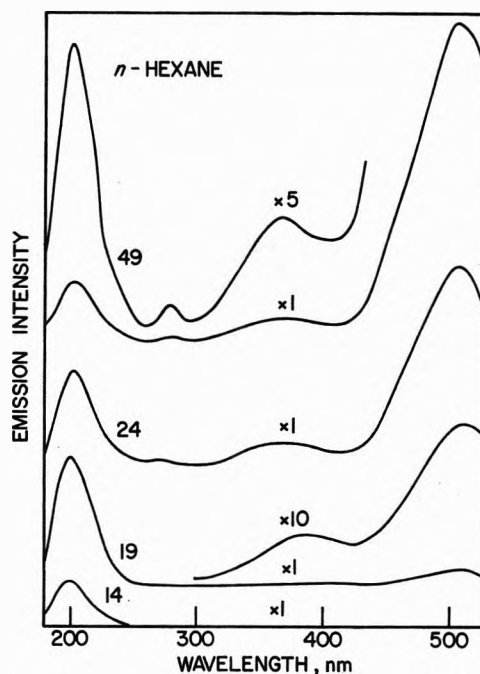


Figure 3. Emission spectra for thin-film *n*-hexane, conditions same as in Figure 1.

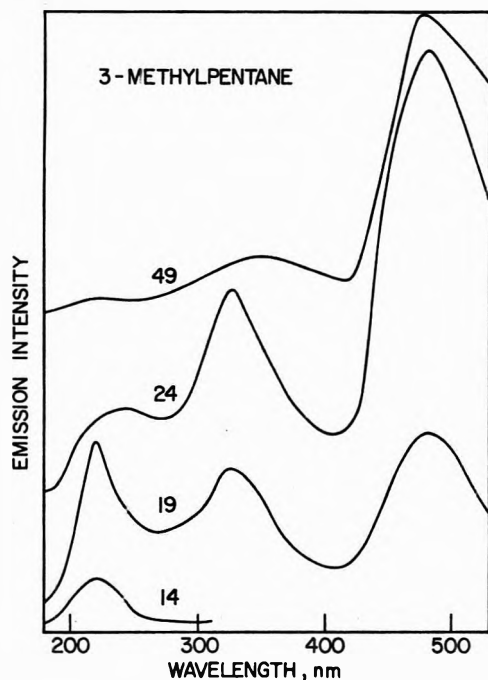


Figure 2. Emission spectra for thin-film 3-methylpentane, conditions same as in Figure 1.

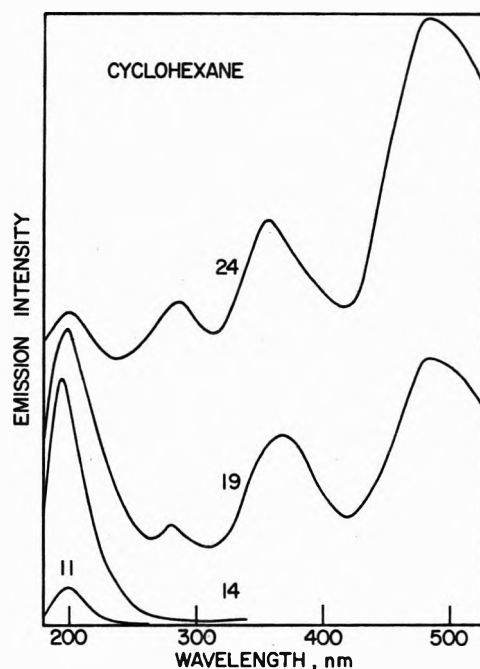


Figure 4. Emission spectra for thin-film cyclohexane, conditions same as in Figure 1.

bands in Figures 1-5, however, can account for the ~ 420 nm recombination luminescence.

The emission and excitation spectra of the alkanes observed are sufficiently typical that they can be considered together by selecting cyclohexane as an example. The band at ~ 202 nm corresponds to the fluorescence from liquid *n*-hexane at 207 nm under uv excitation.² In the thin-film solid at 77°K, however, the intensity increases with increasing electron energy over a range of >10 eV before decreasing. In the liquid the contrary was observed and was probably due to decomposition. The emissions at 360 (3.46 eV) and 485 nm (2.56 eV) have a common exci-

tation onset at 12 eV. Allowing for the electron energy distribution, which has a half-width of ~ 0.6 eV, the adjusted onset becomes 12.6 eV. It lies well within the region of ionization. The zero on this energy scale was taken arbitrarily at the peak for electron injection but the bulk electron affinity of *n*-hexane appears to be approximately zero, both in the solid⁴ and in the liquid,⁸ and no zero shift is required.

The two low-energy emissions cannot arise from transitions from one of the higher filled orbitals of an ion to two

(8) R. A. Holroyd and M. Allen, *J. Chem. Phys.*, **54**, 5014 (1971).

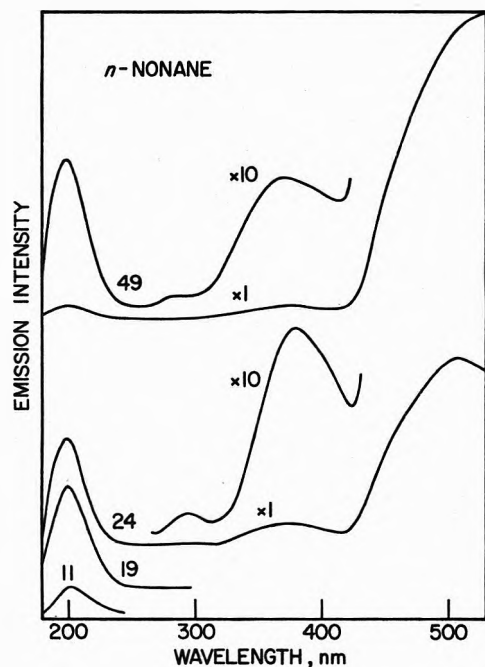


Figure 5. Emission spectra for thin film *n*-nonane, conditions same as in Figure 1.

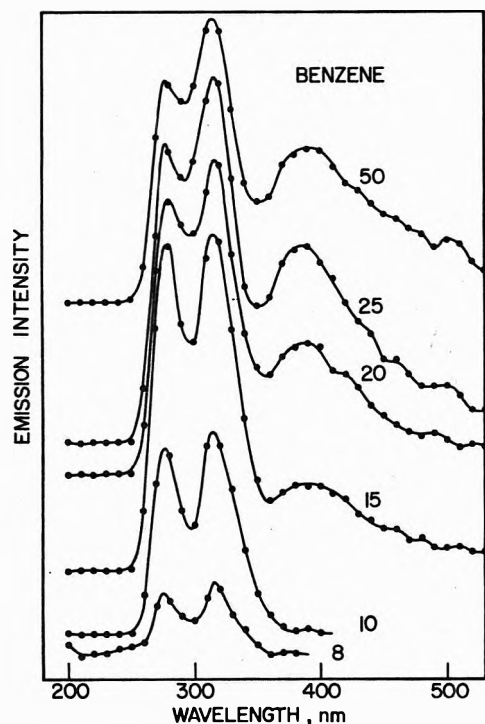


Figure 6. Emission spectra for thin-film benzene, conditions same as in Figure 1.

lower half-filled orbitals because the energy difference is too small.⁹ The high-energy limits of these two emissions approximate 3 and 4 eV. Also, the alkane radical ions have much lower energy optical absorptions.¹⁰ It is improbable that the low-energy bands are due to accumulated products of decomposition because of their high luminescence excitation energy. They may arise from a primary excited decomposition product, but allowed transitions of olefin radical ions are much too low in energy,¹¹ carbonium ions do not absorb in the required region, and

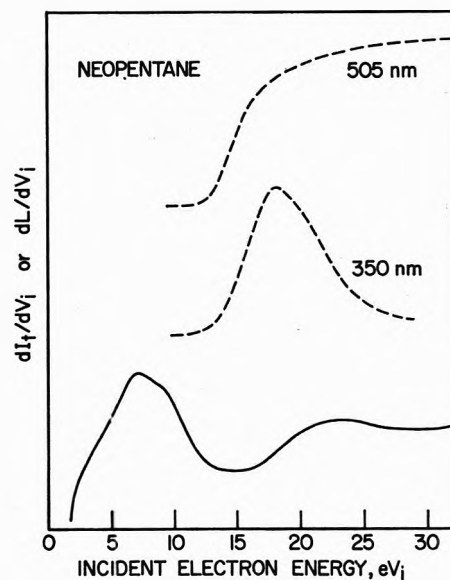


Figure 7. Excitation spectra for luminescence for thin-film neopentane at 77°K under slow electron impact expressed as dI_t/dV_i vs. eV_i . The characteristic electron energy loss spectrum dI_t/dV_i vs. eV_i appears below for comparison.

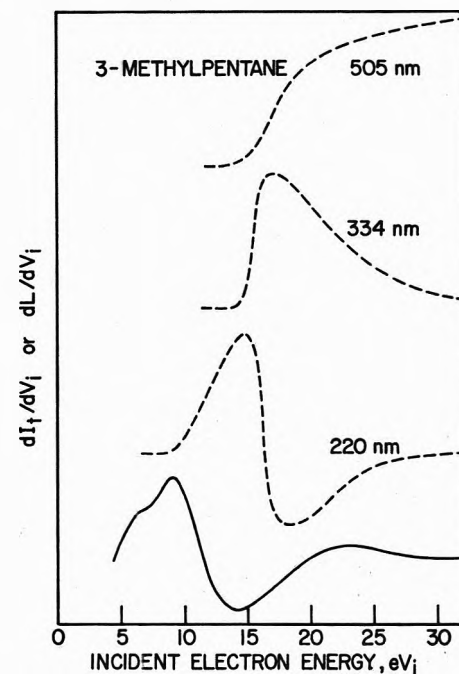


Figure 8. Excitation spectra for luminescence for thin-film 3-methylpentane, conditions same as in Figure 7.

simple olefins do not emit. One or two decomposition products or impurities common to all alkanes can be excluded by the spectral differences, while random impurities would be unlikely to have a common spectral pattern. There is no evident explanation.

The emission at 275 nm for benzene is consistent with the envelope of the fluorescence of benzene in methylcyclohexane at 195°K.¹² Although the emitting state is ${}^1B_{2u}$, the excitation spectrum (Figure 12) shows that the onset of fluorescence coincides with ${}^1E_{1u}$ excitation. The second

(9) M. J. S. Dewar and S. D. Worley, *J. Chem. Phys.*, **50**, 654 (1969).

(10) P. W. F. Louwrier and W. H. Hamill, *J. Phys. Chem.*, **72**, 3878 (1968).

(11) T. Shida and W. H. Hamill, *J. Amer. Chem. Soc.*, **88**, 5376 (1966).

(12) F. Hirayama and S. Lipsky, *J. Chem. Phys.*, **51**, 1939 (1969).

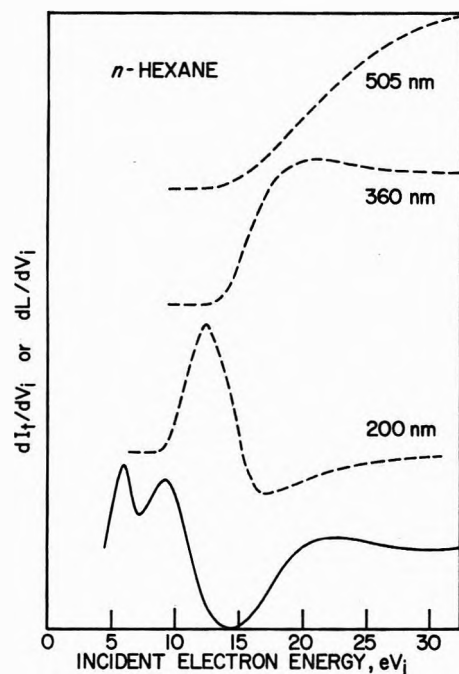


Figure 9. Excitation spectra for luminescence for thin-film *n*-hexane, conditions same as in Figure 7.

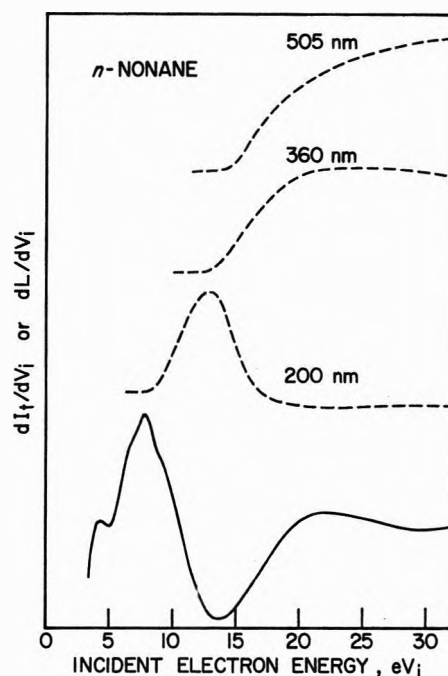


Figure 11. Excitation spectra for luminescence for thin-film *n*-nonane, conditions same as in Figure 7.

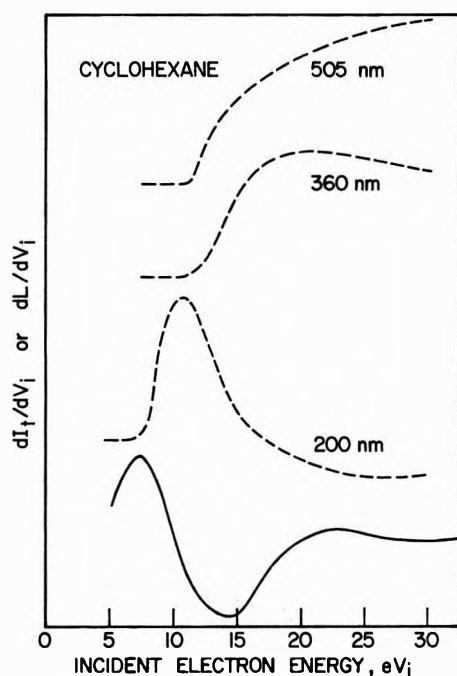


Figure 10. Excitation spectra for luminescence for thin-film cyclohexane, conditions same as in Figure 7.

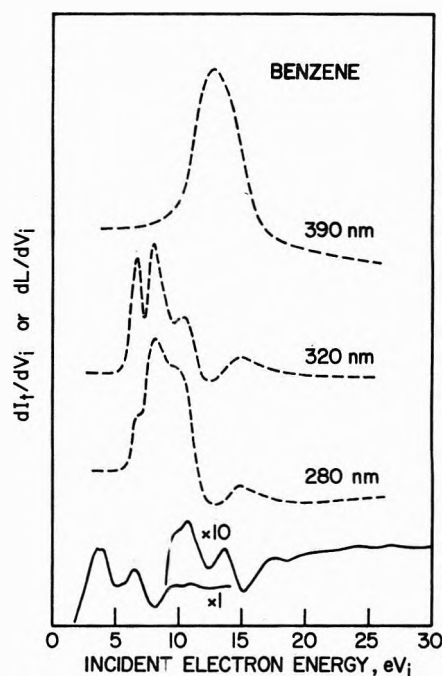


Figure 12. Excitation spectra for luminescence for thin-film benzene, conditions same as in Figure 7.

peak in the derivative excitation spectrum matches a minimum at 9 eV for the first ionization.⁶ The fourth excitation peak matches a minimum at 14 eV due to an excited ionic state.⁶ The third peak is unaccounted for.

The half-width of the 315-nm emission from the benzene film is ~ 49 nm. Excimer emission at 324 nm from benzene in methylcyclohexane at 195°K has a half-width of 46 nm.¹² The ratio of band heights at 315 and 275 nm for the film remained approximately constant for seven successive scans of the emission as the electron energy was raised stepwise from 8 to 50 eV. Emission at 315 nm from the film does not arise from a decomposition product of

benzene, while it does resemble excimer emission and is so identified.

Benzene luminescence at 390 nm was excited at ≤ 9 eV. Its relative intensity for successive scans at 20, 25, and 50-eV excitation was 42, 54, and 55% referred to 280-nm fluorescence. Consequently, it does not arise from accumulated radiolytic product. The emission spectrum at $\lambda > 350$ nm is complex and quite similar to that of polycrystalline benzene at 77°K under 1-MeV electron irradiation.¹³

Excimer fluorescence has not been reported for crystalline benzene and this is apparently due to constraints im-

posed by the lattice on attainment of a suitable configuration. The structure of the benzene thin film is not known, but condensation of $\sim 10^{-7}$ Torr vapor on the 77°K substrate to a $\sim 10^2$ Å film should favor randomness in the solid. Suitable molecule pair configurations for excimer formation may preexist and act as trapping sites for excited monomer.

The ratio of the 315- and 280-nm emission intensities of benzene is constant within 3% for 8–15-eV excitation. At higher energies the 315-nm intensity steadily increases. It can be seen in Figure 12 that every feature in the excitation spectrum of 280-nm emission appears in that for 315-nm emission but the relative amplitudes are not constant. Consequently, the excimer has more than one immediate precursors. Excepting the lowest, these states may be ionic and the self-trapped positive hole, $(C_6H_6)_2^+$, provides a possible intermediate.

The emission at >350 nm has been attributed to benzene triplet monomer and excimer.¹³ The present results show that this luminescence is not excited at low energy, although slow electron impact induces $t \leftarrow s$ excitation efficiently.⁶

On chemical grounds it is necessary to consider luminescence from biphenyl, Ph_2 , since it is the principal

radiolytic product of benzene. Its fluorescence appears at 350–300 nm and its phosphorescence at 550–435 nm, both in *n*-heptane at 77°K.¹⁴ The shorter wavelength emissions from benzene films may contain contributions from biphenyl at >9 eV, but the spectra are quite different in shape. The 8 and 10 eV emissions in Figure 5 cannot contain any biphenyl fluorescence. Emission at 425 nm correlates rather well with biphenyl phosphorescence, which may be due to $2Ph \cdot \rightarrow Ph_2^*$, or to $Ph_2^+ + e \rightarrow Ph_2^*$, since $C_{12}H_{10}^+$ is a prominent secondary ion in the high-pressure mass spectrum of benzene.¹⁵ Ion recombination produces a preponderance of triplets as primary states, and intersystem crossing would further enhance the triplet-singlet ratio.

The onset of 390 emission at ~ 9 eV excludes benzene phosphorescence and indicates another radiolytic product. Biphenyl does not emit in this region and the only other luminescent product of significance is phenylcyclohexadiene. Its phosphorescence should be intermediate in energy between that of benzene at ~ 365 nm and that of biphenyl at ~ 425 nm.

- (13) D. H. Phillips and J. C. Schug, *J. Chem. Phys.*, **50**, 3297 (1969).
 (14) E. C. Lim and Y. H. Li, *J. Chem. Phys.*, **52**, 6416 (1970).
 (15) L. P. Theard, Ph.D. Thesis, University of Notre Dame, 1960.

Flash Photolysis of Phenylglycine in Aqueous Solutions

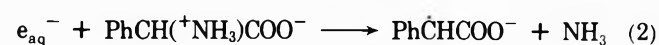
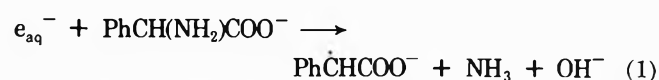
L. J. Mittal,^{1a,b} J. P. Mittal,^{1a} and E. Hayon*

Pioneering Research Laboratory, U. S. Army Natick Laboratories, Natick, Massachusetts 01760 (Received January 11, 1973)

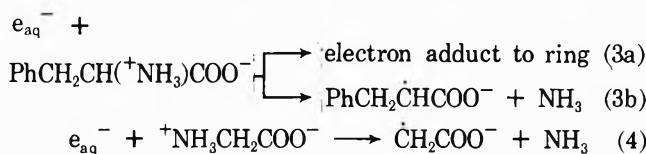
Publication costs assisted by the U. S. Army Natick Laboratories

The main photolytic reaction observed on flash photolysis of oxygen-free aqueous solutions of phenylglycine at pH 6.7 was a photoionization process, $NH_2C(Ph)HCOO^- + h\nu \rightarrow e_{aq}^- + Ph\dot{C}HNH_2 + CO_2$, leading to decarboxylation of the molecule. The hydrated electron was shown to subsequently react with phenylglycine and to lead almost exclusively to deamination: $e_{aq}^- + NH_2C(Ph)HCOO^- \rightarrow NH_3 + Ph\dot{C}HCOO^- + OH^-$. The characteristic transient spectra of the $Ph\dot{C}HCOO^-$ and $Ph\dot{C}HNH_2$ radicals have been assigned. The photolysis of $PhCH(^+NH_3)COO^-$ produced similar results, while the nature of the reactions occurring when both the amino and the carboxyl groups were protonated is distinctly different. The photoionization processes were shown to occur biphotonically *via* a long-lived excited state, probably the triplet state. The flash photolysis of benzylamine in water at pH 11.1 was also found to take place *via* a biphotonic process.

Phenylglycine, $PhCH(^+NH_3)COOH$, is a rather interesting molecule. The benzene nucleus exerts a particularly strong effect on the ionization constant of the amino group ($pK_a^1 = 1.83$ and $pK_a^2 = 4.39$). This is to be compared with glycine, $^+NH_3CH_2COOH$, which has $pK_a^1 = 2.34$ and $pK_a^2 = 9.6$, and with phenylalanine, $PhCH_2CH(^+NH_3)COOH$, $pK_a^1 = 1.83$ and $pK_a^2 = 9.13$. In a recent study,² significant and interesting differences were found in the reactivity and nature of the products produced from the reaction of hydrated electrons, e_{aq}^- , with phenylglycine and phenylalanine. Thus



- (1) (a) Permanent address, Chemistry Division, Bhabha Atomic Research Center, Trombay, Bombay, India. (b) Based on a thesis to be submitted in partial fulfillment of the Ph.D. degree, University of Bombay, Bombay, India.
 (2) J. P. Mittal and E. Hayon, to be submitted for publication.



where $k_1 = 3.0 \times 10^8$ (ref 2), $k_2 > 2 \times 10^9$ (ref 2), $k_3 = 1.6 \times 10^8$ (ref 2), and $k_4 = 8.3 \times 10^6 \text{ M}^{-1} \text{ sec}^{-1}$ (ref 3 and 4). Whereas phenylglycine underwent² almost exclusive ($\geq 90\%$) reductive deamination by e_{aq}^- , most of the electrons appear to add to the aromatic ring of phenylalanine to produce a cyclohexadienyl type of radical.

It seemed of interest to study the photochemistry of phenylglycine in aqueous solution and compare it with the recent detailed study^{5,6} on phenylalanine. Furthermore, the flash photolysis of some substituted benzyl derivatives in water, PhCH_2X (where $\text{X} = \text{NH}_2, \text{OH}, \text{Br}$), showed^{7,8} that the main photolytic process is the rupture of the C-X bond with the formation of the benzyl radical. No photoionization reaction was observed.⁸ Since phenylalanine, as well as numerous phenylalkylcarboxylic acids, undergo photoionization^{5,8,9} in water it appeared important to determine the photolytic processes in phenylglycine, a disubstituted benzyl derivative. The results obtained on flash photolysis of phenylglycine and benzylamine in water are reported below.

Experimental Section

The flash photolysis apparatus used has already been described.¹⁰ Flash intensities of $\sim 2000 \text{ J}$ were normally used with a flash duration of $\tau_{1/2} \sim 10 \mu\text{sec}$. The biphotonic experiments were done by varying the charging voltage (V) across the flash lamps (from ~ 17 to 23 kV) at constant capacitance. The light intensity (I) was shown to be directly proportional to V^2 . The absorbances measured were plotted against $I(V^2)$ and $I^2(V^4)$.

The quartz optical cells were 20 cm long and a 240-nm cut-off filter (15% acetic acid in water) was placed in the outer jacket of the cell. Experiments were carried out at room temperature, 20–22°. The solutions were buffered using perchloric acid, potassium hydroxide, phosphates ($\leq 1 \text{ mM}$), and borate ($\leq 1 \text{ mM}$). Phenylglycine was obtained from Cyclochemicals and benzylamine from Eastman (White Label). The pulse radiolysis set-up used has also been described.¹¹

Results

The absorption spectra of phenylglycine and benzylamine¹² in neutral aqueous solutions are somewhat similar to that of toluene. Substitution in the methyl group of toluene by an electron-withdrawing group, e.g., $-\text{COOH}$, $-\text{OH}$, or $-\text{NH}_2$, decreases its inductive effect. Unless stated otherwise, the work reported below was carried out using a 240-nm cut-off filter. In this way, only the absorption band corresponding to the ${}^1\text{A}_{1g} \rightarrow {}^1\text{B}_{2u}$ benzene transition ($\epsilon_{\text{max}} \sim 180\text{--}200 \text{ M}^{-1} \text{ cm}^{-1}$) was optically excited.

The transient optical spectrum produced on flash photolysis of oxygen-free aqueous solutions of 2 mM phenylglycine (pK_a 1.83 and 4.39) at pH 6.7 is shown in Figure 1a. A band with a maximum at $\sim 282 \text{ nm}$ and shoulders at ~ 310 and $\sim 350 \text{ nm}$ can be seen. This spectrum is clearly not that due to the benzyl radical, which has been recently redetermined.¹³ Indeed one would not expect its formation in this system.

Photoionization of phenylglycine was anticipated since e_{aq}^- was observed from the flash photolysis of phenylala-

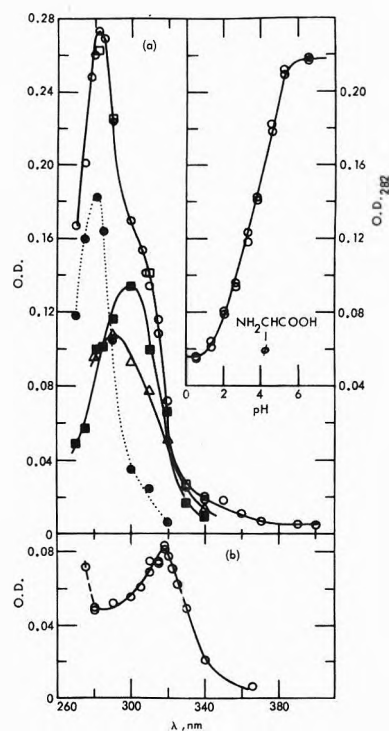


Figure 1. Absorption spectra of transients produced in the flash photolysis of oxygen-free aqueous solutions of 2 mM phenylglycine (a) at pH 6.7 in presence of N_2 (O), N_2 and 1.0 M *t*-BuOH (□), 1.0 M *t*-BuOH plus N_2O (■), difference spectrum between N_2 and N_2O (●), and spectrum obtained on photolysis at pH 3.3 in presence of *t*-BuOH and N_2O (Δ). Insert shows change in absorbance at 282 nm as a function of pH; (b) spectrum at pH 0.8 in presence of N_2 (O). A 240-nm cut-off filter (15% acetic acid in water) was used throughout.

nine^{5,6,8} and phenylalkylcarboxylic acids.^{8,9} In view of the relatively high reactivity of e_{aq}^- with phenylglycine, $k_1 = 3.0 \times 10^8 \text{ M}^{-1} \text{ sec}^{-1}$ [ref 2], the absorption spectrum of e_{aq}^- ($\lambda_{\text{max}} 720 \text{ nm}$) could not be observed even on flash photolysis of dilute solutions, $\sim 1\text{--}2 \times 10^{-4} \text{ M}$. On flash photolysis of 2 mM phenylglycine in presence of (a) N_2O , 1 atm, to scavenge hydrated electrons



$k_5 = 6.0 \times 10^9 \text{ M}^{-1} \text{ sec}^{-1}$ (ref 14), and (b) 1.0 M *tert*-butyl alcohol to scavenge the OH radicals produced, an absorption band with $\lambda_{\text{max}} \sim 300 \text{ nm}$ was observed at pH 6.7 (see Figure 1a). The $\cdot\text{CH}_2(\text{CH}_3)_2\text{COH}$ radical produced absorbs¹¹ below $\sim 260 \text{ nm}$, is relatively unreactive, and was found not to give rise to the observed intermediates.

- (3) E. Hayon and M. Simic, *Intra-Sci. Chem. Rep.*, **5**, 357 (1971).
- (4) P. Neta, M. Simic, and E. Hayon, *J. Phys. Chem.*, **74**, 1214 (1970).
- (5) L. J. Mittal, J. P. Mittal, and E. Hayon, *Chem. Phys. Lett.*, **18**, 319 (1973).
- (6) L. J. Mittal, J. P. Mittal, and E. Hayon, *J. Amer. Chem. Soc.*, submitted for publication.
- (7) G. Porter and M. W. Windsor, *Nature (London)*, **180**, 187 (1957).
- (8) H. J. Joschek and L. I. Grossweiner, *J. Amer. Chem. Soc.*, **88**, 3261 (1966).
- (9) L. J. Mittal, J. P. Mittal, and E. Hayon, *J. Phys. Chem.*, submitted for publication.
- (10) L. Dogliotti and E. Hayon, *J. Phys. Chem.*, **71**, 2511 (1967); M. Langmuir and E. Hayon, *ibid.*, **71**, 3808 (1967).
- (11) M. Simic, P. Neta, and E. Hayon, *J. Phys. Chem.*, **73**, 3794 (1969); J. P. Keene, E. D. Black, and E. Hayon, *Rev. Sci. Instrum.*, **40**, 1199 (1969); E. Hayon, *J. Chem. Phys.*, **51**, 4881 (1969).
- (12) J. Tournon and M. A. El-Bayoumi, *J. Chem. Phys.*, **56**, 5128 (1972).
- (13) J. P. Mittal and E. Hayon, *Nature (London)*, **240**, 20 (1972).
- (14) M. Anbar and P. Neta, *Int. J. Appl. Radiat. Isotopes*, **18**, 493 (1969).

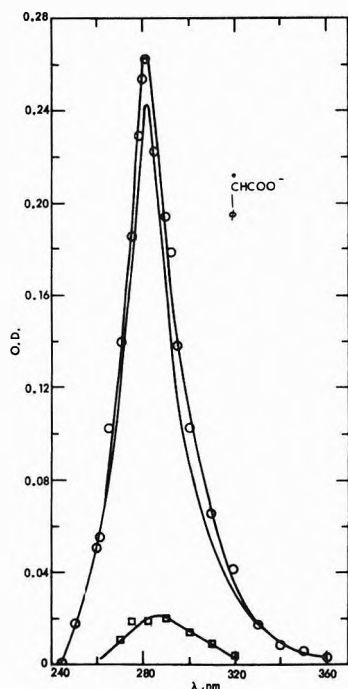
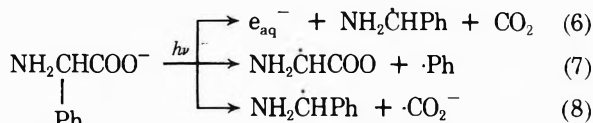


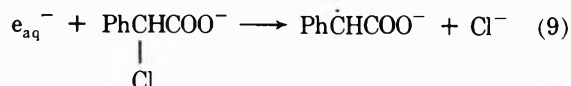
Figure 2. Absorption spectrum of the PhCHCOO^- radical produced by pulse radiolysis from the reaction of e_{aq}^- with 1 mM α -chlorophenylacetic acid (at pH 9.2, in presence of 1.0 M *t*-BuOH to scavenge the OH radicals), in N_2 (O) and N_2O (□). Difference spectrum drawn as full line.

This was determined by producing this alcohol radical in 1-atm N_2O solutions under pulse radiolytic conditions. The "difference spectrum" between N_2 and N_2O solutions shows, Figure 1a, a maximum at ~ 300 nm.

The following primary photolytic processes are suggested



Evidence for process 6 is available from the formation of a transient with $\lambda_{\text{max}} \sim 280$ nm produced by the reaction of e_{aq}^- with phenylglycine. The formation of the PhCHCOO^- radical, according to reaction 1, was established. This radical was produced independently by pulse radiolysis of 1 mM α -chlorophenylacetic acid, 1.0 M *t*-BuOH, and argon (1 atm) at pH 9.2. Under these experimental conditions, electron dissociative capture takes place

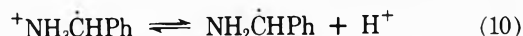


with $k_9 = 2.7 \times 10^9 \text{ M}^{-1} \text{ sec}^{-1}$. The transient spectrum obtained is shown in Figure 2. A maximum at ~ 282 nm is observed and $\epsilon_{282} = 3.5 \times 10^4 \text{ M}^{-1} \text{ cm}^{-1}$. The spectrum of this radical appears to be quite similar to that "difference" spectrum obtained from the flash photolysis of phenylglycine (Figure 1a).

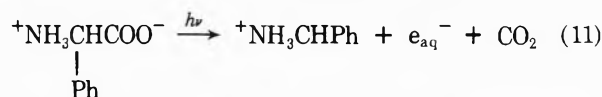
Based on the determined extinction coefficient of PhCHCOO^- , it can be calculated that 0.26 μM of e_{aq}^- are produced. Similarly, since $[e_{\text{aq}}^-] = [\text{NH}_2\dot{\text{C}}\text{HPh}]$, the $\epsilon_{300} = 2.6 \times 10^4 \text{ M}^{-1} \text{ cm}^{-1}$ for the $\text{NH}_2\dot{\text{C}}\text{HPh}$ was derived. This ϵ is appreciably higher than $\epsilon_{318} = 9.0 \times 10^3 \text{ M}^{-1} \text{ cm}^{-1}$ for the $\text{PhCH}_2\cdot$ radical.¹³

No evidence is available for process 7, except that a similar reaction was observed⁹ in the flash photolysis of phenylacetic acid, $\text{PhCH}_2\text{COO}^-$. The spectrum of the $\text{NH}_2\dot{\text{C}}\text{HCOO}^-$ radical is known,⁴ but there is no indication that it is produced. Similarly the $\cdot\text{CO}_2^-$ radical is known,¹⁵ but process 8 does not seem to take place. Indeed the corresponding process in the photolysis of phenylalanine⁵ and phenylalkylcarboxylic acids⁹ was also not observed.

On flash photolysis of 2 mM phenylglycine at pH 3.3, in presence of N_2O (1 atm) and 1.0 M *t*-BuOH, a transient spectrum with $\lambda_{\text{max}} \sim 290$ nm is observed, Figure 1a. Under these experimental conditions, all the e_{aq}^- are converted to OH radicals by N_2O , reaction 5, and *t*-BuOH scavenges the OH radicals. This spectrum is assigned to the $^+\text{NH}_3\dot{\text{C}}\text{HPh}$, and the radical has acid-base properties



The spectrum of the protonated form is blue-shifted compared to the deprotonated form. This observation is characteristic of the acid-base properties^{4,15,16} of most free radicals, and it would appear that $\Phi(6) \sim \Phi(11)$.

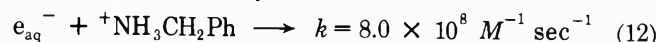


Flash photolysis of phenylglycine at pH 0.8, when both amino and carboxyl groups are protonated, yields a relatively very weak transient with a maximum at ~ 318 nm, Figure 1b. The nature of this transient is not known. It looks like a cyclohexadienyl radical, produced by the addition of a radical (H atoms formed directly or *via* $e_{\text{aq}}^- + \text{H}^+ \rightarrow \text{H}$) to the benzene ring, on which is superimposed the absorption of a second radical.

The change in absorbance at 282 nm with pH is shown in Figure 1a (insert). Similar changes with pH have been observed in the flash photolysis of phenylalanine⁵ and aromatic carboxylic acids.⁹ In these cases the midpoint change corresponded exactly to the pK_a of the ground-state amino and carboxyl groups. In phenylglycine, the midpoint value is ~ 3.7 while the $\text{pK}_a^2 = 4.39$. This difference may be due to (a) the change in the extinction coefficients of the ionized and nonionized radicals with pH at 282 nm, (b) the conversion of e_{aq}^- into H atoms, $k(e_{\text{aq}}^- + \text{H}^+ \rightarrow \text{H}) = 2.3 \times 10^{10} \text{ M}^{-1} \text{ sec}^{-1}$ (ref 14), and the addition of H atoms to the benzene ring. Such a conversion would be in competition with reactions 1 and 2 and, indeed, from such a competition one can calculate a midpoint value at pH 3.7, and (c) the pK_a of the triplet excited state precursor (see below) could be expected¹⁷ to be somewhat lower than that of the ground state.

Benzylamine. The flash photolysis of oxygen-free aqueous solutions of benzylamine ($\text{pK}_a = 9.34$) was reinvestigated. At pH 11.1, an absorption band with $\lambda_{\text{max}} \sim 305$ nm is obtained, Figure 3. In presence of N_2O , a somewhat similar but weaker absorption is observed. The "difference" spectrum shows (Figure 3) a maximum at ~ 300 nm. On flash photolysis at pH 7.3, a very weak absorption with $\lambda_{\text{max}} \sim 318$ nm is produced which could be due to the benzyl radical.

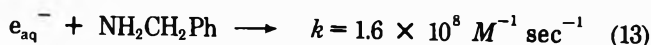
Due to the volatility of benzylamine and its relatively high reactivity with e_{aq}^-



(15) P. Neta, M. Simic, and E. Hayon, *J. Phys. Chem.*, **73**, 4207 (1969).

(16) M. Simic, P. Neta, and E. Hayon, *J. Phys. Chem.*, **73**, 4214 (1969).

(17) E. Van der Donck, *Progr. React. Kinet.*, **5**, 273 (1970).



it was not possible to prepare dilute solutions and look for the formation of e_{aq}^- at 720 nm. Pulse radiolysis experiments² showed that reaction 12 leads mainly to deamination with the formation of the $\text{PhCH}_2\cdot$ radical, while reaction 13 produced a different transient with $\lambda_{\text{max}} \sim 320$ nm, $\epsilon_{320} \sim 11,000 \text{ M}^{-1} \text{ cm}^{-1}$ attributed to the addition of e_{aq}^- to the benzene ring, followed by rapid protonation. It is possible that one of the radicals produced in the flash photolysis of $^+\text{NH}_3\text{CH}_2\text{Ph}$ may be the NH_2CPh radical.

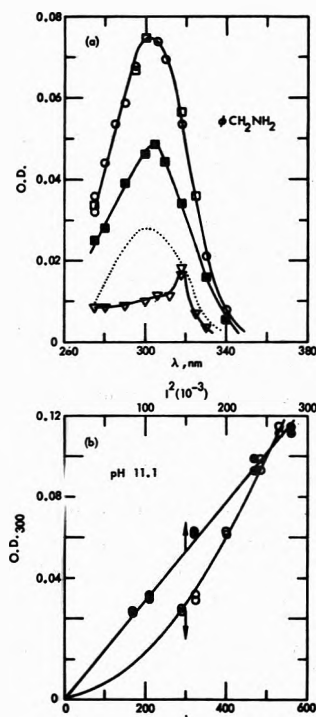


Figure 3. Flash photolysis of aqueous solutions of 2 mM benzylamine. (a) at pH 11.1, in the presence of N_2 (O), N_2 plus 1.0 M *t*-BuOH (□), N_2C plus 1.0 M *t*-BuOH (■), and difference between N_2 and N_2O spectra (Δ). Spectrum obtained at pH 7.3 (Δ). (b) Dependence of OD_{300} formed in the flash photolysis of 2 mM benzylamine, N_2 , pH 11.1, upon the intensity (I and I^2) of the exciting light.

TABLE I: Decay Kinetics of Intermediates Produced on Flash Photolysis of Oxygen-Free Aqueous Solutions of Phenylglycine and Benzylamine

System ^a	pH	λ , nm	Second-order $2k/\epsilon$ rate
Phenylglycine	6.7	280	$8.6 \pm 0.8 \times 10^4$
	0.8	318	$1.5 \pm 0.3 \times 10^5$
Benzylamine	11.0	300	$1.1 \pm 0.2 \times 10^5$

^a 2 mM concentrations used and a 240-nm cut-off filter.

Discussion

Benzyl derivatives have been shown¹² to exhibit an enhancement of phosphorescence yields, a quenching of fluorescence intensities, and a shortening of their natural phosphorescence lifetimes compared to toluene. An intramolecular charge-transfer mechanism was suggested¹² which enhances spin-orbit coupling between states of different multiplicities. The flash photolysis of phenylalanine and

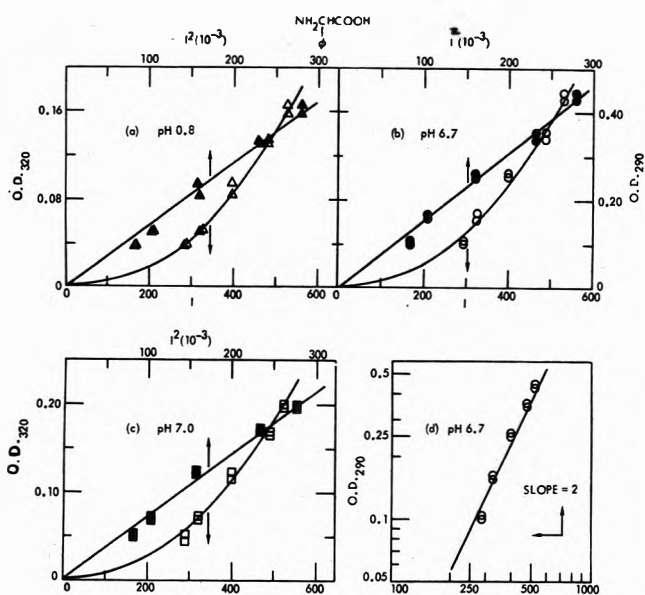


Figure 4. Dependence of the concentration of intermediates produced in the flash photolysis of 2 mM phenylglycine, N_2 , upon the intensity (I and I^2) of the exciting light. Data obtained at different wavelengths and different pH values.

derivatives^{5,6} and of various phenylalkylcarboxylic acids⁹ were shown to lead to photodissociation and photoionization processes *via* a long-lived triplet excited state. Under most conditions, these processes were found^{5,6,9} to be biphotonic, *i.e.*, to require two successive photons.

The flash photolysis of phenylglycine was examined at 320 and 290 nm and at pH values 7.0 and 0.8. Under all these conditions, the intermediates formed were found to be produced by a biphotonic process, see Figure 4. This result differs from those obtained with phenylalanine where the intermediates observed in the photolysis of $\text{PhCH}_2\text{CH}(^+\text{NH}_3)\text{COO}^-$ were produced biphotonically, while those produced from $\text{PhCH}_2\text{CH}(\text{NH}_2)\text{COO}^-$ were monophotonic. The influence exerted by the proximity of the amino group to the ring probably accounts for an increased intramolecular interaction, and the need for a second quantum to bring about the photoionization processes 6 and 11.

The flash photolysis of PhCH_2NH_2 in water was also found to be biphotonic, see Figure 3b. Again in this case, as with phenylglycine (but not with phenylalanine), the photolysis at pH values where the amino group is deprotonated occurs *via* a biphotonic process. In support of these conclusions is the fact¹² that the fluorescence quantum yields at room temperature are very low and the rate constants k_{ISC} for intersystem crossing are relatively high.

These results, in agreement with the work on phenylalanine and derivatives,^{5,6} phenylalkylcarboxylic acids,⁹ tyrosine, *p*-cresol, and phenol,^{18,19} all show that the main photochemical processes of substituted aromatic compounds in water take place *via* a long-lived triplet excited state. Furthermore, they show that biphotonic processes play an important role in both photodissociation and photoionization reactions.

(18) J. Feitelson and E. Hayon, *J. Phys. Chem.*, **77**, 10 (1973).

(19) J. Feitelson, E. Hayon, and A. Treinin, *J. Amer. Chem. Soc.*, **95**, 1025 (1973).

Kinetics of OH⁻ and H⁺ Reactions of Pyrimidines and Purines by Pulse Radiolysis

C. L. Greenstock,*

Medical Biophysics Branch, Atomic Energy of Canada Ltd., Whiteshell Nuclear Research Establishment, Pinawa, Manitoba, Canada ROE 1L0

P. C. Shragge, and J. W. Hunt

Department of Medical Biophysics, University of Toronto, and The Ontario Cancer Institute, Toronto, Ontario, Canada M4X 1K9
(Received September 5, 1972)

Publication costs assisted by Atomic Energy of Canada Ltd.

The kinetics of proton transfer to and from nucleic acid derivatives in aqueous solution has been studied as a function of pH, dose per pulse, and solute concentration by pulse radiolysis. The method involves monitoring the narrow-band transient uv absorption produced by the differences in absorption spectra between ionized and neutral solute. The OH⁻ ions produced by the radiation pulse deprotonate the pyrimidine and purine molecules; the rates of this reaction are in the range $1-2 \times 10^{10} M^{-1} \text{ sec}^{-1}$. At high doses per pulse and low solute concentrations the rate constant for the competing second-order charge neutralization between solvent ions is measured to be $(4.1 \pm 1.2) \times 10^{11} M^{-1} \text{ sec}^{-1}$, three times that measured by relaxation methods. The rate constants for protonation of the ionized nucleic acid derivatives are close to $5 \times 10^{10} M^{-1} \text{ sec}^{-1}$. The complex kinetics of recombination have been simulated with a computer program using the measured parameters; the calculated and observed kinetics agree well.

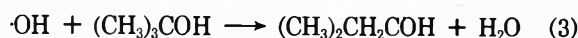
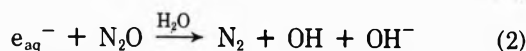
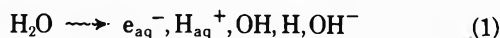
Introduction

Much is known about the kinetics of proton transfer reactions in aqueous solutions from relaxation studies.^{1,2} This work, together with the pulse radiolysis studies of charge neutralization,^{3,4} uses conductivity to detect ions.

In this paper we wish to describe some kinetic studies of solvent ion reactions of nucleic acid derivatives using standard spectrophotometric detection of transient absorbing species.

Several groups of workers have observed a short-lived transient uv absorption in pulse irradiated pyrimidines.⁵⁻⁹ Fielden, *et al.*,⁹ studied the kinetics of thymine, and proposed that the transient species is the result of an acid-base reaction. The spectral and kinetic data presented here for a wide range of purine and pyrimidine derivatives, HX (HX is the protonated, and X⁻, is the ionized molecule), support this hypothesis. Analysis of the kinetic data yields absolute rate constants for the various competing ionic reactions.

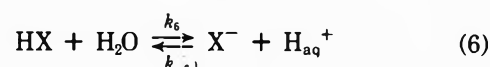
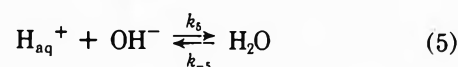
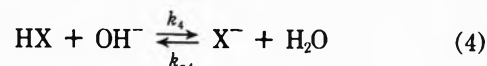
In the radiolysis of water, the three primary species e_{aq}⁻, H, and OH are formed, together with H_{aq}⁺ and OH⁻. In order to study reactions involving the solvent ions alone we have used nitrous oxide saturated aqueous solutions containing 0.5 M *tert*-butyl alcohol to scavenge e_{aq}⁻, OH, and H by the following reactions.



Both reactions 2 and 3 have lifetimes of <10 nsec, hence in ≈ 50 nsec we are left with yields of H_{aq}⁺ and OH⁻ both approximately equal to $G(\text{e}_{\text{aq}}^-)$. The *t*-BuOH radical is

unreactive toward nucleic acid derivatives and its absorption below 250 nm does not interfere.

In the absence of reactive free radicals the following ionic reactions can be considered.



Reaction 4 shows the dissociation of HX caused by reaction with the radiolytic yield of OH⁻. The H_{aq}⁺ present will also compete for OH⁻ as shown in reaction 5; this will be especially important at acidic pH and at high doses. The complete kinetic equations for the species OH⁻, H_{aq}⁺ (\equiv H⁺), X⁻, and HX are

$$\frac{d[\text{OH}^-]}{dt} = -(k_4[\text{HX}][\text{OH}^-] + k_5[\text{H}^+][\text{OH}^-]) + k_{-4}[\text{X}^-] + k_{-5} \quad (7)$$

$$\frac{d[\text{H}^+]}{dt} = -(k_5[\text{H}^+][\text{OH}^-] + k_6[\text{H}^+][\text{X}^-]) + k_6[\text{HX}] + k_{-5} \quad (8)$$

- (1) M. Eigen, *Angew. Chem., Int. Ed. Engl.*, **3**, 1 (1964).
- (2) M. Eigen, W. Kruse, G. Maass, and L. deMaeyer, *Progr. React. Kinet.*, **2**, 287 (1964).
- (3) K. H. Schmidt and S. M. Ander, *J. Phys. Chem.*, **73**, 2846 (1969).
- (4) J. Rabani, M. Grätzel, S. A. Chaudri, G. Beck, and A. Henglein, *J. Phys. Chem.*, **75**, 1759 (1971).
- (5) R. L. Willson, Ph.D. Thesis, University of Newcastle upon Tyne, 1966.
- (6) C. L. Greenstock, M. Ng, and J. W. Hunt, *Trans. Faraday Soc.*, **65**, 3279 (1969).
- (7) E. Hayon, *J. Amer. Chem. Soc.*, **91**, 5397 (1969).
- (8) L. S. Myers, Jr., M. L. Hollis, L. M. Theard, F. C. Peterson, and A. Warnick, *J. Amer. Chem. Soc.*, **92**, 2875 (1970).
- (9) E. M. Fielden, J. M. Phillips, G. Scholes, G. C. Stevens, and R. L. Willson, *Nature (London)*, **225**, 632 (1970).

$$d[X^-]/dt = -(k_{-4}'[X^-] + k_{-6}[H^+][X^-]) + k_4[HX][OH^-] + k_6'[HX] \quad (9)$$

$$d[HX]/dt = -(k_4[HX][OH^-] + k_6'[HX]) + k_{-4}'[X^-] + k_{-6}[H^+][X^-] \quad (10)$$

where $k_{-4}' = k_{-4}[H_2O]$ and $k_6' = k_6[H_2O]$.

These four simultaneous equations cannot be solved analytically, however, under specific conditions they simplify and estimates of the rate constants can be made from the experimental data. For instance, at pH 7 and at low dose per pulse (800 rads, $[OH^-] \approx 2.5 \times 10^{-6} M$) and relatively high uracil concentrations, the buildup of U⁻ is pseudo-first order in [HU] ([HU] = concentration of unionized uracil); thus k_4 can be estimated. The approximations used are described in the Appendix.

Experimental Section

The pulse radiolysis experiments were conducted at the Linac in the Physics Department, University of Toronto, and the 4-MeV Van de Graaff in the Whiteshell Nuclear Research Establishment, Pinawa, Manitoba. Pulse lengths from 5 to 100 nsec and doses from 0.4 to 4 krads were used.

The optical and electronic systems have been discussed in detail elsewhere.¹⁰ For kinetic analysis, the XY coordinates of each oscilloscope trace on polaroid film were analyzed by a hand-operated electronic digitizer and the tape output analyzed by computer. All chemicals (Sigma) were dissolved in triply distilled water and used without further purification. Samples were handled remotely by a flow system using high-pressure medical grade nitrous oxide (Linde) or high-purity nitrogen (Matheson).

Small amounts of perchloric acid or potassium hydroxide were used to adjust the pH of the solutions. A Radiometer 22 pH meter which was calibrated with standard buffers was used to measure the pH's. Because of the importance of pH, measurements were made both during bubbling and after irradiation to verify that the pH had not drifted.

The dose was measured by irradiating N₂O saturated solutions of KCNS (0.005 M), and measuring the absorption of the transient species (CNS)₂⁻ at 475 nm ($\epsilon_{475} = 7600 M^{-1} cm^{-1}$).¹¹ The yield of OH⁻ was taken to be equal to $G(e_{aq}^-) = 2.8$ ¹² for the calculation of the second-order charge neutralization, reaction 5.

Results and Discussion

A. Difference Spectra. The absorption spectrum of the pyrimidine nucleic acid base uracil is shown in Figure 1. At neutral pH, the 5,6 double bond uv absorbing chromophore absorbs strongly at 259 nm. However, at higher pH's (beyond the pK_a of ~ 9.5) the spectrum of the ionized form of uracil shifts to the red, the absorption maximum becoming 285 nm. The difference spectrum, shown by the dashed line, is a narrow band peaking at 287 nm with molar extinction coefficient of $5700 M^{-1} cm^{-1}$.

Although the ionized form is stable at high pH, at neutral pH the ionized solute will rapidly protonate by the back reactions 4 and 6. Such a transient uv absorption at 290 nm has been observed in the pulse radiolysis of $5 \times 10^{-4} M$ uracil at neutral pH (Figure 2). There is good agreement between its spectrum and the difference spectrum shown dotted in Figure 1. The slightly lower extinction and red shift is believed to be due to self-absorption

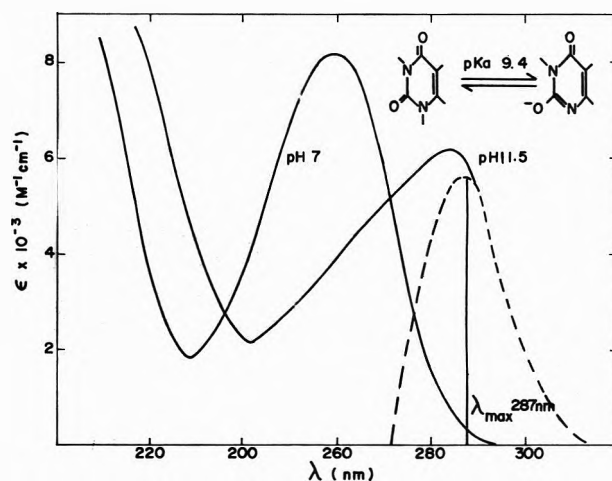


Figure 1. Absorption spectra of uracil at pH 11.5 and 7. The difference spectrum for the ionized and un-ionized forms is shown dotted.

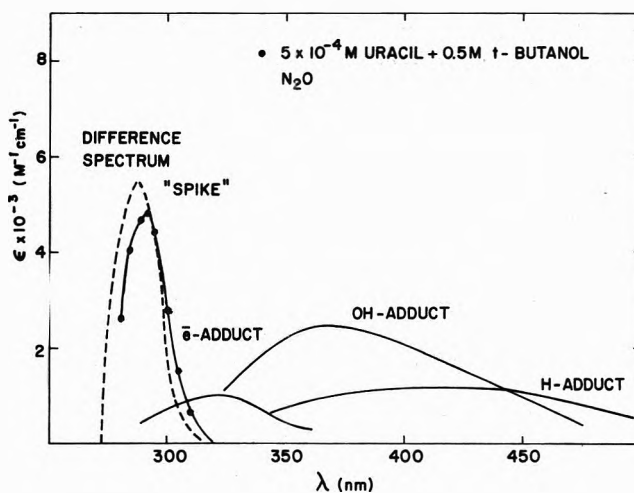


Figure 2. Spectra of various transient species formed under pulse radiolysis conditions. The absorption spike formed as a result of the acid-base dissociation (filled circles) is compared with the difference spectrum replotted from Figure 1. The adduct spectra were taken from ref 6.

of the solute. The transient uv absorption spectra and $G\epsilon$ of the e_{aq}^- , OH, and H adducts which form weaker absorption bands peaking at 325, 370, and 420 nm, respectively, are shown for comparison. In flash photolysis experiments, intense and complex spectra attributed to the triplet species of the pyrimidines have been observed.^{13,14} However, these spectra are quite different from the observed narrow absorption band. This transient is quenched by small amounts of acid or base, but is insensitive to oxygen, unlike the adduct species or the excited triplet states. At neutral pH, the narrow absorption band decays with a half-life of $\sim 10 \mu sec$ independent of uracil concentration or dose.

The transient absorption "spike" was observed in a wide range of purines and pyrimidines (Table I) and in all

(10) J. W. Hunt, C. L. Greenstock, and M. J. Bronskill, *Int. J. Radiat. Phys. Chem.*, **4**, 87 (1972).

(11) J. H. Baxendale, P. L. T. Bevan, and D. A. Stott, *Trans. Faraday Soc.*, **64**, 2389 (1968).

(12) E. M. Fielden and E. J. Hart, *Radiat. Res.*, **32**, 564 (1967).

(13) D. W. Whillans and H. E. Johns, *J. Amer. Chem. Soc.*, **93**, 1358 (1971).

(14) M. A. Herbert and H. E. Johns, *Photochem. Photobiol.*, **14**, 693 (1971).

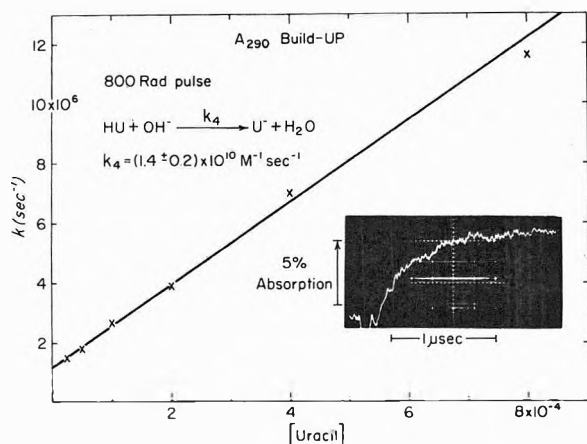


Figure 3. Kinetics of uracil dissociation by OH^- reaction. First-order dependence of U^- buildup on uracil concentration for a dose of 800 rads per pulse ($2.5 \mu\text{M OH}^-$). The pH is 7 ± 0.5 . The inset is an oscilloscope trace of the buildup for 10^{-4} M uracil.

TABLE I: Wavelengths of Absorption Maxima (λ_{max}) Obtained by Pulse Radiolysis or from Difference Spectra

Compounds	λ_{max} , nm	
	Pulse radiolysis	Difference spectra
Cytosine	292	288
Thymine	300	295
Uracil	292	287
Adenine	284	279
1-Methyluracil	290	286
5-Bromouracil	308	302
Isobarbituric acid	318	312
Isoorotic acid	310	295
Uric acid ^a	300	300
5-Nitrouracil ^a	355	365
Xanthine	290	287
Purine		280
5-Methylcytosine		296
Orotic acid		307

^a Bleaching spectra.

cases there is very good agreement between the wavelength of maximum absorption of the pulse radiolysis transient and that of the difference spectrum of ionized and un-ionized solute obtained by steady-state titration. The 4–5-nm red shift in the pulse radiolysis spike is due to self-absorption of the solute.

No difference spectra are observed when the dissociable groups are blocked. Nucleosides and nucleotides and the pyrimidines 1,3-dimethyluracil and 2,4-dithioxypyrimidine fall into this group. Another derivative, dihydrouracil, has no absorption band from 260 to 300 nm, and no narrow band absorption signals are observed. Three other compounds, purine, orotic acid, and 5-methylcytosine, might be expected to show a shift of the spectra in the radiation products. However, these compounds can only be ionized by the application of very large pulses of OH^- (larger than those available using pulse radiolysis) to overcome the effect of the H^+ ions in unbuffered solution. In summary, all of the compounds which do not show an absorption spectrum shift do not show the narrow band absorption in pulse radiolysis. All the spectral evidence is consistent with a proton transfer process.

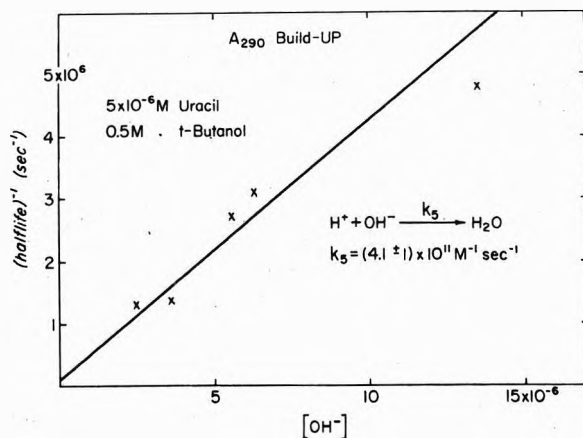


Figure 4. Kinetics of uracil dissociation as a function of OH^- concentration. At the low uracil concentration ($5 \mu\text{M}$) the reaction of OH^- with H^+ predominates.

B. Kinetics. The kinetics of the reactions between OH^- , H^+ , and the ionizable molecules are complex. However, by carefully studying the formation of the difference spectra at different concentrations, pH's, and doses, useful rate constants have been obtained. There is no means of monitoring OH^- directly in the pulse radiolysis system, so instead, OH^- reactivity must be studied by observing changes in the absorption signal of the spike. At low radiation doses and higher concentrations of HX most of the OH^- will react with HX and a smaller fraction will react with H^+ . In the Appendix, it is shown that the first-order rate of buildup becomes

$$\frac{1}{[X^-]_{\infty}} \frac{d[X^-]_0}{dt} = k_4[\text{HX}] + k_5[\text{H}^+] \quad (\text{sec}^{-1})$$

where $d[X^-]_0/dt$ is the initial rate of formation of X^- , and $[X^-]_{\infty}$ is the final concentration of the species.

The rate of buildup of transient absorption at 290 nm for pulse irradiated uracil as a function of uracil concentration at pH 7 is shown in Figure 3. At the low dose of 800 rads and high uracil concentration, reaction 4 predominates over reaction 5 and from the slope of the line a pseudo-first-order rate constant, $k_4 = (1.4 \pm 0.2) \times 10^{10} \text{ M}^{-1} \text{ sec}^{-1}$ for the reaction of OH^- with uracil, is obtained. The positive intercept is a measure of the competing reaction of $\text{OH}^- + \text{H}^+$. The rate of buildup of absorption at 290 nm extrapolated to zero uracil concentration is equivalent to a rate of $(1.2 \pm 0.3) \times 10^6 \text{ sec}^{-1}$. This rate is approximately equal to $k_5[\text{OH}^-]$; taking $[\text{OH}^-] = 2.5 \times 10^{-6} \text{ M}$, $k_5 = (4.8 \pm 1.2) \times 10^{11} \text{ M}^{-1} \text{ sec}^{-1}$.

Under conditions of high dose and low uracil concentration ($5 \mu\text{M}$), the buildup of U^- is approximately second order. The half-life for the buildup, $t_{1/2}$, is approximately the half-life for the recombination of OH^- and H^+ (see Appendix). In Figure 4, a plot of $1/t_{1/2}$ against initial OH^- concentration (\propto dose) is shown. The slope of the line yields the rate constant, $k_5 = (4.1 \pm 1.2) \times 10^{11} \text{ M}^{-1} \text{ sec}^{-1}$. This value is about three times higher than that of Eigen using relaxation techniques.^{1,2} We have no explanation for this discrepancy at the present time, but our value for k_5 is consistent with our observations and a computer simulation of them is discussed in a later section.

The dissociated uracil ion, U^- , will react with H^+ with the rate constant, k_{-6} ; it will also react slowly with H_2O with rate constant, k_{-4} . The rate of decay as a function of the increasing acidity is shown in Figure 5. The decay rate

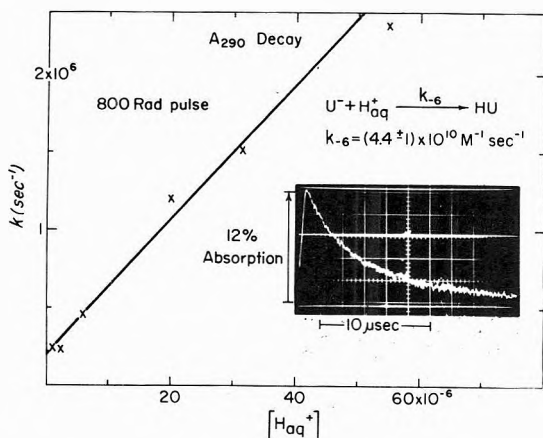


Figure 5. Kinetics of protonation of ionized uracil U^- as a function of acidity (expressed as H^+ concentration). The dose per pulse is 800 rads. The inset shows the decay of U^- at pH 6.

is exponential, and pseudo-first order in H^+ concentration, and the rate constant of the protonation reaction k_{-6} is $(4.4 \pm 1) \times 10^{10} M^{-1} sec^{-1}$.

C. Dissociation Constants. Reactions 4-6 must be consistent with normal steady-state dissociation theory. However, if reaction 9 is solved for the steady-state case (*i.e.*, $d[X^-]/dt = 0$), then

$$\frac{[X^-]}{[HX]} = \frac{k_4[OH^-] + k_6'}{k_{-4}' + k_{-6}[H^+]} \quad (11)$$

The usual equation used to describe dissociation is

$$[X^-]/[HX] = K_a/[H^+] \quad (12)$$

where K_a is the acidic ionization constant. Reaction 11 can be made consistent with reaction 12 if the following conditions hold

$$K_a = k_6'/k_{-6} = K_w k_4/k_{-4}'$$

where $K_w = 10^{-14}$. For uracil the $pK_a = 9.45^{15}$ and $K_a = 3.45 \times 10^{-10}$. Using the measured values of k_{-6} and k_4 in the above reactions, values for k_6' and k_{-4}' are 14 and $3.9 \times 10^5 sec^{-1}$, respectively. This value for k_{-4}' can be measured experimentally from slowest decay of U^- seen at pH 6.5. The rate constant k_6' has very little effect on the reaction scheme.

D. Computer Simulation. In order to test the validity of the model (reactions 4-6), and the estimated parameters, a simple computer program was written to calculate the concentrations of the species OH^- , H^+ , HU , and U^- as functions of time. The input consisted of the values of the six rate constants and the initial concentrations of the four species OH^- , H^+ , HU , and U^- . The calculated decay rate of U^- as a function of pH is shown in Figure 6. It can be seen that the calculated curve using the parameters summarized in Table II agrees closely with the observed data. It should be emphasized that the calculated line was not fitted to the data. Better agreement with the data could have been obtained with curve-fitting procedures but we did not feel that this was justified in light of the inaccuracies in the data.

For $pH < 6$ the line increases with a slope of -1 ; this is exactly what is expected for the case of a species reacting with H^+ . Between pH 6 and 7 it was found that the shape of the decay curves deviated from exponential. This led us to examine the observed decays more carefully. They were found to be nonexponential and essentially the same

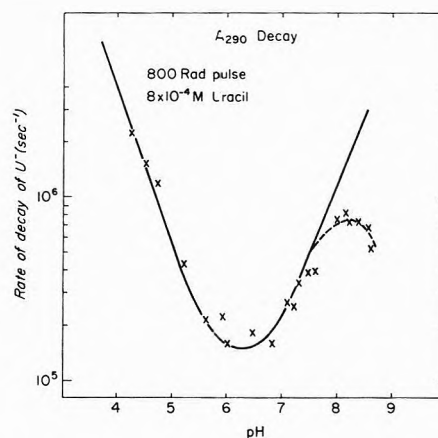


Figure 6. Rate of decay of U^- as a function of pH. The solid line is calculated.

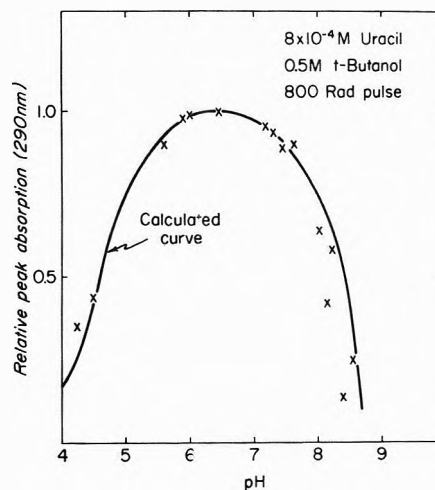


Figure 7. Relative peak yield of absorption at 290 nm as a function of pH. The solid line is calculated.

shape as the calculated curves. This is good evidence for the validity of the model.

Above pH 7 the calculated rate of decay increases steadily with a slope of $+1$. In order to explain this, several reactions must be considered. At pH 8, the steady-state concentrations of species are $[HU] \approx 8 \times 10^{-4} \mu M$, $[U^-] \approx 30 \mu M$, and $[OH^-] = 1 \mu M$. A radiation pulse of 800 rads creates an additional $2.5 \mu M$ concentration of OH^- and H^+ . Initially the predominating reaction will be between HU and OH^- ; this will remove the radiolytic yield of OH^- and create some excess U^- . The excess U^- will be removed by reaction with the radiolytic yield of H^+ ; because $[U^-] \gg [H^+]$ this reaction will be pseudo-first order in $[U^-]$. For pH's well below the pK_a $[U^-] \propto [OH^-]$ and, as a result, the rate of U^- will increase with a slope of $+1$ as shown in Figure 6. The measured rates of decay of U^- agree quite well with the calculated curve for $pH \leq 8$. However, above pH 8, the measured rate for decay of U^- levels off and begins to decrease; this disagrees with the calculated rates which continue to increase. This phenomenon must be due to some mechanism not included in reactions 4-6. We have not yet found an explanation for it.

In Figure 7 a graph of the maximum amplitude of the absorption signal against pH is shown for a uracil concen-

(15) D. Shugar and J. J. Fox, *Biochim. Biophys. Acta*, **9**, 199 (1952).

TABLE II: Rate Constants for Proton Transfer Reactions with Purines and Pyrimidines

Compound	Rate constants, $M^{-1} \text{sec}^{-1}$ ^a			
	k_4	$k_{-4}[\text{H}_2\text{O}]$	k_5	k_{-6}
Uracil	$(1.4 \pm 0.2) \times 10^{10}$ 1×10^{10} ^b	$3.9 \times 10^5 \text{sec}^{-1}$ 2.8×10^5 ^b	$(4.1 \pm 1) \times 10^{11}$	$(4.4 \pm 1) \times 10^{10}$
Thymine	2×10^{10}	$<3 \times 10^5$		
Cytosine		$<3 \times 10^4$		
Adenine	1×10^{10} ^b	$<8 \times 10^4$ 6.3×10^5 ^b		
Isobarbituric acid		$<8 \times 10^5$		
5-Bromouracil		$<3 \times 10^5$		
5-Nitrouracil		$<3 \times 10^5$		
H ₂ O			1.4×10^{11} ^b	

^a $k_4 = k_{\text{HX} + \text{OH}^-}$, $k_{-4} = k_{\text{X}^- + \text{H}_2\text{O}}$, $k_5 = k_{\text{H}^+ + \text{OH}^-}$, $k_{-6} = k_{\text{X}^- + \text{H}^+}$. ^b Reference 1.

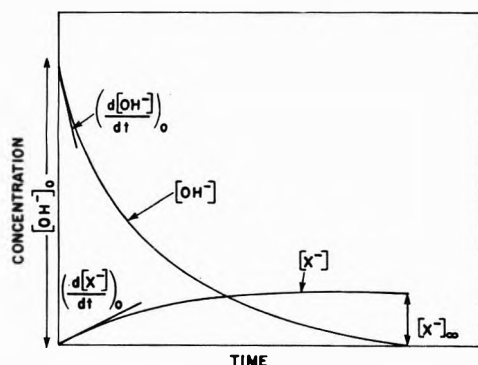


Figure 8. The transient species X^- is a monitor of reactions involving OH^- . Rate constants are obtained from the initial rates of buildup of the species, $(d[\text{X}^-]/dt)_0$, and the final product, $[\text{X}^-]_\infty$.

tration of $8 \times 10^{-4} M$. The solid line is calculated. Again the agreement between experiment and theory is quite good. Above pH 8 the experimental points drop off somewhat faster than the calculated line. This is not surprising in view of the fact that the model is obviously incomplete for pH > 8.

A summary of corrected rate constants for solvent ion reactions with purines and pyrimidines is shown in Table II. The proton transfer reactions of OH^- with the purines and pyrimidines fall within the range $1-2 \times 10^{10} M^{-1} \text{sec}^{-1}$ which is slightly faster than the corresponding reactions of H , OH , and e_{aq}^- . The rates for the back reactions k_{-4} vary from $3 \times 10^4 \text{sec}^{-1}$ for cytosine to $3.9 \times 10^5 \text{sec}^{-1}$ for uracil. The rate constants for the protonation reactions involving X^- and H^+ are typically around $5 \times 10^{10} M^{-1} \text{sec}^{-1}$. Both the rate constants for charge neutralization and for OH^- reactions with certain purines and pyrimidines are in good agreement with those measured by conductivity techniques using relaxation methods.²

These experiments demonstrate the applicability of pulse radiolysis to the study of proton transfer in aqueous solutions of nucleic acid derivatives. The technique is being extended to other systems and other solvents to measure the chemical yields and kinetics of solvent ions.

Acknowledgments. We thank Mr. T. Horrigan and his staff of the linear accelerator, Physics Department, University of Toronto, and Mr. L. Geoffrey in charge of the 4-MeV Van de Graaff generator at Whiteshell Nuclear Research Establishment for their assistance. We also acknowledge the many helpful discussions of our colleagues at both laboratories.

Appendix

A. Low Doses and High Solute Concentrations. Under these conditions, the term $k_4[\text{HX}][\text{OH}^-]$ predominates in reactions 7 and 9 and the buildup of U^- becomes pseudo-first order in solute concentration.

Solving for X^- from eq 7 and 9

$$\frac{d[\text{X}^-]_0}{dt} \cong k_4[\text{HX}][\text{OH}^-]_0 \exp[-(k_4[\text{HX}] + k_5[\text{H}^+])t] \quad (13)$$

$$[\text{X}^-]_t = \frac{k_4[\text{HX}][\text{OH}^-]_0}{k_4[\text{HX}] + k_5[\text{H}^+]} \{1 - \exp[-(k_4[\text{HX}] + k_5[\text{H}^+])t]\} \quad (14)$$

At infinite times, the final signal, $[\text{X}^-]_\infty$ becomes

$$[\text{X}^-]_\infty \cong k_4[\text{HX}][\text{OH}^-]_0 / (k_4[\text{HX}] + k_5[\text{H}^+]) \quad (15)$$

As well, the initial rate at $t = 0$ becomes

$$\frac{1}{[\text{X}^-]_\infty} \frac{d[\text{X}^-]_0}{dt} = k_4[\text{HX}] + k_5[\text{H}^+] \quad (16)$$

B. High Dose and Low Scavenger Concentration. In this case the $k_5[\text{H}^+][\text{OH}^-]$ term predominates in eq 7 and the disappearance of OH^- is essentially second order. Inasmuch as only a small fraction of the initial $[\text{OH}^-]$ will react with the HX , the buildup of X^- absorption will be second order and will be a monitor for the recombination of OH^- and H^+ (see Figure 8), *i.e.*

$$\frac{d[\text{OH}^-]/[\text{OH}^-]_0}{dt} = -\frac{d[\text{X}^-]/[\text{X}^-]_\infty}{dt}$$

and

$$\frac{1}{[\text{X}^-]_\infty} \frac{d[\text{X}^-]_0}{dt} = k_4[\text{HX}] + k_5[\text{H}^+]$$

This is the same as the low dose approximation.

Electron Spin Resonance Study of the Reaction of Hydroxyl Radicals with Pyrrole, Imidazole, and Related Compounds¹

A. Samuni and P. Neta*

Radiation Research Laboratories and Center for Special Studies, Mellon Institute of Science, Carnegie-Mellon University, Pittsburgh, Pennsylvania 15213 (Received January 12, 1973)

Publication costs assisted by Carnegie-Mellon University and the U. S. Atomic Energy Commission

Radicals produced by the reaction of OH with pyrrole, 2-pyrrolicarboxylic acid, *N*-methylpyrrole, *N*-methyl-2-pyrrolicarboxylic acid, imidazole, 2-methylimidazole, 4,5-imidazoledicarboxylic acid, isoxazole, pyrazole, 3,5-pyrazoledicarboxylic acid, maleimide, and *N*-ethylmaleimide have been studied by the *in situ* radiolysis steady-state esr technique. In all cases OH has been found to add to a carbon rather than to abstract H. With pyrroles addition takes place at the position adjacent to the nitrogen and with imidazoles addition to both positions 2 and 5 has been found. In contrast to the furans the OH adducts do not undergo ring opening in alkaline solutions. In the case of pyrrole, imidazole, and 2-methylimidazole the OH adducts have been found to undergo a base-catalyzed water elimination involving the OH and the H from NH. In the carboxy derivatives water elimination is a slow process and was not detected. In the latter radicals a small splitting by the OH proton has been observed in neutral solution but disappeared at pH >10 for imidazoles and >11 for pyrroles. The disappearance of the OH proton splitting is a result of rapid proton exchange. Furthermore, dissociation of the OH proton occurs with pK = 12 for the 4,5-imidazoledicarboxylate adduct and pK = 13.5 for the adducts of 2-pyrrolicarboxylate and *N*-methyl-2-pyrrolicarboxylate. Hydroxyl radicals add to isoxazole at the 5 position adjacent to the oxygen rather than that adjacent to the nitrogen. Addition to pyrazole also takes place at the 5 position, next to the NH group, and in both cases of isoxazole and pyrazole comparable allylic type radicals are observed. With 3,5-pyrazoledicarboxylic acid, however, OH adds to the 4 position probably because the 5 position is sterically hindered by the carboxyl group.

Introduction

Hydroxyl radicals react with aromatic and heterocyclic compounds very rapidly,² mostly by addition to an unsaturated carbon atom. The radicals produced by this addition may undergo further chemical changes before decaying into stable products. For example, OH adducts of phenols and anilines have been found to lose a water molecule,³⁻⁵ and certain OH adducts of uracils have been found to undergo a ring opening in alkaline solutions.⁶ A recent esr study of the furans⁷ has shown that OH adds almost exclusively to the positions adjacent to the oxygen, and that between these positions OH adds preferentially to the unsubstituted carbon. Furthermore, the resulting radicals undergo a rapid ring opening in alkaline solutions to produce the anion radicals of butenedial.^{7,8} The OH adducts of pyrroles have only been investigated by pulse radiolysis⁸ where it has been suggested that a ring opening takes place in acid solution after the radical protonates on the nitrogen.

An esr study of this system seems warranted in order to identify the OH adducts and to follow any possible rearrangements they might undergo. Although one does not expect the pyrrole ring to open in alkaline solutions, a loss of water molecule may take place from adjacent OH and NH groups. This study has been extended to include several derivatives of pyrrole, imidazole, pyrazole, isoxazole, and maleimide. In most cases OH adduct radicals have been identified by their esr spectra and the changes they undergo with change of pH have been followed. In the case of pyrrole, imidazole, and 2-methylimidazole radicals resulting formally from H abstraction from the NH have

been observed and are probably produced *via* addition of OH followed by elimination of a water molecule.

Experimental Section

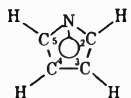
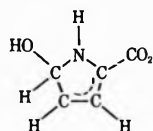
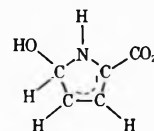
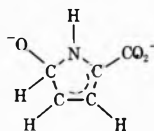
The organic compounds were of the purest grade available from Eastman Organic Chemicals and from Aldrich Chemical Co. and were used without further purification. Solutions were prepared in water which was distilled and the vapor passed with oxygen through a silica tube at 600°. Potassium hydroxide, perchloric acid, sodium borate, and the potassium phosphates, all Baker Analyzed Reagents, were used for pH adjustment and as buffers. Solutions were bubbled with N₂O, which reacts with e_{aq}⁻ to produce OH, so that the organic solutes react mainly with OH. All the other experimental details of the steady-state *in situ* irradiation of solutions while flowing through a silica cell located within the esr cavity are similar to those previously described.⁹

Results and Discussion

The radicals formed by reaction of OH with pyrrole, imidazole, and their derivatives have been studied in

- (1) Supported in part by the U. S. Atomic Energy Commission.
- (2) See, e.g., the compilation by M. Anbar and P. Neta, *Int. J. Appl. Radiat. Isotopes*, **18**, 493 (1967). See also ref 3, 4, and 8.
- (3) E. J. Land and M. Ebert, *Trans. Faraday Soc.*, **63**, 1181 (1967).
- (4) G. E. Adams and B. D. Michael, *Trans. Faraday Soc.*, **63**, 1171 (1967).
- (5) P. Neta and R. W. Fessenden, *J. Phys. Chem.*, submitted for publication.
- (6) P. Neta, *Radiat. Res.*, **49**, 1 (1972).
- (7) R. H. Schuler, G. P. Laroff, and R. W. Fessenden, *J. Phys. Chem.*, **77**, 456 (1973).
- (8) J. Lilie, *Z. Naturforsch. B*, **26**, 197 (1971).
- (9) K. Eiben and R. W. Fessenden, *J. Phys. Chem.*, **75**, 1186 (1971).

TABLE I: ESR Parameters of Radicals Produced by Reaction of OH with Pyrroles^a

	Pyrrole pH 6-11	2-Pyrrolecarboxylic acid		
		pH 4.9-10.5	pH 11-12	pH >14 ^b
<i>g</i> factor	2.00232	2.00290	2.00290	2.00294
<i>a</i> _N	2.91	3.41	3.41	4.60
<i>a</i> _{5H}	} 13.26 (2)	} 22.91	} 22.92	} 24.15
<i>a</i> _{2H}				
<i>a</i> _{4H}	} 3.55 (2)	} 8.84	} 8.86	} 8.27
<i>a</i> _{3H}				
<i>a</i> _{NH^H}		0.0	0.0	0.35
<i>a</i> _{OH^H}		0.28	<i>c</i>	
Suggested radical structure				

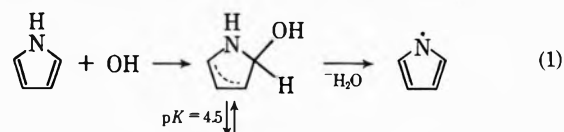
^a All solutions contained 10^{-3} – 10^{-2} M of the pyrrole and were saturated with N_2O . Hyperfine constants are given in gauss and are accurate to ± 0.03 G. The *g* factors are measured relative to the peak from the silica cell and are accurate to ± 0.00005 . Second-order corrections have been made [R. W. Fessenden, *J. Chem. Phys.*, **37**, 747 (1962)]. The number of nuclei displaying the splitting is given in parentheses if different than one. ^b Values used to obtain the best fit with the experimental data, see Figure 1. ^c Splitting by the hydroxyl proton is not observed at this pH because of rapid exchange.

aqueous solutions. The hydroxyl radical is produced in irradiated water along with H and e_{aq}^- . In order to concentrate on the reaction of OH all solutions have been saturated with N_2O which reacts very rapidly with e_{aq}^- to produce an additional OH. The contribution of H in this system is small, only $\sim 10\%$, and no organic radicals resulting from the reaction of H have been detected. In fact, attempts to identify such radicals in acid solutions, where the yield of H becomes large (by the reaction $e_{aq}^- + H^+ \rightarrow H$), were not successful because of the poor signal-to-noise ratio of the esr spectra resulting from low steady-state concentrations. All the spectra recorded in neutral and alkaline solutions are those of the radicals produced by the reaction of OH. In most cases the spectrum of only one radical has been observed. It should be pointed out, however, that, because of the steady-state nature of these experiments, the lack of observation of the spectrum of a certain radical does not rule out its possible formation with low yields or as a shorter-lived intermediate.

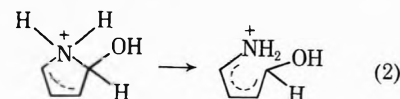
Pyrrole. The esr spectra recorded with irradiated aqueous solutions of pyrrole, both neutral and alkaline, show the presence of one nitrogen and two sets each with two equivalent protons. The most obvious structure that would show this kind of splittings is the symmetric one resulting formally from abstraction of H from the NH (Table I). This radical can be either a σ radical, similar to phenyl¹⁰ or pyridyl,¹¹ or a π radical, similar to cyclopentadienyl¹² or pyridinyl.¹³ The small hyperfine constant of the nitrogen strongly suggests that this is a π radical. The 2.9-G nitrogen splitting results from the difference between the contributions of the spin density on the nitrogen itself ($Q_N^N \rho_N$) and those on the adjacent carbons ($Q_{CN}^N \rho_C$). In parallel to the case of pyridinyl,¹³ the protons which are more adjacent to the nitrogen are expected to have the larger hyperfine constants, as assigned in Table I. The spin densities on the carbons can be calculated from McConnell's relation using $|Q_{CH}^H| = 25.7$ G from cyclohexadienyl.¹² Thus carbons 2 and 5 carry spin densities of 0.516 each and carbons 3 and 4 carry 0.138 each. The total spin density on the carbons is, therefore, 1.308, which requires a negative spin density on the nitrogen of -0.308 . Alternatively, if the spin density on carbons 3 and 4 is negative, that on the nitrogen will have to

be positive, with a value of 0.244. It is not possible at present to use any reliable values of Q_N^N and Q_{CN}^N in order to distinguish between the two possibilities. The results for imidazole presented below suggest, however, that the nitrogen carries a negative spin density.

The radical from pyrrole, although schematically resulting from H abstraction, is not likely to be produced *via* such a mechanism. The rate constant for H abstraction from NH is at least two orders of magnitude lower than that of OH addition to the ring, which is diffusion controlled.⁸ It is reasonable to assume, therefore, that the initial step is addition of OH which is then followed by elimination of water (eq 1). In the case of 2-pyrrolecarboxylic



acid the OH adduct has, indeed, been observed (see Table I) and water elimination from that adduct must be a much slower process. The pulse radiolysis experiments⁸ have shown that the radical formed by addition of OH to pyrrole protonates in acid solutions and the protonated form undergoes a ring opening (eq 2). Unfortunately, no esr lines could



be detected in the acid region apparently as a result of line broadening caused by proton exchange.

2-Pyrrolecarboxylic Acid. All the spectra recorded with irradiated solutions of 2-pyrrolecarboxylic acid between pH 5 and 12 were somewhat similar in their general patterns and are assigned to the radical produced by OH addition to the 5 position (Table I). This radical has an allylic structure at positions 2, 3, and 4. The proton in the

(10) P. H. Kasai, E. Hedaya, and E. B. Whipple, *J. Amer. Chem. Soc.*, **91**, 4364 (1969).

(11) P. H. Kasai and D. McLeod, Jr., *J. Amer. Chem. Soc.*, **94**, 720 (1972).

(12) R. W. Fessenden and R. H. Schuler, *J. Chem. Phys.*, **39**, 2147 (1963).

(13) R. W. Fessenden and P. Neta, *Chem. Phys. Lett.*, **18**, 14 (1973).

central position of the allylic structure has a small hyperfine constant of 1.7 G and that at the 4 position shows an 8.8-G splitting, in agreement with similar findings with the furancarboxylic acids.⁷ This radical parallels the OH adducts of furans⁷ also in that the proton at the 5 position has a large 23-G splitting while the spin density on the adjacent carbon atom is only 0.34 (8.84/25.7). The nitrogen hyperfine constant is small, 3.4 G, which is reasonable by comparison to the 6.1-G nitrogen splitting in the radical from glycine¹⁴ ($\text{H}_2\text{N}\dot{\text{C}}\text{HCO}_2^-$) when account is taken of the fact that the spin density on carbon 2 of the present radical is only ~ 0.5 (judging, for example, from the case of *N*-methylpyrrole given below).

In the pH region of 5–10 an additional small proton splitting of 0.28 G is observed. This splitting can be assigned to either the OH or the NH proton. Because a proton splitting of a similar magnitude is observed with the *N*-methyl derivative (see below) it can be concluded that this splitting is caused by the OH proton. Furthermore, in both radicals from 2-pyrrolecarboxylic acid and *N*-methyl-2-pyrrolecarboxylic acids this splitting disappears at pH 11–12 with no change in the other hyperfine constants. This disappearance is expected to be a result of rapid exchange of the OH proton¹⁵ as was similarly found for the OH adduct of 2,5-furandicarboxylic acid.⁷

When the pH is increased above 12 all the hyperfine constants change. These changes appear to be the result of an acid–base dissociation which can take place either at the OH or at the NH group. Because the OH proton exchanges (*via* dissociation) at pH 11 it must be the one to dissociate at this higher pH. The fact that similar changes take place in the radical derived from *N*-methyl-2-pyrrolecarboxylic acid also supports this assignment. An additional small proton splitting appears at pH >12 (Table I) which can be assigned to the NH proton.

In order to verify that the changes in hyperfine constants at pH >12 are the result of proton dissociation and to determine the *pK* for this process a detailed study of the effect of pH has been undertaken. Four different hyperfine constants have been plotted as a function of pH (Figure 1) and the experimental points fitted with the best theoretical curve. The high pH plateau of the curve is not reached at pH 14 and, therefore, the corresponding values had to be determined by curve fitting. It can be seen in Figure 1 that very good agreement is obtained between the experimental points and the curves calculated using the plateau values given in Table I and *pK* = 13.5. This agreement also shows that the spectra observed at all pH values can be assigned to one radical present in solution at different protonation stages.

***N*-Methylpyrrole.** Hydroxyl radicals add to the 2-position of *N*-methylpyrrole and the adduct cannot undergo a water elimination, such as was found with pyrrole. The esr spectrum observed shows one large proton hyperfine constant of 24.8 G and splittings by three protons of the allylic structure (11.8, 11.5, and 1.1 G), by one nitrogen, and by three equivalent protons of the methyl group (2.3 G). The assignment is, therefore, straightforward as given in Table II.

***N*-Methyl-2-pyrrolecarboxylic Acid.** All the observations with this compound (Table II) are similar to those with the nonmethylated derivative (Table I), except for the obvious difference caused by the methyl group. The very small NH proton splitting in the radical from 2-pyrrolecarboxylic acid is replaced here by a 3.9-G quartet and

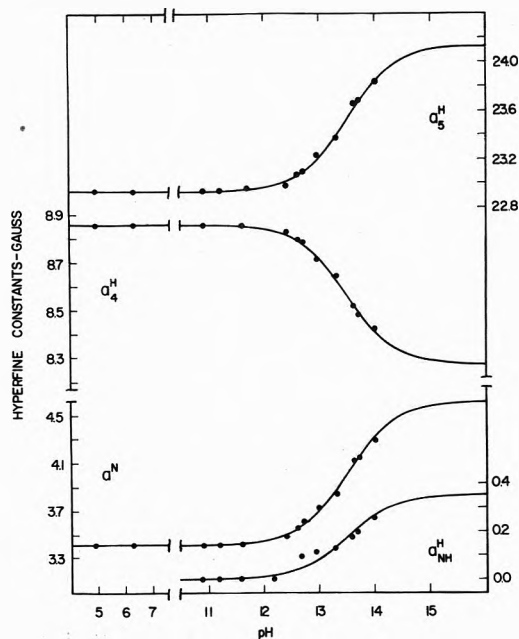


Figure 1. Effect of pH on the hyperfine coupling constants observed for the radical formed by addition of OH to 2-pyrrolecarboxylic acid. The theoretical curves which give the best fit with the experimental points have been calculated from $a = (a_{\text{HA}} + a_{\text{A}^-}K/[\text{H}^+]) / (1 + K/[\text{H}^+])$; where a is the experimentally observed hyperfine constant, a_{HA} and a_{A^-} are those of the acid and basic forms, respectively, and K is the equilibrium constant. The hyperfine constants for the basic form could not be measured experimentally and the values of these constants which give the best agreement with the measurement made at pH ≤ 14 are summarized in Table I.

this large difference in the magnitude of the splittings is somewhat unexpected.¹⁶ However, all the other hyperfine constants remain very similar and undergo the same type of changes with pH. The *pK* for the dissociation of the OH group has been determined in the same way as with 2-pyrrolecarboxylate and found to be 13.4, similar to the value of 13.5 found for the nonmethylated analog. This finding supports the previous conclusion that the OH group, rather than NH, undergoes dissociation. In neutral solution the small splitting by the OH proton was also observed and this again disappeared at pH 11 because of rapid exchange.

Imidazole. The reaction of OH with imidazole can follow the same pattern as that with pyrrole, with possible changes in the rate constants. The esr spectra recorded with irradiated solutions of imidazole at pH 9 and 12 were different. The spectrum at the higher pH showed splittings by two equivalent nitrogens, two equivalent protons, and one additional proton. The obvious structure which fulfills these requirements is that formed by the loss of hydrogen from the NH (Table III). At the lower pH a completely different spectrum is observed. The nitrogens are not equivalent, though they have hyperfine constants of 1.4 and 2.6 G, the average of which is identical with that found for the two nitrogens at pH 12. Moreover, five different proton hyperfine constants are observed, one of

(14) P. Neta and R. W. Fessenden, *J. Phys. Chem.*, **75**, 738 (1971).

(15) G. P. Laroff and R. W. Fessenden, *J. Phys. Chem.*, submitted for publication.

(16) It should be pointed out, however, that the very small NH proton splitting can result from canceling contributions by spin densities on C_2 and N_1 , whereas in the case of N-CH_3 the contribution of the spin density on C_2 to the CH_3 proton hyperfine constant will be negligible as compared to that of the N_1 spin density, so that the cancellation effect is removed.

TABLE II: ESR Parameters of Radicals Produced by Reaction of OH with *N*-Methylpyrroles^a

	<i>N</i> -Methylpyrrole pH 12	<i>N</i> -Methyl-2-pyrrolecarboxylic acid		
		pH 7	pH 11	pH >14 ^b
<i>g</i> factor	2.00252	2.00299	2.00299	2.00303
a^N	2.69	3.90	3.90	4.93
a_5^H	24.77	23.32	23.32	24.90
a_2^H	11.80			
a_4^H	11.45	8.28	8.28	7.63
a_3^H	1.06	1.56	1.56	1.67
$a_{CH_3^H}$	2.30 (3)	3.90 (3)	3.90 (3)	4.83 (3)
a_{OH^H}	c	0.31	c	
Suggested radical structure				

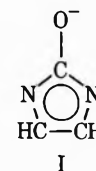
^a See footnote a, Table I. ^b Values used to obtain the best fit with the experimental data of pH 12–14. ^c See footnote c, Table I.

them (26.4 G) being characteristic of that of a proton on the same carbon where OH adds to the ring. Two others, 9.8 and 16.3 G, can be reasonably assigned to the allylic type structure given in Table III, and the remaining small splittings result from the NH and OH protons.

At the intermediate pH values, around pH 10, lines attributable to both radicals have been observed with varying intensities. It can be estimated that at pH 10 both radicals are present at similar concentrations. This gradual change in the concentration of the two radicals can be the result of either a change in the mechanism of reaction, where each radical is formed independently, or a transformation of one radical into the other affected by pH. The first possibility does not seem reasonable because OH is not expected to abstract H from NH directly to any appreciable extent and because there appears to be no reason to assume a change in mechanism around pH 10 (the *pK* for OH is 11.8 and the *pK* for imidazole is 7.0). On the other hand, it is very likely that the mechanism involves addition of OH as a first step at all pH values, and that the OH adduct undergoes a slow elimination of water, a process that can be catalyzed by the base. Thus the second radical in Table III is formed from the first.

The symmetric radical formed by elimination of water from the OH adduct of imidazole is somewhat similar in structure to that obtained from pyrrole. Both radicals show small nitrogen hyperfine constants but the proton splittings are different. In the case of imidazole all proton hyperfine constants are above 10 G. These constants indicate, therefore, positive spin densities on all the carbon atoms, which then require negative spin densities on the nitrogens. Using $Q_{CH^H} = 25.7 \text{ G}^{12}$ the spin density at the 2 position is 0.53 and those at the 4 and 5 positions are 0.41. The total spin density on the carbon atoms is 1.35 and, therefore, each nitrogen must carry a negative spin density of -0.175 . This conclusion suggests that in the case of the radical from pyrrole the spin density on the nitrogen is also negative.

At pH 13 esr lines of an additional radical appear in the spectrum and their intensity increases in more strongly basic solutions. The parameters calculated from these lines are $a^N = 0.53 \text{ G}(2)$, $a^H = 8.31 \text{ G}(2)$, and $g = 2.00357$. A possible assignment for these parameters is the hydroxy-imidazole radical I produced by secondary reactions.



Methylimidazole. Several methyl derivatives have been investigated but only with 2-methylimidazole was the spectrum sufficiently intense to allow analysis. The parameters calculated and the suggested structure of the radical are given in Table III. The observation of two equivalent nitrogens of 1.75-G splitting and two equivalent protons with a hyperfine constant of 10.2 G allows the assignment given in the table, which is parallel to that for the case of imidazole at the same pH. The single proton splitting of 13.6 G in imidazole is replaced here by a 15.3-G quartet, in very good agreement with the expected relative values of α and β protons (taking the values for the isopropyl radical, 22.1 and 24.7 G, as a reference).¹²

4,5-Imidazolecarboxylic Acid. The esr parameters and the suggested structures of the radicals produced by reaction of OH with this compound are summarized in Table IV. In neutral solutions spectra ascribable to two different radicals have been observed simultaneously. One radical shows a 27-G proton splitting and must, therefore, be that formed by addition of OH at the 2 position. The other radical shows no such large hyperfine constant and is most probably that produced by OH addition on a carbon bearing a carboxyl group. The structure given in Table IV for this radical, with the OH adding to the 5 position, is one possibility. The other, the adduct to the 4 position, seems less likely to be produced or to fit the observed parameters because it would not contain an allylic structure.

The two radicals observed in neutral solutions undergo different changes at pH >9. The 2-hydroxy radical undergoes an exchange of the OH proton at pH >10, followed by dissociation of this proton with $pK = 12 \pm 0.5$. Elimination of water from this radical, resulting in a symmetric structure, appears to be a slow process and is not detected. The 5-hydroxy radical disappears at pH 11 and no radical was observed which could result directly from it by dissociation or water elimination. However, spectra of two additional radicals have been recorded at pH 11.5 for which no certain assignment can be made at present. One

TABLE III: ESR Parameters of Radicals Produced by Reaction of OH with Imidazoles^a

	Imidazole		2-Methylimidazole pH 11.9
	pH 9-10	pH 10-12	
<i>g</i> factor	2.00226	2.00226	2.00235
<i>a</i> ₁ ^N , <i>a</i> ₃ ^N	1.43, 2.63	2.00 (2)	1.75 (2)
<i>a</i> ₂ ^H	9.85	13.62	
<i>a</i> ₄ ^H	} } 16.30	} 10.55 (2)	} 10.20 (2)
<i>a</i> ₅ ^H			
<i>a</i> _{NH} ^H	1.43		
<i>a</i> _{OH} ^H	0.35		
<i>a</i> _{CH3} ^H			15.30(3)
Suggested radical structure			

^a All solutions contained 10^{-3} – 10^{-2} M of the imidazole and were saturated with N₂O. Hyperfine constants are given in gauss and are accurate to ± 0.03 G. The *g* factors are measured relative to the peak from the silica cell and are accurate to ± 0.00005 . Second-order corrections have been made [R. W. Fessenden, *J. Chem. Phys.*, 37, 747 (1962)]. The number of nuclei displaying the splitting is given in parentheses if different than one.

TABLE IV: ESR Parameters of Radicals Produced by Reaction of OH with 4,5-Imidazoledicarboxylic Acid^a

	pH			
	6-9	7-9	(>10) ^b	12.3
<i>g</i> factor	2.00292	2.00332	2.00332	2.00334
<i>a</i> ₁ ^N , <i>a</i> ₃ ^N	1.62, 1.74	4.49, 5.29	4.49, 5.29	4.52, 6.14
<i>a</i> ₂ ^H	7.56	27.36	27.36	27.80
<i>a</i> _{NH} ^H	1.89	3.11	3.11	2.94
<i>a</i> _{OH} ^H	0.25	0.44	c	
Suggested radical structure				

^a All solutions contained 10^{-3} – 10^{-2} M of the imidazole and were saturated with N₂O. Hyperfine constants are given in gauss and are accurate to ± 0.03 G. The *g* factors are measured relative to the peak from the silica cell and are accurate to ± 0.00005 . Second-order corrections have been made [R. W. Fessenden, *J. Chem. Phys.*, 37, 747 (1962)]. ^b The parameters determined at pH > 10 were not identical with those at pH 7-9 (without the OH splitting) but were slightly affected by the dissociation with $pK = 12$. ^c See footnote c, Table I.

of these showed splittings by two equivalent nitrogens only, with $a^N = 0.56$ G and $g = 2.00382$. It had very intense lines and was also present at pH 14, where all the other radicals had spectra of very low intensity. This radical has somewhat similar parameters to those of the radical formed in very alkaline solutions of imidazole, without the proton splittings, and it is most probably the dicarboxy derivative of the hydroxyimidazole radical. The other radical observed at pH 11.5 shows two different nitrogen hyperfine constants of 1.23 and 0.28 G, one 8.23-G proton splitting, and $g = 2.00368$, but again the assignment is not clear.

Isoxazole. The spectrum recorded with a neutral solution of isoxazole was analyzed in terms of one nitrogen splitting and four different proton splittings. The assignment (Table V) is based on the previous results with the furans⁷ and on the other results in the present paper. Addition of OH to any of the other carbons will not produce a radical which would be expected to show the observed parameters and, furthermore, will not result in a stabilized allylic structure. In alkaline solutions this radical is expected to undergo a ring opening similar to the case of furan. Unfortunately, isoxazole itself hydrolyzes in alkali, and in fact no spectrum was observed at pH 12.4.

In comparing the esr parameters for the isoxazole OH adduct with those for the furan OH adduct⁷ it is seen that the hyperfine constants of the protons of the 3 and 4 positions are very similar (2.18 and 13.57 G in isoxazole *vs.* 1.97 and 13.59 G in furan). On the other hand the large splitting of the proton at the 5 position is 26 G in the OH adduct of isoxazole, considerably larger than the 21 G observed in the case of furan. This difference indicates that the nitrogen atom of the isoxazole radical allows the transfer of a larger fraction of spin density onto the oxygen, as compared to the fraction transferred in the case where carbon is at the 2 position.

Pyrazole. The spectrum recorded with irradiated solutions of pyrazole, both neutral and mildly alkaline, showed the presence of one radical only and the splittings by all the magnetic nuclei were observed. The esr parameters and the suggested structure of the OH adduct are shown in Table V. The OH adduct of pyrazole and that of isoxazole are similar in structure and the esr parameters are very similar as well (Table V). Again the OH adds preferentially to the 5 position, which is the only case that results in an allylic type radical. The hyperfine constants of the protons at positions 1 and 3 are similar and cannot be distinguished. The splittings of the nitrogen and the

TABLE V: ESR Parameters of Radicals Produced by Reaction of OH with Isoxazole, Pyrazole, and 3,5-Pyrazoledicarboxylic Acid

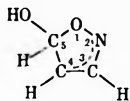
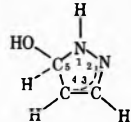
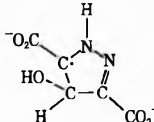
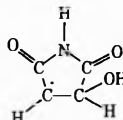
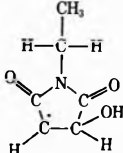
	Isoxazole pH 6.9	Pyrazole pH 9.4	3,5-Pyrazoledicarboxylic acid pH 4.7–10.7
<i>g</i> factor	2.00225	2.00320	2.00269
a_1^N		5.37	2.35
a_2^N	9.43	8.76	0.75
a_{NH}^H		1.39	3.29
a_3^H	2.18	1.58	
a_4^H	13.57	10.32	29.35
a_5^H	26.19	30.96	
a_{OH}^H	0.15	0.42	0.41
Suggested radical structure			

TABLE VI: ESR Parameters of Radicals Produced by Reaction of OH with Maleimide and *N*-Ethylmaleimide

	Maleimide pH 6.5	<i>N</i> -Ethylmaleimide pH 4.7
<i>g</i> factor	2.00307	2.00313
a^N	0.87	1.27
a_3^H	28.61	26.79
a_4^H	20.66	20.55
a_{NH}^H	1.59	
$a_{CH_2}^H$		1.55, 1.05
a_{OH}^H	0.24	0.22
Suggested radical structure		

two protons of the allylic structure (positions 2, 3, and 4) are all smaller than the corresponding ones for the radical from isoxazole. This difference shows that a relatively larger portion of spin density is transferred from the allylic structure to the 1 position in the case of pyrazole as compared to the case of isoxazole. This effect results also in a larger hyperfine constant for the proton at the 5 position of pyrazole as compared to the value in the case of isoxazole.

In alkaline solutions of pyrazole the spectrum recorded consisted of low-intensity lines which did not allow accurate analysis.

3,5-Pyrazoledicarboxylic Acid. The addition of OH to 3,5-pyrazoledicarboxylic acid does not take place at the 5 position as in the case of pyrazole, apparently because this position is somewhat sterically hindered by the carboxyl group. Addition takes place at position 4 instead, resulting in the radical shown in Table V. The assignment is straightforward because it is the only possibility which agrees with a 29-G proton splitting. The spectrum of this radical has been observed at pH 4.7–10.7 along with many additional lines. Some of these lines, which appeared only at pH <9, did not show any clear pattern and were not analyzed. Other lines were observed only at pH >7, grew more intense at higher pH values, and were also observed at pH 11.7, 12.5, and 13.7, where the main radical (given in Table V) was not detected. These lines could be analyzed in terms of two radicals which appear to result from secondary reactions similar to the case of the imidazolidi-

carboxylic acid. One radical shows two nitrogen splittings of 0.87 and 4.90 G and a 4.90-G proton splitting with $g = 2.00425$. The other radical shows only splittings by two equivalent nitrogens with a 2.04-G constant and $g = 2.00456$. A radical with a carbonyl group at the 4 position might account for the latter parameters.

Maleimide and *N*-Ethylmaleimide. These compounds contain the basic pyrrole ring but are obviously of a different nature. They were investigated because of their possible importance as radiation sensitizers. The esr parameters for the radicals produced by reaction of OH are summarized in Table VI. In both compounds OH adds to carbon 3 resulting in a radical with a 20-G α proton splitting and a 27–28-G β proton splitting. A hyperfine constant of 0.2 G for the OH proton is also observed and the nitrogen splitting is ~ 1 G. The NH proton splitting in maleimide is 1.6 G, which in the *N*-ethyl derivative is replaced by two proton splittings. It is interesting to note, however, that these two protons are not equivalent. This inequivalence could result from hindered rotation around the N–CH₂ bond, as suggested by a constructed model. However, even if rotation was not hindered the CH₂ protons can still be inequivalent owing to the lack of plane of symmetry on the ring.

Summary and Conclusions

It has been demonstrated in the present study that OH radicals react with pyrroles and imidazoles by addition at a carbon adjacent to the nitrogen. The adducts do not un-

dergo ring opening in neutral and alkaline solutions, although previous optical pulse radiolysis results⁸ suggested that the OH adduct to pyrrole undergoes a ring opening in acid solution. On the other hand, elimination of a water molecule (the OH added and the H from NH) takes place with some OH adducts of pyrroles and imidazoles. This elimination is more rapid in pyrroles than in imidazoles, is more rapid in the unsubstituted compounds as compared to the carboxy derivatives, and is catalyzed by base. In fact, water elimination from any of the carboxy derivatives examined was not detected at all, whereas with pyrrole the initial OH adduct was not observed.

All the OH adducts undergo a rapid exchange of the OH proton, at pH >10 for imidazoles and >11 for pyrroles, resulting in a loss of the OH proton splitting with no change in the other hyperfine constants. The OH group of the adducts dissociates with $pK = 12$ for the case of 4,5-imidazoledicarboxylic acid and $pK = 13.5$ for 2-pyrrole-

carboxylic acid and its *N*-methyl derivative. This dissociation results in changes in all the hyperfine constants, and in the intermediate region weighted average hyperfine constants have been observed, with no apparent change in line width. This fact indicates a rapid exchange between the acid and basic forms.¹⁵

The addition of OH to isoxazole was found to take place on the carbon adjacent to the oxygen rather than that adjacent to the nitrogen. The OH adduct is expected to undergo ring opening in alkaline solutions as in the similar case of furans, but this process could not be detected because of basic hydrolysis of isoxazole itself.

Addition of OH to pyrazole occurs at the 5 position next to the NH group and results in an allylic type radical. When the 5 position is sterically hindered by a carboxyl group as in the case of 3,5-pyrazoledicarboxylic acid, addition was found to take place preferentially at the 4 position.

Electron Spin Resonance Studies of Spin-Labeled Polymers. III. The Molecular Weight Dependence of Segmental Rotational Correlation Times of Polystyrene in Dilute Solution

A. T. Bullock,* G. G. Cameron, and P. M. Smith

Department of Chemistry, University of Aberdeen, Old Aberdeen, AB9 2UE, Scotland (Received December 13, 1972)

Seven narrow fraction polystyrenes have been spin labeled with nitroxide radicals and electron spin resonance spectra of dilute solutions of the polymers in toluene have been recorded over a range of temperatures. Line width analysis yields values of the rotational correlation time. A local mode of segmental reorientation has been characterized at high molecular weights and has an activation energy of 4.3 kcal mol⁻¹. Rotation of the whole molecule makes a significant contribution to the relaxation process at low molecular weights. The activation energy for this rotational mode agrees well with that for viscous flow of the solvent, namely, 2.15 kcal mol⁻¹.

Introduction

The technique of spin labeling is now reasonably well established. Briefly, a stable free radical is covalently bonded to a macromolecule and the electron spin resonance (esr) spectrum of the labeled polymer is examined. In solution, which is our concern here, measurement of the widths of the esr lines can give information about the dynamics of the polymer chain.

The class of free radicals most widely used for labeling to date is the nitroxide group.¹ Members of this class have the necessary properties of high stability and well-defined anisotropic *g* tensors and hyperfine coupling tensors to the ¹⁴N nucleus. Most of the published work in this field relates to biopolymers² but recently Lindberg and coworkers^{3,4} together with the present authors^{5,6} have demonstrated that spin labeling provides a useful additional

technique to the established methods of nmr spin-lattice relaxation, dielectric dispersion, viscoelastic relaxation, and fluorescence depolarization in the study of the dynamics of synthetic macromolecules in solution.

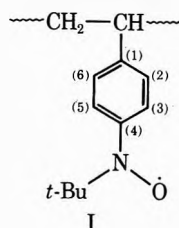
In part I of this series⁵ we described the preparation of a "lightly labeled" polystyrene which had a wide distribu-

- (1) J. D. Ingham, *J. Macromol. Sci., Rev. Macromol. Chem.*, **2**, 279 (1968).
- (2) O. H. Griffith and A. S. Waggoner, *Accounts Chem. Res.*, **2**, 17 (1969).
- (3) P. Törmälä, K. Silvennoinen, and J. J. Lindberg, *Acta Chem. Scand.*, **25**, 2659 (1971).
- (4) P. Törmälä, J. J. Lindberg, and L. Koivu, *Pap. Puu, A Painos*, **4**, 1 (1972).
- (5) A. T. Bullock, J. H. Butterworth, and G. G. Cameron, *Eur. Polym. J.*, **7**, 445 (1971).
- (6) A. T. Bullock, G. G. Cameron, and P. Smith, *Polymer*, **13**, 89 (1972).

tion of molecular weights centered on *ca.* 115,000. Comparison of the results with those obtained by other techniques, notably dielectric dispersion in poly(*p*-chlorostyrene),^{7,8} suggested that a segmental or "local mode" of rotational diffusion of the polymer was observed. The present study is concerned with a careful delineation of the dependence upon molecular weight of the correlation time for diffusive rotation of the nitroxide label and hence of that part of the macromolecule to which the label is attached.

Experimental Section

Seven narrow fraction polystyrenes were obtained from Waters Associates. The number average molecular weights were 2025, 3550, 10,000, 19,700, 50,000, 97,200, and 196,000. The method of labeling and characterization of the resultant polymer has been described in part II.^{6,9} The labeled monomer unit has the structure shown in I.



The labeled polymers were finally purified by two precipitations from toluene solution by the addition of methanol. Gel permeation chromatograms were run on the unlabeled, iodinated and labeled polymer to ensure that neither cross linking nor degradation had occurred. To avoid contributions to line widths from spin exchange, labeling was carried out in such a way that no sample contained more than one nitroxide radical per 160 monomer units. Usually the ratio was much smaller than this. Solutions (1% by weight) of the labeled fractions in toluene were prepared and degassed by repeated freeze-pump-thaw sequences.

Esr spectra were recorded for each fraction at intervals in the temperature range 278–363 K using a Decca X3 spectrometer. Field measurements were made with a Systron-Donner 3193 digital Gaussmeter. The uncertainty in an individual field measurement is ± 0.01 G (0.03 MHz) but field differences can be obtained to a slightly greater precision by careful interpolation.

Spectral simulations and least-squares analyses were performed on an I.C.L. system 4/50 computer.

Theory and Method of Line Width Analysis

The spectrum of the labeled polymer in solution is shown in Figure 1. Clearly the electron couples not only with the ^{14}N nucleus but also with the aromatic protons. These will have anisotropic hyperfine tensors and the rotational motion of the radical will modulate the coupling between the electron, the protons, and the ^{14}N nucleus. This, combined with the effect of an anisotropic g tensor, gives rise to line widths which depend on the various nuclear quantum numbers m_i and which are expressed by the equation¹⁰

$$T_2^{-1}(m_1, m_2, \dots, m_n) = A + \sum_{i=1}^n B_i m_i + \sum_{i=1}^n C_i m_i^2 + \sum_{i \neq j=1}^n E_{ij} m_i m_j \quad (1)$$

The coefficients A , B , C , and E are defined in the literature.¹⁰ At present it is only necessary to note that they are

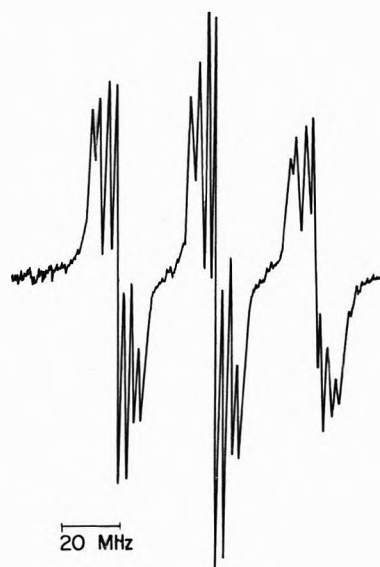


Figure 1. Esr spectrum of spin-labeled polystyrene ($\bar{M}_n = 2025$) in toluene solution (1%) at room temperature.

functions of the applied magnetic field, certain spectral densities, and various inner products of the g and hyperfine tensors. Fortunately in the present case it is possible to select lines for which Σm_H , the resultant proton spin quantum number, is zero. The line width expression then depends only on m_z , the component of the ^{14}N nuclear spin, the g anisotropy, and the anisotropy of the coupling tensor to ^{14}N . Explicitly¹¹

$$T_2(m_1)^{-1} = \left[\frac{b^2}{20}(3 + 7u) + \frac{1}{15}(\Delta\gamma B_0)^2 \left(\frac{4}{3} + u \right) + \frac{1}{8} b^2 m_1^2 \left(1 - \frac{u}{5} \right) - \frac{1}{5} b \Delta\gamma B_0 m_1 \left(\frac{4}{3} + u \right) \right] \tau_c + X \quad (2)$$

where $\Delta\gamma = -(|\beta| \hbar^{-1} [g_z - \frac{1}{2}(g_x + g_y)])$, $b = (4\pi/3)[A - \frac{1}{2}(B + C)]$, and $u = 1/(1 + \omega_0^2 \tau_c^2)$. The symbols have the following meanings: A , B , and C represent the z , x , and y components of the hyperfine tensor in Hz; ω_0 , represents the Larmor angular frequency of the electron; B_0 , the applied magnetic field; τ_c , the rotational correlation time, and X , the broadening by other mechanisms independent of m_1 . The parameter u represents nonsecular contributions to the line widths. As τ_c in all cases in this work was greater than *ca.* 10^{-10} sec, u was negligible at the microwave frequency employed ($\omega_0 = 2\pi \times 9.27 \times 10^9$ rads sec^{-1}). Omitting nonsecular contributions, eq 2 becomes

$$T_2(m_1)^{-1} = \left[\frac{3b^2}{20} + \frac{4}{45}(\Delta\gamma B_0)^2 + \frac{b^2 m_1^2}{8} - \frac{4}{15} b \Delta\gamma B_0 m_1 \right] \tau_c + X \quad (3)$$

A more convenient form of this has been proposed by Stone, *et al.*¹²

- (7) W. H. Stockmayer, *Pure Appl. Chem.*, **15**, 539 (1967).
- (8) B. Baysal, B. A. Lowry, H. Yu, and W. H. Stockmayer, "Dielectric Properties of Polymers," F. E. Karasz, Ed., Plenum Press, New York, N. Y., 1971, p 343.
- (9) Minor modifications of the labeling technique have been made recently. Details are available on request.
- (10) A. Hudson and G. R. Luckhurst, *Chem. Rev.*, **69**, 191 (1969).
- (11) G. Poggi and C. S. Johnson, Jr., *J. Magn. Resonance*, **3**, 436 (1970).
- (12) T. J. Stone, T. Buckman, P. L. Nordio, and H. M. McConnell, *Proc. Nat. Acad. Sci. U. S.*, **54**, 1010 (1965).

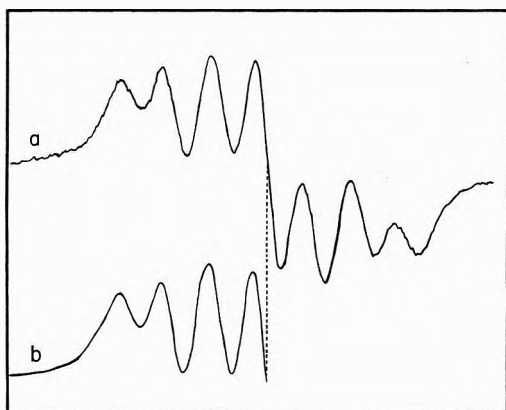


Figure 2. Recorded (a) and simulated (b) spectra of the central multiplet ($m_I = 0$); see text.

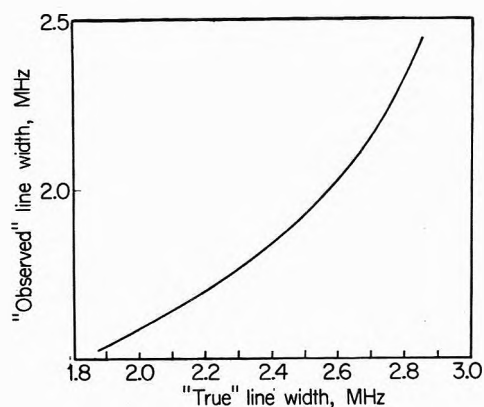


Figure 3. Calibration plot of observed vs. true peak-to-peak line width.

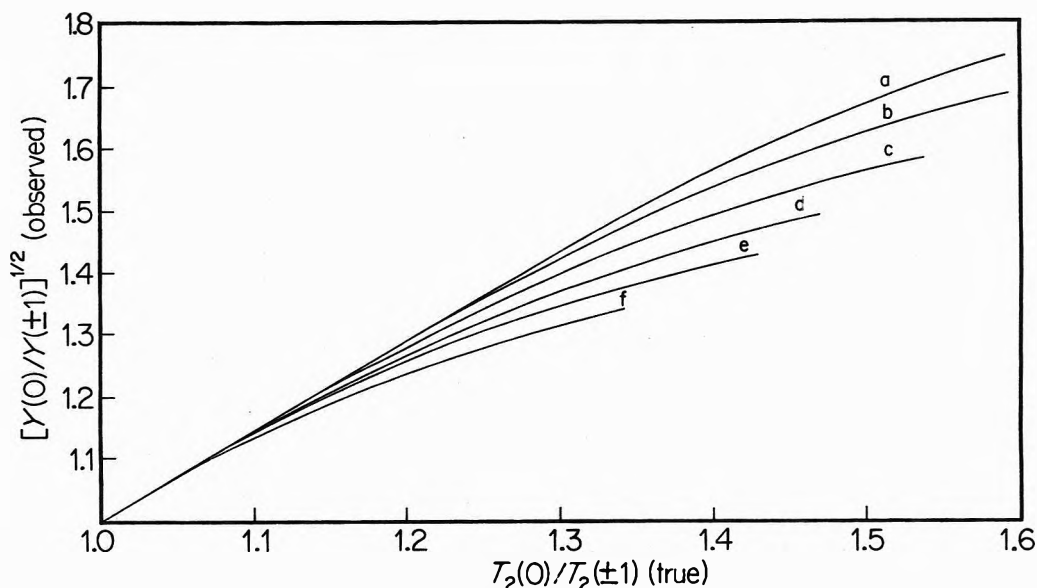


Figure 4. Calibration plots of observed $[Y(0)/Y(\pm 1)]^{1/2}$ vs. $T_2(0)/T_2(\pm 1)$ for the following values of $\Delta\nu (= [1.732\pi T_2(0)]^{-1})$ in MHz: (a) 1.90, (b) 2.00, (c) 2.10, (d) 2.20, (e) 2.30, and (f) 2.40.

$$T_2(0)/T_2(m_1) = 1 - \frac{4}{15} \tau_c b \Delta \gamma B_0 T_2(0) m_1 + \frac{1}{8} \tau_c b^2 T_2(0) m_1^2 \quad (4)$$

Defining the ratios $T_2(0)/T_2(+1)$, $T_2(0)/T_2(-1)$ as R_+ and R_- , respectively, it is readily shown that

$$R_+ + R_- - 2 = (1/4) \tau_c b^2 T_2(0) \quad (5)$$

Sensitive measures of R_+ and R_- are obtained from the ratios of peak-to-peak intensities, Y , of the relevant lines, thus

$$R_{\pm} = [Y(0)/Y(\pm 1)]^{1/2} \quad (6)$$

The parameter b was obtained by measuring the separation between extremes in the powder spectrum of the solid labeled polymer and combining this measurement with the isotropic solution value of a_N as described in part I.⁵ $T_2(0)$ and R_{\pm} are measured from the experimental spectra but both must be corrected for the inhomogeneous broadening which results from the unresolved coupling to the *tert*-butyl protons.¹¹

An experimental spectrum was chosen arbitrarily and the center multiplet ($m_I = 0$) was synthesized with various values of the ring proton couplings, the *tert*-butyl pro-

ton couplings, and $T_2(0)$, the line width parameter of the input Lorentzian line. Figure 2 shows a comparison between the recorded central multiplet and a simulated spectrum. The values of the hyperfine coupling constants finally selected were $a_{H(2,6)} = 2.48$ MHz, $a_{H(3,5)} = 5.56$ MHz, and $a_{t-Bu} = 0.21$ MHz. Previously a_N had been found to be 35.4 MHz.⁶ More recent and extensive measurements give the revised value of 35.0 ± 0.1 MHz.

A series of simulated spectra were then produced using the above coupling parameters and a range of values of T_2 . Calibration plots of observed line widths vs. true, or input, widths¹³ and observed (peak-to-peak ratios)^{1/2} vs. true line width ratios were obtained and are shown in Figures 3 and 4. True values of R_{\pm} and $T_2(0)$ could thus be obtained from experimental intensity ratios and center line widths, respectively.

Results and Discussion

Figure 5 shows the dependence of the rotational correlation time upon molecular weight at three temperatures. At high molecular weights τ_c is independent of chain length and it seems that a "local mode" or segmental relaxation process is being observed. This will be character-

(13) The input widths were the peak-to-peak widths $\Delta\nu$ (Hz) and are related to T_2 by $T_2^{-1} = 1.732\pi\Delta\nu$.

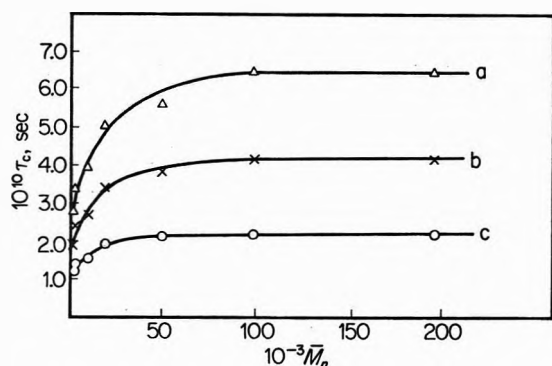


Figure 5. Dependence of the rotational correlation time τ_c upon molecular weight at (a) 294.2, (b) 312.6, and (c) 345.2 K.

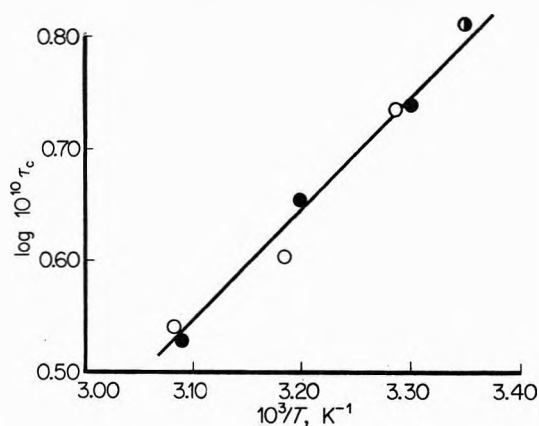
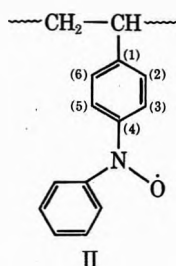


Figure 6. Composite Arrhenius plot for heterodisperse polystyrene with labels I and II: O, label I; ●, label II; ●, nmr from ref 14.

ized by a correlation time τ_{lm} . As the molecular weight decreases the rotational frequency of the whole macromolecule increases sharply and ultimately the magnitude of the correlation time τ_{eoe} describing this "end-over-end" rotation becomes comparable to τ_{lm} and contributes significantly to the relaxation process.

Before making a definite assignment of the relaxation process at high molecular weight to a segmental relaxation involving rotation about the main chain carbon-carbon bonds it is important to eliminate two other possibilities. These are rotation about the $C_{(4)}-N$ and $C_{(1)}-main$ chain bonds. In part I⁵ of this series we described results obtained from a spin-labeled heterodisperse sample of polystyrene having an average molecular weight of ca. 115,000. The labeled unit in this case had the structure shown by II. The same heterodisperse polymer was labeled



to give structure I and the correlation times of each sample were measured over a range of temperatures. Figure 6 shows the composite Arrhenius plot which includes a point calculated from some proton spin-lattice relaxation measurements made by McCall and Bovey.¹⁴ While the

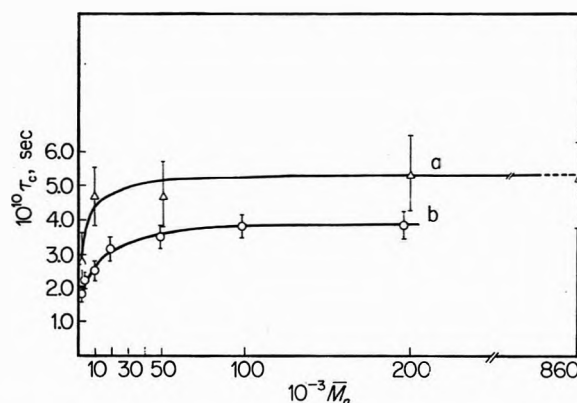


Figure 7. (a) τ_c from the ^{13}C T_1 measurements of ref 15; (b) spin-labeling results (this work). Both sets of results are at 317.2 K. The error bars in a contain the correlation times for all of the carbon atoms in polystyrene. The ordering of the correlation times at a given molecular weight is random.

close agreement between the correlation times for the sterically dissimilar spin labels I and II is not perhaps conclusive it strongly suggests that there is no significant contribution to the line widths arising from rotation about either the $C_{(4)}-N$ or the $C_{(1)}-main$ chain bonds. The activation energy for the reorientational process found from the composite data of Figure 6 is 4.7 kcal mol⁻¹ (19.5 kJ mol⁻¹).

Further support for this assignment of the chain-length-independent relaxation process was published by Allerhand and Hailstone⁵ during the course of the present work. These authors made T_1 measurements on naturally abundant ^{13}C in all positions in polystyrene using partially relaxed Fourier transform techniques. Again, a series of narrow fraction polystyrenes was used. Earlier, Allerhand, *et al.*,¹⁶ had demonstrated that ^{13}C spin-lattice relaxation was dominated by the rotationally modulated dipolar coupling between the ^{13}C nucleus and the proton or protons bonded to it. For the case where $(\omega_C + \omega_H)\tau_c \ll 1$, where $\omega_{C,H}$ are the Larmor frequencies of the nuclei concerned, they showed that

$$T_1^{-1} = \hbar^2 \gamma_H^2 \gamma_C^2 N r_{CH}^{-6} \tau_c \quad (7)$$

In this equation, γ_H and γ_C are the magnetogyric ratios of 1H and ^{13}C , respectively, N is the number of protons bonded to the carbon atom under consideration, and r_{CH} the C-H bond length. We have used eq 7 to calculate τ_c for all the carbon atoms in the polymer using the values of T_1 given by Allerhand and Hailstone. The most important result is that for a given molecular weight, τ_c is the same within experimental error for all carbon atoms. This leads to the conclusion that segmental reorientation is the dominant factor at high molecular weights since internal rotation of the phenyl group cannot contribute to the $^{13}C-^1H$ dipolar relaxation of carbon 4 or of the two aliphatic carbon atoms. Figure 7 compares the rotational correlation times found by the nmr and spin-labeling techniques. The results generally agree to within the combined error limits although it is worth pointing out that the neglect of minor contributions to T_1 from sources other than the $^{13}C-^1H$ dipolar mechanism will lead to high values of τ_c through the use of eq 7.

(14) D. W. McCall and F. A. Bovey, *J. Polym. Sci.*, **45**, 530 (1960).

(15) A. Allerhand and R. K. Hailstone, *J. Chem. Phys.*, **56**, 3718 (1972).

(16) A. Allerhand, D. Doddrell, and R. Komoroski, *J. Chem. Phys.*, **55**, 189 (1971).

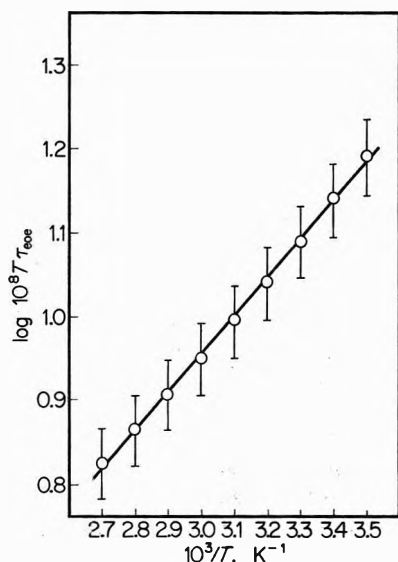


Figure 8. A plot of $\log(10^8 T \tau_{ee})$ vs. $10^3/T$ for polystyrene ($M_n = 2025$) in toluene (1%); $E_a = 2.1 \pm 0.4$ kcal mol $^{-1}$.

Activation energies, E_a , for the reorientational process have been derived for all seven labeled fractions. At low molecular weights E_a increases monotonically with chain length from its lowest value of 3.5 ± 0.1 kcal mol $^{-1}$ but asymptotically approaches the value of 4.3 ± 0.2 kcal mol $^{-1}$ at high molecular weights. The values of E_a for those fractions, which are in the region where τ_c depends upon M_n , have little direct physical significance since the reorientational process is a complex one involving segmental and whole molecule rotation. At high molecular weights, however, the value of 4.3 ± 0.2 kcal mol $^{-1}$ should be characteristic of the segmental reorientation and is very close to the values of 4.5 ± 0.5 and *ca.* 4.8 kcal mol $^{-1}$ found by Stockmayer and coworkers⁸ for dielectric relaxation in poly(*p*-fluorostyrene) and poly(*p*-chlorostyrene), respectively. The unexpected conclusion to be reached from this comparison is that the "stiffness" of the chain seems to be little influenced by large polar substituents in the para position of the styryl ring. Dielectric relaxation results on solutions of copolymers of styrene and *p*-chlorostyrene with varying polar monomer content lead to the same conclusion.¹⁷

Finally, we have calculated the activation energy for end-over-end rotation of the whole polymer molecule for the three fractions of lowest molecular weight. The relaxation time of the first normal mode of the polymer molecule, τ_1 , essentially describes the time evolution of a vector joining the ends of the chain with respect to some vector fixed in the laboratory frame. The coordinate function involved is the first-order spherical harmonic $\cos \theta$, where θ is the angle between the two vectors. This relaxation time is given for various models in dilute solution by the equations⁷

$$\tau_1 = 1.21M[\eta]\eta_0/RT \quad (\text{free draining}) \quad (8a)$$

$$\tau_1 = 0.85M[\eta]\eta_0/RT \quad (\text{nondraining}) \quad (8b)$$

$$\tau_1 = 1.20M[\eta]\eta_0/RT \quad (\text{rigid impenetrable sphere}) \quad (8c)$$

where M is the molecular weight, $[\eta]$ the limiting viscosity number, and η_0 the viscosity coefficient of the solvent. Correlation times in magnetic resonance are normally concerned with second-order spherical harmonics of the position coordinates, and it may be shown that $\tau_{eoe} = \tau_1/3$.

With toluene, which is a thermodynamically "good" solvent for polystyrene, $[\eta]$ varies by less than 1% in the range 298–338 K for a fraction of molecular weight 144,000.¹⁸ If we assume a similar independence for the fractions studied in the present work than eq 8 all predict that a plot of $\log(T\tau_{eoe})$ vs. $1/T$ should give an activation energy equal to that for viscous flow in the pure solvent, namely, 2.15 kcal mol $^{-1}$.¹⁹ Values of τ_{eoe} were calculated for fractions of molecular weight 2025, 3550, and 10,000 over a range of temperatures using the expression

$$1/\tau_c = (1/\tau_{eoe}) + (1/\tau_{lm}) \quad (9)$$

Figure 8 shows the results of this analysis for the fraction having the lowest molecular weight. Since this fraction shows the largest differences between τ_c and τ_{lm} , it is to be expected that the calculations will give more precise values of τ_{eoe} than those for the other fractions. The activation energy obtained from Figure 8 is indeed in excellent agreement with that for viscous flow of the solvent, being 2.1 ± 0.4 kcal mol $^{-1}$. The other two fractions gave greater deviations from the viscous flow value but the mean activation energy for the three cases considered was 2.15 ± 0.33 kcal mol $^{-1}$.

The above separation into the shortest and longest normal modes is undoubtedly oversimplified and other modes must be considered in a more complete analysis. However, the procedure seems valid for the shortest polystyrene chain ($M_n = 2025$) for which $\tau_1/3 = 4.8 \times 10^{-10}$ sec at 298 K from eq 8b (nondraining coil). The experimental τ_{eoe} for this sample is 4.4×10^{-10} sec. This agreement breaks down at higher molecular weights presumably due to the participation of higher modes.

The relative role of solvent reorganization as a factor in the ease of local mode relaxation processes is subject to discussion. It is hoped that current work in this laboratory on the effect of solvent viscosity on τ_c for "good" and "poor" solvents will throw some light on this.

Acknowledgment. The authors wish to thank Professor W. H. Stockmayer for helpful correspondence and discussion and Professor G. M. Burnett of this department for his continued encouragement. An equipment grant from the Science Research Council and a maintenance award to P. M. S. from Imperial Chemical Industries, Ltd., are gratefully acknowledged.

(17) G. P. Mikhailov, A. M. Lobanov, and M. P. Platonov, *Polym. Sci. USSR*, **9**, 2565 (1967).

(18) L. H. Cragg and J. E. Simkins, *Can. J. Res., Sect. B*, **27**, 961 (1949).

(19) Derived from data obtained from "Selected Values of Physical and Thermodynamic Properties of Hydrocarbons and Related Compounds," American Petroleum Institute Research Project 44, 1953.

Matrix Infrared Spectrum and Evidence for Photoisomerism of $\text{Li}^+(\text{ON})^-$. Infrared Spectrum of $\text{Li}^+(\text{ON})^2-\text{Li}^+$

David E. Tevault and Lester Andrews*

Chemistry Department, University of Virginia, Charlottesville, Virginia 22903 (Received February 9, 1973)

Matrix reactions of lithium atoms and nitric oxide have been reinvestigated using approximately equimolar concentrations of Li and NO at high dilution in argon. Intense bands at 1352 and 651 cm^{-1} and isotopic counterparts were assigned to intraionic $(\text{N}-\text{O})^-$ and interionic $\text{Li}^+(\text{NO})^-$ vibrational modes. Mercury arc photolysis decreased the 651-cm^{-1} band while the 1352-cm^{-1} band increased, and a new 447-cm^{-1} absorption appeared. This observation suggests photoisomerization of the triangular $\text{Li}^+(\text{ON})^-$ species to another form where the $(\text{NO})^-$ frequency is the same but the interionic Li-O frequency is shifted to 447 cm^{-1} . Absorptions at 886 , 796 , and 415 cm^{-1} were assigned to the secondary reaction product $\text{Li}^+(\text{NO})^2-\text{Li}^+$; the 886-cm^{-1} frequency is primarily an intraionic $(\text{NO})^2-$ mode whereas the latter two frequencies are interionic modes.

Introduction

The molecule lithium nitroxide, LiON, has been synthesized by Andrews and Pimentel¹ following matrix reactions of lithium atoms and nitric oxide. Isotopic data suggested a bent molecule with the Li more strongly bonded to the oxygen end of NO; the NO frequency was significantly lowered, indicating that antibonding electron density was added to NO from the Li atom. In order to explain the bonding in LiON, two schemes were suggested: lithium p orbitals participating in a π molecular orbital system, and the simple electrostatic picture $(\text{Li}^+)(\text{ON})^-$ with the Li^+ more strongly bound to the more electronegative oxygen of NO^- .

Recent vibrational analysis of LiON using an acute triangular model² produced an excellent frequency fit and suggested a reinterpretation of the structure and bonding in LiON along the lines reported by Andrews³ for LiO_2 . Oxygen isotopic spectra for LiO_2 indicated an isosceles triangular structure; the bonding was suggested to be electrostatic Li^+O_2^- owing to the agreement in O_2^- and LiO_2 oxygen-oxygen stretching frequencies.³

Subsequently, an *ab initio* MO study was reported, which indicated an acute triangular structure with an LiON angle of 80° and an ionic charge distribution⁴ for LiON. These calculations were reinforced by very recent CNDO calculations⁵ on the LiON species which found a minimum energy for the LiON angle of 80° . While this work was nearing completion, a paper by Milligan and Jacox⁶ appeared which described Li atom matrix reactions with nitrogen oxides including NO. These workers observed two frequencies assigned previously to LiON, the N-O stretch at 1352 cm^{-1} and the Li-O stretch at 651 cm^{-1} ; mercury arc photolysis decreased the Li-O stretching absorption while the N-O absorption remained or was slightly enhanced. Milligan and Jacox⁶ concluded that the 1352 - and 651-cm^{-1} bands must belong to two different species, in disagreement with the earlier assignment of these two bands to the same LiON species by Andrews and Pimentel.¹ Clearly, further work is needed to satisfactorily explain the photolysis of LiON or to identify the two different LiON species suggested by Milligan and Jacox.

A two-lithium feature was observed in the spectrum of Andrews and Pimentel,¹ but no details on this absorber were reported. In the recent lithium-oxygen work,³ secondary reactions produced the molecule LiO_2Li . The rhombus structure and $\text{Li}^+(\text{O}_2)^2-\text{Li}^+$ bonding picture suggested³ for the peroxide invite further consideration of the Li_2NO species reported earlier.¹ We have studied lithium atom-nitric oxide reactions under a variety of reagent conditions which favor the secondary lithium reaction, *i.e.*, the two lithium species. Here follows a discussion of these new results and a reanalysis of the structures, photochemistry, and bonding in the LiON and $\text{Li}(\text{ON})\text{Li}$ species.

Experimental Section

The cryogenic refrigeration system, apparatus, and experimental techniques have been described in earlier papers from this laboratory.^{3,7} Isotopically enriched samples of lithium metal, 99.99% ^7Li and 95.6% ^6Li -4.4% ^7Li (ORNL), were used without purification. Nitric oxide (Matheson) was purified by fractional distillation on a vacuum line to remove traces of N_2O . Nitrogen-15 enriched nitric oxide (99% ^{15}NO , Prochem, Ltd.) and argon (Air Products, 99.995%) were used without purification. Oxygen-18 labeled nitric oxide was synthesized by partial reaction and exchange between NO and $^{18}\text{O}_2$ (Miles Laboratories). The resulting NO_2 -NO mixture was fractionated using repeated bulb-to-bulb distillations; traces of NO_2 were removed by shaking the gas in a small bulb containing mercury.

Samples of nitric oxide in argon (M/R = 250/1 to 600/1) were deposited onto a cesium iodide window at 15°K along with an atomic beam of lithium; Knudsen cell temperatures ranging from 415 to 465° were employed. According to the lithium vapor pressure data of Hicks,⁸ the

- (1) W. L. S. Andrews and G. C. Pimentel, *J. Chem. Phys.*, **44**, 2361 (1966).
- (2) L. Andrews, unpublished calculations.
- (3) L. Andrews, *J. Chem. Phys.*, **50**, 4288 (1969).
- (4) J. Peslak, Jr., D. S. Klett, and C. W. David, *J. Amer. Chem. Soc.*, **93**, 5001 (1971).
- (5) L. F. Hayes, Ph.D. Thesis, University of Virginia, 1970.
- (6) D. E. Milligan and M. E. Jacox, *J. Chem. Phys.*, **55**, 3404 (1971).
- (7) L. Andrews, *J. Chem. Phys.*, **48**, 972 (1968).

temperature 450° , which was used in most of the present experiments, gives a lithium vapor pressure of 0.65μ , a five-fold increase over the previous¹ experiments. Deposition times ranged from 21 to 24 hr. Selected samples were subjected to mercury arc photolysis using the full light of a high-pressure General Electric BH-6 lamp; the output radiation was passed through a 5-cm water bath and focused onto the sample using a quartz lens system. Infrared spectra were recorded during and after sample deposition on a Beckman IR-12 spectrophotometer which was calibrated using vibration-rotation bands of standard molecules. Final accurate scans were run at 8 or $3.2 \text{ cm}^{-1}/\text{min}$. Frequency accuracy was $\pm 0.5 \text{ cm}^{-1}$; spectral slit widths were near 0.8 cm^{-1} in the $700\text{--}1300\text{-cm}^{-1}$ region, 1.5 cm^{-1} at 600 cm^{-1} , 2.1 cm^{-1} at 500 cm^{-1} , and 2.5 cm^{-1} at 300 cm^{-1} .

Results

Lithium atom-nitric oxide matrix reactions have been reinvestigated using higher lithium atom concentrations. Thirteen of these samples have been subjected to mercury arc photolysis followed by infrared examination in the $200\text{--}2000\text{-cm}^{-1}$ spectral region.

Lithium and Nitric Oxide. Fifteen experiments involved the reaction of lithium-6 or lithium-7 atoms with nitric oxide diluted with argon in mole ratios of matrix to reactant of 250/1 to 600/1. The lithium atom source at 450° provided a fivefold increase in lithium atom concentration over previous experiments¹ resulting in a lithium atom concentration comparable to nitric oxide. All experiments produced bands in the $1700\text{--}1900\text{-cm}^{-1}$ region due to NO and $(\text{NO})_2$ along with traces of H_2O and CO_2 impurities. In the most concentrated lithium-7 experiments ($\text{Ar}/\text{NO} = 250$) involving 24 hr of sample deposition, as many as thirteen reaction product bands were observed; these bands are listed in the first column of Table I. In the present most dilute experiments ($\text{Ar}/\text{NO} = 600$) only the eight most intense features appeared. The present work contrasts the earlier Andrews-Pimentel work using markedly lower lithium concentrations where the present six most intense bands were observed and the recent Milligan-Jacox work using intermediate lithium source temperatures and shorter (6 hr) deposition periods where only the 1352- and 651-cm^{-1} LiON bands plus a new 1359-cm^{-1} feature⁵ were produced. The bands of most interest, the 1352- and 651-cm^{-1} LiON features,¹ persist in the shortest, most dilute experiments.

Figure 1 shows typical spectra obtained from the reaction of several isotopic combinations of lithium with nitric oxide; Table I lists the lithium isotopic frequencies and isotopic shifts for these bands. Of particular interest are the LiON bands at 1352.5 and 651.4 cm^{-1} which show 0.5- and 40.9-cm^{-1} lithium-6 shifts in agreement with the earlier observations.¹ In the mixed lithium isotopic experiment, the higher frequency band broadened; unfortunately this feature could not be resolved into isotopic components, while the lower frequency band appeared as a doublet. The fourth spectrum in Figure 1 illustrates an experiment in which lithium-7 and cesium atoms were simultaneously treated with NO. Two points are noteworthy. First, only four bands were observed in this short 6-hr experiment, two at 1352 and 651 cm^{-1} corresponding to ν_1 and ν_2 of LiON and two at 1374 and 219 cm^{-1} which will be assigned to ν_1 and ν_2 of CsON in the following paper.⁹ In short experiments with low reactant concentrations,

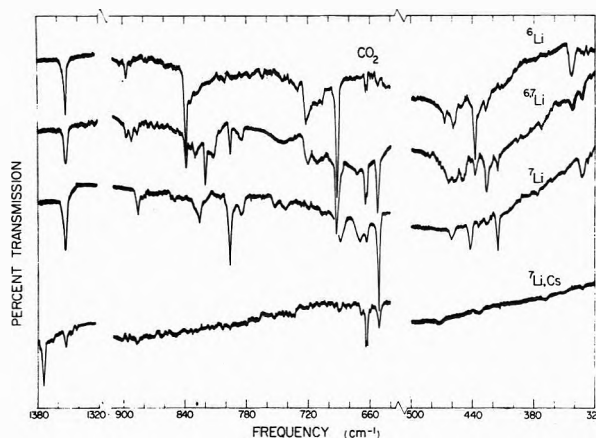


Figure 1. Infrared spectra of the products of matrix reactions of lithium-6, equimolar lithium-6 and -7, lithium 7, and mixed cesium and lithium-7 with natural isotopic nitric oxide using Ar/NO ratios of 400 and 500. Deposition temperature 15°K .

TABLE I: Lithium Isotopic Data (Frequencies, cm^{-1}) from Lithium-7 and Lithium-6 Nitric Oxide Matrix Reaction Products

Lithium-7	Lithium-6	Shift $6\mu\text{-}7\mu$	$6\text{Li}/7\text{Li}$ multiplet ^a	Identification
1352.5	1353.0	0.5	U	A
885.6	896.8	11.2	T	B
824 broad				
795.8	838.3	43.5	T	B
689	720	31	D	C
671	705	34	D	C
651.4	692.3	40.9	D	A
602 broad	614 broad	12	W	C
508	521	13	W	C
461	467	6	U	C
443	458	15	T	C
415.5	437.6	22.1	T	B
333	342	9	D	C

^a Multiplet observed in mixed isotopic experiment: U, unresolved; T, triplet; D, doublet; W, too weak to observe.

the 1352- and 651-cm^{-1} bands are the only features observed, as the last trace shows. Secondly, since there is a cesium shift for the ν_1 band, cesium provides a pseudo isotope for lithium; the absence of any band between 1352 and 1374 cm^{-1} indicates that these bands are due to a single alkali metal atom species, consistent with the conclusion from earlier concentration studies.¹

The two bands, called species B in the earlier Andrews-Pimentel study,¹ were produced in greater yield in the present experiments. A weaker feature at 885.6 cm^{-1} is associated by concentration dependence and sample warming behavior with the B bands at 795.8 and 415.5 cm^{-1} . These bands show 11.2- , 43.5- , and 22.1-cm^{-1} lithium-6 isotopic shifts. As Figure 1 indicates, these three bands become $1/2/1$ triplets in the equimolar $6\text{Li-}7\text{Li}$ experiment, which indicates the presence of two equivalent lithium atoms in this absorber.

Seven other bands which show lithium isotopic shifts are labeled C in Table I; their behavior in two mixed lithium isotopic experiments is also noted.

Lithium and ^{15}NO . A similar series of experiments was done with 99% ^{15}N -enriched nitric oxide using $\text{Ar}/^{15}\text{NO}$

(8) W. T. Hicks, *J. Chem. Phys.*, **38**, 1873 (1963).

(9) D. E. Tevault and L. Andrews, *J. Phys. Chem.*, **77**, 1646 (1973).

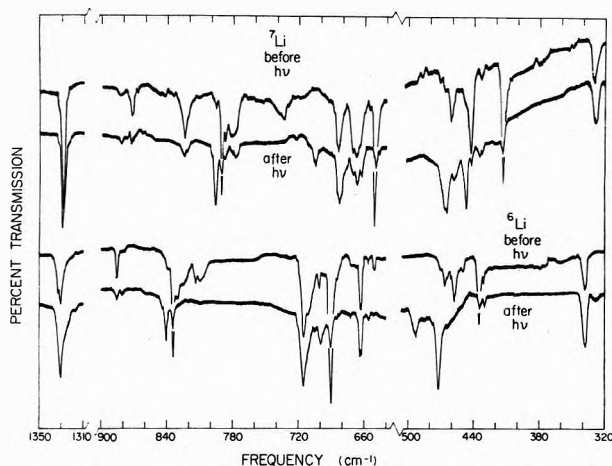


Figure 2. Infrared spectra of the 320–500-, 640–920-, and 1310–1350-cm⁻¹ regions for reactions of lithium-7 and lithium-6 with Ar/¹⁵NO = 350 samples. Spectra are traced before and after 80-min mercury arc photolysis.

TABLE II: Lithium Isotopic Frequencies (cm⁻¹) from Reactions of Lithium-7 and Lithium-6 with ¹⁵NO Showing Effects of Mercury Arc Photolysis and Sample Warming to 33°K and Recooling to 15°K

⁷ Li + ¹⁵ NO	Photolysis ^a	Temperature cycling ^b	⁶ Li + ¹⁵ NO	Photolysis
1329.1	inc	0.50	1330.5	inc
872.5	dec	0.3	885.3	dec
824	dec	0.5		
796.5	new inc	n	839.8	new inc
790.5	dec	0.28	833.8	dec
683	con	1.0	715	con
669	con	1.0	700	con
650.4	dec	0.47	691.6	dec
602	con	1.0	614	dec
588	new inc	n	621	new inc
466.0	new inc	n	492.2	new inc
460	dec	1.0	465	dec
447.2	new inc	n	472.0	new inc
442.2	dec	0.8	457.5	dec
413.2	dec	0.25	435.1	dec
329	con	1.0	338	inc

^a Photolysis behavior: inc, increased; dec, decreased; new inc, new band which appeared; con, constant. ^b Ratio optical density (after warming/before warming): n, band not observed without photolysis.

ratios ranging from 250 to 500. Figure 2 and Table II describe lithium isotope experiments with ¹⁵NO; the photolysis of these samples will be described in a following section. All of these bands (except the broad 824-cm⁻¹ ⁷Li feature) showed nitrogen-15 isotopic shifts. The two intense LiON bands appeared at 1329.1 and 650.7 cm⁻¹ resulting in N-15 shifts of 23.4 and 0.7 cm⁻¹, respectively. The B species bands were observed at 872.5, 790.5, and 413.2 cm⁻¹ representing 13.1-, 5.3-, and 2.3-cm⁻¹ N-15 shifts. Temperature cycling to 33°K for a ⁷Li-Ar/¹⁵NO = 500 sample is also given in Table II; reported is the ratio of optical densities (after warming/before warming) which is the fraction of the band remaining.

Finally, Figure 3 illustrates spectra for the lithium-7 reaction with equimolar ^{14,15}NO. The important features of this experiment are the three well-resolved doublets at 1352.5 and 1329.1 cm⁻¹, 885.6 and 872.5 cm⁻¹, and at 795.8 and 790.5 cm⁻¹. These features correspond to

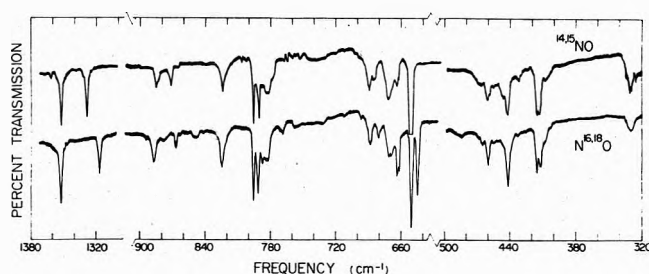


Figure 3. Infrared spectra of the principal regions for reactions of lithium-7 atoms with ^{14,15}NO (Ar/¹⁴NO/¹⁵NO = 600/1/1) and N^{16,18}O (Ar/N¹⁶O/N¹⁸O = 900/2/1).

TABLE III: Absorptions (cm⁻¹) Observed from Lithium-7 Matrix Reactions with Nitric Oxide Isotopic Mixtures ¹⁴NO/¹⁵NO = 1/1 and N¹⁶O/N¹⁸O = 2/1

¹⁴ NO- ¹⁵ NO	N ¹⁶ O-N ¹⁸ O	¹⁴ NO- ¹⁵ NO	N ¹⁶ O-N ¹⁸ O
1352.5, 1329.1	1352.3, 1317.2	650.9	651.8, 646.2
885.6, 872.5	885.6, 866.0	507.5	507.8
824 broad	824 broad	442.6	441.9
795.8, 790.8	795.8, 791.6	415.5, 413.3	415.2, 411.7
688 broad	689 broad	331	329
667 broad			

vibrational motions involving a single nitrogen atom, which implies the presence of one NO molecule. The bands at 650.9 and 414.4 cm⁻¹ are unresolved due to their N-15 shifts being smaller than the bandwidths. The 331-cm⁻¹ feature contained an unresolved shoulder at 333 cm⁻¹ and a component at 329 cm⁻¹; this feature could be a triplet band.

Lithium and N¹⁸O. The experiments done with oxygen-18 enriched nitric oxide involved mixtures with oxygen-18 enrichments between 35 and 65%. Figure 3 illustrates the codeposition of lithium-7 with 45% N¹⁸O; observed frequencies are listed in Table III. The five bands belonging to the two molecules of chief interest appeared as well-resolved doublets indicating that a one oxygen atom motion is responsible for these bands. Accordingly, these absorbers must contain a single NO molecule, the same conclusion reached from the mixed ^{14,15}NO experiments. The lithium nitroxide bands observed at 1317.2 and 646.2 cm⁻¹ resulted in 35.2- and 5.6-cm⁻¹ oxygen-18 shifts. The B species doublets appeared at 885.6 and 866.0 cm⁻¹, 795.8 and 791.5 cm⁻¹, and at 415.5 and 412.0 cm⁻¹. The remaining bands in Table III showed very small or no O-18 shift; a single broad feature appeared at 329 cm⁻¹.

Similar experiments were done with lithium-6 and N^{16,18}O. Again the five bands of primary interest appeared as doublets; the O-18 components were observed at 1319, 881, 834.0, 686.4, and 437.3 cm⁻¹. A weak broad band appeared at 338 cm⁻¹.

The sharp 1359-cm⁻¹ feature reported by Milligan and Jacox⁶ was observed in one experiment using ⁶Li and N^{16,18}O where the Knudsen cell was accidentally overheated due to a thermocouple short. This sample was deep red after 3 hr whereas 20 hr of sample deposition were normally required to produce the deep red color. The sharp band was observed at 1359.5 cm⁻¹ (1-cm⁻¹ half-width) and the other feature 1353 cm⁻¹ (3-cm⁻¹ half-width) with oxygen-18 counterparts at 1324.0 and 1318 cm⁻¹, respectively.

Photolysis. After sample deposition for 18–24 hr, final spectra were recorded at 8 cm⁻¹/min, and selected sam-

ples were subjected to mercury arc photolysis. Thirteen photolysis studies were performed; seven of these will be described in some detail. In general the effect of photolysis is a function of illumination time, sample transparency, and reagent concentrations; in these studies filters showed no effect.

Figure 2 contrasts the results of an 80-min *in situ* photolysis for each lithium isotope with ^{15}NO ; these relatively concentrated ($\text{Ar}/^{15}\text{NO} = 350$) samples were deposited for 22 hr. Note that the ν_1 and ν_2 bands of LiON show opposite photolysis behavior; the 1330-cm^{-1} bands remain or grow slightly while the $651\text{-}692\text{-cm}^{-1}$ bands are almost completely destroyed. These results are in agreement with the photolysis observations of Milligan and Jacox;⁶ however, a different interpretation of the photolysis behavior will follow. Also notice that the B species bands at $872\text{-}885$, $790\text{-}834$, and $413\text{-}435\text{ cm}^{-1}$, which were not observed by Milligan and Jacox, markedly decreased upon photolysis. Other features at 442 , 459 , and 465 cm^{-1} were destroyed while the 683 -, 715 -, and $328\text{-}338\text{-cm}^{-1}$ bands remained. These latter two bands were assigned to LiON by Andrews and Pimentel,¹ an assignment which must now be reconsidered. The most important observation of the present photolysis studies is the growth of intense new bands at 447 , 466 and 472 , and 492 cm^{-1} which follow the disappearance of the $651\text{-}692\text{-cm}^{-1}$ $^7\text{Li}\text{-}^6\text{Li}$ bands. Also in this study, bands appeared just above the intense B bands at 796 and 840 cm^{-1} and at 588 and 621 cm^{-1} which accompanied the loss of the original B absorptions. These latter features were observed on photolysis *only* when the B bands were destroyed.

A similar experiment was run with equimolar $^6\text{Li}\text{-}^7\text{Li}$ reacting with ^{15}NO . In this mixed isotopic experiment, photolysis produced only the same bands which were observed in the pure lithium isotopic reactions with the exception of a broad triplet band at 588 , 601 , and 621 cm^{-1} .

Photolysis of the sample producing the spectrum at the top in Figure 3 produced a 30% increase in the $1352\text{-}1329\text{-cm}^{-1}$ bands, a 40% decrease in the B bands, an 80% decrease in the 651-cm^{-1} band, while the 331-cm^{-1} band increased 50% and new bands appeared at 447 (0.10 OD) and 465 (0.16 OD, broad). A similar photolysis of a "dilute" sample ($\text{Ar}/\text{NO} = 600$, 415° lithium source), where the five A and B bands were observed in good yield but *all other* features were very weak, produced the 447- and 466-cm^{-1} features as weak new bands.

In lithium-6 and lithium-7 experiments with natural isotopic NO , sample photolysis produced the 447- , 466- and 472- , and 492-cm^{-1} bands as measured in the ^{15}NO experiments. The nitrogen isotopic shift for the new bands was immeasurably small. In all cases the lower frequency 447- and 472-cm^{-1} bands were sharper than the upper 466- and 492-cm^{-1} bands. In an experiment using ^7Li with 50% O-18 enriched NO , the new bands appeared $1\text{-}2\text{ cm}^{-1}$ lower following photolysis, indicating oxygen-18 isotopic shifts of about $2\text{-}3\text{ cm}^{-1}$ for these features.

A particularly informative experiment was performed with lithium-6 and 65% N^{18}O . This sample was photolyzed for 20 min using a CoSO_4 solution filter. Only four changes were noted in the spectrum: the ν_1 bands of LiON at 1353 and 1313 cm^{-1} were doubled, the ν_2 bands at 692 and 685 cm^{-1} were almost completely destroyed, and the broad 338-cm^{-1} feature doubled, while one intense new band appeared at 470 cm^{-1} . All other spectral features remained unchanged following this initial 20-min photoly-

sis period. Further photolysis for 90 min using only a water filter diminished all bands, including the ν_1 bands and the 470-cm^{-1} feature; and a new band appeared near 490 cm^{-1} . These data again provide oxygen-18 isotopic shifts of about 3 cm^{-1} for the new photolysis bands.

The photolysis studies of $\text{Li}\text{-NO}$ matrix samples are characterized by the appearance of lithium isotopic bands in the 450-cm^{-1} region which follow the disappearance of similar lithium isotopic bands in the 650-cm^{-1} region while the 1352-cm^{-1} band intensity increases. The integrated intensity of the 1352-cm^{-1} band remains proportional to the weighted sum of the integrated intensities of the lithium isotopic bands near 450 and 650 cm^{-1} before and after photolysis.

Discussion

The structure, bonding, photoisomerization, and potential constants of lithium nitroxide will be discussed in light of new results. The two lithium absorber $\text{Li}(\text{ON})\text{Li}$ will be compared to the lithium peroxide molecule LiO_2Li .

LiON. In the original work, Andrews and Pimentel¹ associated three bands at 1352 , 651 , and 333 cm^{-1} with LiON using concentration studies. Present and past isotopic^{1,6} studies leave little doubt that the 1352-cm^{-1} band is a relatively pure N-O stretching vibration of a single NO species. The present Cs-Li mixed experiment indicates that a single alkali atom is associated with the 1352-cm^{-1} absorption. Isotopic data confirm that the 651-cm^{-1} band is due to the motions of single lithium and single oxygen atoms. However, the low-frequency 333-cm^{-1} band is not sharp like the 1352- and 651-cm^{-1} features, and in mixed isotopic experiments counterparts of the 333-cm^{-1} feature cannot be resolved. This finding suggests that the 333-cm^{-1} band is not due to LiON but to some higher aggregate like $\text{Li}(\text{ON})_2$, a point which is strengthened by photolysis studies.

Recent low-energy electron impact studies¹⁰ have provided a measurement of the NO^- fundamental at 1355 cm^{-1} . Milligan and Jacox conclude that the 1352-cm^{-1} band in lithium-nitric oxide reactions is due to NO^- . In a literature search for the NO^- fundamental in 1965, Andrews and Pimentel¹ were forced to rely on nitrosyl complex ions in the 1100-cm^{-1} range, a comparison which is obsolete in view of the electron impact data. We agree with Milligan and Jacox⁶ that the 1352-cm^{-1} band is the intraionic mode of a NO^- anion, but at the same time, we disagree on the origin of the 651-cm^{-1} band.

The present work shows that the 651-cm^{-1} band is the interionic $\text{Li}^+\text{-ON}^-$ mode of the same species giving rise to the 1352-cm^{-1} intraionic mode. We have shown that a single alkali atom is associated with the 1352-cm^{-1} mode. The species Li^+ON^- must exist; if NO^- is produced, Li^+ is also produced and the Li^+ must remain coulombically bound to NO^- . The association of Li^+ and NO^- is required on energetic grounds; NO has a small electron affinity and the coulombic association of Li^+ cation and NO^- anion is required to compensate for ionization of the lithium atom. Even mercury arc photolysis cannot effect the separation of Li^+ and NO^- since the 2500-\AA cutoff (115 kcal/mol) is less energetic than the coulomb poten-

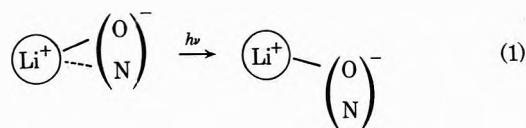
(10) D. Spence and G. J. Schulz, *Phys. Rev. A*, **3**, 1968 (1971).

tial (150 kcal/mol, 90% of e^2/r at 2.0-Å separation). Now, the Li^+ON^- ion pair should have a very intense interionic vibrational mode; this mode has been observed³ at 699 cm^{-1} for Li^+O_2^- . The intense 651- cm^{-1} band in the present spectra shows lithium and oxygen isotopic data consistent with the Li^+ON^- interionic mode. The lack of nitrogen isotopic shifts indicate stronger bonding of lithium to oxygen as discussed previously for a bent LiON structure.¹ However, we presently believe that, like Li^+O_2^- , Li^+ON^- possesses a triangular structure, which in the latter case must be scalene with the lithium more strongly bound to the oxygen end of NO^- .

We confirm the Milligan and Jacox photolysis observation that ν_1 of $\text{Li}^+(\text{ON})^-$ slightly increases while ν_2 decreases markedly. This behavior is usually interpreted to associate two such modes with two different molecular species, the conclusion reached by Milligan and Jacox.⁶ However, ionic species are not the usual molecule; an interionic rearrangement may change the cation-anion structure without affecting the electronic environment and fundamental frequency of the anion. Essential to this proposal is the observation of new bands in the 440-500- cm^{-1} spectral region which were produced by the radiation which destroyed the 651- cm^{-1} interionic mode. Apparently, Milligan and Jacox did not investigate this spectral region after photolysis.

The sharper of the new bands which appeared at 447 cm^{-1} after photolysis of lithium-7 samples shifted to 472 cm^{-1} with lithium-6. This 25- cm^{-1} lithium isotope shift is in accord with a lithium stretching mode; the per cent shift is nearly the same observed for the ν_2 band of LiON . The 447-472- cm^{-1} bands showed approximately 3- cm^{-1} O-18 shifts, again nearly the same per cent shift as the destroyed ν_2 bands, and less than 0.5- cm^{-1} N-15 shifts, also in agreement with the ν_2 bands. We conclude that the 447-472- cm^{-1} ^7Li - ^6Li bands are due to the interionic mode of a different $\text{Li}^+(\text{ON})^-$ structural isomer; their broader counterparts at 466-492 cm^{-1} may be due to a different matrix site or a still different cation-anion arrangement. The position of the NO^- mode was not altered by the photoisomerization although the intensity was slightly increased.

The photoisomerism may be explained by the following reaction



It must be pointed out that these proposed structures are not precisely known, but the above reaction represents a plausible photoisomerism mechanism. The photolysis product could also be another triangular arrangement different from the first one. Interpretation of the photolysis observations requires a change in cation-anion structure and normal mode without affecting the electronic environment and vibrational mode of the anion within the observed bandwidth of 3 cm^{-1} .

The assignment of two bands, an intraionic mode (1352 cm^{-1}) and an interionic mode (651 cm^{-1}) to Li^+ON^- , is supported by the heavy alkali metal-nitric oxide results where only two bands were observed. In the following paper, the species Na^+NO^- , K^+NO^- , Rb^+NO^- , and Cs^+NO^- are reported, each of which exhibited a NO^- mode between 1359 and 1374 cm^{-1} and a M^+NO^- mode

between 366 and 218 cm^{-1} . Mercury arc photolysis of these samples produced no spectral changes. Apparently only the smaller lithium cation can relocate itself about NO^- in an argon matrix site during photolysis.

The 333- cm^{-1} band was associated with the 1352- and 651- cm^{-1} bands in the concentration studies of Andrews and Pimentel.¹ While the present experiments show that the band in question is a single lithium feature, sample warming separates 333 cm^{-1} from 651 and 1352 cm^{-1} . In photolysis studies, the 333 cm^{-1} remains and sometimes increases. We believe that the 333- cm^{-1} feature is most likely due to the species $\text{Li}(\text{NO})_2$. The missing low-frequency mode of Li^+ON^- probably falls in the 300-500- cm^{-1} frequency range; the two weak bands observed in this region could not be associated with Li^+ON^- . Perhaps the Li-N vibration is appreciably weaker than the Li-O mode, a contention supported by the failure to observe Li-N modes for the species Li^+N_2^- whose intraionic (N-N) $^-$ mode was observed¹¹ near 1800 cm^{-1} .

Table I lists seven bands identified with the label C. These bands are broader than the sharp A and B bands which supports the view that the C bands are due to higher aggregate species. Sample warming operations confirm this view. Infrared absorptions in the 1700-1900- cm^{-1} range attest the presence of $(\text{NO})_2$ in these samples; it is expected that reactions of Li with $(\text{NO})_2$ should produce observable bands, particularly in the lithium stretching region. The bands at 671 and 689 cm^{-1} could be lithium stretching modes of $\text{Li}(\text{NO})_2\text{Li}$ species; however, no bands were observed which could be assigned to the hyponitrite ion,¹² $\text{N}_2\text{O}_2^{2-}$. The present information indicates that the broader bands identified by C in Table I are due to higher aggregate species, which are not of primary interest here.

Milligan and Jaccx⁶ have suggested that the 1359- cm^{-1} band is due to the NO^- mode of a species Li_2^+NO^- . The present lithium reaction data support this assignment since the 1359- cm^{-1} feature was observed only in the experiment with excess lithium. We suggest that Li_2^+NO^- is produced by dimerization of lithium atoms upon matrix formation.¹³ The polarizable ion pair model⁹ for the M^+NO^- species supports the assignment of a higher frequency band to NO^- in Li_2^+NO^- (1359 cm^{-1}) than in Li^+NO^- (1352 cm^{-1}) with the assumption that the polarizability of Li_2^+ is greater than the polarizability of Li^+ . This follows from the fact that the ionization potential of Li_2 is 0.25 eV less than the ionization potential of Li .¹⁴

Normal coordinate calculations were done for LiON using the scalene triangular geometry with the estimated bond distances N-O = 1.29 Å, Li-O = 1.67 Å, and Li-N = 1.96 Å; these bond lengths define the Li-O-N angle to be 78°. The ν_1 and ν_2 data for six isotopic molecules were used along with an estimate of 333 cm^{-1} for the missing third mode. The NO force constant, 7.79 ± 0.05 mdyn/Å, which should not be affected by the use of an estimated low-frequency mode, compares favorably with 7.97 mdyn/Å reported for the bent LiON geometry.¹ The LiO force constant, 0.98 ± 0.03 mdyn/Å, is lower than the value for LiO_2 , 1.18 ± 0.02 mdyn/Å.³ The LiN force constant of 0.57 mdyn/Å is not of interest since it was based on an

(11) R. C. Spiker, Jr., L. Andrews, and C. Trindle, *J. Amer. Chem. Soc.*, **94**, 2401 (1972).

(12) R. J. W. LeFevre, W. T. Oh, I. H. Reese, and R. L. Werner, *Aust. J. Chem.*, **10**, 361 (1957).

(13) L. Andrews and G. C. Pimentel, *J. Chem. Phys.*, **47**, 2905 (1967).

(14) R. D. Hudson, *J. Chem. Phys.*, **43**, 1790 (1965).

estimated frequency; the three small interaction force constants made minimal contribution to the potential energy distribution. The triangular model for LiON produced an excellent fit ($\Delta\nu = 0.3 \text{ cm}^{-1}$) to the observed frequencies, showing that the vibrational analysis is consistent with a triangular structure. The obvious analogy with triangular Li^+O_2^- and the molecular orbital calculations^{4,5} support the triangular model proposed for $\text{Li}^+(\text{ON})^-$.

The interionic mode can be approximated as a diatomic like motion, that is Li-ON, considering the NO molecule as a single mass unit. This approximate diatomic analysis gives a Li-ON force constant of $1.412 \pm 0.009 \text{ m dyn/\AA}$ for six isotopic frequencies. This average force constant reproduces the six observed frequencies with $\pm 1.3 \text{ cm}^{-1}$. A similar analysis for LiO_2 as Li-O₂, produced an average of Li-O₂ force constant of $1.652 \pm 0.004 \text{ m dyn/\AA}$ which reproduced four frequencies within $\pm 0.7 \text{ cm}^{-1}$.

Li(ON)Li. In the earlier study, Andrews and Pimentel¹ identified bands at 796 and 415 cm^{-1} , which showed 43- and 22- cm^{-1} Li-6 shifts and 6- and 3- cm^{-1} N-15 shifts, as species B. The present work confirmed these observations and found 4- cm^{-1} O-18 shifts for the B bands. A new weaker feature was observed at 886 cm^{-1} in the present experiments using higher lithium concentrations; this feature showed a 13- cm^{-1} N-15 shift, a 20- cm^{-1} O-18 shift, an 11- cm^{-1} Li-6 shift, and parallel growth, diffusion, and photolysis behavior with the 796- and 415- cm^{-1} bands.

The B bands are the most sensitive to decrease upon sample warming; the B bands diminish more than the A bands, as Table II shows. This behavior is analogous to diffusion experiments with LiO_2Li and LiO_2 .³

Prolonged photolysis, as illustrated in Figure 2, markedly decreased the B bands; however, concomitant with the loss of the B bands was the growth of new absorptions 6 cm^{-1} above the intense 796-840- cm^{-1} bands and near 600 cm^{-1} which are appropriate for modes of the photoisomerized B species. These new bands were observed *only* when the B bands were almost completely destroyed, as is shown in Figure 2.

Mixed lithium isotopic experiments produced triplets while mixed ^{14,15}NO and ^{N16,18}O experiments gave doublets for the 886-, 796-, and 415- cm^{-1} bands indicating that these modes involve two equivalent Li atoms and single N and O atoms. The 796- and 415- cm^{-1} frequencies map closely with the frequencies, and lithium and single O-18 isotopic shifts of bands at 796 and 445 cm^{-1} assigned to the LiO_2Li species, which was suggested to have a rhombus structure.³ We postulate that Li(ON)Li is a planar species of C_{2v} symmetry, a slightly distorted rhombus. This species has three A_1 modes and two B_1 modes in the molecular plane, and one B_2 mode, the out-of-plane bend. Two of the A_1 modes are totally symmetric stretching motions; the N-O stretch, $\nu_1(A_1)$ and the Li-NO-Li stretch, $\nu_2(A_1)$. The A_1 mode, ν_3 correlates with the B_{3u} mode in the D_{2h} point group. The B_1 modes, ν_4 and ν_5 , correlate with the B_{2u} and B_{1g} modes, and the B_2 mode, ν_6 originates from the B_{1u} mode in D_{2h} symmetry. Here we follow the symmetry designation of Berkowitz¹⁵ for the normal vibrations of $(\text{MX})_2$.

The 796- cm^{-1} band is assigned to the antisymmetric mode of lithium cations perpendicular to the N-O bond, $\nu_4(B_1)$, and the 415- cm^{-1} absorption the motion of lithi-

um cations parallel to the N-O bond, $\nu_3(A_1)$. These motions are analogous to $\nu_5(B_{2u})$ and $\nu_6(B_{3u})$ of the LiO_2Li species.³

The remaining band observed for Li(ON)Li at 886 cm^{-1} is assigned to $\nu_1(A_1)$. Isotopic shifts for the 886- cm^{-1} band identify it as primarily an N-O stretching mode (calculated N-15 shift 15 cm^{-1} , observed 13- cm^{-1} ; calculated O-18 shift 23 cm^{-1} , observed 20 cm^{-1}). The 11- cm^{-1} lithium-6 shift is probably due to slight mixing with the unobserved lithium stretching mode $\nu_2(A_1)$, which is expected to be near 800 cm^{-1} and very weak in the infrared.

No force constant calculations were attempted for Li(ON)Li since only two of three A_1 modes and one of two B_1 modes were observed.

The frequency reported here for NO^{2-} , 890 cm^{-1} , is reasonable by comparison with similar molecules. The first electron added to NO (1886- cm^{-1} fundamental) is antibonding which reduces the frequency 534 cm^{-1} . This reduction predicts 818 cm^{-1} for NO^{2-} , some 70 cm^{-1} below the observed 890 cm^{-1} . O_2^- (1097- cm^{-1} fundamental)³ is isoelectronic with NO^{2-} , but extra electronic repulsion not counterbalanced by correspondingly increased nuclear attraction leads to weaker binding for a double negative anion such as NO^{2-} . Hence, the NO^{2-} fundamental should fall below O_2^- . The isoelectronic pair O_2 (1552- cm^{-1} fundamental) and NO^- (1352 cm^{-1}) illustrate this point, and suggest that perhaps NO^{2-} should fall 200 cm^{-1} below O_2^- , in good agreement with the NO^{2-} fundamental of 890 cm^{-1} .

These data suggest that the $\text{Li}^+\text{ON}^{2-}\text{Li}^+$ species is a secondary reaction product formed by reaction of a second lithium atom with the triangular Li^+ON^- species. The same reaction sequence has been postulated to form $\text{Li}^+\text{O}_2^{2-}\text{Li}^+$ from reaction of another lithium with isoelectronic triangular Li^+O_2^- . It is reasonable to expect that the two similar diatomic molecules, NO and O_2 , should have similar lithium atom matrix reaction products.

Conclusions

The lithium-nitric oxide matrix reaction has been reinvestigated using approximately equimolar concentrations of the two reagents. Intense bands at 1352 and 651 cm^{-1} were assigned to intraionic (N-O)⁻ and interionic $\text{Li}^+(\text{NO})^-$ vibrational modes of a triangular $\text{Li}^+(\text{ON})^-$ species. Mercury arc photolysis destroyed the 651- cm^{-1} band while the 1352- cm^{-1} band increased and a new 447- cm^{-1} absorption appeared. These data suggest that the triangular $\text{Li}^+(\text{ON})^-$ species photoisomerized to a bent form where the (NO)⁻ frequency is unchanged but the interionic Li-O frequency is shifted to 447 cm^{-1} .

Absorptions at 886, 796, and 415 cm^{-1} were assigned to the $\text{Li}^+(\text{ON})^{2-}\text{Li}^+$ species, a secondary reaction product. The lower two frequencies are interionic modes; the 886- cm^{-1} band is predominantly an intraionic (N-O)²⁻ motion. This frequency for NO^{2-} is reasonable by comparison with similar molecules.

Acknowledgment. The authors gratefully acknowledge financial support for this research by the National Science Foundation under Grant No. GP-28582.

(15) J. Berkowitz, *J. Chem. Phys.*, **29**, 1386 (1958).

Matrix Reactions of Sodium, Potassium, Rubidium, and Cesium Atoms with Nitric Oxide. Infrared Spectra of the $M^+(NO)^-$ Species

David E. Tevault and Lester Andrews*

Chemistry Department, University of Virginia, Charlottesville, Virginia 22903 (Received February 9, 1973)

The 15°K condensation of beams of Na, K, Rb, and Cs atoms with NO at high dilution in argon produced two intense product bands for each metal reaction product. Absorptions in the 1358–1374-cm⁻¹ region were assigned to the intraionic (N-O)⁻ mode and bands in the 361–219-cm⁻¹ region were assigned to interionic M⁺-(NO)⁻ vibration. The small M⁺ effect on the (N-O)⁻ mode is explained by the ionic model of polarizable ion pairs. The large ¹⁵N shift for ν_2 of the heavy metal species suggests a bent or linear M⁺NO⁻ arrangement in contrast to the acute triangular Li⁺(ON)⁻ structure.

Introduction

The previous paper¹ describes a reinvestigation of the lithium-nitric oxide matrix reaction and of the structure, photochemistry, and bonding in the principal product species LiON and Li(ON)Li. The position of the N-O frequency of the Li⁺(ON)⁻ species in the NO⁻ spectral region invites consideration of the other M⁺(ON)⁻ species and the resulting M⁺ effect on the NO⁻ frequency.

An interesting trend has been observed for O₂⁻ frequencies in the M⁺O₂⁻ species;² the O₂⁻ fundamental increases over a 20-cm⁻¹ range with increasing M⁺ size.³ This trend has been explained in terms of an ionic model³ of polarizable ion pairs, M⁺O₂⁻. The ionic model for sodium nitroxide has received support from recent *ab initio* molecular orbital calculations.⁴ In order to test the ionic model hypothesis, it was desired to obtain the NO⁻ frequencies for all the M⁺(ON)⁻ species.

Milligan and Jacox⁵ recently reported Na and Cs atom matrix reactions with NO; these workers assigned frequencies of 1359 and 1374 cm⁻¹ to the Na⁺(ON)⁻ and Cs⁺(ON)⁻ species. However, the region between 200 and 400 cm⁻¹, which also contains important spectral features due to these species, was not examined. We report here a complete study of matrix reactions of Na, K, Rb, and Cs atoms with isotopic nitric oxide species with infrared spectroscopic examination in the 200–2000-cm⁻¹ spectral region before and after mercury arc photolysis.

Experimental Section

The instrumentation and experimental techniques have been described in previous publications from this laboratory.^{1,6} Nitric oxide and isotopically enriched nitric oxides were handled as described in the previous paper;¹ matrix samples of NO and ¹⁵NO at Ar/NO = 500 were used whereas mixed N^{16,18}O samples were made to a total Ar/NO = 300/1 ratio. Elemental sodium and potassium were cut and loaded into Knudsen cells in an argon atmosphere. Rubidium and cesium atom beams were produced from the reaction of RbCl and CsCl with melted lithium in the Knudsen cell. Typical Knudsen cell operating temperatures were 225° for Na, 165° for K, 300° for RbCl-Li, and 320° for CsCl-Li. These temperatures produce approximately 1- μ vapor pressures⁷ for Na and K and for Rb and Cs as well.

Results

In all of these experiments, NO and (NO)₂ bands were observed in the 1700–1900-cm⁻¹ region along with traces of water and carbon dioxide. When sodium atoms were codeposited with nitric oxide-argon samples, Ar/NO = 500/1, two prominent new features were observed, as Figure 1 and Table I indicate. The sharp intense band at 1358.0 cm⁻¹ is in good agreement with the 1358.6-cm⁻¹ band of Milligan and Jacox; the broad absorption at 361 cm⁻¹ was not reported by these workers.⁵ In isotopic substitution experiments the sharp band shifted to 1335.7 cm⁻¹ for ¹⁵NO and 1323 cm⁻¹ for N¹⁸O; these features agree with the data of Milligan and Jacox.⁵ The lower frequency band shifted to 357 cm⁻¹ with ¹⁵NO and 358 cm⁻¹ with N¹⁶O/N¹⁸O = 2/1 precursors, although accurate frequency measurement of this broader feature is more difficult.

The reaction of potassium atoms with nitric oxide likewise yielded only two bands; intense features at 1372.0 and 280.4 cm⁻¹ are shown in Figure 1. Andrews⁶ has demonstrated that simultaneous deposition of two different alkali metals provides a reasonable mixed "pseudo" isotopic experiment for the heavy alkali atoms. Accordingly the mixed Na-K reaction with NO depicted at the top of Figure 2 was studied. Note that four bands appeared: the two observed in separate Na reactions and the two produced in K experiments. The observation of two doublets in this mixed metal experiment indicates that these absorbers contain single alkali metal atoms. Similar conclusions were reached from mixed Li-Cs and ⁶Li-⁷Li experiments in the previous paper.¹

Figure 2 also contrasts the reactions of K atoms with natural isotopic NO, ¹⁵NO, and N¹⁶O/N¹⁸O = 1/1 samples. The sharp intense feature was shifted 23.6 cm⁻¹ to 1348.4 cm⁻¹ with ¹⁵NO and 35.2 cm⁻¹ to 1336.8 cm⁻¹ with N¹⁸O. The lower frequency band shifted 2.6 cm⁻¹ to 277.8 cm⁻¹ upon ¹⁵N substitution and 1.6 cm⁻¹ to 278.8 cm⁻¹ using equimolar N¹⁶O-N¹⁸O. Hence, a 3-cm⁻¹ ¹⁸O

(1) D. E. Tevault and L. Andrews, *J. Phys. Chem.*, **77**, 1640 (1973).

(2) L. Andrews, *J. Chem. Phys.*, **50**, 4288 (1969).

(3) L. Andrews and R. R. Smardzewski, *J. Chem. Phys.*, **58**, 2258 (1973).

(4) J. Peslak, Jr., D. S. Klett, and C. W. David, *J. Chem. Phys.*, **55**, 1993 (1971).

(5) D. E. Milligan and M. E. Jacox, *J. Chem. Phys.*, **55**, 3404 (1971).

(6) L. Andrews, *J. Chem. Phys.*, **54**, 4935 (1971).

(7) W. T. Hicks, *J. Chem. Phys.*, **38**, 1873 (1963).

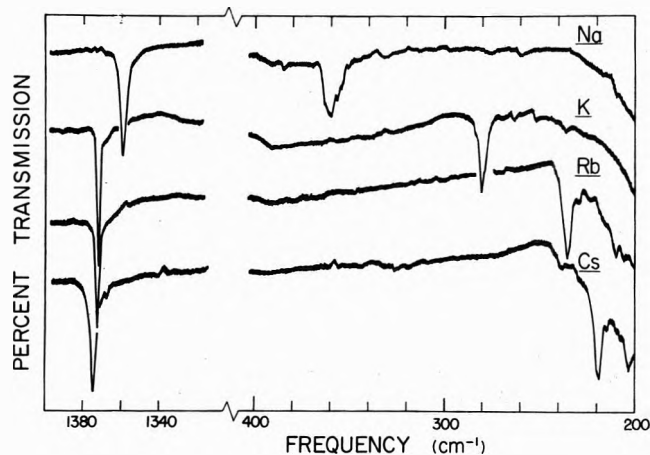


Figure 1. Infrared spectra in the 200–400- and 1320–1400- cm^{-1} regions for matrix reactions of Na, K, Rb, and Cs atoms with nitric oxide diluted in argon, $\text{Ar}/\text{NO} = 500$. Sample deposition temperature 15°K .

TABLE I: Absorptions (cm^{-1}) Observed Following Matrix Reactions of Heavy Alkali Metal Atoms with Isotopic Nitric Oxide Diluted in Argon

Isotopic sample	Na	K	Rb	Cs
NO	1358.0	1372.0	1373.0	1374.0
	361	280.4	235.0	219.0
^{15}NO	1335.7	1348.4	1349.6	1350.1
	357	277.8	231.1	214.8
N^{18}O^a	1323.8	1336.8	1338.0	1338.8
	358	278.8	234.5	218.0

^a Samples mixed $\text{N}^{16}\text{O}/\text{N}^{18}\text{O}$; ratios were 2/1 for Na, 1/1 for K, 3/1 for Rb, and 2/3 for Cs.

shift is deduced for the lower frequency K feature from the N^{16}O – N^{18}O isotopic mixture. The mixed oxygen isotopic spectrum in Figure 2 shows a well-resolved doublet in the 1300-cm^{-1} region indicating a single oxygen atom motion and implying the incorporation of a single nitric oxide molecule in this new molecular species. The lower frequency band could not be resolved owing to the large bandwidth relative to the small isotopic shift. Isotopic frequency data are listed in Table I.

Figure 1 illustrates the matrix reaction of rubidium atoms with nitric oxide using $\text{Ar}/\text{NO} = 500$. Again, only two new features were observed, a sharp intense band at 1373.0 cm^{-1} and an intense feature at 235.0 cm^{-1} . In an experiment using ^{15}NO , these features shifted to 1349.6 and 231.1 cm^{-1} ; in an equimolar ^{14}NO – ^{15}NO experiment the 1373 - and 1350-cm^{-1} features formed a well-resolved doublet, but the lower broad 233-cm^{-1} band was not resolved. The doublet indicates the presence of a single nitrogen atom in the species responsible for the higher frequency band, which implies the presence of one NO molecule in the new product species, the same conclusion reached from mixed oxygen isotopic experiments. In an experiment using mixed $\text{N}^{16}\text{O}/\text{N}^{18}\text{O} = 3/1$, the upper bands were observed at 1373.0 and 1338.0 cm^{-1} and the lower band at 234.5 cm^{-1} .

The cesium atom reaction with NO produced only two bands, an intense feature at 1374.0 cm^{-1} in agreement with the Milligan–Jacox observation⁵ and an intense band at 219.0 cm^{-1} . The isotopic experiments on the cesium species produced bands at 1350.1 and 214.8 cm^{-1} using

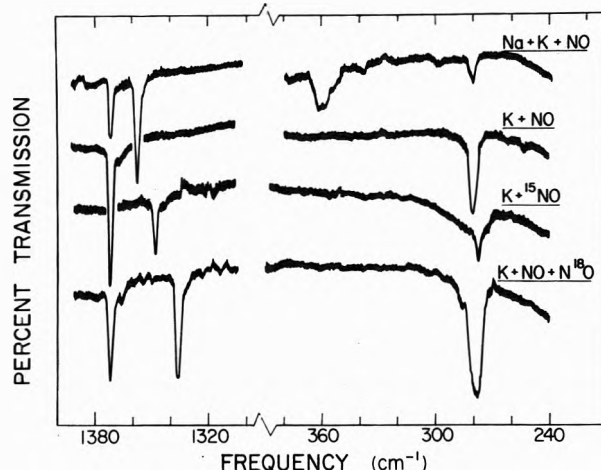


Figure 2. Infrared spectra in the 220–380- and 1300–1400- cm^{-1} spectral regions for matrix reactions of alkali metal atoms with nitric oxide at high dilution in argon: top spectrum, equimolar Na/K, $\text{Ar}/\text{NO} = 400$; second spectrum, K, with $\text{Ar}/\text{NO} = 500$; third spectrum, K with $\text{Ar}/^{15}\text{NO} = 500$; bottom spectrum, K with $\text{Ar}/\text{N}^{16}\text{O}/\text{N}^{18}\text{O} = 600/1/1$.

TABLE II: Frequencies (cm^{-1}) Assigned to ν_1 Intraionic and ν_2 Interionic Modes of $M^+(\text{ON})^-$ Species^a

Metal	ν_1	ν_2	ν_2 of $M^+\text{O}_2^-$ ^b
^6Li	1353.5	692.3	743.8
^7Li	1352.5	651.8	698.8
Na	1358.0	361	390.7
K	1372.0	280.4	307.5
Rb	1373.0	235.0	255.0
Cs	1374.0	219.0	236.5

^a ν_2 of the $M^+\text{O}_2^-$ species are listed for comparison. ^b L. Andrews, et al., *J. Phys. Chem.*, **77**, 1065 (1973), see also ref 2 and 6.

^{15}NO and 1338.8 and 218.0 cm^{-1} using 60% oxygen-18 enriched NO. These frequency data are listed in Table II.

Most of the above heavy alkali metal–nitric oxide matrix samples were subjected to high-pressure mercury arc photolysis. In contrast to the previous^{1,5} photolysis behavior of $\text{Li}^+(\text{ON})^-$, the two absorptions discussed above for each metal reaction sustained no discernible intensity or frequency changes upon photolysis. Milligan and Jacox reported⁵ that the higher frequency bands in Na and Cs experiments showed no changes with photolysis.

Discussion

In the previous paper, evidence was presented associating two absorptions with intraionic and interionic vibrational modes of the $\text{Li}^+(\text{ON})^-$ molecular species. The frequencies presented above are appropriate for the analogous heavy alkali metal species.

The mixed Na–K experiment illustrated at the top of Figure 2 shows doublets at 1358 – 1372 and 361 – 280 cm^{-1} without intermediate components; this observation indicates that the molecular species absorbing in these two spectral regions contains a single alkali metal atom. Mixed $^{14,15}\text{NO}$ and $\text{N}^{16,18}\text{O}$ experiments indicate that the upper absorption arises from a single NO species; the lower frequency bands could not be resolved owing to the much smaller isotopic shifts. The above data indicate a molecular formula MON for the new species.

TABLE III: Nitrogen and Oxygen Isotopic Shifts (cm⁻¹) for the ν_2 Interionic Modes of the M⁺(ON)⁻ Species^a

Alkali metal	$\Delta\nu_2^{15\text{N}}$	$\Delta\nu_2^{18\text{O}}$	$\Delta\nu_2^{18\text{O}}$ for M ⁺ ¹⁶ O ¹⁸ O
⁶ Li	0.8	6.3	3.0
⁷ Li	0.8	5.8	3.1
Na	(4) ^b	(6) ^b	4.0
K	2.6	3 ^c	5
Rb	3.9	2 ^c	6.5
Cs	4.2	2 ^c	6.8

^a Single oxygen-18 isotopic shifts of M⁺O₂⁻ are listed for comparison. ^b Data less accurately known due to difficulty in accurately measuring broader bands. ^c Deduced from mixed N¹⁶O-N¹⁸O experiments.

The bands in the 1300-wave number region show isotopic shifts appropriate for a fundamental N-O vibration. For the potassium case illustrated in Figure 2, the observed ¹⁵N shift was 23.6 cm⁻¹ while the diatomic harmonic oscillator calculation predicts 24.5 cm⁻¹; the observed ¹⁸O shift was 35.2 cm⁻¹ and the diatomic shift is 36.1 cm⁻¹. These small 0.9-cm⁻¹ discrepancies could be due to anharmonicity or to a very small amount of alkali metal participation in the vibrational mode. As pointed out by Milligan and Jacox,⁵ the proximity of these bands to the 1355-cm⁻¹ NO⁻ fundamental deduced from low-energy electron impact studies⁸ indicates that these molecular species contain the NO⁻ moiety. The present data show that this NO⁻ anion is coulombically bound to an alkali cation forming a M⁺(ON)⁻ species. The small alkali metal shift confirms this point. The upper frequency bands are assigned to ν_1 the intraionic (N-O)⁻ mode in the M⁺(ON)⁻ species.

The lower frequency band is clearly appropriate for an interionic mode M⁺ ↔ (ON)⁻. Note the large alkali metal shift which closely follows the analogous M⁺ ↔ O₂⁻ mode, as is compared in Table II for ν_2 frequencies, and the small ¹⁵N and ¹⁸O shifts which are listed in Table III for the ν_2 M⁺(ON)⁻ modes.

Any force constant calculations for the M⁺NO⁻ molecules must involve approximations since only two of the three normal modes were observed. Although the M⁺NO⁻ diatomic approximation using NO as a single mass worked well for Li⁺ON⁻,¹ this approach is not successful for the heavier M⁺NO⁻ species. This is expected from comparison of the data of Table III. In the Cs⁺NO⁻ case, ν_2 is predicted at 216 cm⁻¹ for 133-15-16 isotopes and 213 cm⁻¹ for 133-14-18. This represents too much O-18 shift and insufficient N-15 shift. If ν_2 were a Cs-O mode, the simple diatomic approximation predicts an 11-cm⁻¹ O-18 shift; 2 cm⁻¹ was observed. Likewise, if ν_2 were a simple Cs-N mode, a 8-cm⁻¹ shift is predicted whereas 4 cm⁻¹ was observed. Clearly ν_2 is a mode involving both N and O, but the increased N-15 shift and decreased O-18 shift indicates a greater participation of N in ν_2 of Cs⁺NO⁻ relative to ν_2 of Li⁺ON⁻.

Interpretation of the above infrared observations as arising from an M⁺(ON)⁻ species raises two interesting points: the 22-cm⁻¹ dependence of the NO⁻ frequency upon M⁺ and the structure of the M⁺(ON)⁻ species. Now, the alkali metal influence on the NO⁻ frequency must be put into proper perspective. Upon going from NO to the NO⁻ anion, an antibonding electron is added which reduces the fundamental frequency more than 500 cm⁻¹;

TABLE IV: Ionic Model Dipole Moment Calculations for the M⁺NO⁻ Molecules

Molecule	$r, \text{\AA}$	e_r	$(\alpha_c + \alpha_a)e / r^2$ ^b	μ, calcd	$\mu, \text{calcd} / e_r$
Li ⁺ NO ⁻	1.83	8.79	3.50	5.29	0.601
Na ⁺ NO ⁻	2.19	10.51	2.19	8.32	0.791
K ⁺ NO ⁻	2.47	11.86	2.56	9.32	0.786
Rb ⁺ NO ⁻	2.58	12.39	2.77	9.62	0.777
Cs ⁺ NO ⁻	2.68	12.88	3.24	9.64	0.749

^a Interionic distance r estimated to be average of M⁺F⁻ and M⁺Cl⁻ gas-phase internuclear distances plus 2%. ^b NO⁻ anion polarizability estimated using NO polarizability data, the assumption that $\alpha(\text{NO}^-) / \alpha(\text{O}_2^-) = \alpha(\text{NO}) / \alpha(\text{O}_2)$ and the solution for α_{\perp} described in ref 3. A value of 2.41 Å³ was used for α_{\perp} of NO⁻.

this contrasts the 22-cm⁻¹ spread from Li⁺ up to Cs⁺. Clearly, the increase in (NO)⁻ frequency with increasing M⁺ mass cannot be a mass effect since such an effect would be expected to lower the (NO)⁻ frequency.

The Rittner ionic model of polarizable ion pairs⁹ has been recently applied to the M⁺O₂⁻ species.³ The first two terms of Rittner's equation for the dipole moment μ , a measure of charge separation and hence antibonding electron density on NO⁻, are as follows

$$\mu = er - \frac{\alpha_c e}{r^2} - \frac{\alpha_a e}{r^2} \quad (1)$$

ion dipole induced dipoles

This treatment can only be interpreted qualitatively because r , the interionic distance, and α_a , the NO⁻ anion polarizability, are not accurately known. Using reasonable values of r and α_a , dipole moments for the M⁺NO⁻ species were calculated; values are listed in Table IV. The last column in the table represents the fractional ionic character which is a measure of the charge transferred from M to NO. With the exception of the Li⁺ species, which is the difficult one to calculate for Li⁺F⁻ and Li⁺Cl⁻ as well,³ the fractional ionic character decreases from the Na⁺NO⁻ species to the Cs⁺NO⁻ species. The important point here is the qualitative trend not the quantitative values; as the alkali cation polarizability, α_c , increases, the induced dipole on M⁺ increases which opposes the ion-dipole charge transfer and decreases the fractional ionic character and the antibonding electron density on NO⁻. Accordingly the NO⁻ frequency increases with increasing alkali cation polarizability. Similar behavior has been observed for O₂⁻ as a function of M⁺ in the M⁺O₂⁻ species.³ Clearly, the ionic model of polarizable ion pairs provides an adequate explanation for the small frequency increase with increasing cation size.

Three observations invite consideration of the M⁺(ON)⁻ structure. First, the ν_2 isotopic shifts change from a major ¹⁸O dependence and minor ¹⁵N shift with Li⁺ to more ¹⁵N shift than ¹⁸O effect in the Cs⁺ species. Secondly, no heavier M(ON)M secondary reaction products were observed, in contrast to the heavier MO₂M peroxides. Finally, photolysis did not change the band intensities or, accordingly, the M⁺(ON)⁻ structure which contrasts the Li⁺(ON)⁻ photolysis behavior.^{1,5}

Although a definite conclusion cannot be reached, the above observations suggest a different structural arrange-

(8) D. Spence and G. J. Schulz, *Phys. Rev. A*, **3**, 1968 (1971).

(9) E. S. Rittner, *J. Chem. Phys.*, **19**, 1030 (1951).

ment for the K^+ , Rb^+ , and $Cs^+(NO)^-$ species as compared to the acute triangular models for $Li^+(ON)^-$ and $M^+O_2^-$. The breadth of the 361-cm^{-1} $Na^+(NO)^-$ band may indicate that more than one cation-anion arrangement is matrix isolated for this species; the isotopic shift data for the 361-cm^{-1} band (see Table III) are not conclusive on suggesting whether Na^+NO^- is most likely like Li^+ON^- or K^+NO^- . The large ^{15}N shift and small ^{18}O shift data for the K^+ , Rb^+ , and Cs^+ species suggest a bent or linear $M^+(NO)^-$ arrangement for the three heaviest alkali metals, in contrast to the triangular models proposed^{1,4} for $Li^+(ON)^-$ and $Na^+(ON)^-$. It should be noted that the K^+ ion is comparable in size to NO^- , and Rb^+ and Cs^+ are larger than NO^- ; hence, a different structural arrangement for these larger cations may not be too unreasonable. If the $K^+(NO)^-$, $Rb^+(NO)^-$, and $Cs^+(NO)^-$ species are produced in a stable bent or linear form, photolysis cannot effect isomerism, which rationalizes the photolytic stability of the observed bands. Perhaps the open $M^+(NO)^-$ structure is less susceptible to second-

dary reaction forming a two metal species, than the triangular $Li^+(ON)^-$ or $M^+O_2^-$ species.

Conclusions

When Na, K, Rb, and Cs are deposited with matrix samples of NO, two intense product bands appear which correspond to the two most intense features in lithium-nitric oxide reactions. The higher frequency in the $1358\text{--}1374\text{-cm}^{-1}$ range is assigned to ν_1 , the intraionic (N-O)-mode and the lower frequency in the $361\text{--}219\text{-cm}^{-1}$ region is assigned to ν_2 , the interionic $M^+(NO)^-$ motion. The M^+ effect on the NO^- mode is explained by the Rittner ionic model of polarizable ion pairs. The large ^{15}N shifts for ν_2 of the heavy metal species suggest the bent or linear structures M^+NO^- for the K^+ , Rb^+ , and Cs^+ species, in contrast to the triangular $Li^+(ON)^-$ species.

Acknowledgment. The authors gratefully acknowledge financial support of this research by the National Science Foundation under Grant No. GP-28582.

Infrared Spectra of the Ammonia-Hydrochloric Acid Complex in Solid Nitrogen

Bruce S. Ault and George C. Pimentel*

Department of Chemistry, University of California, Berkeley, California 94720 (Received February 20, 1973)

Publication costs assisted by the U.S. Office of Naval Research

The infrared spectrum was obtained for the 1:1 complex of NH_3 and HCl isolated in a nitrogen matrix at $15^\circ K$. The $NH_3 \cdot HCl$ complex absorbs at 630 , 705 , 1246 , and 1438 cm^{-1} , while bands of the perdeuterio counterpart $ND_3 \cdot DCl$ were identified at 470 and 505 cm^{-1} . The spectra of the mixed isotopic species indicate that the hydrogen atoms of the complex are not equivalent. Comparison to known spectra of prototype compounds shows that a very strong hydrogen bond is formed, involving specifically the hydrogen atom attached to the HCl molecule. However, this complex contains a hydrogen bond in which the hydrogen atom of the HCl is nearly equally shared by the chlorine and the nitrogen. These results are compared to Clementi's extensive theoretical calculations on this complex, with very good agreement. Thermodynamic arguments about the stability of an isolated $NH_3 \cdot HCl$ complex support these conclusions as well.

Introduction

Recently Ault and Pimentel¹ reported the infrared spectrum of the hydrogen bonded complex formed between H_2O and HCl in a nitrogen matrix at $20^\circ K$ (hereafter, this paper will be called AP). The spectra show that HCl forms a hydrogen bond in which its hydrogen remains chemically distinct from the hydrogens of the base, H_2O , and that the ion pair, $H_3O^+ \cdot Cl^-$, does not form. We report here a parallel study of the ammonia-hydrochloric acid complex in solid nitrogen. This system was selected because the higher base strength of NH_3 should encourage more complete transfer of the hydrogen-bonded proton and, thus, reveal the extent to which ion pair formation, $NH_4^+ \cdot Cl^-$, depends upon stabilization by an ionic lattice.

The $H_3N \cdot HCl$ molecular complex has been detected by Goldfinger and Verhaegen² using high-temperature mass spectrometry. The results give no clue to the structure of the complex. Clementi has made an intensive set of *ab initio* LCAO-SCF calculations on $H_3N \cdot HCl$.³⁻⁵ These calculations, which omit correlation energy, provide an estimate of the bond energy (19 kcal/mol) and they indicate a partial proton transfer. Without experimental validation, the significance of these calculations is difficult to assess. The spectra we have obtained provide the needed experimental tie point.

- (1) B. S. Ault and G. C. Pimentel, *J. Phys. Chem.*, **77**, 57 (1973).
- (2) P. Goldfinger and G. Verhaegen, *J. Chem. Phys.*, **50**, 1467 (1969).
- (3) E. Clementi, *J. Chem. Phys.*, **46**, 3851 (1967).
- (4) E. Clementi, *J. Chem. Phys.*, **47**, 2323 (1967).
- (5) E. Clementi and J. N. Gayles, *J. Chem. Phys.*, **47**, 3837 (1967).

Experimental Section

The same liquid hydrogen cold cell used in AP was used here. To prevent condensation of crystalline NH_4Cl , two jets were always used to deposit the sample onto the CsI cold windows. Deposition was conducted at about 5 mmol/hr from each jet, for 8 hr in most cases. The window was maintained at 15°K, as monitored by a Au-Co *vs.* Cu thermocouple embedded in the CsI window. The infrared spectrum was recorded from 4000 to 200 cm^{-1} on a Perkin-Elmer Model 225 infrared spectrophotometer. Frequency accuracy was $\pm 0.5 \text{ cm}^{-1}$ and the spectral slit width was roughly constant at 2.0 cm^{-1} .

Samples were prepared by adding an appropriate pressure of NH_3 or HCl to a 3-l. bulb and then N_2 to reach the desired concentration, which ranged from 1:500 to 1:175. The HCl (Matheson, 99%), NH_3 (Matheson, 99%), DCl (Merck Sharp and Dohme, Ltd., Canada), and ND_3 (Biorad Labs, 99%) were each purified by double distillation from a Dry Ice-acetone bath into a liquid nitrogen cold trap.

Results

The spectrum of each of the parent molecules was recorded, in turn, at a concentration of 1:300 in a nitrogen matrix. The spectra of each of the deuterated samples revealed partial hydrogen exchange with the vacuum line surfaces; D/H ratios ranged from 2 to 5. A representative spectrum of NH_3 and its deuterium counterparts in the spectral range 1400–400 cm^{-1} is shown in Figure 1. Neither HCl nor DCl absorb in this region. With this background, the spectra obtained on simultaneous deposition of ammonia and hydrochloric acid and their deuterated counterparts could be interpreted.

NH₃ and HCl. By simultaneous codeposition of $\text{NH}_3:\text{N}_2 = 1:175$ and $\text{HCl}:\text{N}_2 = 1:175$, a matrix sample was prepared with composition $\text{NH}_3:\text{HCl}:\text{N}_2 = 1:1:350$. The infrared spectrum of this sample is shown in Figure 2 and the observed bands are listed in Table I. Four absorption features not observed in the parent molecule spectra were observed: 630 (0.24), 705 (0.29), 1246 (0.10), and 1438 (0.03) cm^{-1} (optical densities are given parenthetically). (The features at 905 and 1140 cm^{-1} are due, respectively, to NH_2D , a trace impurity from earlier experiments, and to NH_3 .⁶) The intense features at 630 and 705 cm^{-1} are broad (half-width, 60–70 cm^{-1}) so they overlap considerably. This makes the location of the 705- cm^{-1} band uncertain by about $\pm 10 \text{ cm}^{-1}$. Furthermore, the band at 705 cm^{-1} has a reproducible shoulder at 745 cm^{-1} . Both the distinct feature at 1246 cm^{-1} and the weak feature at 1438 cm^{-1} appear to be somewhat narrower (half-width, 20–25 cm^{-1}).

When the sample was warmed to 40°K (to permit diffusion) and recooled to 15°K, the new bands listed above all disappeared and were replaced by two large, broad peaks near 1400 and 3100 cm^{-1} .

This experiment was repeated at higher dilution: $\text{NH}_3:\text{HCl}:\text{N}_2 = 1:1:1000$. With the exception of 1438 cm^{-1} , all of the new bands were again observed, though considerably weaker, and the relative intensities were about the same as in the earlier experiment.

ND₃, NHD₂, and NH₂D with DCl. Through codeposition, a sample containing $\text{ND}_3:\text{DCl}:\text{N}_2 = 1:1:250$ was prepared and a complete spectrum was recorded. Figure 3 shows the 400–1400- cm^{-1} spectral region. The presence of NH_2D and NHD_2 (as well as of HCl near 2900 cm^{-1}) showed that the D/H ratios were roughly 4. Two new

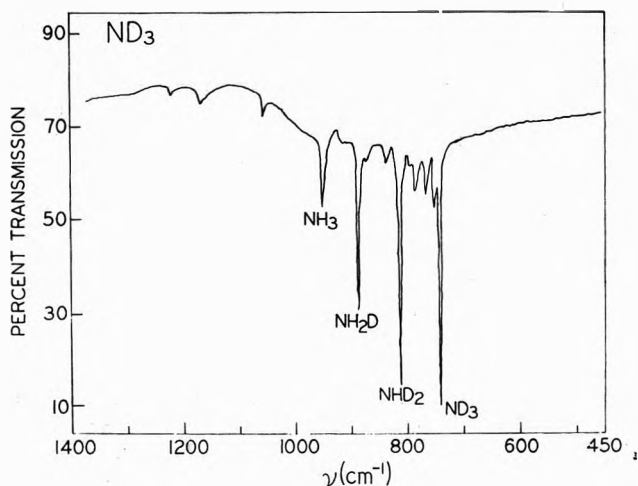


Figure 1. Infrared spectrum of ND_3 , ND_2H , NH_2D , and NH_3 in the spectral region 1400–450 cm^{-1} , isolated in a nitrogen matrix at 20°K.

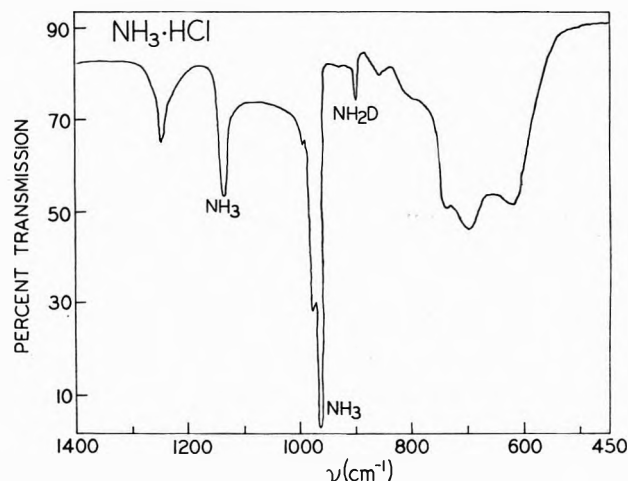


Figure 2. Infrared spectrum of codeposited HCl and NH_3 with $\text{NH}_3:\text{HCl}:\text{N}_2 = 1:1:350$ in the spectral region 1400–450 cm^{-1} .

broad peaks appeared at 505 and 470 cm^{-1} with a poorly defined shoulder near 536 cm^{-1} . The contour of these features resembles rather closely that of the 705–630- cm^{-1} absorptions (see Figure 2). In addition, weaker peaks at 721 and 633 cm^{-1} were observed, evidently due to residual hydrogen-containing species. The bands at 1236 and 1438 cm^{-1} were not detected, nor were shifted counterparts, but the partially deuterated parent ammonia spectra encumber the relevant spectral region. The observed features and their optical densities are listed in Table I.

NH₃, NH₂D, and NHD₂ with HCl. In this experiment, ammonia:hydrogen chloride:nitrogen = 1:1:500. There was considerable isotopic dilution in the ammonia, with D/H near 2. However, the exchange had not affected the HCl; no bands ascribable to parent DCl near 2062 cm^{-1} were observed. The spectrum, presented in Figure 4, includes the broad, overlapping bands (at 719 and 640 cm^{-1}) with a shoulder at 745 cm^{-1} and an absorption at 1244 cm^{-1} , all resembling closely the $\text{NH}_3\text{-HCl}$ spectrum shown in Figure 2. No bands were observed near 500 or 470 cm^{-1} .

This experiment was repeated with a still different degree of deuteration in the ammonia (this time, D/H \approx 4)

(6) G. C. Pimentel, M. O. Bulanin, and M. Van Thiel, *J. Chem. Phys.*, **36**, 500 (1962).

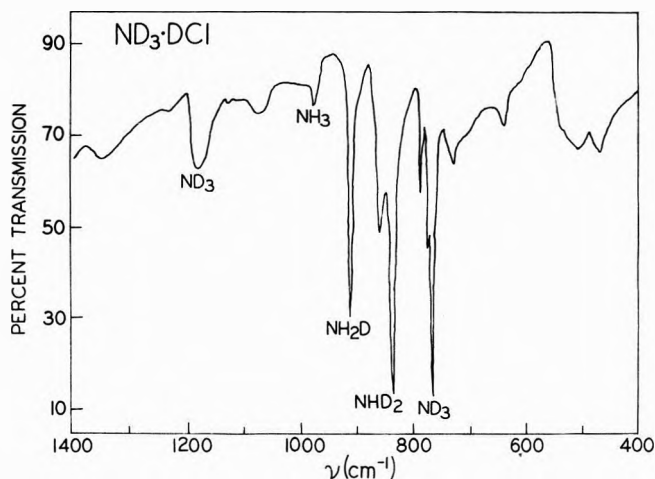


Figure 3. Infrared spectrum of codeposited DCl and ND₃ with DCl:ND₃:N₂ = 1:1:250 in the spectral region 1400–400 cm⁻¹ (D/H ≈ 4).

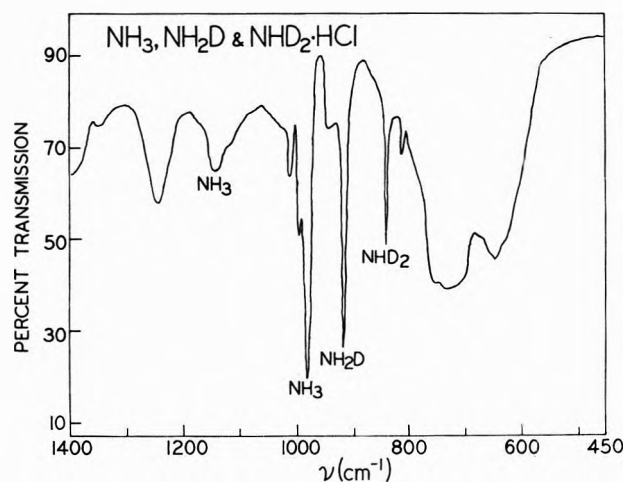


Figure 4. Infrared spectrum of codeposited HCl and ND₃ with HCl:ND₃:N₂ = 1:1:500 in the spectral region 1400–450 cm⁻¹ (D/H ≈ 2).

TABLE I: Absorption Frequencies of Ammonia and Hydrogen Chloride Mixtures in an N₂ Matrix at 15°K^a

NH ₃ + HCl, ν, cm ⁻¹	ND ₃ + DCl, ^b ν, cm ⁻¹	ND ₃ + HCl, ^c ν, cm ⁻¹
1438 (0.03)		
1246 (0.10)		1240 (0.13)
745 (d)		745 (d)
705 (0.29)	721 (0.05)	719 (0.38)
630 (0.24)	633 (0.04)	640 (0.32)
	536 (d)	
	505 (0.17)	
	470 (0.17)	
Parent Molecule Absorptions		
2854 (HCl, >1.0)	2854 (HCl, 0.15)	2854 (0.22)
	2062 (DCl, 0.10)	
970 (NH ₃ , >1.0)	970 (NH ₃ , 0.05)	970 (0.59)
	905 (NH ₂ D, 0.46)	905 (0.48)
	830 (NHD ₂ , 0.90)	830 (0.20)
	760 (ND ₃ , >1.00)	760 (0.05)

^a Optical densities are given parenthetically. ^b D/H ≈ 4. ^c D/H ≈ 2. ^d Shoulder.

but with undeuterated HCl. The spectral features not ascribable to parent molecules again resembled those observed in Figure 2 and did not include those shown in Figure 3.

Discussion

We shall follow the pattern of interpretation used in AP,¹ examining the spectral features and their deuteration shifts in the light of potential prototype spectra.

Mixed Isotope Spectra. When both HCl and DCl are present, counterpart spectra appear in the regions 705–630 and 505–470 cm⁻¹ but no intermediate absorptions are observed. Thus the spectra indicate that the broad 705–630-cm⁻¹ doublet is to be ascribed to vibrations dominated by a single hydrogen atom. This doublet is relatively unaffected by deuteration (or partial deuteration) of the ammonia but it shifts to 505–470 cm⁻¹ upon deuteration of the hydrogen chloride. Hence, it is clear that the single hydrogen atom has its parentage in the hydrogen chloride and not in ammonia. The deuteration shifts are 705/505 = 1.40 and 630/470 = 1.34.

Vibrational Assignments. In view of the deuteration shifts displayed by the two most intense features, they must both be assigned as vibrations dominated by movement of the hydrogen atom provided by HCl. It is, then, probable that one of the bands is due to the hydrogen stretching motion in a linear (or near-linear) hydrogen-bonded complex and that the other is due to the hydrogen bending motion perpendicular to the bond. The frequencies of the bands at 1246 and 1438 cm⁻¹ are consistent with their assignment as overtones of these two fundamentals (1438/705 = 2.04 and 1246/630 = 1.98).

The evidence does not permit an unambiguous decision concerning which band should be assigned as the stretching mode. The high intensity of the 1246-cm⁻¹ overtone absorption can be taken as presumptive evidence that 630 cm⁻¹ should be assigned as the bending mode fundamental. This choice would be consistent with earlier observations of exceptionally intense bending overtones in hydrogen-bonded complexes.^{7,8} This behavior has been attributed to the fact that the dipole derivative terms that activate the bending overtone include a component parallel to the hydrogen bond, thus tapping the high electron mobility that accounts for the stretching fundamental's high intensity.⁹ We shall accept this assignment, 705 cm⁻¹ as the stretching mode and 630 cm⁻¹ as the bending mode, though our major conclusions would not be changed critically if the assignment were reversed.

The 745-cm⁻¹ shoulder is undoubtedly a combination involving one of the two prominent bands, 705 or 630 cm⁻¹. If it is associated with the lower frequency component, the splitting changes from 745 – 630 = 115 cm⁻¹ to 536 – 470 = 66 cm⁻¹. Since this deuteration shift is not readily explained, the 745-cm⁻¹ feature is more likely due to a combination band involving 705 cm⁻¹, which would identify a very low-frequency motion near 40 cm⁻¹.

Prototype Compounds. In AP, four structure types were considered and the anticipated spectrum of each was given.¹ Figure 5 shows the corresponding H₃N·HCl possibilities. Type I, for which the (CH₃)₂O·HCl^{10,11} and

- (7) W. E. Thompson and G. C. Pimentel, *Z. Elektrochem.*, **64**, 748 (1960).
 (8) J. W. Nibler and G. C. Pimentel, *J. Chem. Phys.*, **47**, 710 (1967).
 (9) G. C. Pimentel and A. ... McClellan, "The Hydrogen Bond," W. H. Freeman, San Francisco, Calif., 1960, pp 70 and 248.
 (10) J. E. Bertie and D. J. Millen, *J. Chem. Soc.*, **497**, 514 (1965).
 (11) R. M. Seel and N. Sheppard, *Spectrochim. Acta, Part A*, **25**, 1287 (1969).

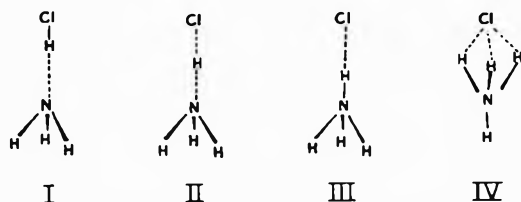


Figure 5. Four possible prototype structures for the isolated $\text{NH}_3\cdot\text{HCl}$ complex (all structures could have C_{3v} symmetry; structure IV might include free rotation of the NH_4^+ ion).

$\text{H}_2\text{O}\cdot\text{HCl}^1$ complexes furnish prototypes, would be characterized by much smaller hydrogen bond shifts than observed here. Hence, the ammonia-hydrochloric acid matrix complex cannot be regarded as a simple HCl hydrogen bond, as implied by the type I structure.

Both types III and IV picture an ion pair structure, $\text{NH}_4^+\cdot\text{Cl}^-$, and they differ in that type III preserves the uniqueness of one of the protons of the NH_4^+ ion. Each would be expected to display shifted but nonetheless characteristic absorptions of NH_4^+ near 1400 and 3100 cm^{-1} . Since such bands are not observed in the matrix-isolated samples (though they do appear after diffusion has occurred) we conclude that these structures, too, cannot be applicable.

We are left with the type II structure, which in AP was called a "completely shared" proton and represented by several centrosymmetric prototypes, $(\text{FHF})^-$, $(\text{H}_2\text{O}\cdot\text{H}\cdot\text{OH}_2)^+$, and a number of acid salt $(\text{O}\cdots\text{H}\cdots\text{O})^-$ hydrogen bonds. All of these prototypes display stretching mode frequency shifts exceeding 1000 cm^{-1} and quite high bending mode frequencies.¹² They lead to the expectation that in a type II structure, these two vibrations will absorb, respectively, in the ranges 1800–600 and 1600–600 cm^{-1} . Plainly, the observed spectrum is in complete accord with this picture and we can conclude with confidence that the $\text{H}_3\text{N}\cdot\text{HCl}$ matrix-isolated complex is bound by an extremely strong hydrogen bond in which the bridge proton is preferentially attached neither to the chlorine nor to the nitrogen atom. Such a hydrogen bond would be characterized by (a) very short $\text{N}\cdots\text{Cl}$ distance, (b) rather long $\text{N}\cdots\text{H}$ and $\text{H}\cdots\text{Cl}$ distances, both much longer than the corresponding bond lengths in the "parent" molecules, NH_4^+ and HCl and, (c) relatively high hydrogen bond energy, with $-\Delta H$ undoubtedly above 10 kcal and possibly as high as 20 kcal.

Theoretical Predictions. Clementi's³⁻⁵ LCAO-SCF-MO calculations for the $\text{NH}_3 + \text{HCl}$ system use a truncated basis set for the core electrons and neglect electron correlations. For a linear $\text{N}\cdots\text{H}\cdots\text{Cl}$ structure, he varied both the $\text{N}\cdots\text{Cl}$ and the $\text{H}\cdots\text{Cl}$ distance to find the optimum geometry. For large $\text{N}\cdots\text{Cl}$ separations, the calculations showed a double minimum for the proton position. However, at the smaller $\text{N}\cdots\text{Cl}$ distances, the double minimum was lost. At the minimum energy configuration, the calculations predicted⁵ a single energy minimum for the proton position with an $\text{N}\cdots\text{Cl}$ distance of 2.86 Å, an $\text{N}\cdots\text{H}$ distance of 1.24 Å, and $\text{H}\cdots\text{Cl}$ distance of 1.62 Å, and a hydrogen bond energy of 19.5 kcal/mol. Thus, the $\text{N}\cdots\text{H}$ distance is calculated to be 0.23 Å longer than the 1.01-Å N-H bond length in gaseous ammonia and 0.21 Å longer than the 1.03-Å hydrogen bonded N-H bond length of NH_4^+ in crystalline ammonium chloride. Similarly, the $\text{H}\cdots\text{Cl}$ distance is calculated to be 0.34 Å longer than in gaseous HCl, 1.28 Å. Finally, the calculated $\text{N}\cdots\text{Cl}$ distance is 0.40 Å

shorter than the 3.26-Å $\text{N}\cdots\text{Cl}$ separation in the face-centered cubic ammonium chloride crystal (NaCl lattice) and 0.49 Å shorter than in the body-centered cubic ammonium chloride (CsCl lattice). All of these bond distance changes and the calculated bond energy are in remarkable accord with our deductions from the matrix infrared spectra presented here. We feel that our observations provide a strong validation of the approximations required in Clementi's calculations, the most uncertain of which is probably the neglect of electron correlation.

Clementi also deduces a set of vibrational frequencies for the $\text{H}_3\text{N}\cdot\text{HCl}$ complex.⁵ He mentions an $\text{H}\cdots\text{Cl}$ stretching frequency of 2745 cm^{-1} (rather close to the parent HCl frequency at 2885 cm^{-1}) and an $\text{N}\cdots\text{H}$ stretching frequency of 2479 cm^{-1} . These frequencies do not, however, correspond to normal modes, so they cannot be compared to our experimental observations and they do not detract from the agreements already pointed out.¹³

Vibrational Potential Function. In a diatomic, harmonic approximation of a symmetrical $\text{X}\cdots\text{H}\cdots\text{X}$ hydrogen bond, the reduced mass for the asymmetric stretch is $\frac{1}{2} [m_{\text{H}}(2m_{\text{X}})/(m_{\text{H}} + 2m_{\text{X}})]$. With this same simplified view, a "completely shared" proton might be assigned a reduced mass of $\frac{1}{2} [(m_{\text{H}})(m_{\text{X}} + m_{\text{X}})/(m_{\text{H}} + m_{\text{X}} + m_{\text{X}})]$. Choosing $m_{\text{X}} = 18$ and $m_{\text{X}'} = 35$ leads to a predicted deuteration shift of 1.40, exactly the shift observed for the 705- cm^{-1} feature. This tends to affirm (though not compellingly) the preferred assignment given earlier and it gives an average $\text{X}\cdots\text{H}$ stretching force constant of 0.14 $\text{mdyn}/\text{Å}$. (The 630- cm^{-1} frequency would give a force constant of 0.11 $\text{mdyn}/\text{Å}$.) This is very much lower than the stretching force constant of gaseous HCl, 5.15 $\text{mdyn}/\text{Å}$, and of the $\text{H}_2\text{O}\cdot\text{HCl}$ complex, 3.98 $\text{mdyn}/\text{Å}$, whereas it is of the same order of magnitude as that of the HCl_2^- symmetrical (Evans and Lo's type II) hydrogen bond,¹⁴ $(k_1 - k_{12}) = 0.19 \text{mdyn}/\text{Å}$.

The bending motion can also be treated in this approximation with the reduced mass of a hydrogen atom moving against the combined masses of the terminal atoms. Hence, the 630- cm^{-1} frequency gives a bending force constant $a_{\theta}/l^2 = 0.055 \text{mdyn}/\text{Å}$. This can be compared to the bending force constant in HCl_2^- symmetrical hydrogen bond,⁸ 0.058 $\text{mdyn}/\text{Å}$.

Thermodynamic Considerations. The proton affinity of ammonia has been measured to be 209 kcal/mol.¹⁵ Hence ΔH for the gas-phase formation of NH_4^+ and Cl^- from NH_3 and HCl can be calculated.



$$\Delta H = +124 \text{ kcal/mol}$$

This endothermicity is returned if the two charges (regarded as point charges) are placed 2.67 Å apart. To make the ion pair formation exothermic by 19.5 kcal/mol, the point charges would have to be 2.31 Å apart. Each of these distances is much shorter than the 2.86-Å distance calculated by Clementi, at which distance the point charge approximation indicates a net endothermicity of 8 kcal/mol for ion pair formation. Thus, this simple model

(12) H. N. Shrivastava and J. C. Speakman, *J. Chem. Soc.*, 1151 (1961).

(13) In collaboration with Dr. Clementi, an improved, normal mode frequency prediction will be attempted, based upon his original calculations. In addition, the thermodynamic quantities given in Clementi's Table IV (ref 5) must be recalculated because significant changes in several frequencies will result.

(14) J. C. Evans and G. Y-S. Lo, *J. Phys. Chem.*, 70, 11 (1966).

(15) M. A. Haney and J. L. Franklin, *J. Chem. Phys.*, 50, 2028 (1969).

provides a rationalization of the absence of ion pair formation in the isolated complex. It also permits the prediction that proton transfer and ion pair formation will occur between HCl and a nitrogen base B if the proton affinity of the base exceeds about 225 kcal/mol.

In a similar way, we can predict the N...X distances needed to form ion pairs in $\text{H}_3\text{N}\cdot\text{HBr}$ and $\text{H}_3\text{N}\cdot\text{HI}$ complexes. Because of its low bond energy, HBr could form an ion pair at an N...Br distance of 2.90 Å, which is 0.55 Å shorter than the 3.45-Å N...Br distance in ammonium bromide (NaCl lattice). For HI, an ion pair could form at an N...I distance of 3.17 Å, 0.46 Å shorter than the 3.63-Å N...I distance in ammonium iodide (NaCl lattice). These contractions are quite close to that implied by the calculated N...Cl distance in $\text{H}_3\text{N}\cdot\text{HCl}$, *i.e.*, 0.40 Å shorter than in ammonium chloride. Hence we are led to the conclusion that proton transfer *will* occur in $\text{H}_3\text{N}\cdot\text{HI}$ and that it *might* occur in $\text{H}_3\text{N}\cdot\text{HBr}$ as well.¹⁶

Conclusions

The matrix spectra show clearly that the $\text{H}_3\text{N}\cdot\text{HCl}$ complex is not an ion pair, $\text{NH}_4^+\cdot\text{Cl}^-$, but it can be re-

garded as a strongly hydrogen-bonded complex with a proton shared by the adjacent heavy atoms. This is entirely consistent with the results calculated in an *ab initio* fashion by Clementi and it validates his application of self-consistent field calculations without configuration interaction (electron correlation) to a hydrogen-bonded complex. Thus, the present work shows that the ionic character of the ammonium chloride crystals must be attributed to the long-range ionic lattice forces, without which ammonium chloride ion pairs do not form. It reassures, as well, the validity of *ab initio* calculations at the sophistication level used by Clementi and it should encourage such studies of other hydrogen-bonded systems that may not be experimentally accessible.

Acknowledgment. We gratefully acknowledge support of this research by the U.S. Office of Naval Research under Grant No. N00014-A-0200-102.

(16) Preliminary experiments with $\text{NH}_3\text{-HBr}$ codepositions produced spectra that include absorption near 1380 cm^{-1} , a region in which NH_4^+ displays intense and characteristic absorption.

Optical Activity of Oriented Helices. Quadrupole Contributions¹

Joseph Snir and John Schellman*

Chemistry Department, University of Oregon, Eugene, Oregon 97403 (Received January 11, 1973)

Publication costs assisted by The University of Oregon

Formulas are developed for the optical activity of oriented helices specifically including the quadrupole matrix elements. Only short helices are considered so that the Rosenfeld approximation is valid. Cyclic excitons are assumed in an initial derivation and the effects of reentrance, finite size, and additional exciton bands are then investigated. The helical bands of Loxsam, Deutsche, and Ando lie dormant in the Moffitt theory as cancelling degenerate contributions and are brought out by any breakdown of perfect reentrant boundary conditions or by extension to great length. For oriented helices, the decomposition of the ρ matrix element into magnetic and quadrupole terms complicates rather than simplifies the picture.

Introduction

Recently progress has been made in the measurement of optical activity of oriented helical molecules.¹⁻³ As pointed out by Tinoco a number of years ago, the informational content of optical rotatory dispersion (ORD) is doubled when the effects of orientation are studied quantitatively.⁴ The current emphasis on circular dichroism (CD) within absorption bands adds considerably to the power of such measurements. Taken in conjunction with the more easily measured linear dichroism, oriented CD studies aid in resolving overlapping absorption bands, provide spectral assignments to monomer units on the basis of polarization properties, determine the orientation and degree of order of chromophores in the macromolecule, and are extremely sensitive to the interaction of chromophores, particularly exciton phenomena.

Theoretical calculations of the oriented CD of a macromolecule are carried out in the same fashion as those for ordinary CD⁵⁻⁹ and involve the same set of structural and spectroscopic parameters.⁵ The major difference lies in the quadrupole terms which vanish on the average but

- (1) This work was supported by grants from the National Science Foundation (GB6972X) and the Cancer Institute of the National Institutes of Health (CA 4216).
- (2) (a) G. Holzwarth, *J. Amer. Chem. Soc.*, **93**, 4066 (1971); (b) J. Hofrichter, Thesis, University of Oregon, 1971; J. Hofrichter and J. Schellman, 5th Jerusalem Symposium (1972).
- (3) S. Hoffman and R. Ullman, *J. Pol. Sci., Part C*, **31**, 205 (1970).
- (4) I. Tinoco, *J. Amer. Chem. Soc.*, **79**, 2428 (1957).
- (5) I. Tinoco and R. Woody, *J. Chem. Phys.*, **46**, 4927 (1967).
- (6) P. M. Bayley, E. Nielsen, and J. Schellman, *J. Chem. Phys.*, **73**, 228 (1969).
- (7) E. S. Pysh, *J. Chem. Phys.*, **52**, 4723 (1970).
- (8) V. Madison and J. Schellman, *Biopolymers*, **11**, 1041 (1972).
- (9) M. L. Tiffany and S. Krimm, *Biopolymers*, **8**, 347 (1969).

make contributions for individual orientations.¹⁰ Consequently, a more generalized expression for the rotatory strength must be used (eq 3). The usual Rosenfeld expression for the rotatory strength $R_{0a} = \text{Im} \{ \mu_{0a} \cdot M_{a0} \}$ results from assuming that the molecule is small compared to the wavelength of light, expanding the general expression (given below) into magnetic dipole and electric quadrupole terms, discarding the latter (legitimate for spacial averaging), and averaging over orientations. In the present work the quadrupole terms will be explicitly evaluated for α helices. It will be seen that the magnetic dipole and electric quadrupole terms are of equivalent magnitude. In addition, the segregation of quadrupole and magnetic dipole terms usually has the effect of complicating, rather than simplifying, the results so that it appears advisable to use the general rotatory strength tensor in undecomposed form. It should be pointed out that in a somewhat different context the importance of the quadrupole terms to helical optical activity has been explicitly recognized previously (Tinoco and Woody,⁵ Loxsom,¹¹ Deutsche,¹² and Philpott¹³).

The discussion will center around the properties of simple cyclic excitons in molecules, small compared to the wavelength of light. Such excitons were the basis of the original theory of Moffitt. Though it is doubtful that these excitons represent any real physical system, it will be seen that their especially simple spectral properties provide a basis for understanding of real excitons in small molecules. They are also easily compared with the limiting case of infinitely long molecules where it has been recently shown that cyclic exciton theory is valid, but the Rosenfeld expansion is not.¹¹⁻¹⁴

The Rotatory Strength Tensor

In 1958 Stephen¹⁵ gave the formula for the optical rotation of an oriented molecule based on quantum scattering theory. For comparison with experiment, it is more expedient to have a formula for circular dichroism. Stephen's formula, in the form appropriate for a broad absorption band, is given by

$$\epsilon_1 - \epsilon_r = \Delta\epsilon = K' \phi(\nu) \mathbf{k} \cdot \mathbf{p}_{0a}^- \times \mathbf{p}_{a0}^+ \quad (1)$$

where $\mathbf{p}^\pm = \sum_j \exp[\pm i(\mathbf{k}_p \cdot \mathbf{r}_j)] \mathbf{p}_j$; \mathbf{r}_j and \mathbf{p}_j are the position and momentum operators of the j th electron; 0 and a refer to the ground and excited electronic state for the transition under consideration, $\mathbf{k}_p = (n\omega/c)\mathbf{k}$ is the propagation vector of the radiation, \mathbf{k} is a unit vector in the direction of propagation, n is the refractive index of the medium $K' = -i2 e^2 N/m^2 c h \omega n (2303)$, N is Avogadro's number, ω is the circular frequency of the radiation, e and m are the charge and mass of the electron, and $\phi(\nu)$ is a transition probability density (dependent on solvent and temperature) which empirically gives the shape of the band. It is normalized such that $\int \phi(\nu) d\nu = 1$ when integrated over the entire vibronic envelope of the electronic absorption band $0 \rightarrow a$.

Equation 1 was derived on the basis of the semi-classical time-dependent perturbation theory. It can be converted to Stephen's formula for optical rotation by performing the Kronig-Kramers transform. Since Stephen's formula is a line spectrum formula, the shape function $\phi(\nu)$ should be taken as a delta function at the absorption maximum for the transform.

If the molecule is short compared to the wavelength of light, the exponentials can be expanded

$$\mathbf{p}_{a0}^+ = \langle a | \sum \exp(i\mathbf{k}_p \cdot \mathbf{r}_j) \mathbf{p}_j | 0 \rangle = \mathbf{p}_{a0} + i\mathbf{k}_p \cdot (\mathbf{r}\mathbf{p})_{a0} \quad (2)$$

$$\mathbf{p}_{0a}^- = \langle 0 | \sum \exp(-i\mathbf{k}_p \cdot \mathbf{r}_j) \mathbf{p}_j | a \rangle = \mathbf{p}_{0a} - i\mathbf{k}_p \cdot (\mathbf{r}\mathbf{p})_{0a}$$

where $\mathbf{r}\mathbf{p} = \sum_j \mathbf{r}_j \mathbf{p}_j$ and $\mathbf{r}_j \mathbf{p}_j$ is a diad operator for the j th electron. After these substitutions and making use of the transformation

$$\mathbf{p}_{0a} = -i\omega_{a0}(m/e)\mu_{0a}$$

the circular dichroism formula may be written as follows

$$\Delta\epsilon = K\phi(\nu)\mathbf{k} \cdot \mathbf{R} \cdot \mathbf{k} \quad (3)$$

where $K = 32\pi^3 N \nu_{a0} / (3hc)(2303)$ and where \mathbf{R} is the rotatory strength tensor

$$\mathbf{R} = (-3e/2mc) \text{Im} [\mu_{0a} \times (\mathbf{p}\mathbf{r})_{a0}] \quad (4)$$

The coefficient in (4) has been chosen so that when averaged over all orientations, the term $\mathbf{k} \cdot \mathbf{R} \cdot \mathbf{k}$ becomes the conventional rotatory strength $R = \text{Im}[\mu_{0a} \cdot \mathbf{M}_{a0}]$ where \mathbf{M} is the electronic magnetic dipole operator. In our work we have found it convenient to eliminate the cross diad product by introducing the appropriate antisymmetric tensor

$$\mathbf{U}_{0a} = \begin{pmatrix} 0 & -\mu_3 & \mu_2 \\ \mu_3 & 0 & -\mu_1 \\ -\mu_2 & \mu_1 & 0 \end{pmatrix}_{0a} \quad (5)$$

so that the rotatory strength becomes

$$\mathbf{R} = -(3e/2mc) \text{Im} [\mathbf{U}_{0a} \cdot (\mathbf{p}\mathbf{r})_{a0}] \quad (6)$$

For application to helical molecules, the diagonal elements of the tensor will be required. The first diagonal element of (6) is easily calculated to be

$$R_{11} = (3e/2mc) [(\mu_3)_{0a} (P_2 r_1)_{a0} - (\mu_2)_{0a} (P_3 r_1)_{a0}] \quad (7)$$

R_{22} and R_{33} are found by a cyclic permutation of the indices 1, 2, 3.

The $(\mathbf{p}\mathbf{r})_{a0}$ tensor may be decomposed into its symmetric and antisymmetric parts leading to terms in the rotatory strength which are related to electric transition quadrupoles and magnetic dipoles, respectively. Thus

$$\mathbf{R} = \mathbf{R}_Q + \mathbf{R}_M$$

where

$$\mathbf{R}_Q = -(3e/4mc) \text{Im} [(\mathbf{U})_{0a} \cdot (\mathbf{p}\mathbf{r} + \mathbf{r}\mathbf{p})_{a0}] \quad (8)$$

and

$$\mathbf{R}_M = -(3e/4mc) \text{Im} [(\mathbf{U})_{0a} \cdot (\mathbf{p}\mathbf{r} - \mathbf{r}\mathbf{p})_{a0}] \quad (9)$$

Recalling the relation $e/m(\mathbf{p}\mathbf{r} + \mathbf{r}\mathbf{p})_{a0} = i\omega_{a0}(\mathbf{Q})_{a0}$ where \mathbf{Q} is the electronic electric quadrupole operator $\mathbf{Q} = e\sum_j \mathbf{r}_j \mathbf{r}_j$, where $\mathbf{r}_j \mathbf{r}_j$ is a diad operator for the j th electron, (8) may be transformed to

$$\mathbf{R}_Q = -(3\omega_{a0}/4c) \text{Re} [(\mathbf{U})_{0a} \cdot (\mathbf{Q})_{a0}] \quad (8a)$$

Though (8) and (8a) are equivalent (with exact eigenfunctions) it turns out that the relationship between quadrupole and magnetic dipole contributions to oriented cir-

(10) I. Tinoco and W. Hamerle, *J. Phys. Chem.*, **60**, 1619 (1956).

(11) F. M. Loxsom, *J. Chem. Phys.*, **51**, 4899 (1969).

(12) C. W. Deutsche, *J. Chem. Phys.*, **52**, 3703 (1970).

(13) M. Philpott, *J. Chem. Phys.*, **56**, 683 (1972).

(14) T. Ando, *Progr. Theor. Phys. (Kyoto)*, **40**, 471 (1968).

(15) M. J. Stephen, *Proc. Cambridge Phil. Soc.*, **54**, 81 (1958).

cular dichroism are more easily brought out in terms of (8). Equation 9 can be equivalently transformed to

$$R_M = (3/2) \text{Im} [(\mu)_{0a} \cdot (\mathbf{M})_{a0} I - (\mu)_{0a} (\mathbf{M})_{a0}] \quad (9a)$$

where I is the unit tensor or diad. The algebra includes the recognition that the components of $(\mathbf{pr} - \mathbf{rp})_{a0}$ are identical with those of the electronic orbital angular momentum $(\mathbf{L})_{a0}$ and that $(\mathbf{M})_{a0} = (e/2mc)(\mathbf{L})_{a0}$. The 11 (first diagonal) components of (8), (8a), and (9a) are given respectively by

$$R_{Q,11} = -(3e/4mc) \text{Im} [(\mu_2)_{0a} (p_3 r_1 + r_3 p_1)_{a0} - (\mu_3)_{0a} (p_2 r_1 + r_2 p_1)_{a0}] \quad (10)$$

$$= (3\omega_{a0}/4c) \text{Re} [(\mu_3)_{0a} (Q_{21})_{a0} - (\mu_2)_{0a} (Q_{31})_{a0}]$$

$$R_{M,11} = (3/2) \text{Im} [(\mu)_{0a} \cdot (\mathbf{M})_{a0} - (\mu_1)_{0a} (M_1)_{a0}] \quad (11)$$

with the other diagonal elements obtainable by cyclic permutation. It is easily seen that one-third of the trace of (9a) is identical with the average rotatory strength and that the trace of (8) vanishes.

The CD Tensor of Long Molecules with Cylindrical Averaging

In this section we will consider a helical array of chromophores each considered to have only a single state of excitation. The helices will be short enough so that Rosenfeld's equation may be applied; cyclic boundary conditions will be assumed so that the wave functions are identical with those of Moffitt. The helices will also be taken to be reentrant so that the physical symmetry of the helix as well as the cyclic symmetry of the exciton wave functions is preserved. The simple excitons which result can be regarded as a limiting model or (as suggested in the Discussion section) as a basis set with simple optical properties. In the next section, calculations will be performed in which the reentrance and cyclic conditions are separately relaxed. The relation between these calculations and those for long helices¹¹⁻¹⁴ will be considered in the Discussion section.

Equations 6-11 are generally applicable whenever the phase of the light may be regarded as varying linearly over the molecule (Rosenfeld's approximation). When they are applied to molecules which are randomly oriented about their long axes, they may be simplified considerably. For oriented helices the following notation is useful. The z axis is taken as the helical axis and the components of the R , R_Q , and R_M transform on rotation about the helix axis with equations of the form

$$\mu_1 = c\mu_1' - s\mu_2'$$

$$\mu_2 = s\mu_1' + c\mu_2'$$

$$Q_{13} = cQ_{13}' - sQ_{23}'$$

$$Q_{12} = cs(Q_{11} - Q_{22}) + (c^2 - s^2)Q_{12}$$

etc., where c and s represent $\cos \phi$ and $\sin \phi$, respectively, and ϕ is the angle of rotation. Averaging over all orientations can then be accomplished by averaging over ϕ . This has the result of diagonalizing the tensor and making the x and y axes equivalent.

Applying this averaging to the diagonal components from (7) and cyclic permutation, we obtain

$$R_{\perp} = R_{11} = R_{22} = (3e/4mc) \{ (\mu_3)_{0a} \{ (p_2 r_1)_{a0} - (p_1 r_2)_{a0} \} + (\mu_1)_{0a} (p_3 r_2)_{a0} - (\mu_2)_{0a} (p_3 r_1)_{a0} \} \quad (12a)$$

$$= (3e/4mc) [(\mu_3)_{0a} (L_3)_{a0} + (\mu_1)_{0a} (p_3 r_2)_{a0} - (\mu_2)_{0a} (p_3 r_1)_{a0}]$$

$$R_{\parallel} = R_{33} = (3e/2mc) [(\mu_2)_{0a} (p_1 r_3)_{a0} - (\mu_1)_{0a} (p_2 r_3)_{a0}] \quad (12b)$$

where L_3 is the angular momentum about the z axis. It can be seen from (7) and its permutations that each diagonal element of \mathbf{R} contains two halves of a component of the scalar product $(\mu)_{0a} \cdot (\mathbf{L})_{a0}$ but not matching halves. In averaging over all orientations, only the trace is of importance. The summation over the diagonal brings the disjointed terms together so that the scalar product $\mu \cdot \mathbf{L}$ emerges. The physical significance of this is that it is only for the average over orientations that the angular momentum or magnetic moment plays a simple role and that for oriented circular dichroism the (\mathbf{pr}) tensor is more direct and natural. Since any tensor can be expressed as the sum of a symmetric and antisymmetric tensor, the magnetic moment can always be introduced, but only by adding cancelling terms to the quadrupole contribution. In eq 12, the partial averaging about the z axis has brought together the operator for the z component of angular momentum in R_{\perp} .

Performing cylindrical averaging on R_M and R_Q , we obtain

$$R_{M,\perp} = R_{M,11} = R_{M,22} = (3/4) \text{Im} [(\mu_2)_{0a} \cdot (M_2)_{a0} + (\mu_3)_{0a} (M_3)_{a0}] \quad (13)$$

$$R_{M,\parallel} = R_{M,33} = (3/2) \text{Im} [(\mu)_{0a} \cdot (\mathbf{M})_{a0} - (\mu_3)_{0a} (M_3)_{a0}]$$

and

$$R_{Q,\perp} = (3e/8mc) \text{Im} [(\mu_1)_{0a} (p_3 r_2 + r_3 p_2)_{a0} - (\mu_2)_{0a} (p_3 r_1 + r_3 p_1)_{a0}] \quad (14)$$

$$= (3\omega_{a0}/8mc) \text{Re} [(\mu_1)_{0a} (Q_{32})_{a0} - (\mu_2)_{0a} (Q_{31})_{a0}]$$

$$R_{Q,\parallel} = -2R_{Q,\perp}$$

Equation 12 shows that the ingredients necessary for the calculation of the rotatory strength tensor are the six off-diagonal components of the (\mathbf{pr}) tensor and the three components of the transition electric dipole. For helices, the formulas are greatly simplified because selection rules will usually allow only μ_1 , μ_2 , or μ_3 to be nonvanishing for a given transition and the cyclic geometry and wave functions lead to very simple expressions.

The Oriented Optical Activity of Idealized Helices

The helix is assumed to proceed along the z axis and to contain N identical groups where N is the appropriate number for reentrance (18 for the α helix, 10 for DNA, etc.). The x and y coordinate system is determined by the condition that the transition moment of the first unit is oriented in the y direction as shown in Figure 1. Use of this coordinate convention implies no loss of generality since the rotatory strength formulas have been averaged about the z axis. r_0 is the distance of the chromophore from the helix axis and δ is the angle made by the position

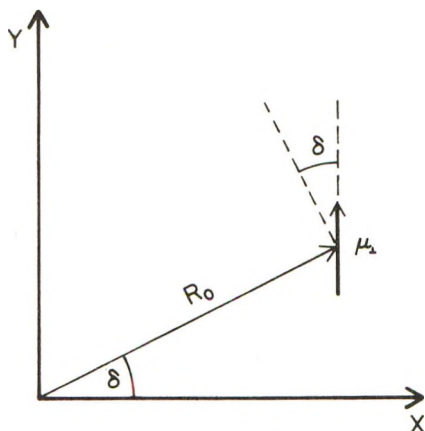


Figure 1. Helical coordinate system. The origin is the helix axis. The coordinate system is oriented so that the transition moment of the first group is pointing in the y direction. R_0 and δ are the polar coordinates of the transition moment in this coordinate system.

vector of the first group with the x axis. It is also the angle which the transition moment makes with the tangential direction, as shown in the figure. μ_{\perp} is the component of the electric transition moment in the xy plane; μ_{\parallel} is the component in the z direction. If μ_{\perp} is positive as shown in the figure, then the sign of μ_{\parallel} depends on the geometry of the helix. The sign of the rotatory strength eventually depends on the sign of μ_{\parallel} . This is negative, for example, for the right-handed α helix.

Assuming a right-handed helix and the conventions of Figure 1, the coordinates and transition moments of the j th residue may be written

$$\begin{aligned} x_j &= r_0 \cos(j\epsilon + \delta) & \mu_{xj} &= -\mu_{\perp} \sin j\epsilon \\ y_j &= r_0 \sin(j\epsilon + \delta) & \mu_{yj} &= \mu_{\perp} \cos j\epsilon \\ z_j &= jt & \mu_{zj} &= \mu_{\parallel} \end{aligned}$$

Here t is the translation per residue along the helical axis and ϵ is the screw angle per residue. If n is the number of residues per turn, then $\epsilon = 2\pi/n$ and $P = nt$ where P is the pitch of the helix.

Following Moffitt,¹⁶ the wave functions of the excited states K are assumed to be cyclic and of the form

$$\psi_K = \sum a_{jK} \phi_j \quad (15)$$

where ϕ_j represents excitation on chromophore j with all other chromophores in their ground state. The coefficients a_{jK} are the normalized characters of the K th representation of the Abelian group C_n

$$a_{jK} = \frac{1}{\sqrt{N}} e^{ijK2\pi/N} \quad (16)$$

Transitions are allowed only to levels with $K = 0$ (z polarization) and $K = \pm N/n$ (xy polarization). Taking the sum and difference of the latter pair leads to the set of functions

$$\begin{aligned} \psi_0 &= \frac{1}{\sqrt{N}} \sum_j \phi_j \\ \psi_S &= \frac{\sqrt{2}}{\sqrt{N}} \sum_j (\sin j\epsilon) \phi_j \\ \psi_C &= \frac{\sqrt{2}}{\sqrt{N}} \sum_j (\cos j\epsilon) \phi_j \end{aligned}$$

TABLE I: Matrix Elements for Cyclic Excitons Normalized by $1/N$

	$K = 0$	$K = C$	$K = S$
$(\mu_1)_{OK}$	0	0	$-\mu_{\perp} / \sqrt{2}$
$(\mu_2)_{OK}$	0	$\mu_{\perp} / \sqrt{2}$	0
$(\mu_3)_{OK}$	μ_{\parallel}	0	0
$(\rho_{2r_2})_{KO}$	0	-	$(i\omega_{SO} / \sqrt{2})$ $(m/e) \mu_{\perp} r_0$
$(\rho_{2r_1})_{KO}$	0	$(i\omega_{CO} / \sqrt{2})$ $(m/e) \mu_{\perp} r_0$	-
$(\rho_{2r_1})_{KO}$	$i\omega_{O0} m \mu_{\perp} r_0 / 2e$	0	0
$(\rho_{1r_2})_{KO}$	$-i\omega_{O0} m \mu_{\perp} r_0 / 2e$	0	0
$(\rho_{2r_3})_{KO}$	0	-	$i\omega_{SO} m \mu_{\perp} P$ $\cot \epsilon / 2^{1/2} e$
$(\rho_{1r_3})_{KO}$	0	$-i\omega_{CO} m \mu_{\perp} P$ $\cot \epsilon / 2^{1/2} e$	-

These specific K levels will be symbolized by O, S, and C, respectively. The allowed excitons in the Moffitt scheme which have perpendicular polarization are those in which the phase advance per residue in the exciton equals the screw angle of the helix.

With the aid of the above formulas and the transformation $e/m(\mathbf{p})_{a0} = i\omega_{a0}\mu_{a0}$ the desired matrix elements are easily calculated. All the sums are listed in ref 17, for example. The results, normalized to a residue basis, are shown in Table I. The calculations of the rotatory strength tensor have been marked with a dash except for those which vanish identically. Of these, the matrix elements of p_{2r_3} and p_{1r_3} , for the C and S transitions, respectively, depend on length even after residue normalization. The spuriousness of this result for very long helices (therefore beyond the bounds of the present model) has been amply explained as the result of using the linear Rosenfeld expansion beyond its range of validity.^{11,12,14}

With these results, the rotatory strength components of R_{\perp} and R_{\parallel} are easily calculated for the excitations O, S, and C. The results are shown in Table II for R , R_M , and R_Q . The calculations for the latter two quantities are similar to those for R and are not given explicitly. The table shows that the rotatory strength components of reentrant helical systems are describable in terms of two parameters indicated by A and B. Terms with the structure of the B terms (products of perpendicular moments) have been called helical terms by Loexsam.¹¹ We adopt this terminology and will refer to A and B as the Moffitt and helical contributions, respectively.

The first three rows of the table present the rotatory strength component for the three transitions $0 \rightarrow O, S, C$. In accordance with the strict degeneracy of the model, the $0 \rightarrow S$ and $0 \rightarrow C$ should be combined. The fourth row is the combined result for the perpendicularly polarized transitions. The orientation averaged rotatory strengths of the parallel and perpendicularly polarized transition are given as one-third of the trace of R , *i.e.*

$$R_{0O} = 2\omega_{O0} \mu_{\perp} \mu_{\parallel} r_0 \cos \delta / 8c$$

$$R_{0C,S} = -2\omega_{C0} \mu_{\perp} \mu_{\parallel} r_0 \cos \delta / 8c$$

These are not equal in magnitude because of the exciton splitting which separates ω_{O0} from $\omega_{SO} = \omega_{CO}$. These equations represent the Moffitt result.¹⁶ The presence of $\cos \delta$ indicates that only the tangential component of μ contrib-

(16) W. Moffitt, *J. Chem. Phys.*, **25**, 467 (1956).

(17) L. Jolley, "Summation of Series," Dover Publications, New York, N. Y., 1961.

TABLE II: Rotatory Strength Tensor for Cyclic Excitons of Reentrant Helices^a

Level	Polarization	R_{\perp}			R_{\parallel}		
		M	Q	R	M	Q	R
R_O	Z	$2A$	0	$2A$	0	0	0
R_S	X	$-\frac{1}{2}A' - \frac{1}{2}B$	$-\frac{1}{2}A' + \frac{1}{2}B$	$-A'^b$	$-A' + B$	$A' + B$	B
R_C	Y	$-\frac{1}{2}A' + \frac{1}{2}B$	$-\frac{1}{2}A' - \frac{1}{2}B$	$-A'$	$-A' - B$	$A' - B$	$-B$
$R_S + R_C$	X, Y	$-A'$	$-A'$	$-2A'$	$-A'$	$+A'$	0

$$A = (3/8c)\omega_{00}\mu_{\perp}\mu_{\parallel}r_0^{1/2}$$

$$B = (3/8c)\omega_{S0}\mu_{\perp}^2P \cot \epsilon$$

^a Q and M represent the electric quadrupole and magnetic dipole contributions (eq 13 and 14). R represents the total strength (eq 12). b A' differs from A only by the presence of $\omega_{S0} = \omega_{C0}$ rather than ω_{O0} . The zero order exciton mechanism does not conserve rotatory strength.

utes to the rotatory strength. As discussed earlier, the sign of the product depends on the geometry of the transition moment in the helix. It is negative for the lowest $\pi\pi^*$ transition of the α helix giving results which are in agreement with experiment.

Only the terms under R in the first and fourth rows of the table are physically relevant. Nevertheless, the decomposition into M and Q terms and into the S and C transition reveals several interesting features. In the first place, use of the magnetic dipole approximation leads to erroneous results. The rotatory strength associated with light propagated perpendicular (fourth row of Table II) to the axis is undervalued by a factor of 2. Simultaneously, the Moffitt contribution to the rotatory strength for light propagating parallel to the helix axis is given by $-A'$ whereas it vanishes in the complete expression. Both of these artifacts result from the artificial decomposition of the rotatory strength, since both are compensated for by the quadrupole terms. It is also seen that the complete rotatory strength is much simpler than either the magnetic or quadrupole component since the decomposition introduced B terms in R_{\perp} and A' terms in R_{\parallel} which are entirely spurious. A further result is that the sums of the tensor components of R_Q and R_M do not vanish whereas the components of the complete tensor do sum to zero. Summation rules for tensor components are given in the Appendix.

An additional fact to be gleaned from the table is that the helical B terms are present in the Moffitt formalism in the perpendicular modes but vanish as a sum because of the complete degeneracy of the modes. Clearly any perturbation on the ideal properties of the model could break this degeneracy and lead to "helical" optical activity. Several ways in which this happens to real systems will be discussed in the next section.

Effect of Lower Symmetry, Real Helices

The artificial simplicity of the previous section can be relaxed in several ways: (1) maintenance of cyclic boundary conditions but introduction of nonreentrance, (2) retention of reentrance but introduction of end effects, (3) removal of both idealizations, and (4) interaction with other exciton bands. In this section these situations will be investigated in turn. The calculations will be performed for α helices with the geometry and parameters described in a previous publication.⁸

Cyclic, but Nonreentrant α Helices. The wave functions are as given in eq 15 and 16 but N is not a multiple of 18. For a given helix with length $18a + b$ (a and b are integers) the results depend both on the overall length and the "remainder" b . Explicit formulas can be given for the

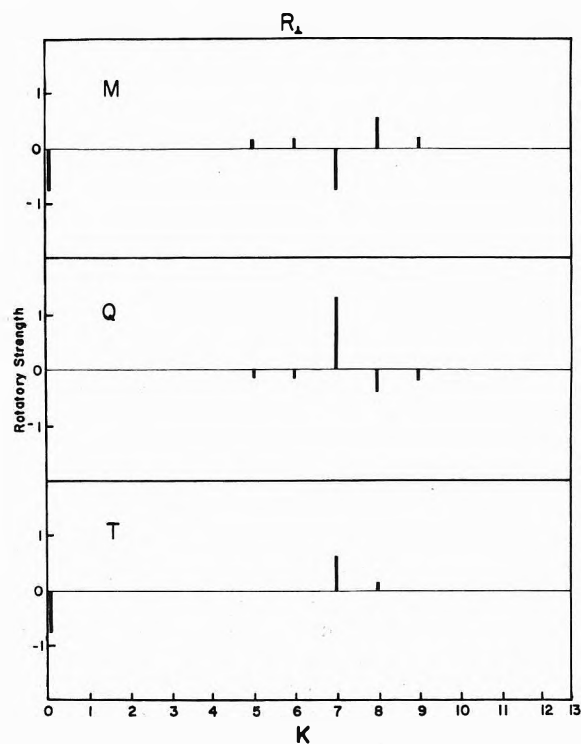


Figure 2. The rotatory strength of an α helix of 26 residues calculated with cyclic boundary conditions. Radiation propagated perpendicular to the helix. The abscissa represents the K indices of the exciton band. The $K = 0$ band is essentially parallel polarized and the other bands essentially perpendicularly polarized though these conditions are no longer strict. All bands but $K = 0$ and $K = 13$ are doubly degenerate and the figure represents the combined rotatory strength for each level. The three graphs represent the magnetic dipole (M), electric quadrupole (Q), and total contributions (T) in descending order. The units of rotatory strength are the Debye magneton.

energy and optical properties but we have preferred to enter the wave functions of eq 15 directly into a computer program for calculating the rotatory strength tensor of helical molecules. A typical calculation is shown in Figures 2 and 3.

Figure 2 represents the rotatory strength for 26 units, the light propagated perpendicular to the helices. Looking at the lowest curve T , which gives the complete rotatory strength, it is seen that the general features of the Moffitt theory are produced with a large negative contribution for the parallel polarized band and the converse for the perpendicularly polarized band. Practically all of the perpendicular rotatory strength is concentrated in the $K = 7$ mode which has a phase advance of 97° per unit, which is rather close to the allowed cyclic mode of 100° . Viewed in

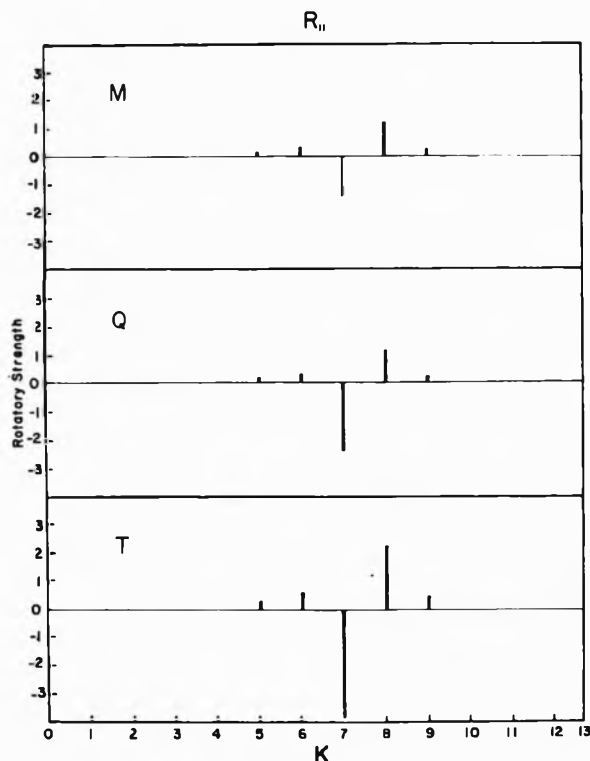


Figure 3. Same as Figure 2 but with light propagated parallel to the helix.

terms of the decomposition into magnetic and quadrupole contributions, the perpendicular mode is the sum of strongly opposing terms. The magnetic and quadrupole contributions to R_{\perp} and R_{\parallel} do not sum separately to zero over the exciton system (see Appendix).

Figure 3 gives the results for R_{\parallel} . Here the contributions come most prominently from the $K = 5-9$ modes with phase advances of 69, 83, 97, 111, and 124°, respectively. The magnetic and quadrupole contributions reinforce one another for this direction of propagation. The rotatory strengths for parallel propagation are helical modes in that they involved only μ_{\perp} . Thus we conclude that these terms make their appearance even with cyclic boundary conditions.

Moffitt, Fitts, and Kirkwood arrived at a similar conclusion¹⁸ for the spatially averaged rotatory strength.

Reentrant α Helices with End Effects. The presence of end effects in helical excitons was demonstrated by Bradley, Woody, and Tinoco in two types of calculation: (1) a nearest neighbor theory¹⁹ leading to a noncyclic secular determinant which can be solved exactly, and (2) the solution of the secular equation which follows from the optical and interaction parameters of real α helices.⁵ Calculations of the latter types emphasizing tensor properties are shown in Figure 4 where the helix has been maintained at the reentrant level of 18. The parameters used in this computation are identical with those of ref 6 and 8.

Separate presentation of the results for the magnetic dipole and quadrupole contributions has been abandoned in Figure 4 in the interest of simplicity. The upper part of the figure represents the contributions to R_{\perp} . The degeneracy of the Moffitt bands is now split. The perpendicularly polarized component appears as two positive and equal bands. The parallel polarized components consist of two bands which have been combined in the figure since

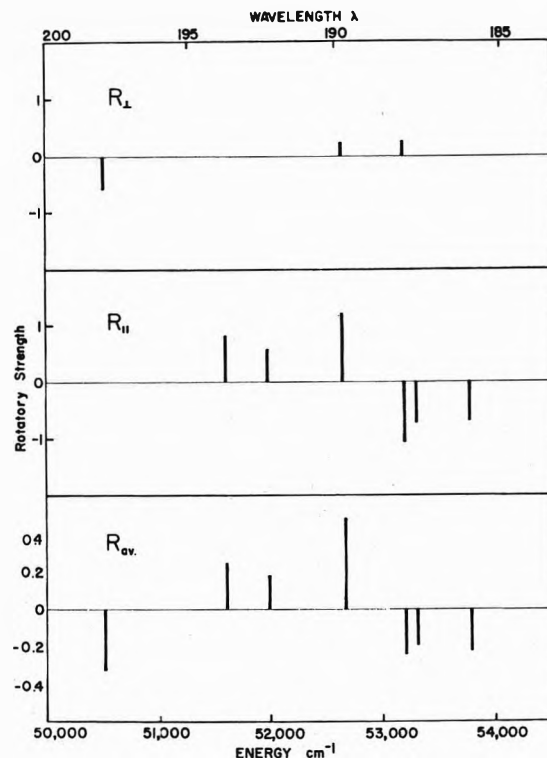


Figure 4. A real calculation of the rotatory strength of the $\pi\pi^*$ transition of an 18 unit α helix using the parameters of ref 6 and 8. The upper part of the figure represents the results for light propagated perpendicular to the helix, the middle for light parallel to the helix, and the bottom for the average over all orientations.

they are too close to be presented separately. For parallel propagation, there are now three pairs of helical bands giving rise to three positive couplets. The central couplet arises from the pair of perpendicularly polarized bands. The principal results for this model are the presence of the split Moffitt system in R_{\perp} and the appearance of helical bands in R_{\parallel} .

The figure has been simplified. With this model all levels are optically active. The eight principal bands were selected for presentation.

Real Helical Excitons. The average rotatory strength for realistic models of the α helix (and other helices) has been extensively studied, first by Woody and Tinoco and subsequently by our own group and Pysch. The results are qualitatively similar to those obtainable from the nearest neighbor interaction model¹⁹ for which there is an analytical solution. Tinoco²⁰ has made use of this analogy for predicting the qualitative features of exciton circular dichroism. The general features of exciton bands are in fact much simpler in appearance when presented as tensor components rather than average rotatory strength since the bands segregate nicely into two types. Figure 5 shows the results of a calculation utilizing the same interaction and optical parameters as in the previous section for a 72 residue α helix. With a helix this long with end effects, the predicted optical properties are a continuous function of length with no special properties to be ascribed to the reentrant situation $N = 72$. The general form of the Mof-

(18) W. Moffitt, D. Fitts, and J. Kirkwood, *Proc. Nat. Acad. Sci. U. S.*, **43**, 723 (1957).

(19) D. F. Bradley, I. Tinoco, and R. W. Woody, *Biopolymers*, **1**, 239 (1963).

(20) I. Tinoco, *J. Amer. Chem. Soc.*, **86**, 297 (1964).

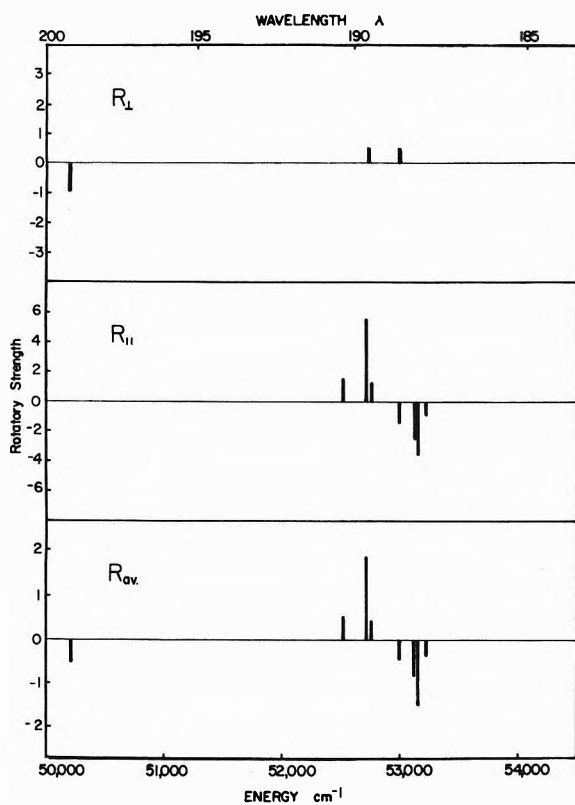


Figure 5. A real calculation of the rotatory strength of the $\pi\pi^*$ transition of a 72 unit helix using the parameters of ref 6 and 8. As in Figure 4, the graphs represent perpendicular, parallel, and average propagation, respectively.

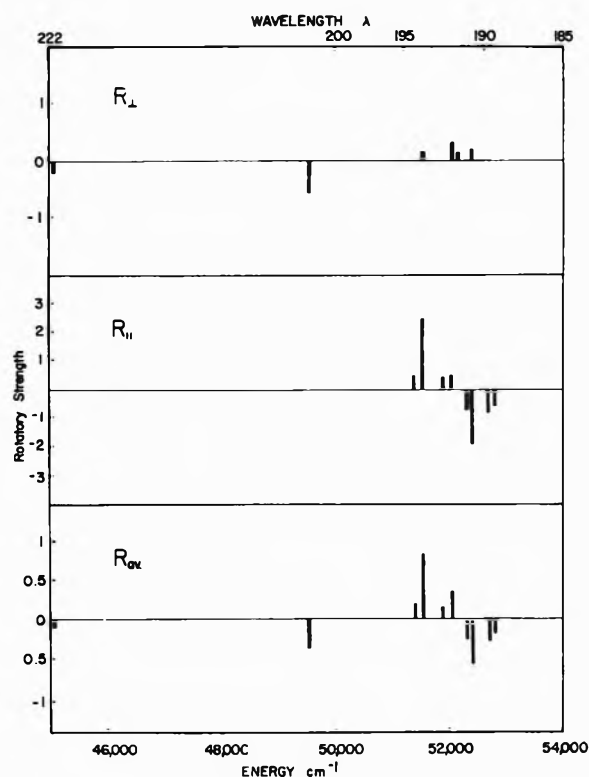


Figure 6. A real calculation of the rotatory strength of a 30 unit α helix including the interactions of the $n\pi^*$ and $\pi\pi^*$ transitions using the parameters of ref 6 and 8. As in Figure 4, the graphs represent perpendicular, parallel, and average propagation, respectively.

fit system is preserved in R_{\perp} as shown in the upper part of the figure except that the perpendicular band remains significantly split. It is doubtful that this splitting could be detected experimentally. There are no strict selection rules for this case so that there are nonvanishing rotatory strengths for all 72 transitions. The contribution of bands not shown in the figure are too small to be presented on the graph. Contributions to R_{\parallel} are shown in the middle part of the figure and to the average R at the bottom. The noteworthy feature of the figure is again the separation of the exciton circular dichroism into two classic patterns for the two modes of propagation. Since it is unlikely that the fine-grained splittings of Figure 5 would be detectable experimentally, the predicted behavior of the 72 unit helix in a disoriented solution would behave like the four-band system described by Tinoco.²⁰

Interaction with Other Absorption Bands. The calculations given above have included only the nearest $\pi\pi^*$ transition of the peptide bond. As is well known, there is an $n\pi^*$ transition of lower energy and a number of nearby transitions of higher energy of this chromophore. Since the optical parameters of the latter have not yet been well characterized, we shall concentrate our attention to the interaction of the $\pi\pi^*$ and $n\pi^*$ systems. Figure 6 shows the results of a calculation for a helix containing 30 residues which includes both bands. This calculation has been performed with the same parameters as were used in a previous publication⁸ except that the center of energy of the $\pi\pi^*$ band has been moved to 195 nm from the monomer value of 190 nm (crystal shift approximation) and the program has been altered to calculate tensor components as well as average values.

Because of the low oscillator strength of the $n\pi^*$ band, there is practically no splitting and exciton effects are neither predicted nor observed. The single $n\pi^*$ rotatory strength indicated in the figure was obtained by summing the 30 contributions.

In the discussion of the $\pi\pi^*$ transition, it was emphasized that quadrupole and magnetic contributions to the rotatory strength tensor are of necessity of the same order of magnitude. For the $n\pi^*$ transition, a somewhat different situation arises which requires discussion.

The quadrupole operator of an electron is given by

$$Q = e\mathbf{r}\mathbf{r}$$

where \mathbf{r} is the position vector of the electron and e its charge. Since in this type of calculation it is assumed that there is negligible exchange of electrons between groups, the operator is normally applied locally to a given group, say the j th group. It is then convenient to define a local origin at the "center" of the group so that the position vector may be written as $\mathbf{r}_{ij} = \mathbf{R}_j + \rho_{ij}$. \mathbf{R}_j is now the position vector of the j th group (a constant) and ρ_{ij} is the position vector of the i th electron at the j th group relative to \mathbf{R}_j as origin. The quadrupole operator may now be written

$$Q_j = e\mathbf{R}_j\mathbf{R}_j + e\sum_i(\rho_{ij}\mathbf{R}_j + \mathbf{R}_j\rho_{ij}) + e\sum_i(\rho_{ij}\rho_{ij})$$

The first quantity may be neglected in any transition matrix element because it is constant. The second term leads to expressions such as

$$(0|e\rho\mathbf{R}|a) = e\mathbf{R}(0|e\rho|a) = \mathbf{R}\mu_{0a}$$

because of the constancy of \mathbf{R} . We have called such terms

the extrinsic quadrupole contribution. It is composed of the diad products of the position vector of the group and the transition moment. This is the type of quadrupole that entered into all of the calculations given in the previous sections. The third term is the intrinsic quadrupole of the group. Probably the best way of defining the origin in a group (for a given transition) is to minimize the local quadrupole transition moment. The intrinsic quadrupoles of both the $\pi\pi^*$ and $n\pi^*$ transitions have been utilized in our calculations. The intrinsic quadrupole contributions to the $\pi\pi^*$ rotatory strength are negligibly small compared with the extrinsic contributions and for this reason were ignored in the discussion. On the other hand, the $n\pi^*$ transition has a large intrinsic quadrupole and it might be anticipated that large contributions could arise. This is not the case. The reason is, that because of the special geometry of the α helix, practically all of the quadrupole moment is contained in Q_{12} . As was shown in eq 14, this term cancels out when the helix orientation is averaged about its axis. Consequently, for the α helix, there is little difference between evaluation of the components of R with the rp diad or with the magnetic moment. Different results will presumably be obtained with helices without this special property.

Once again the simple pattern of rotatory strengths of R_{\perp} and R_{\parallel} remain though there is a considerable mixing of the two absorption bands. The tensor properties of the $n\pi^*$ band are in agreement with previous calculations of Woody and Tinoco.⁵

The predictions of Figure 6 are in qualitative agreement with circular dichroism measurements on oriented α helices performed in our laboratory by Hofrichter² and with the results of Mandel and Holzwarth.²¹ Comparison of theory and experiment will appear in a forthcoming publication.²²

Discussion

The purposes of this paper have been (1) to evaluate the relative magnitude of quadrupole contributions to the rotatory strength tensor, (2) to relate the results of the "helical" contribution to rotatory strength developed with studies of infinite helices, and (3) to supply theoretical results to aid in the interpretation of oriented CD measurements which are going on in our laboratory.

It has been shown that it is logically inconsistent to ignore quadrupole terms in the rotatory strength tensor. The necessity for the inclusion of these terms has been discussed by other authors as well^{10,11} and included in the calculations of Woody and Tinoco.⁵ These remarks apply to the extrinsic quadrupole moments discussed immediately above. For strong transitions there are intrinsic quadrupole moments and intrinsic magnetic moments but by choice of the proper origin (position) of a group, these can be made very small compared to the extrinsic quadrupoles. For weak transitions (such as the $n\pi^*$ of the peptide group) the extrinsic contributions to Q are small because of the smallness of the electric transition moment but there are usually large intrinsic quadrupoles. The manner in which these contribute depends on the geometry of the helix. For the α helix, where the axis of the quadrupole is essentially parallel to the helix axis, only Q_{12} is large and this does not contribute to the rotatory strength of a helix which can rotate freely about its axis.

The discussion of the various models for calculation has been centered about cyclic exciton theory. This can al-

ways be done. Since the cyclic excitons are related to the group excitations by a unitary transformation, they can serve equally well as a basis set for an arbitrary state of excitation. An alternative procedure for the calculation of the optical properties of an arbitrary excitation is to evaluate the optical properties of the few cyclic excitons which are of importance (closed formulas can be obtained) and then decompose the arbitrary excitation into these cyclic components

$$\psi_{\alpha} = \sum_i a_{i\alpha} \phi_i = \sum_K C_{K\alpha} \psi_K \quad C_{K\alpha} = \sum_i (a^{-1})_{Ki} a_{i\alpha}$$

where ψ_{α} is the arbitrary excitation and ψ_K the K th cyclic exciton and ϕ_i is the localized excitation.

We have tried to understand why the "helical" terms have arisen in the theory under such diverse circumstances as the general formalism of Moffitt, Fitts, and Kirkwood,¹⁸ the nearest neighbor theory of Woody, Bradley, and Tinoco,¹⁹ and the retention of the phase of the radiation for infinite helices. If the latter is excluded for the moment, the answer for short helices (compared to the wavelength of light) is to be found in the structure of the optical properties of reentrant cyclic excitons. The helical contributions are contained in this simplest of theories as two terms of equal magnitude and energy which are opposite in sign. In any real system, which does not have this idealized symmetry, the degeneracy is broken and helical bands appear. It was shown that the removal of either the reentrance or cyclic condition is sufficient to bring out the helical terms.

In the limit of infinite helices, it becomes permissible to describe the optical properties of the helix in terms of cyclic excitons. In discussing the orientational properties, some care must be taken because the rotatory strength is no longer a second rank tensor when the phase of the radiation is retained in the matrix elements.

Light Propagating Perpendicular to a Very Long Helix. For this orientation, the Rosenfeld expansion is valid and there is no significant nonlinear phase change over the molecule with plane waves. As shown by Deutsche¹² and Loxsam,¹¹ the Moffitt terms are retained as two transitions as in the original theory. This is the limit our calculations are approaching as the length is increased (top of Figure 5).

Light Propagating Parallel to a Very Long Helix. In the limit of an infinite helix, the exciton system is so fine grained that there exist excitons with wavelengths which match those of the radiation leading to special helical selection rules for the absorption of right and left circularly polarized light.^{11,12,14} Another way of stating this is that the pitch of the exciton matches the pitch of the circularly polarized light at the absorption wavelength. The pitch of an exciton is defined as the phase advance per unit translation along the helix. It is interesting to note that the helical bands were predicted by Rhodes on the bases of conservation laws for linear and angular momentum²³ long before the quantitative theories were developed. This is to be contrasted with the selection rule for short helices which requires the matching of the pitch of the exciton with the pitch of the helix.

Some idea of what is meant by a very long helix can be gleaned from the fact that an α helix must contain of the

(21) R. Mandel and G. Holzwarth, *J. Chem. Phys.*, **57**, 3469 (1972).

(22) J. Hofrichter and J. Schellman, manuscript in preparation.

(23) W. Rhodes, *J. Amer. Chem. Soc.*, **83**, 3609 (1961); W. Rhodes and D. Barnes, *J. Chim. Phys.*, **65**, 78 (1968).

order of 700 peptide units before any exciton has a wavelength long enough to match that of radiation at 200 nm. The helix would have to be orders of magnitude longer before the presence of excitons satisfying the conditions of Loxsam and Deutsche is guaranteed. This remark is true only if the electronic exciton band is regarded as a line system. The relatively broad widths of real bands presumably allows the selection rules to be satisfied for significantly shorter helices.

It is of interest that the behavior of the helical bands in the infinite limit is qualitatively the same as that for short helices in the Rosenfeld limit. Presumably as helix length is increased through the intermediate region, the short helix selection rule with the approximate matching of exciton pitch and helical pitch is collapsing while the infinite selection rule of the matching of exciton pitch and radiation pitch (for the wavelength of absorption) is gradually coming into play.

Appendix. Tensor Sum Rules

Let ϕ_i be the wave function for localized excitation on group j , and let ψ_K represent a nonlocalized eigenfunction resulting from the interaction of the groups. Because of the Hermitian character of the interaction Hamiltonian passage from the ϕ_i to the ψ_K is accomplished by a unitary transformation with matrix elements C_{jK} .

$$\psi_K = \sum_j C_{jK} \phi_j$$

Let α and μ be one-electron operators which may be components of vectors or tensors, then

$$\alpha_{OK} = \sum_j C_{jK} \alpha_{Oj}$$

when α_{Oj} is the local matrix element of the j th group which is defined because exchange between groups is neglected. Also $\beta_{KO} = \sum_i C_{iK}^* \beta_{iO}$. The product of the matrix elements is given by

$$\alpha_{OK} \otimes \beta_{KO} = \sum_j \sum_i C_{jK} C_{iK}^* \alpha_{Oj} \otimes \beta_{iO}$$

where \otimes may be an ordinary product or a dot or cross product. Summing over all excitons K , we have

$$\sum_K \alpha_{OK} \otimes \beta_{KO} = \sum_j \alpha_{Oj} \otimes \beta_{jO}$$

because C is unitary. Consequently, the sum over excitons must equal the sum over groups.

If $\alpha = \mu$ and $\beta = \mathbf{m}$ and the dot product is involved, one has the rule that the sum of the rotatory strengths of the excitons equals the sum over the groups. The latter vanishes by definition in our model since local dissymmetry has been excluded.

If $\alpha = \mu$, $\beta = \mathbf{pr}$, and a cross product is involved, we have the sum over $\sum_j \mu_{0j} \times (\mathbf{pr})_{j0}$. This has two components. If we put $\mathbf{r} = \mathbf{R}_j + \rho_j$ where \mathbf{R}_j is the (constant) position vector of the j th group, then

$$(\mu_{0j}) \times (\mathbf{pr})_{j0} = \mu_{0j} \times \mathbf{p}_{j0} \mathbf{R}_j + \mu_{0j} \times (\mathbf{p}\rho)_{j0}$$

The first part vanishes because μ_{0j} and \mathbf{p}_{j0} are parallel; the second vanishes because of the defined symmetry of the group. This applies to all nine components of the tensor.

If, however, individual matrix elements such as $(\mu_x)_{0j}$ $(m_x)_{j0}$ are involved as they are in the magnetic moment part of the rotatory strength (eq 11), we have local terms

$$(e/2mc)(\mu_x)_{0j} (Yp_z - Zp_y)_{j0}$$

Such terms depend on the definition of the coordinate axes and there is no reason for the component to vanish. A similar conclusion is to be drawn for quadrupole contributions.

In conclusion, conservation laws exist over an exciton system for the average rotatory strength and for the tensor $(\mu)_{0j} \times (\mathbf{pr})_{j0}$ but not for the tensors of the magnetic and quadrupole contributions.

Energy Parameters and Charge-Transfer Spectra of the Complexes of Bromine with Substituted Pyridines

P. Huyskens,* J. D'Hondt, F. Govaerts, and Th. Zeegers-Huyskens

Laboratory for Physical Chemistry, University of Louvain, 3030 Heverlee, Belgium (Received July 27, 1972)

Publication costs assisted by Katholieke Universiteit te Leuven and F. K. F. O. Belgium

The frequencies ν_{CT} at maximal absorption, the extinction coefficients ϵ_{max} , and the bandwidths $\Delta\nu_{1/2}$ of the charge-transfer bands were determined for complexes of bromine with several substituted pyridines. These values were compared with the force constants k_{Br-Br} and $k_{N\dots Br_2}$ previously determined by far-infrared spectrometry, with the complexation enthalpy W_N and with the pK_a of the donor. The peculiarities of the relations that exist between these experimental values can be explained in terms of the simplified resonance theory of Mulliken. From the above experimental data the weight of dative structure F_1 and the energy parameters W_{01} , W_0 , and W_1 of this theory were computed. While for all the complexes studied here W_0 and W_1 can be described by quadratic functions of F_1 , systematic positive deviations occur for W_{01} in the case of the ortho-substituted compounds. These deviations are caused by the increase in the $N\dots Br$ interdistance and are responsible for the deviations these compounds show relatively to the linear relationship of $h\nu_{CT}$ vs. F_1 observed for the other complexes. When W_0 and W_1 are plotted vs. pK_a , the ortho-substituted compounds also show significant deviations. The observed positive deviations of the complexation enthalpy W_N vs. pK_a for these compounds are the consequence of the fact that the positive deviations of W_1 , caused by the increasing of $N\dots Br$ interdistance and by an additional repulsion between the ortho-methyl group and the Br^- ion, are not completely compensated by the decreasing of W_0 . The transition moment μ_{CT} is roughly proportional to the weight of dative structure: $\mu_{CT} \approx 17F_1$.

The complexes of bromine with several substituted pyridines were previously studied in our laboratory by means of various experimental techniques: far-infrared¹ and visible spectrometry,² determination of dipole moments,¹ and adiabatic calorimetry.³ From these studies it was possible to show the existence of a linear relationship between the logarithm of the complexation constants and the weight of dative structure in the complex. A similar relationship holds for the complexation enthalpy.

In this work, the charge-transfer bands of these complexes that appear in the ultraviolet region are studied. The characteristics of these bands are then compared with the previous experimental data and the peculiarities are explained in terms of the simplified resonance theory of Mulliken.⁴

Characteristics of the Charge-Transfer Bands

The ultraviolet spectrum was studied in the region between 210 and 300 $m\mu$ where the charge-transfer bands appear. The solvent was 1,2-dichloroethane and the temperature was 25°. At a given wavelength, the absorbance A of the ternary solutions can be related to the formal concentrations C_D^0 and C_A^0 of the donor and of the acceptor, and to the real concentration of the complex C_K through the expression

$$A = [\epsilon_D(C_D^0 - C_K) + \epsilon_A(C_A^0 - C_K) + \epsilon_K C_K]d \quad (1)$$

where d is the cell thickness (0.025 cm) and ϵ_D , ϵ_A , and ϵ_K are the molar extinction coefficients of the free donor, the free acceptor, and the complex.

The reference cell was filled with a solution of the same concentration C_D^0 of the donor. The value of ϵ_K is then found from the difference in absorbance $A - A^0$ between the two cells, using the expression

$$\epsilon_K = \frac{1}{C_K} \left[\frac{A - A^0}{d} \right] + \epsilon_D + \epsilon_A \left(1 - \frac{C_A^0}{C_K} \right) \quad (2)$$

The concentration of the complex is computed from the values of the formal concentrations, using the complexation constants determined in the previous work.

In our determinations C_A^0 and C_D^0 are of the order of 10^{-3} mol l.⁻¹. Equation 1 assumes that only 1:1 complexes are present in the solution. In a previous work,² it was shown by the method of Briegleb-Liptay, by this method of continuous variations and by the method of the isosbestic points, that under the circumstances of our experiments, the appearance of higher complexes is negligible.

It is then possible to determine the wavelength, where ϵ_K is maximal (ϵ_{max}), and also the bandwidth $\Delta\nu_{1/2}$. The transition moment μ_{CT} was then computed using the empirical equation of Tsubomura and Lang.⁵

$$\mu_{CT} = 0.0958 \left[\frac{\epsilon_{max} \Delta\nu_{1/2}}{\nu_{max}} \right]^{1/2} \quad (3)$$

In Table I, the experimental values determined in this work are shown against the other characteristics of the complexes which were determined in the previous works: k_{Br-Br} , the Br-Br stretch force constant (directly related to the weight of dative structure), $k_{N\dots Br}$, the force constant of the vibration associated with the charge-transfer

- (1) J. D'Hondt and Th. Zeegers-Huyskens, *J. Mol. Struct.*, **10**, 135 (1971).
- (2) J. D'Hondt, C. Dorval, and Th. Zeegers-Huyskens, *J. Chim. Phys.*, **68**, 516 (1972).
- (3) B. Tilquin and L. Lamberts, *Z. Phys. Chem.*, in press.
- (4) R. S. Mulliken and W. B. Person, "Molecular Complexes," Wiley-Interscience, London, 1969.
- (5) H. Tsubomura and R. Lang, *J. Amer. Chem. Soc.*, **83**, 2085 (1961).

bond, and W_N , the enthalpy of the bond. In this table we also give the pK_a value of the donor taken from the literature.⁶ The complexes are classified by decreasing k_{Br-Br} force constant, and thus increasing weight of dative structure.

Comparison between the Direct Experimental Data

The comparison of the experimental data in Table I brings some interesting peculiarities to light. For all the complexes studied here which do not bear substituents in the ortho position, one observes the following relationships between $k_{N...Br}$, W_N , pK_a , $h\nu_{CT}$, and k_{Br-Br}

$$W_N = 1.38 - 0.61k_{Br-Br} \quad (\text{max dev } 0.01 \text{ eV}) \quad (4)$$

$$h\nu_{CT} = 5.50 - 0.049pK_a \quad (\text{max dev } 0.025 \text{ eV}) \quad (5)$$

$$W_N = -0.22 - 0.045pK_a \quad (\text{max dev } 0.015 \text{ eV}) \quad (6)$$

$$h\nu_{CT} = 4.34 + 0.67k_{Br-Br} \quad (\text{max dev } 0.025 \text{ eV}) \quad (7)$$

$$k_{N...Br} = 2.43 - 1.92k_{Br-Br} \quad (\text{max dev } 0.02 \text{ m dyn } \text{\AA}^{-1}) \quad (8)$$

It must be noted here that these analytical expressions hold only for the studied range of the variables (see Table I) and that these quantities do not necessarily exhibit linear relationships in the whole range of values. It appears that, within the same limits, eq 4 and 5 also hold for the ortho-substituted complexes. This is not the case, however, for expressions 6 and 7: the ortho-disubstituted compounds show W_N values that are 0.06–0.09 eV too high and $h\nu_{CT}$ values that are 0.05–0.09 too low. For the ortho-substituted compounds the deviations are of the order of 0.03 eV.

Significant negative deviations also occur for the ortho-disubstituted complexes for eq 8. These peculiarities can be explained in terms of the simplified resonance theory of Mulliken.⁴ On the other hand, the data in Table I show the existence of a rough linear relationship between the transition moment μ_{CT} and W_N . This relation can be written

$$\mu_{CT} \sim -16W_N \quad (9)$$

Determination of the Parameters of the Simplified Mulliken Theory

The wave function ψ_N of the complex in the ground state is considered as a combination of only two resonance structures: the no-bond wave function ψ_0 with the energy W_0 , and the dative function ψ_1 with the energy W_1

$$\psi_N = a\psi_0 + b\psi_1 \quad (10)$$

The fraction in dative structure F_1 is given by

$$F_1 = \frac{b^2}{b^2 + abS_{01}} \quad (11)$$

where S_{01} is the overlap integral. It can be expected that this integral does not differ appreciably for the various complexes studied here. We assumed therefore in all cases that S_{01} was equal to 0.3, a value generally admitted for this kind of complexes.⁴

Following a method presented by Person,⁷ F_1 can be computed from the force constants of the Br-Br stretching vibration respectively in the complex (k_{Br-Br}) and in the free molecule (k_{Br-Br}^0) by means of the equation

$$F_1 = \left(\frac{k_{Br-Br}^0 - k_{Br-Br}}{k_{Br-Br}^0} \right) \left(\frac{1}{1 - (k_{Br-Br}^0/k_{Br-Br})} \right) \quad (12)$$

k_{Br-Br}^0 is the force constant in the Br_2^- ion. We calcu-

lated F_1 from k_{Br-Br} using the value of 2.29 m dyn \AA^{-1} for k_{Br-Br}^0 and 0.25 for the ratio k_{Br-Br}^0/k_{Br-Br} . From F_1 it is then possible to calculate the coefficients a and b , using eq 10 and taking normalizing requirements into account.

According to the simplified resonance theory of Mulliken, the bond energy W_N and $h\nu_{CT}$ are related by the expression

$$-W_N = \frac{1}{2}h\nu_{CT} + \frac{1}{1 - S_{01}^2} \left(W_{01}S_{01} - \frac{W_0 + W_1}{2} \right) \quad (13)$$

where W_{01} is the integral.

$$W_{01} \equiv \int_0^\infty \psi_0 H \psi_1 \, d\tau \quad (14)$$

W_{01} , W_0 , and W_1 can be calculated from the coefficients a and b and from the experimental values of W_N and $h\nu_{CT}$, using the following equations derived from the basic expressions of the theory of Mulliken (ref 4, p 12).

$$W_{01} = W_N S_{01} - \left[\frac{\frac{1}{2}h\nu_{CT}(1 - S_{01}^2)}{S_{01} + \frac{1}{2}\left(\frac{b}{a} + \frac{a}{b}\right)} \right] \quad (15)$$

$$W_0 = W_N + \frac{b}{a} \left[\frac{\frac{1}{2}h\nu_{CT}(1 - S_{01}^2)}{S_{01} + \frac{1}{2}\left(\frac{b}{a} + \frac{a}{b}\right)} \right] \quad (16)$$

$$W_1 = W_N + \frac{a}{b} \left[\frac{\frac{1}{2}h\nu_{CT}(1 - S_{01}^2)}{S_{01} + \frac{1}{2}\left(\frac{b}{a} + \frac{a}{b}\right)} \right] \quad (17)$$

In Table II we give the values of these energy parameters with those of F_1 , a , and b for the various complexes studied in this work.

Discussion of the Results

It is interesting to consider the evolution of the various parameters with increasing weight of dative structure. The complexes which do not bear ortho substituents obey within 0.01 eV the relation

$$W_{01} = -1.59 - 0.90F_1 \quad (18)$$

Again, this linear relation only holds for the studied range of F_1 .

The ortho-substituted complexes and the ortho-disubstituted complexes show values that are systematically higher by a few hundredths of an electron volt. These deviations are responsible for the deviations in the $h\nu_{CT} - k_{Br-Br}$ relations. As a matter of fact, $h\nu_{CT}$ is very sensitive to variations in W_{01} , according to the Mulliken equation

$$h\nu_{CT} = \frac{2\sqrt{\left(\frac{W_0 - W_1}{2}\right)^2 + (W_{01} - W_0S)(W_{01} - W_1S)}}{(1 - S_{01}^2)} \quad (19)$$

If we recalculate $h\nu_{CT}$ from this expression replacing only the experimental value of W_{01} by that of expression 18, the deviations of the ortho-substituted complexes in the $h\nu_{CT} - k_{Br-Br}$ relations disappear. The reason for the effect of ortho substitution on W_{01} must be sought in an increase in the interdistance N-Br caused by the steric hindrance of the ortho substituent. This increase in the inter-

(6) D. D. Perrin, "Dissociation Constants of Organic Bases in Aqueous Solutions," Butterworths, London, 1965.

(7) H. B. Friedrich and W. B. Person, *J. Chem. Phys.*, **44**, 2161 (1966).

TABLE I: Experimental Characteristics of Bromine-Substituted Pyridine Complexes

Substituent of pyridine	$k_{\text{Br}-\text{Br}}^{\text{a}}$ mdyn Å ⁻¹	$k_{\text{N}-\text{Br}}^{\text{a}}$ mdyn Å ⁻¹	W_{N}^{b} eV	ρK_{a} donor ^c	λ_{max} , Å	$h\nu_{\text{CT}}$, eV	$\Delta\bar{\nu}_{1/2}$, cm ⁻¹	ϵ_{max} , l. mol ⁻¹ cm ⁻¹	μ_{CT} , D
3-Cl	1.70	0.38		2.84					
3-Br	1.67	0.40	-0.35	2.84	2270	5.46		39480	
3-I	1.62	0.46		3.25					
2,6-Me ₂	1.54	0.42	-0.43	6.60	2340	5.28		37600	
2-Me	1.52	0.49		5.96	2330	5.32	6740	39420	7.5
2-Et	1.51	0.16	-0.46	5.89	2340	5.30	7010	37600	7.5
	1.50	0.48	-0.45	5.22	2310	5.37	6580	36150	7.1
3-Et	1.49	0.50	-0.48	5.56	2331	5.32	6500	42900	7.7
3-Me	1.48	0.49	-0.47	5.63	2327	5.33	6320	43920	7.7
4-Me	1.45	0.48	-0.49	5.98	2339	5.30	7220	38240	7.7
4-Et	1.45	0.51	-0.49	5.87	2341	5.30	6410	44200	7.8
2,5-Me ₂	1.44	0.52		6.40	2355	5.27			
4- <i>t</i> -C ₄ H ₉	1.43	0.51		5.99					
3,5-Me ₂	1.42	0.51	-0.51	6.15	2341	5.30		46090	
3,4-Me ₂				6.16	2362	5.26			
2,4-Me ₂	1.42	0.51	-0.51	6.63	2359	5.26	6550	45680	8.1
2,4,6-Me ₃	1.41	0.44	-0.50	7.43	2372	5.23	7410	35800	7.6

^a Reference 1. ^b Reference 3. ^c Reference 6.

TABLE II: Parameters of the Simplified Mulliken Theory for Pyridine-Bromine Complexes (Energy Terms in eV)

Substituent of pyridine	F_1	a	b	W_{01}	W_0	W_1
3-Br	0.338	0.745	0.481	-1.89	0.80	2.40
2,6-Me ₂	0.410	0.691	0.544	-1.94	1.00	1.87
2-Et	0.425	0.680	0.558	-1.96	1.05	1.77
None	0.430	0.675	0.562	-1.99	1.10	1.78
3-Et	0.435	0.671	0.567	-1.98	1.07	1.70
3-Me	0.441	0.666	0.572	-1.99	1.12	1.68
4-Me	0.458	0.654	0.586	-1.99	1.16	1.57
4-Et	0.459	0.653	0.587	-1.99	1.17	1.56
3,5-Me ₂	0.476	0.639	0.601	-2.01	1.24	1.46
2,4-Me ₂	0.476	0.639	0.601	-1.99	1.22	1.44
2,4,6-Me ₃	0.481	0.635	0.604	-1.98	1.25	1.43

distance for a given F_1 value for ortho-disubstituted complexes also explains the lowering of the $k_{\text{N}\cdots\text{Br}}$ force constant in this case.

It can be pointed out here that the extrapolated value of -2.04 eV at $F_1 = 0.5$ seems to be little dependent on the approximations made in calculating the weight of dative structure. For instance, if in eq 12 the term $k_{\text{Br}-\text{Br}}^{\text{0}}/k_{\text{Br}-\text{Br}}^{\text{0}}$ is disregarded the extrapolated value becomes -1.95 eV. If the overlap integral is 0.2 instead of 0.3 a value of -2.10 is found. It must be noted here that, under these circumstances, all the values of W_{01} of Table II will be shifted in a similar manner and that the calculated effect of ortho substituents on W_{01} will remain the same.

When the values of W_{N} in Table I are compared with those of F_1 in Table II, the data are observed to obey the following relation

$$W_{\text{N}} = -1.07F_1 \quad (\text{max dev } 0.015 \text{ eV}) \quad (20)$$

This linear relationship between the complexation enthalpy and the weight of dative structure was observed by Tilkwin³ and holds for all the complexes studied here. Although this result involves a long linear extrapolation it seems unlikely that it is the consequence of good luck. This result can be expected when the classical, non-charge-transfer forces between donor and acceptor are equal to the separate solvent-solute forces. However, as pointed out by the reviewer of this work, this result does

not exclude the possibility that experimental W_{N} values, and consequently, the calculated W_0 , W_1 , and W_{01} could involve some solvent contribution.

Owing to the fact that in the absence of charge transfer W_0 equals W_{N} , W_0 must also vanish when F_1 equals zero. However, it is not possible to fit the experimental data in Table II with a linear relation without a constant term. It is necessary to introduce a quadratic term. As a matter of fact, all the experimental points obey the relationship

$$W_0 = 1.80F_1 + 1.68F_1^2 \quad (\text{max dev } 0.02 \text{ eV}) \quad (21)$$

Let us first consider the case of the complexes without ortho substituents. Owing to the very similar neighborhood of the N \cdots Br-Br group it may be expected that the stabilizing energy W_0 , of the no-bond structure varies in the same manner with the N-Br distance for all these complexes. This means that for all the complexes without ortho substituents W_0 depends only on r . We can then write

$$\frac{dW_0}{dF_1} = \left(\frac{\delta W_0}{\delta r} \right) \frac{dr}{dF_1} \quad (22)$$

When F_1 increases the N-Br interdistance decreases, passing from the sum of van der Waals radii of the N and of the Br atom (1.5 + 1.9 = 3.4 Å) in the absence of charge transfer to an order of magnitude corresponding to

the sum of the N^+ radius and of the Br^- radius ($0.25 + 1.95 \approx 2.20 \text{ \AA}$) when the charge transfer is complete. From this point of view it is noticeable that the force constant $k_{N...Br}$, which is related to the equilibrium distance $r_{N...Br}$, is found in the previous work to be proportional to F_1 .

The variation of the slope dW_0/dF_1 when F_1 increases can then be related to the marked increase in the repulsion force ($\delta W_0/\delta r$) when the interdistance N-Br decreases.

Another noticeable point is that the ortho-substituted compounds do not show deviations from eq 21, even though owing to the deductions concerning W_{01} the N-Br interdistance must be greater for the same values of F_1 . This can be explained if the lowering of the repulsion energy between the N and the Br atom arising from the increase of the distance is somewhat compensated by a new repulsion term arising from the interaction between the ortho methyl group and the bromine atom. Owing to the fact that, for $F_1 = 0.5$, W_1 must be equal to W_0 , all the experimental values fit with the equation

$$W_1 = 5.66 - 11.65F_1 + 5.94F_1^2 \quad (\text{max dev } 0.03 \text{ eV}) \quad (23)$$

It must be noted here that this relation cannot be extrapolated to low values of F_1 .

W_1 is related to the stabilizing energy G_1 of the dative structure relative to the free ions by the expression

$$W_1 = G_1 + I_D^v - E_A^v \quad (24)$$

where I_D^v is the vertical ionization potential of the donor and E_A^v is the electron affinity of the acceptor. E_A^v depends on F_1 , passing in the gas phase from a value of -1.2 eV^8 when $F_1 = 0$ and the Br-Br interdistance is that of the neutral molecule, to a value of -2.6 eV when $F_1 = 1$ and the Br-Br interdistance is that of the Br_2^- ion. These values must be corrected when passing from the gas to the solution. However, at a given value of F_1 , the electron affinity E_A^v must show a given value, independent of the other terms of eq 24.

For ortho-substituted and -disubstituted compounds G_1 must show positive deviations: the repulsion energy of the interaction of the methyl group and Br_2^- must be taken into account (and may be more important than in the case of W_0 owing to the increase in the van der Waals radius of Br^- comparative to Br) but in addition the increase in the N...Br interdistance must here have an opposite effect relative to W_0 , reducing the attraction energy between the charges and the exothermic polarization effects to the ions upon the molecule of the partner.

If there is no marked difference in W_1 for a given value of F_1 , it must then be concluded that the reduction in G_1 is compensated by the lowering of I_D^v .

In order to obtain the same W_1 , the same weight of dative structure F_1 and the same W_N value for ortho-substituted and ortho-disubstituted complexes, the ionization potential of the donor has to be lower. This should therefore appear in the curves of F_1 vs. I_D . Unfortunately, the data of the literature concerning the ionization potentials

of pyridine and of substituted pyridines show differences of several hundredths of an electron volt. Moreover, there is some doubt in the attribution of the values to the loss of an n or π electron.⁹

On the other hand, there must exist some correlation between the ability of a base to take up a proton from water and the energy needed to lose an electron. We may therefore expect that the deviations predicted in the relations of F_1 vs. I_D should also appear in the relations of F_1 vs. the pK_a of the donor. This behavior is in fact observed where F_1 is plotted against the values of pK_a . While for nonortho-substituted complexes the relation

$$F_1 = 0.220 + 0.040pK_a \quad (\text{max dev } 0.008) \quad (25)$$

holds, the disubstituted compounds show deviations as high as 0.08 and the deviations for the monosubstituted ortho-derivatives are significant.

These deviations of F_1 vs. pK_a for ortho-substituted compounds produce deviations in W_0 , W_1 , and W_{01} . However, the deviations of W_{01} compensate these of W_0 and W_1 in expression 19 in such a manner that eq 5 still retains its validity in the same case of ortho-substituted compounds.

In expression 13 the positive deviations of ortho-substituted complexes of W_1 for a given pK_a value are not compensated by the negative deviations of W_0 (and to a smaller extent by the deviations of W_{01}) so that the complexation energy for these complexes remains lower.

It can consequently be concluded that the deviations of W_N vs. pK_a for the ortho-substituted complexes are due to the increase in the energy W_1 of the dative structure brought about by the additive repulsion between the acceptor and the methyl group and by the increase in the N^+-Br^- interdistance that is not entirely compensated by the decrease in the energy W_0 of the no-bond structure.

Owing to eq 20, expression 9 can be written

$$\mu_{CT} \sim 17.1 F_1 \quad (26)$$

The transition moment is proportional to the weight of dative structure.

Experimental Section

The spectroscopic measurements were made with the Unicam SP 700 spectrophotometer, with a monochromator held at constant temperature.

Pyridine and its methyl and ethyl derivatives were Fluka purissimum products. 3-Bromopyridine was a Reilly purum product. These compounds were distilled before using. Bromine was a Fluka purissimum product. The solvent CH_2Cl-CH_2Cl was a Merck purissimum product.

Acknowledgment. The authors are indebted to the Instituut voor Aanmoediging van het Wetenschappelijk onderzoek in de Nijverheid en in de Landbouw and to the Fonds voor Kollektief Fundamenteel Onderzoek for their financial support for this work.

(8) W. B. Person, *J. Chem. Phys.*, **38**, 109 (1963).

(9) D. W. Turner, "Molecular Photoelectron Spectroscopy," Wiley-Interscience, London, 1970, p 324.

Vibrational Transitions in Atom + Diatomic Systems. Use of the Lennard-Jones Potential^{1a}

Hyung Kyu Shin

Department of Chemistry,^{1b} University of Nevada, Reno, Nevada 89507 (Received December 11, 1972)

Publication costs assisted by the U.S. Air Force Office of Scientific Research

An analytic expression for the vibrational transition probability has been formulated by use of the perturbing force derived from the Lennard-Jones potential for which potential parameters are obtained from crossed-beam experiments. The dependences of the probabilities on collision velocity, orientation angle, attractive forces, impact parameter, and temperature are shown in detail. Numerical results of the transition probabilities ($0 \rightarrow 1$, $0 \rightarrow 2$, $0 \rightarrow 3$, $1 \rightarrow 2$, $1 \rightarrow 3$, $2 \rightarrow 3$) for $N_2 + Ar$ show a complicated structured dependence on collisions velocity in the range of 4×10^5 to 4×10^6 cm/sec. All transitions under consideration are quite effective in the velocity range. The temperature dependence of the deexcitation probability $P_{10}(T)$ is also discussed; it is shown that $\log P_{10}(T)$ varies almost linearly with $T^{-7/19}$, particularly at higher temperatures.

I. Introduction

In developing a theory of molecular energy transfer we often encounter serious difficulties connected with the form of the interaction potential energies when the colliding molecules are interacting at short range and also with the mathematical treatment of the translational motion.²⁻⁴ Some of the potentials frequently used in the theory are described in terms of powers of the separation r between the centers of mass of the colliding particles; of these the Lennard-Jones (12-6) function is most commonly used.^{2b,4-8} Probably this function is the most realistic two-parameter potential. Sometimes, exponential potentials are used to calculate transition probabilities, but the potential parameters are usually determined by fitting such potentials to the Lennard-Jones (LJ) function.^{2a,7a} The quantitative knowledge that is available on the LJ potential has been derived from a knowledge of macroscopic properties of the gas, such as the viscosity and the second virial coefficient; *i.e.*, the knowledge obtained from the properties depends on the behavior of a gas in near-equilibrium.⁹ Therefore, use of such knowledge to calculate transition probabilities or collision cross sections is unsatisfactory since we are now interested in the properties of a gas in short range which is far removed from equilibrium. In recent years, important progress, however, has been made in determining intermolecular potentials from molecular beam experiments.¹⁰⁻¹² Tully and Lee¹¹ have determined the potential parameters for the LJ (20-6), (12-6), and (8-6) functions from crossed-beam experiments for $N_2 + Ar$, $N_2 + Kr$, $O_2 + Ar$, and $O_2 + Kr$ systems. High-velocity beam scattering experiments by Colgate, *et al.*, reveal that simpler potentials of the form K/r^s , where K and s are the potential parameters, are appropriate for $O_2 + Ar$, $N_2 + Ar$, and $CO + Ar$. The LJ functions contain the effect of molecular attraction, while the latter forms do not. It should be mentioned that with the advent of large memory high-speed computers, accurate *a priori* interaction potentials have become available for simple molecular systems.¹³⁻¹⁵

In this paper we use the LJ (12-6) potential for which potential parameters are obtained from crossed-beam ex-

periment¹¹ to derive an analytical expression for the vibrational transition probability of atom + diatomic system, which provides a framework for discussing the dependences of vibrational transitions on collision velocity, orientation angle, attractive forces, impact parameter, and temperature. For this purpose, we start with analysis of the dynamics of an encounter of the colliding system, from which we determine the collision trajectory and collision time. The formulation will be applied to $N_2 + Ar$; application to other collision systems, such as $N_2 + Kr$, is straightforward.

II. Atom + Diatomic Interaction

A. Development of the Overall Interaction Potential. In the interaction of rare gas atoms with the homonuclear diatomic molecules such as N_2 and O_2 the anisotropy of the interaction potential is not strong so that the angular locations of the rainbow extrema can provide information on the potential. From differential cross section measurements of $N_2 + Ar$, $N_2 + Kr$, $O_2 + Ar$, and $O_2 + Kr$, Tully and Lee¹¹ have obtained potential parameters for various

- (1) (a) This work was supported by the U. S. Air Force Office of Scientific Research, Grant AFOSR-72-2231. (b) Theoretical Chemistry Group Contribution No. 1043.
- (2) (a) K. F. Herzfeld and T. A. Litovitz, "Absorption and Dispersion of Ultrasonic Waves," Academic Press, New York, N. Y., 1959, Chapter VII; (b) T. L. Cottrell and J. C. McCoubrey, "Molecular Energy Transfer in Gases," Butterworths, London, 1961, Chapter 6.
- (3) K. Takayanagi, *Progr. Theoret. Phys.*, **25**, 1 (1963); *Advan. At. Mol. Phys.*, **1**, 149 (1965).
- (4) D. Rapp and T. Kassal, *Chem. Rev.*, **69**, 61 (1969).
- (5) B. Widom and S. H. Bauer, *J. Chem. Phys.*, **21**, 1670 (1953).
- (6) E. E. Nikitin, *Opt. Spektrosk.*, **6**, 141 (1959); *Opt. Spectrosc. (USSR)*, **6**, 93 (1959).
- (7) (a) H. Shin, *J. Chem. Phys.*, **41**, 2864 (1964); (b) **42**, 59 (1965).
- (8) B. Hartmann and Z. I. Sawsky, *J. Chem. Phys.*, **47**, 2491 (1967).
- (9) J. O. Hirschfelder, C. F. Curtiss, and R. B. Bird, "Molecular Theory of Gases and Liquids," Wiley, New York, N. Y., 1967.
- (10) S. O. Colgate, J. E. Jordan, I. Amdur, and E. A. Mason, *J. Chem. Phys.*, **51**, 968 (1969).
- (11) E. P. Tully and Y. T. Lee, *J. Chem. Phys.*, **57**, 866 (1972); also see references therein.
- (12) For earlier work, see E. A. Mason and J. T. Vanderslice in "Atomic and Molecular Processes," D. R. Bates, Ed., Academic Press, New York, N. Y., 1962, pp 663-695.
- (13) M. Krauss and F. H. Mies, *J. Chem. Phys.*, **42**, 2703 (1965).
- (14) M. D. Gordon and D. Secrest, *J. Chem. Phys.*, **52**, 120 (1970).
- (15) W. A. Lester, *J. Chem. Phys.*, **53**, 1511, 1611 (1970); **54**, e171 (1971).

forms of the LJ potential; they have found that the LJ (20-6) and (12-6) potentials give best agreement to the angular locations of the rainbow extrema. However, the experimental data provide information only on the spherically symmetric portion of the overall interaction potential; i.e., the potential is a function only of r , $U(r)$. This potential can be used to determine the collision time and/or the collision trajectory of the relative motion. In studying molecular energy transfer problems, in addition to the r dependence, we also need to know the dependence of the interaction energy on the vibrational coordinate(s) and the orientation angle(s). As far as these additional dependences are concerned, it seems that at present we cannot hope for any information from scattering measurements; precise information concerning the angle dependence of the potential can be obtained if rotational energy transfer is measured as a function of angle. On the other hand, from the knowledge of $U(r)$ obtained from scattering experiments, with some reasonably reliable procedures, we can construct a form of the potential, which is appropriate for the study of vibrational transitions. For this purpose, we take the LJ (12-6) potential to represent the spherically symmetric portion of the overall interaction

$$U(r) = 4D[(\sigma/r)^{12} - (\sigma/r)^6] \quad (2.1)$$

It should be pointed out that the method which will be developed below for the derivation of vibrational transition probability is applicable to any power of r including fractional values.

To derive the perturbing force for the atom + diatomic system, we express the overall potential energy as the sum of two atom-atom interactions. Using the procedure shown in ref 16, we obtain the overall energy as

$$\begin{aligned} U(r, \theta, x) = & 4D \left[\left(\frac{\sigma}{r}\right)^{12} - \left(\frac{\sigma}{r}\right)^6 \right] + \\ & 4D \left\{ \left(\frac{\sigma}{r}\right)^{12} \left[\left(21 \cos^2 \theta - \frac{3}{2}\right) \left(\frac{d+x}{r}\right)^2 + \right. \right. \\ & \left. \left(126 \cos^4 \theta - \frac{81}{2} \cos^2 \theta + \frac{21}{16}\right) \left(\frac{d+x}{r}\right)^4 \right] - \\ & \left(\frac{\sigma}{r}\right)^6 \left[\left(6 \cos^2 \theta - \frac{3}{4}\right) \left(\frac{d+x}{r}\right)^2 + \right. \\ & \left. \left(15 \cos^4 \theta - \frac{15}{2} \cos^2 \theta + \frac{3}{8}\right) \left(\frac{d+x}{r}\right)^4 \right] \left. \right\} \\ \equiv & U(r) + V(r, \theta, x) \quad (2.2) \end{aligned}$$

where d is the equilibrium bond distance of the molecule, x is the displacement of the bond distance from the equilibrium value, and θ is the angle between the r and the internuclear axis of the molecule. Unlike the potential function given in ref 16, eq 2.2 is obtained by including all terms up to the fourth order in $(d+x)/r$ which can make a significant contribution to the overall value of transition probabilities. The second term $V(r, \theta, x)$ of eq 2.2 represents the perturbation energy that is responsible for vibrational transitions. Since the molecule is homonuclear, the angle dependence in the perturbation energy always appears as even powers of $\cos \theta$, and it is seen that the anisotropy of the perturbation energy is important. We now propose eq 2.2 to represent the overall interaction potential of the atom + diatomic systems $N_2 + Ar$, $N_2 + Kr$, $O_2 + Ar$, and $O_2 + Kr$.

B. Perturbing Force. To derive the perturbing force in a form which can facilitate the explicit formulation of vibrational transition probabilities, we transform the perturbation energy $V(r, \theta, x)$ into the form $-F(r, \theta)x$, where $F(r, \theta)$ is the orientation-dependent perturbing force which acts on the molecule to cause vibrational transitions. The force can be derived by expanding $V(r, \theta, x)$ in a power series of x/d and taking the terms that are linear in x/d . The result is

$$\begin{aligned} F(r, \theta) = & -4D \left[\left(\frac{2d}{\sigma^2}\right) \left(21 \cos^2 \theta - \frac{3}{2}\right) \left(\frac{\sigma}{r}\right)^{14} + \right. \\ & \left. \left(\frac{4d^3}{\sigma^4}\right) \left(126 \cos^4 \theta - \frac{81}{2} \cos^2 \theta + \frac{21}{16}\right) \left(\frac{\sigma}{r}\right)^{16} - \right. \\ & \left. \left(\frac{2d}{\sigma^2}\right) \left(6 \cos^2 \theta - \frac{3}{4}\right) \left(\frac{\sigma}{r}\right)^8 - \right. \\ & \left. \left(\frac{4d^3}{\sigma^4}\right) \left(15 \cos^4 \theta - \frac{15}{2} \cos^2 \theta + \frac{3}{8}\right) \left(\frac{\sigma}{r}\right)^{10} \right] \\ \equiv & -4D[f_1(\theta)(\sigma/r)^{14} + f_2(\theta)(\sigma/r)^{16} - \\ & g_1(\theta)(\sigma/r)^8 - g_2(\theta)(\sigma/r)^{10}] \quad (2.3) \end{aligned}$$

Then, our immediate problem is the following: an oscillator in a definite, steady state has applied to it at time t a perturbing force, $F(r, \theta)$, to find the subsequent behavior of the oscillator. The next section is devoted to this problem.

III. Vibrational Transition Probability

A. Perturbed Wave Function. In this section we shall derive the expression for vibrational transition probabilities as a function of the collision velocity, impact parameter, and molecular orientation angle. For this purpose we solve the time-dependent Schrödinger equation for the perturbed oscillator

$$i\hbar \frac{\partial \psi(x, t)}{\partial t} = \left[\frac{p^2}{2M} + \frac{1}{2} M \omega^2 x^2 - F(t)x \right] \psi(x, t) \equiv H\psi(x, t) \quad (3.1)$$

where M and ω are the reduced mass and vibrational frequency ($2\pi\nu$) of the oscillator, respectively, and the perturbing force is parameterized in time. In this equation, the position variable x and the momentum p are connected by the commutation relation $[x, p] = i\hbar$. To facilitate the solution of eq 3.1 we introduce the operators¹⁷ \mathbf{a}^+ and \mathbf{a} which are related to these two variables as

$$x = \left(\frac{\hbar}{2M\omega}\right)^{1/2} (\mathbf{a}^+ + \mathbf{a}); \quad p = i \left(\frac{M\hbar\omega}{2}\right)^{1/2} (\mathbf{a}^+ - \mathbf{a}) \quad (3.2)$$

where \mathbf{a} and \mathbf{a}^+ are hermitian conjugates of each other satisfying the relation $[\mathbf{a}, \mathbf{a}^+] = 1$. In terms of these operators, we can express the Hamiltonian as

$$H = \hbar\omega \left(N + \frac{1}{2}\right) - F(t)(\hbar/2M\omega)^{1/2}(\mathbf{a} + \mathbf{a}^+) \quad (3.3)$$

where we put $\mathbf{N} = \mathbf{a}^+ \mathbf{a}$.

We look for a solution of the Schrödinger equation in the form¹⁸

(16) H. Shin, *J. Phys. Chem.*, **73**, 4321 (1969).

(17) A. Messiah, "Quantum Mechanics," Vol. 1, North-Holland, Amsterdam, 1968, Chapter 12.

(18) I. I. Goldman and V. D. Krivchenkov, "Problems in Quantum Mechanics," Addison-Wesley, Reading, Mass., 1961, p 103.

$$\psi(x, t) = c(t) \exp[f(t)\mathbf{a}^+] \exp[g(t)\mathbf{a}] \exp[h(t)\mathbf{N}] \psi_k(x, -\infty) \quad (3.4)$$

where ψ_k is the wave function for the initial state, and $c(t)$, $f(t)$, $g(t)$, and $h(t)$ are functions of time to be determined. Equation 3.4 may be transformed into a form which is some linear combination of the unperturbed oscillator wave functions with expansion coefficients being determined by the nature of the perturbation. To obtain the perturbed wave function, we note the following well-known recursion relations¹⁷

$$\begin{aligned} \mathbf{a}^+ \psi_k &= (k+1)^{1/2} \psi_{k+1}; \quad \mathbf{a} \psi_0 = 0 \\ \mathbf{a} \psi_k &= k^{1/2} \psi_{k-1}; \quad (k \neq 0); \quad \mathbf{N} \psi_k = k \psi_k \end{aligned} \quad (3.5)$$

Performing the first exponential operation of ψ_k in eq 3.4 we obtain

$$\exp[h(t)\mathbf{N}] \psi_k = \left\{ 1 + h(t)\mathbf{N} + \frac{1}{2} [h(t)]^2 \mathbf{N} + \dots \right\} \psi_k = \exp[kh(t)] \psi_k \quad (3.6)$$

Then, two subsequent operations by $\exp[g(t)\mathbf{a}]$ and $\exp[f(t)\mathbf{a}^+]$ give the wave function in the form

$$\psi(x, t) = (k!)^{1/2} c(t) \exp[kh(t)] \sum_{l=0}^k \sum_{r=0}^{\infty} \times \frac{[(k-l+r)!]^{1/2}}{l!(k-l)!r!} [g(t)]^l [f(t)]^r \psi_{k-l+r}(x) \quad (3.7)$$

Once the time-dependent function $\psi(x, t)$ is explicitly determined, an analytic expression of the vibrational transition probability ($k \rightarrow n$) at $t = +\infty$ can be obtained from the integral representation

$$P_{kn} = \lim_{t \rightarrow \infty} \left| \int_{-\infty}^{\infty} \psi_n^*(x) \psi(x, t) dx \right|^2 \quad (3.8)$$

On the basis of the orthogonality relation

$$\int_{-\infty}^{\infty} \psi_n^*(x) \psi_m(x) dx = \delta_{nm}$$

we then obtain the transition probability, from eq 3.7 and 3.8, as

$$P_{kn} = k!n! \lim_{t \rightarrow \infty} \left| c(t) \exp[kh(t)] \sum_{l=0}^k \frac{[g(t)]^l [f(t)]^{n-k+l}}{l!(k-l)!(n-k+l)!} \right|^2 \quad (3.9)$$

Note that the orthogonality requires $n = m = k - l + r$ for the nonvanishing term and that r in eq 3.7 is replaced by $n - k + l$.

B. Amount of Vibrational Energy Transfer. By substituting eq 3.2-3.4 in the Schrödinger equation, and by equating the coefficients of the same operators on the right- and left-hand sides, we can readily find the differential equations^{16, 18} which eventually gives the solutions

$$h(t) = -i\omega t \quad (3.10)$$

$$f(t) = \frac{i \exp(-i\omega t)}{(2M\hbar\omega)^{1/2}} \int_{-\infty}^t F(t') \exp(i\omega t') dt' \quad (3.11)$$

$$c(t) = \exp \left[-\frac{i\omega t}{2} - \frac{1}{2M\hbar\omega} \int_{-\infty}^t \times F(t') \exp(-i\omega t') dt' \int_{-\infty}^{t'} F(t'') \exp(i\omega t'') dt'' \right] \quad (3.12)$$

The solution $g(t)$ is the negative value of the complex con-

jugate of $f(t)$. Therefore, the limiting quantities appearing in the transition probability are

$$\lim_{t \rightarrow \infty} |f(t)|^2 = \frac{1}{2M\hbar\omega} \left| \int_{-\infty}^{\infty} F(t) \exp(i\omega t) dt \right|^2 \quad (3.13)$$

$$\lim_{t \rightarrow \infty} |c(t)|^2 = \left[-\frac{1}{2M\hbar\omega} \left| \int_{-\infty}^{\infty} F(t) \exp(i\omega t) dt \right|^2 \right] \quad (3.14)$$

In these expressions, the limiting integral $[\int_{-\infty}^{\infty} F(t) \exp(i\omega t) dt]$ is real because $F(t)$ is an even function of t . It is then important to recognize that the quantity $\lim_{t \rightarrow \infty} |f(t)|^2$ is the magnitude of vibrational energy transfer measured in units of $\hbar\omega$; i.e., $\Delta E/\hbar\omega$. By denoting this quantity simply by ϵ and by using the relation $g(t) = -f^*(t)$, we finally write the transition probability as

$$P_{kn} = k!n! \epsilon^{|n-k|} \exp(-\epsilon) \left| \sum_{l=0}^k \frac{(-1)^l \epsilon^l}{l!(k-l)!(|n-k|+l)!} \right|^2 \quad (3.15)$$

The amount of vibrational energy transfer which appears in eq 3.16 is a function of v , θ , and b , and takes the form

$$\Delta E = \frac{1}{2M} \left| \int_{-\infty}^{\infty} F[r(t), \theta] \exp(i\omega t) dt \right|^2 \quad (3.16)$$

in which the time-dependent perturbing force is obtained by parameterizing r in time t . Substitution of eq 2.3 in this expression gives

$$\begin{aligned} \Delta E &= \frac{8D^2}{M} \left| f_1(\theta) \int_{-\infty}^{\infty} \left[\frac{\sigma}{r(t)} \right]^{14} \exp(i\omega t) dt + \right. \\ & f_2(\theta) \int_{-\infty}^{\infty} \left[\frac{\sigma}{r(t)} \right]^{16} \exp(i\omega t) dt - \\ & g_1(\theta) \int_{-\infty}^{\infty} \left[\frac{\sigma}{r(t)} \right]^8 \exp(i\omega t) dt - \\ & \left. g_2(\theta) \int_{-\infty}^{\infty} \left[\frac{\sigma}{r(t)} \right]^{10} \exp(i\omega t) dt \right|^2 \quad (3.17) \end{aligned}$$

which contains the integrals of the type

$$I_n = \int_{-\infty}^{\infty} \frac{\exp(i\omega t)}{[r(t)]^n} dt \quad (3.18)$$

We would now like an explicit expression for ΔE in order to calculate transition probabilities. A standard treatment of the dynamics of an encounter starts with the determination of the trajectory $r(t)$ from the equation of motion. We find it convenient to write the equation of motion in the form

$$t = \left(\frac{\mu}{2} \right)^{1/2} \int_{r^*}^r \frac{dr}{\left[E - E \left(\frac{b}{r} \right)^2 - U(r) \right]^{1/2}} \quad (3.19)$$

where the centrifugal energy term is represented by $E(b/r)^2$, b being the impact parameter, μ is the reduced mass of the collision system, and r^* is the distance of closest approach. Using the procedure presented in ref 16, we derive the trajectory $r(t)$ in the form

$$t = i\tau - i(\mu/2D)^{1/2} (\sigma/14)(r/\sigma)^7 \quad (3.20)$$

In this expression τ is defined as the collision time

$$\tau = \left(\frac{\mu}{2} \right)^{1/2} \int_0^{r^*} \frac{dr}{[V - E]^{1/2}} \quad (3.21)$$

where $V = U(r) + E(b/r)^2$. When eq 3.20 is introduced,

the integrals become

$$I_n' = \int_{-\infty}^{\infty} \frac{\exp(i\omega t)}{(t - i\tau)^n} dt \quad (3.22)$$

which can be integrated as¹⁶

$$I_n' = \frac{2\pi(i\omega)^n}{\omega\Gamma(n)} \exp(-\omega\tau) \quad (n = 2, 16/7, 8/7, 10/7) \quad (3.23)$$

We thus obtain the expression for the magnitude of vibrational energy transfer as

$$\begin{aligned} \Delta E = & \frac{18}{49} \frac{(\pi\mu\omega d)^2}{M} \left\{ \left(\cos^2\theta - \frac{1}{14} \right) + \right. \\ & \frac{2}{\Gamma\left(\frac{6}{7}\right)} \left(\frac{d}{\sigma} \right)^2 \left[\left(\frac{\mu}{2D} \right)^{1/2} \frac{\sigma\omega}{14} \right]^{2/7} \times \\ & \left(6 \cos^4\theta - \frac{27}{14} \cos^2\theta + \frac{1}{16} \right) - \\ & - \frac{1}{\Gamma\left(\frac{8}{7}\right)} \left[\left(\frac{\mu}{2D} \right)^{1/2} \frac{\sigma\omega}{14} \right]^{-6/7} \left(\frac{2}{7} \cos^2\theta - \frac{1}{28} \right) - \\ & \frac{2}{\Gamma\left(\frac{10}{7}\right)} \left(\frac{d}{\sigma} \right)^2 \left[\left(\frac{\mu}{2D} \right)^{1/2} \frac{\sigma\omega}{14} \right]^{-4/7} \times \\ & \left. \left(\frac{5}{7} \cos^4\theta - \frac{5}{14} \cos^2\theta + \frac{1}{56} \right) \right\}^2 \exp(-2\omega\tau) \\ \equiv & \frac{18}{49} \frac{(\pi\mu\omega d)^2}{M} G(\theta) \exp(-2\omega\tau) \quad (3.24) \end{aligned}$$

In this expression the energy and impact-parameter dependences appear in the exponential part determining the duration of collision, and the angle dependence in the preexponential part. By use of this expression we can therefore calculate the amount of vibrational energy transfer at any initial angle (or its orientation-averaged quantity) as a function of energy. The second identity in eq 3.24 defines the angle dependent part by $G(\theta)$. Then, the orientation-averaged amount of vibrational energy transfer contains the factor $\bar{G} = \frac{1}{2} \int_0^\pi G(\theta) \sin\theta d\theta$.

C. Collision Time. To complete the derivation of the analytic expression of ΔE given by eq 3.24 and in turn the transition probability, it is necessary to evaluate the integral in eq 3.21 for the collision time. Although the attractive energy term of $U(r)$ was ignored in deriving eq 3.20 for the collision trajectory, we must now retain all terms of the effective potential in evaluating the collision time. Because of the complicated r dependence of V in eq. 3.21, the integral cannot be evaluated directly. To overcome this mathematical difficulty, we write the collision time in the form

$$\tau = (\mu/2)^{1/2} \int_{\infty}^E \frac{r'(V)dV}{(V-E)^{1/2}} \quad (3.25)$$

where $r'(V)$ is the derivative of the inverse function $r(V)$ with respect to V . Since the derivative can be, in principle, obtained in a polynomial of V^{-1} , an analytic evaluation of the integral in eq 3.25 is possible. In Figure 1, we show the behavior of $r'(V)$. Due to the presence of the centrifugal potential barrier, the variation of $r'(V)$ is somewhat complicated; curve a is the negative branch of $r'(V)$ representing the contribution of the repulsive energy of $U(r)$. The attractive term gives the positive branch de-

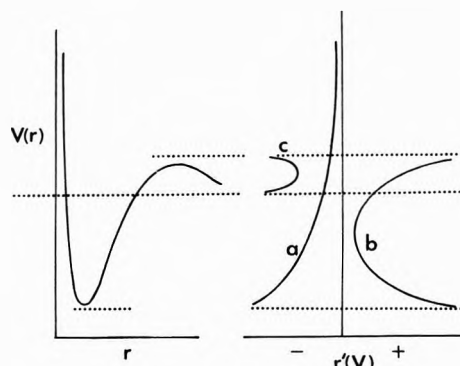


Figure 1. Dependence of the inverse derivative $r'(V)$ on V .

noted by curve b. The upper portion of curve b which lies in the positive V range and the third branch, curve c, are due to the appearance of a maximum value of the effective potential. Therefore, the inverse derivative can be obtained in a sum of these three contributions as well as their higher-order terms. The leading term of this sum should then result from curve a, which will be followed by the contribution from either curve b or c depending on the height of the potential barrier. The inverse derivative is

$$r'(V) = -V^{-13/12} \sum_{i=0}^{\infty} \alpha_i V^{-i} \quad (i = 0, 1/2, 5/6, 3/2, \dots) \quad (3.26)$$

where the coefficients are

$$\begin{aligned} \alpha_0 &= (4D)^{1/12} \sigma / 12; \quad \alpha_{1/2} = -\frac{7}{144} (4D)^{7/12} \sigma, \\ \alpha_{5/6} &= \frac{11}{144} \frac{Eb^2}{(4D)^{1/12} \sigma}; \quad \alpha_{3/2} = -\frac{595}{124,416} (4D)^{19/12} \sigma, \dots \end{aligned}$$

The first term of the sum is due to the repulsive energy of $U(r)$, i.e., $4D(\sigma/r)^{12}$, and the second term represents the contribution of molecular attraction $-4D(\sigma/r)^6$; the third term is responsible for the centrifugal potential. Therefore, if the potential is simply $U(r) = 4D(\sigma/r)^{12}$ with $b = 0$, the inverse derivative is $-(4D)^{1/12} \sigma / 12V^{13/12}$. With eq 3.26 at hand, the collision time can be readily evaluated as

$$\begin{aligned} \tau &= \left(\frac{\mu}{2} \right)^{1/2} \sum_{i=0}^{\infty} \alpha_i \int_E^{\infty} \frac{dV}{V^{13/12+i}(V-E)^{1/2}} = \\ & \left(\frac{\mu}{2} \right)^{1/2} \sum_{i=0}^{\infty} \frac{B \left(\frac{7}{12} + i, \frac{1}{2} \right) \alpha_i}{E^{7/12+i}} \\ &= \frac{\Gamma(7/12)}{\Gamma(1/12)} \frac{\left(\frac{1}{2} \pi \mu \right)^{1/2} \sigma (4D)^{1/12}}{E^{7/12}} - \\ & \frac{\Gamma(13/12)}{12\Gamma(7/12)} \frac{\left(\frac{1}{2} \pi \mu \right)^{1/2} \sigma (4D)^{7/12}}{E^{13/12}} + \\ & \frac{\Gamma(7/12)}{12\Gamma(11/12)} \frac{\left(\frac{1}{2} \pi \mu \right)^{1/2} b^2}{(4D)^{1/2} \sigma E^{5/12}} + \\ & \frac{7}{288} \frac{\Gamma(7/12)}{\Gamma(1/12)} \frac{\left(\frac{1}{2} \pi \mu \right)^{1/2} (4D)^{13/12} \sigma}{E^{19/12}} + \dots \quad (3.27) \end{aligned}$$

where the β function is $\beta(7/12 + i, 1/2) = \pi^{1/2} \Gamma(7/12 + i) /$

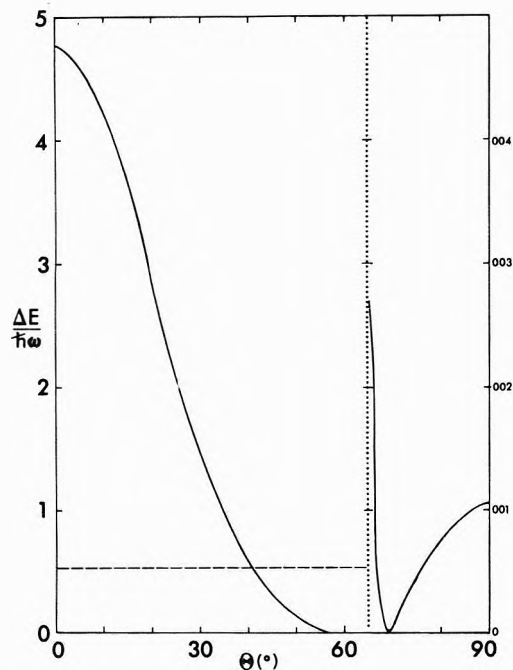


Figure 2. Variation of $\Delta E/h\omega$ with initial relative orientation angle θ at $v = 5 \times 10^5$ cm/sec. Values of $\Delta E/h\omega$ for 65–90° are plotted on an enlarged scale. The broken line represents the orientation-averaged value of $\Delta E/h\omega$.

$\Gamma^{(13/2 + i)}$. The introduction of this expression into eq 3.24 now completes the analytic formulation of the amount of vibrational energy transfer as a function of v , θ , and b .

An approach similar to the above derivation of the perturbing force, eq 2.3, and in turn the amount of energy transfer, eq 3.24, has already been reported elsewhere.¹⁶ Subsequently, Moran and his associates¹⁹ have applied this formulation to their ion beam experiments and have found that it adequately explains their results on vibrational excitations in $O^+ + O_2$, $O_2^+ + Ar$, and $CO^+ + Ar$ collisions at small scattering angles. The difference between that approach¹⁶ and the present one is the form of $U(r)$. While the present treatment is based on the LJ (12-6) potential for which the potential parameters D and σ are available from beam experiments in determining the collision time, the earlier model uses the LJ (12-6) function and additional terms which result from $V(r, \theta, x)$ to determine the collision time. In deriving the perturbing force in the latter work, the contribution containing $[(d+x)/r]^4$ was not considered; no temperature dependence of vibrational energy transfer was formulated.

D. Numerical Results on $N_2 + Ar$. We now present results for the amount of vibrational energy transfer and transition probabilities using the expressions derived above. The potential parameters determined by Tully and Lee¹¹ are $\sigma = r_m/2^{1/6} = 3.47$ Å and $D = 1.88 \times 10^{-14}$ erg; other well-known molecular constants are²⁰ $\omega_e = 2359.61$ cm⁻¹, $\omega_e x_e = 14.456$ cm⁻¹, and $d = 1.094$ Å. We first show the amount of vibrational energy transfer in units of $h\omega$ as a function of the initial orientation angle in Figure 2 by taking $v = 5 \times 10^5$ cm/sec (or 3.41×10^{-12} erg) and $b = 0$. For nonzero impact parameters, $\Delta E/h\omega$ is very small compared to this collinear case; the values for $b/\sigma = 0.5$ and 1.0, along with those for $b = 0$, are listed in Table I. From the figure, we find that the amount of energy transfer decreases very rapidly as θ increases from the collinear

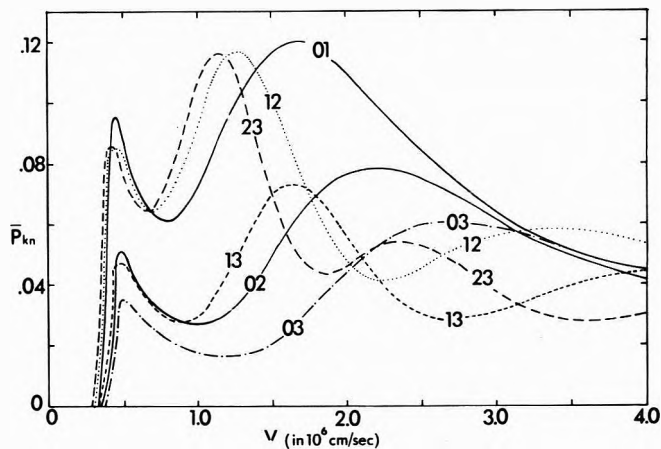


Figure 3. Variation of the orientation-averaged transition probabilities \bar{P}_{kn} with v for $b = 0$.

TABLE I: The θ Dependence of $\Delta E/h\omega$ at $v = 5 \times 10^5$ cm/sec for $b/\sigma = 0, 0.5$, and 1.0

θ , deg	$b/\sigma = 0$	$b/\sigma = 0.5$	$b/\sigma = 1.0$
0	4.77	3.59(1)	1.48(4)
10	4.22	3.17(1)	1.31(4)
20	2.91	2.19(1)	9.06(5)
30	1.52	1.14(1)	4.72(5)
40	5.69(1) ^a	4.27(2)	1.77(5)
50	1.36(1)	1.02(2)	4.24(6)
60	1.54(2)	1.15(3)	4.79(7)
70	5.88(5)	4.42(6)	1.83(9)
80	7.81(4)	5.87(5)	2.43(8)
90	1.08(3)	8.11(5)	3.35(8)

^a Number in parentheses denotes the negative power of 10; e.g., 5.69(1) = 5.69×10^{-1} .

case. After taking a minimum value of zero at 71.2°, the amount slightly increases as θ tends to 90°. Note that when the constants of the angle dependent part $G(\theta)$ are calculated, we have

$$G(\theta) = 7.20(\cos^4 \theta + 0.0465 \cos^2 \theta - 0.0155)^2$$

which becomes zero at 71.2°. At 0°, $\Delta E/h\omega = 4.77$ but it takes a value of only 1.08×10^{-3} at 90°. As shown in Table I, a similar θ dependence is seen for nonzero- b collisions. We therefore find that major portion of the energy transfer takes place in the angle range of 0 to 30°; since the molecule is homonuclear, this means that an equally effective angle range is from 0 to -30°.

If the angle-dependent factor is averaged over all possible values of θ , we get $G = 8.51$. In Figure 2, we also show the orientation-averaged amount of energy transfer for $b = 0$ at $v = 5 \times 10^5$ cm/sec for comparison.

From eq 3.15, we have the expression for any vibrational transition as a function of v , θ , and b . In Figure 3, we plot the values of the orientation-averaged transition probabilities for the first six vibrational excitations at $b = 0$ as a function of the collision velocity; the average probabilities are defined as

(19) P. C. Cosby and T. F. Moran, *J. Chem. Phys.*, **52**, 6157 (1970); F. Petty and T. F. Moran, *Phys. Rev. A*, **5**, 266 (1972).

(20) G. Herzberg, "Spectra of Diatomic Molecules," Van Nostrand, Princeton, N. J., 1950, Table 39.

$$\bar{P}_{kn} = \frac{1}{2} \int_0^\pi P_{kn} \sin \theta d\theta \quad (3.28)$$

The transition probabilities are complicated functions of the angle θ , $G(\theta)$ appearing in both the exponential and preexponential parts, but the integration can be readily carried out numerically. We performed the integration on an XDS Sigma-7 computer by Simpson's $\frac{1}{3}$ rule. Three different spacings and Richardson's extrapolations are used to improve the results.²¹

In Figure 3, we find that the transition probabilities show a complicated structured dependence on collision velocity. For nonzero impact parameters, the amount of vibrational energy transfer decreases from the collinear case at a given velocity so the curves shown in Figure 3 will shift toward high velocity ranges but the general shapes should remain unchanged. Below $v = 3 \times 10^5$ cm/sec, as shown in the figure, the probabilities are very small; e.g., at 10^5 cm/sec, $\bar{P}_{01} = 7.48 \times 10^{-17}$ and $\bar{P}_{02} = 1.34 \times 10^{-32}$, while $\bar{P}_{12} = 1.49 \times 10^{-16}$. At 3×10^5 cm/sec, $\bar{P}_{01} = 1.91 \times 10^{-3}$, $\bar{P}_{02} = 8.88 \times 10^{-6}$, $\bar{P}_{03} = 3.50 \times 10^{-8}$, $\bar{P}_{12} = 3.80 \times 10^{-3}$, $\bar{P}_{13} = 2.63 \times 10^{-5}$, and $\bar{P}_{23} = 5.64 \times 10^{-3}$. As the collision velocity increases, \bar{P}_{kn} rapidly increases to a maximum value; it shows another broad maximum at still higher velocities. For example, for $0 \rightarrow 1$, the first (sharp) maximum value of 9.55×10^{-2} appears at 4.5×10^5 cm/sec and the second (broad) maximum value of 0.120 at 1.6×10^6 cm/sec, indicating that the $0 \rightarrow 1$ transition is efficient over a wide velocity range above 4×10^5 cm/sec. Other one-quantum transition probabilities vary similarly at lower velocities. However, at higher collision velocities, we find one or more very broad but low maximum values compared to the $0 \rightarrow 1$ case. The numbers of maxima are 2, 3, and 4, respectively, for $0 \rightarrow 1$, $1 \rightarrow 2$, and $2 \rightarrow 3$ transitions. The first maximum is the sharpest; thereafter, the maxima become broader. The second maximum always takes the largest value. The $0 \rightarrow 2$ and $1 \rightarrow 3$ transitions take substantially smaller probabilities compared to one-quantum transitions below 1.4×10^6 cm/sec, but at higher collision velocities the probabilities are comparable to those of the latter. The $0 \rightarrow 2$ and $1 \rightarrow 3$ transition probabilities take two and three maximum values, respectively. Finally, the $0 \rightarrow 3$ transition probability is the smallest of the all cases under consideration below 2×10^6 cm/sec, but above 3×10^6 cm/sec it is as large as the $0 \rightarrow 1$ probability; the $0 \rightarrow 3$ probability takes two maximum values, the second maximum being very broad. The figure clearly shows that as the collision velocity increases, many channels are open for vibrational transitions and many of them become important.

We should note that P_{kn} has a much simpler velocity dependence. For example, P_{0n} takes a single maximum value of $n^n \exp(-n)/n!$ at $\epsilon = n$. For the collinear collision, the maximum values of 0.367, 0.270, and 0.224 then appear for $0 \rightarrow 1$, $0 \rightarrow 2$, and $0 \rightarrow 3$, respectively, in the velocity range $4.5 \times 10^5 - 5 \times 10^5$ cm/sec. As shown in Figure 3, this is the range where the first peaks of \bar{P}_{01} , \bar{P}_{02} , and \bar{P}_{03} appear with the values 9.55×10^{-2} , 5.03×10^{-2} , and 3.54×10^{-2} , respectively, which are significantly smaller than the corresponding collinear probabilities. However, beyond this velocity range, the collinear probabilities rapidly decrease with rising velocity. This comparison indicates that even if the anisotropy is not severe (see eq 2.2) the angle dependence can seriously affect the transition probabilities.

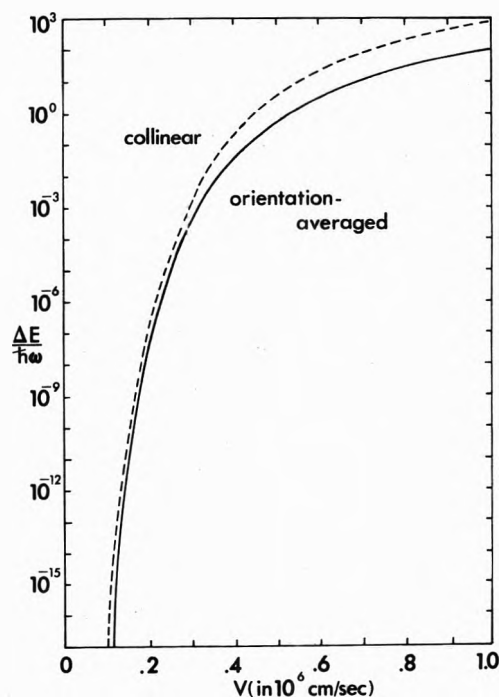


Figure 4. Plot of the orientation-averaged $\Delta E/\hbar\omega$ for $b = 0$ as a function of v . Values of $\Delta E/\hbar\omega$ for collinear collisions are also shown.

IV. Thermal-Averaged Transition Probability

A. General Considerations. The velocity dependence of orientation-averaged transition probabilities shown in Figure 3 indicates that below $v = 4 \times 10^5$ cm/sec all probabilities are very small ($\ll 1$). In Figure 4, we show the orientation-averaged amount of vibrational energy transfer, as well as the amount at collinear collisions. At 3×10^5 cm/sec, these two values are 3.60×10^{-4} and 3.23×10^{-3} , respectively. At 300°K, the average velocity of the collision system is about 6×10^4 cm/sec; it increases to about 2×10^5 cm/sec at 3000°K. Therefore, in thermal ranges, transition probabilities are very small ($\ll 1$) for the present collision system and no structured dependence of the vibrational transition probabilities on collision velocity (or energy) will appear, so that we can satisfactorily set $\exp(-\epsilon) \approx 1$ and neglect terms in second- and higher-orders in ϵ in P_{kn} ; e.g., $P_{01} = \Delta E/\hbar\omega$. The approximate expressions for other probabilities are $P_{02} = \frac{1}{2}\epsilon^2$, $P_{03} = \frac{1}{6}\epsilon^3$, $P_{12} = 2\epsilon$, $P_{13} = \frac{3}{2}\epsilon^2$, and $P_{23} = 3\epsilon$. These approximate expressions may then be used in deriving thermal-averaged transition probabilities. In the present section, we shall consider only the thermal average of the $0 \rightarrow 1$ transition probability in the temperature range of 300 to 3000°K and calculate the number of collisions required to de-excite a quantum of vibration ($1 \rightarrow 0$).

B. Average over Collision Energies. Before making the thermal average, we average P_{01} over molecular orientation angles and impact parameter

$$\langle P_{01} \rangle = \frac{1}{\pi l^2} \int_0^\infty 2\pi b db \int_0^\pi \frac{1}{2} P_{01} \sin \theta d\theta \quad (4.1)$$

where l is the "hard-sphere" collision diameter which will be determined from $U(l) = kT$. Note that the integral $\int_0^\infty 2\pi P_{01} b db$ is the effective inelastic scattering cross section.

(21) J. M. McCormick and M. G. Salvadori, "Numerical Methods in Fortran," Prentice-Hall, Englewood Cliffs, N. J., 1964, pp 312-317.

Assuming a Boltzmann distribution of initial energies (or velocities), we define the thermal-averaged transition probability as

$$P_{01}(T) = \frac{1}{(kT)^2} \int_0^\infty \langle P_{01} \rangle E \exp(-E/kT) dE$$

$$= \frac{Q}{(kT)^2} \int_0^\infty \int_0^\infty bE \times$$

$$\exp\left[-(2\mu)^{1/2} \omega \sum_{i=0}^\infty \frac{B\left(\frac{7}{12} + i, \frac{1}{2}\right) \alpha_i}{E^{7/12+i}} - \frac{E}{kT}\right] dE db \quad (4.2)$$

where Q is the preexponential part of $\langle P_{01} \rangle$ defined in eq 4.1

$$Q = \frac{36}{49} \left(\frac{\pi\omega}{iM}\right) \left(\frac{\mu d}{l}\right)^2 \bar{G} \quad (4.3)$$

where

$$\bar{G} = \frac{1}{2} \int_0^\pi G(\theta) \sin \theta d\theta$$

In eq 4.2 we first carry out the integration over b ; the $i = 5/6$ term of the sum is needed in this integration. The result is

$$P_{01}(T) = \frac{Q}{(kT)^2} \left[\frac{6\Gamma(13/12)}{\Gamma(7/12)} \left(\frac{2}{\pi\mu}\right)^{1/2} \sigma(4D)^{1/12} \right] \times$$

$$\int_0^\infty E^{17/12} \exp\left[-(2\mu)^{1/2} \omega \sum_{i=0}^\infty \frac{B\left(\frac{7}{12} + i, \frac{1}{2}\right) \alpha_i}{E^{7/12+i}} - \frac{E}{kT}\right] dE \quad (4.4)$$

Note that the preexponential part of the integrand now contains $E^{17/12}$ and that the sum does not include the $i = 5/6$ term. The leading term of the sum in the exponent is

$$-\frac{\Gamma(7/12)}{\Gamma(1/12)} \frac{(2\pi\mu)^{1/2} (4D)^{1/12} \omega \sigma}{E^{7/12}} = \frac{\text{constant}}{E^{7/12}}$$

Therefore, the exponential part in eq 4.4 containing the sum, which results from the transition probability, increases with E approximately as $\exp(-\text{constant}/E^{7/12})$, while the Boltzmann factor $\exp(-E/kT)$ decreases, so that the integrand takes a maximum value at some intermediate energy, say E^* . The analytic evaluation of eq 4.4 can then be performed by use of the Laplace method.^{22,23} A straightforward application of this method gives

$$P_{01}(T) = Q \frac{\Gamma(11/12)\Gamma(19/12)}{\Gamma(17/12)\Gamma(13/12)} \left(\frac{6\pi}{19kT}\right)^{1/2} (4D)^{1/6} \chi^{1/3} \times$$

$$\left\{ 1 - \frac{455}{342} \left[\frac{\Gamma(13/12)}{\Gamma(7/12)}\right]^2 \left(\frac{D}{\chi}\right)^{1/2} \right\} \times$$

$$\exp\left\{ -\frac{19\chi}{7kT} + \frac{7}{6} \left[\frac{\Gamma(13/12)}{\Gamma(19/12)}\right]^2 \frac{(D\chi)^{1/2}}{kT} + \frac{95}{72} \left(\frac{91}{114}\right)^2 \times \right.$$

$$\left. \left[\frac{\Gamma(13/12)}{\Gamma(19/12)}\right]^4 \frac{D}{kT} - \frac{D}{6kT} - \frac{\hbar\omega}{2kT} \right\}$$

where

$$\chi = \left[\frac{\Gamma(19/12)}{\Gamma(1/12)} (4D)^{1/12} (2\pi\mu)^{1/2} \sigma \omega kT \right]^{12/19} \quad (4.5)$$

In this equation, the term $-\hbar\omega/2kT$ in the exponent is due to the symmetrization of the initial and final collision energies.^{2b} To obtain the transition probability appropriate to a deexcitation of the oscillator, rather than to an excitation, we have to replace this term by $+\hbar\omega/2kT$; i.e.,

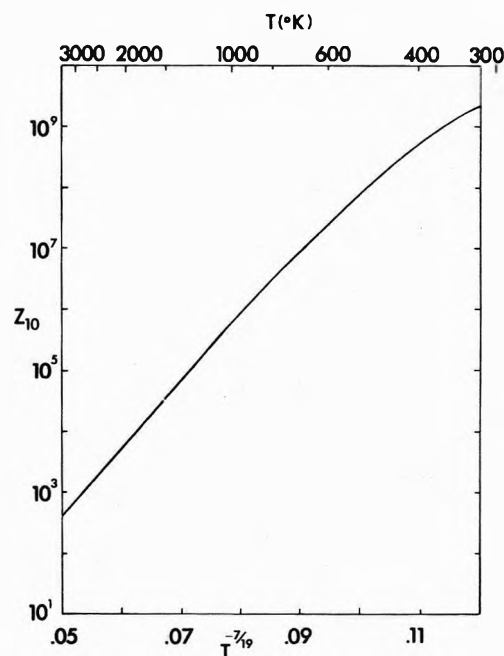


Figure 5. Plot of the collision number $Z_{10} \equiv 1/P_{10}(T)$ as a function of $T^{-7/19}$.

$P_{10}(T) = P_{01}(T) \exp(\hbar\omega/kT)$. The second term of the factor

$$\left\{ 1 - \frac{455}{342} \left[\frac{\Gamma(13/12)}{\Gamma(7/12)}\right]^2 \left(\frac{D}{\chi}\right)^{1/2} \right\}$$

in the preexponential part is due to the attractive energy term $-4D(\sigma/r)^6$ of $U(r)$. This term is normally very small compared to unity so that the molecular attraction does not seriously affect the preexponential part; however, the second, third, and fourth terms in the exponent are also due to the molecular attraction, and can make an important contribution to the overall magnitude of the probability.

We note that the thermal-averaged total cross section for $0 \rightarrow 1$ can be defined as

$$Q_{01}(T) = \frac{2\pi}{(kT)^2} \int_0^\infty \int_0^\infty \bar{P}_{01} E b dE db \quad (4.6)$$

which is then simply $\pi l^2 P_{01}(T)$.

C. Temperature Dependence of Collision Number. In Figure 5, we plot the number of collisions required to deexcite a quantum of vibration ($1 \rightarrow 0$), which is defined as $Z_{10} \equiv 1/P_{10}(T)$, as a function of $T^{-7/19}$. For $P_{10}(T)$, the fifth term in the exponent is now $+\hbar\omega/2kT$. The leading term in the exponent, $-19\chi/7kT$, is very large compared to the others; e.g., at 300°K the leading term takes -42.6 , while the second term is $+3.59$, the sum of the third and fourth terms is $+0.432$, and the fifth term is $+5.59$. Therefore, the logarithmic plot of Z_{10} against $T^{-7/19}$ follows a nearly straight line, particularly at higher temperatures. A deviation from linearity at temperatures below 600°K is mainly due to the contribution of the second term in the exponent of $P_{10}(T)$, which results from the attractive energy $-4D(\sigma/r)^6$. The collision number is very large even at higher temperatures; at 3000°K, $Z_{10} = 540$ or $P_{10}(T) = 1.85 \times 10^{-3}$. At 300°K, it is as large as

(22) N. G. de Bruijn, "Asymptotic Methods in Analysis," North-Holland, Amsterdam, 1961, 2nd ed, Chapter 4.

(23) Also see H. Shin, *J. Chem. Phys.*, **56**, 2617 (1972).

TABLE II: Effect of Nonzero-Impact Parameter Collisions on Vibrational Energy Transfer^a

<i>T</i> , °K	<i>L</i>	<i>l</i> , Å
300	0.0549	3.28
400	0.0606	3.24
600	0.0701	3.14
800	0.0775	3.14
1000	0.0842	3.10
1500	0.0981	3.03
2000	0.109	2.98
2500	0.119	2.94
3000	0.128	2.90

^a Values of the hard-sphere collision diameter are also listed.

3.69×10^9 . The calculated values of *l* obtained from the relation $U(l) = kT$ vary from 3.28 Å at 300°K to 2.90 Å at 3000°K; see Table II.

In eq 4.5 the effect of nonzero-impact parameter collisions contributes to the preexponential part by the factor

$$L = \frac{84}{5} \frac{\Gamma(11/12)\Gamma(7/12)}{\Gamma(5/12)\Gamma(1/12)} \left(\frac{\sigma}{d}\right)^2 \frac{(4D)^{1/6}kT}{\chi^{7/6}} \quad (4.7)$$

In Table II, we show the calculated values of this contribution along with the values of *l*. The effect is very important throughout the temperature range considered; the

consideration of all possible nonlinear collisions leads to the decrease of the thermal-averaged transition probability by a factor of 18.2 at 300°K and 7.78 at 3000°K from the zero-impact parameter result.

V. Concluding Remarks

We have developed a procedure to construct the perturbation energy in an appropriate form for the study of vibrational transitions in atom + diatomic systems on the basis of the knowledge obtained from crossed-beam experiments. By use of this perturbation energy, we have shown in detail the derivation of the vibrational transition probability from the time-dependent perturbed oscillator wave function as a function of the collision energy (velocity), orientation angle, and impact parameter. Application of the formulation to $N_2 + Ar$ shows that the vibrational transition probabilities have complicated structured dependence on collision velocity in the range 4×10^5 – 4×10^6 cm/sec.

The thermal average of the $0 \rightarrow 1$ vibrational transition is explicitly performed, and an essentially linear relation between the logarithm of the collision number and $T^{-7/19}$ is found. A deviation from linearity at temperatures below 600°K is attributed to the effect of attractive forces. The calculation shows that when all nonzero-impact parameter collisions are included, the thermal-averaged transition probability becomes seriously smaller than the zero-impact parameter result.

SCF-MO Calculations of Spectra of Ketyl Radicals and Radical Anions of Uracil and Cytosine

Alec Grimison and Manfred K. Eberhardt*

Puerto Rico Nuclear Center,¹ Caparra Heights Station, San Juan, Puerto Rico 00935 (Received November 13, 1972)

Publication costs assisted by the Puerto Rico Nuclear Center

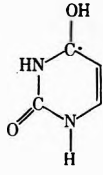
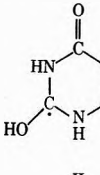
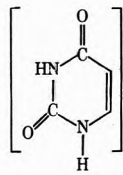
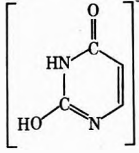
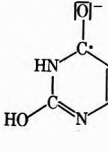
SCF-MO calculations were used to calculate spectral transitions of a series of possible intermediates in the reaction of uracil and cytosine with e_{aq}^- . The calculations were carried out using a specially designed PPP type approximation, including configuration interaction. In some cases the calculations confirm previous spectral assignments, but in other cases new assignments have been made.

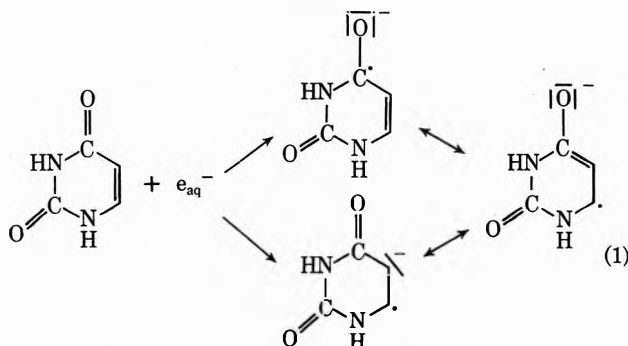
The reaction of solvated electrons e_{aq}^- , produced by radiolysis of water, with a series of pyrimidines was investigated by Hayon² using the technique of flash radiolysis. Hayon concluded that solvated electrons, e_{aq}^- , react with pyrimidines mainly at the C₂ and C₄ carbonyls. This was indicated to be in contradiction to the reaction at the 5,6 carbon-carbon double bond postulated by previous investigators on the basis of quantum mechanical calculations.³ This conclusion appeared rather strange since addition to the C₄ carbonyl group as well as addition to the 5,6 carbon-carbon double bond gives the same mesomeric radical anion (see eq 1). Although one may consider the

solvated electron e_{aq}^- as the simplest radical it does not behave like other free radicals, which react with a molecule at a specific position. A solvated electron e_{aq}^- reacts with a molecule by addition to the lowest unoccupied molecular orbital (LUMO). This is delocalized over the entire molecule.

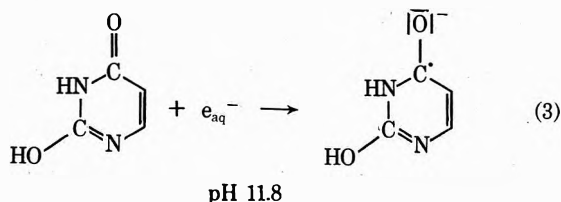
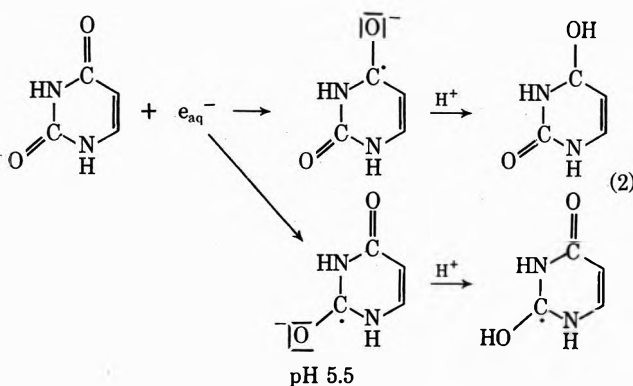
- (1) Puerto Rico Nuclear Center is operated by the University of Puerto Rico for the U. S. Atomic Energy Commission under Contract No. AT (40-1)-1833.
- (2) E. Hayon, *J. Chem. Phys.*, **51**, 4881 (1969).
- (3) B. Pullman and A. Pullman, "Quantum Biochemistry," Interscience, New York, N. Y., 1963.

TABLE I: Calculated and Experimental Transitions for Uracil Radical Anions

Conditions	Experimental transitions, eV	Suggested species with their principal calculated transitions and oscillator strength			Conclusions	
		I	II	III	Hayon	This work
pH 5.1	4.07 >4.4				I (4.07) II (>4.4)	I
Cutoff at >4.4 eV		4.14 (0.050) 4.94 (0.056)	4.72 (0.0002)	4.087 (0.0056)		
pH 11.7	4.00				V	IV
		3.54 (0.0987) 3.64 (0.2669)	4.19 (0.1485) 4.40 (0.1544)			

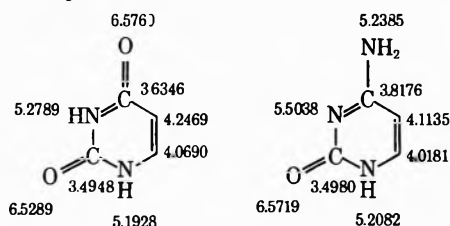


For uracil Hayon found two absorption maxima at pH 5.5 and one maximum at pH 11.8. He proposed the reaction sequence shown by eq 2 and 3. Since, as mentioned



electron distribution of the uracil radical anion using an all valence electron SCF-MO calculation (INDO approximation) in the spin-unrestricted formalism.⁴ The results show (see Chart I) that the maximum total electron density in the uracil anion is at the oxygen of the C₄ carbonyl group and protonation would be expected at that position to form the C₄-ketyl radical of uracil. In order to see whether this species would account for the two observed absorption maxima we have calculated the transitions of the uracil radical anion and the C₂- and C₄-ketyl radicals (see Table I). These calculations were carried out using a PPP type approximation, including configuration interaction. The PPP program contained the special feature of inclusion of nonempirical β values. The β values were calculated using the Linderberg equation. The method is described in detail in a recent publication.⁵ The C₄-ketyl radical gives rise to two absorption maxima at 4.14 and 4.94 eV. This compares favorably with the experimental results (4.07 and >4.4 eV). The calculations on the C₂-ketyl radical show only one weak absorption at 4.72 eV. Also the uracil radical anion gives only one weak absorption at 4.09 eV. The spectral calculations therefore agree very well with the INDO calculations, which predict the formation of the C₄-ketyl radical.

Chart I: INDO Calculations of Total Electron Densities of Uracil and Cytosine Radical Anion



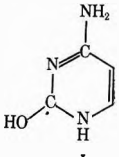
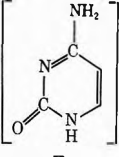
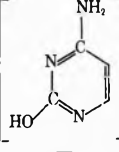
In basic solution at pH 11.8 only one absorption peak at 4.00 eV was reported. The calculations on the uracil lactim radical anion show two maxima at 3.64 and 3.54 eV.

(4) J. A. Pople and D. L. Beveridge, "Approximate Molecular Orbital Theory," McGraw-Hill, New York, N. Y., 1970.

(5) M. K. Eberhardt and A. Grimison, *Rev. Latinoamer. Quim.*, in press.

above, the e_{aq}^- does not react at a specific position of uracil, but adds to the LUMO we have calculated the

TABLE II: Calculated and Experimental Transitions for Cytosine Radical Anions

Conditions	Experimental transitions, eV	Suggested species with their principal calculated transitions and oscillator strength		Conclusions	
				Hayon	This work
pH 5.5	3.88 4.07	 I	 II	I (4.07) ? II (3.88) ?	I II
Cutoff at >4.2 eV		4.16 (0.1461) 4.51 (0.1539)	3.69 (0.1801) 4.55 (0.1053) 4.87 (0.1473)		
pH 13.3	4.00	 III		III ?	III ?
		3.35 (0.2069) 3.84 (0.0958) 4.47 (0.0962)			

The species suggested by Hayon would give two equal maxima at 4.19 and 4.40 eV. The weaker absorption of the uracil lactim radical anion at 3.54 eV may well be hidden under the much stronger absorption at 3.64 eV. If we look at the experimental spectrum of Hayon we can indeed see a weak shoulder at about 3.8 eV. The calculations also correctly predict the stronger absorption at pH 11.8, compared to the two absorption peaks of the C₄-ketyl radical at pH 5.5.

We have also carried out calculations on cytosine (see Table II). The INDO calculation on cytosine lactam radical anion shows (see Chart I) the highest electron density at the carbonyl oxygen and protonation is expected at that position. The experimental data for cytosine have a cutoff above 4.2 eV. Below that value, we calculate the cytosine radical anion to have a maximum at 3.69 eV, and the C₂-ketyl radical maximum at 4.16 eV. The experimental results² at pH 5.5 indicate that two transients are formed: one with a lifetime of ~30 μsec and a maximum at 3.88 ± 0.12 eV, and another with a lifetime of ~100

μsec and a maximum at 4.07 ± 0.06 eV. Hayon² very tentatively assigned the former as the radical anion and the latter as the 2-ketyl radical, possibly formed by protonation of the anion. It is clear from the foregoing that our calculations fully confirm the tentative assignment. We may inquire whether the same mechanism should not obtain for uracil: formation of the radical anion followed by protonation to form the ketyl radical. This is entirely possible, and our calculations suggest that an explanation why only one transient (the 4-ketyl radical) is observed is that the uracil radical anion has only one very weak absorption band (at 4.087 eV) in the experimental region (for uracil <4.4 eV). The situation for cytosine in alkaline solution appears to be more complicated, and no conclusions have been reached so far.

In conclusion, the present data suggest that the solvated electron reacts with uracil and cytosine by addition to the lowest unoccupied molecular orbital, followed at pH 5.5 by protonation to form the C₄-ketyl radical of uracil and the C₂-ketyl radical of cytosine.

Potentials of Glass Membranes in Molten Binary Nitrates

T. J. van Reenen* and W. J. de Wet

Chemistry Division, National Nuclear Research Centre, Pretoria, South Africa (Received November 15, 1972)

Emf measurements were performed on Pyrex and fused silica membranes in molten alkali nitrate media at various temperatures. With the appropriate parameters for each system substituted in the Eisenman equation, good agreements with experimental values were obtained. The temperature and voltage dependence of the mobility ratio, u_{Li}/u_{Na} , for Pyrex membranes is discussed.

Introduction

In a recent communication¹ the scope of an electrolytic transport technique has been emphasized for the purpose of verifying the Eisenman theory² for membrane potentials. Numerical values for the main parameters, namely, the mobility ratio u_1/u_2 , the thermodynamic equilibrium constant K_{ij} , and the nonideality factor n , can be obtained directly for glass membranes in certain alkali molten salt systems at elevated temperatures for a direct study of the above-mentioned theory. It was also demonstrated that for the latter two parameters, results are obtained which are in agreement with those obtained by the equilibrium sorption method³ as applied on powdered glass samples. The results reported for these two parameters were, however, not correct due to the influence of the zinc chloride used in our melts on the ratio of the activity coefficients of the alkali cations. This wrong assumption occurred through misleading and fortuitous results previously obtained using an equation for regular binary mixtures to account for the activity coefficients of the alkali cations in the zinc chloride diluted melts. Fortunately this error was soon discovered experimentally, and appropriately rectified in all subsequent work. The mobility ratio values reported were not affected.

In the present paper the newly determined values of K_{ij} and n for the same alkali cation pairs discussed in the previous paper are reported. By using these new values for the above parameters, and average values for the mobility ratios, as will be discussed below, results of judiciously chosen emf experiments, done with Pyrex and fused silica membranes in various binary alkali nitrate melts, were compared with theoretically calculated values. The correctness of our main assumption, namely, the importance of the mobility ratio dependence on the cationic composition of the membrane for verification of the Eisenman theory, unfortunately cannot be tested rigorously enough using the binary melt systems of this investigation. This would be possible if an inert solvent could be used in the melts to vary the absolute activities of the alkali cations at random once uncertainties about the activity coefficients of these ions in such ternary melts had been eliminated. It was, however, attempted to ascertain that only the ionic composition of a membrane at its two interfaces are of significance in this respect, and that the bulk ionic composition of a membrane is immaterial, at least for situations in which the resistance to ionic migration in the bulk is less than at the interfaces.

For an investigation into the effect of the ionic composition of the bulk of the membrane on the potential across

the membrane, three series of potential measurements were performed on Pyrex membranes. In the first series the membrane was used in its original sodium ion form. For the second series the same membrane was changed to an ionic composition of equal sodium and lithium mole fractions. In the third series the membrane was completely converted to a lithium ion form. These displacements were brought about *in situ* using the electrolytic transport technique described elsewhere.¹

The same technique has also been used to study the variation with temperature of the mobility ratio of Li to Na ions through a Pyrex membrane. The temperature range which could adequately be studied with this technique was 490–670°. The details for carrying out these determinations are exactly the same as described in our previous paper.¹

Experimental Section

K_{ij} and n values using the equilibrium sorption technique³ were obtained for the following systems: Pyrex/(Na-Li)NO₃ at 550°, Pyrex/(Na-Li)NO₃ at 450°, Pyrex/(Na-Li)NO₃ at 350°, Pyrex/(Na-K)NO₃ at 550°, soda lime glass/(Na-Li)NO₃ at 450°, soda lime glass/(Na-K)NO₃ at 450°, and fused silica/(Na-Li)NO₃ at 600°.

Although the light alkali nitrates decompose at relatively low temperatures, Flinn and Stern⁴ conducted experiments with fused silica in binary (Na-K)NO₃ mixtures at 550°. The present investigation showed that the binary nitrate mixtures could even be used at temperatures of 600° for short periods (see Table I). No serious decomposition of the nitrates was observed and after cooling no etching of the glass was found.

Samples of finely divided glass, contained in inert Supramax glass tubes and each weighing 0.5 g, were equilibrated with (Na-Li)NO₃ and (Na-K)NO₃ binary mixtures. The mole fractions of sodium in the binary mixtures ranged from 0.05 to 0.95 in steps of 0.05. The alkali contents of the equilibrated glass samples were obtained by flame photometry, except in the case of fused silica where the sodium contents of the glass samples were determined by neutron activation analysis. The HF used to dissolve the equilibrated glass powders contained trace quantities of sodium as impurities. This could affect the flame photometer readings as fused silica itself has a very

(1) T. J. van Reenen, M. van Niekerk, and W. J. de Wet, *J. Phys. Chem.*, **75**, 2815 (1971).

(2) F. Conti and G. Eisenman, *Biophys. J.*, **5**, 511 (1965).

(3) H. M. Garlinkel, *J. Phys. Chem.*, **72**, 4175 (1968).

(4) D. R. Flinn and K. H. Stern, *J. Phys. Chem.*, **76**, 1072 (1972).

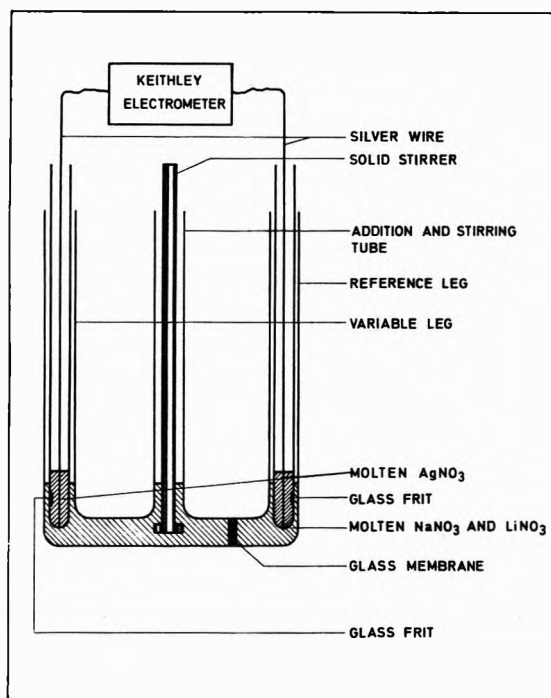


Figure 1. Experimental arrangement used for emf measurements.

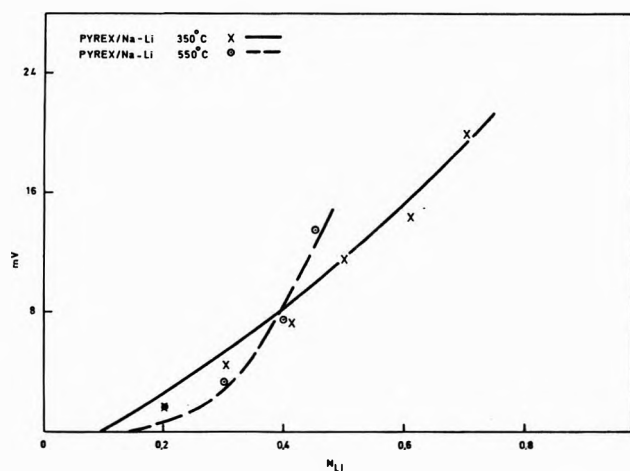


Figure 2. Emf vs. N_{Li} for the system Pyrex/(Na-Li)NO₃ at 550° (O) and Pyrex/(Na-Li)NO₃ at 350° (X).

TABLE I: Equilibration Times and Mesh Sizes

System	Temp. °C	Mesh size	Time, hr
Pyrex/(Na-Li)NO ₃	550	-200	5
Pyrex/(Na-Li)NO ₃	450	-400	94
Pyrex/(Na-Li)NO ₃	350	-400	170
Pyrex/(Na-K)NO ₃	550	-400	96
Soda lime glass/(Na-Li)NO ₃	450	-400	170
Soda lime glass/(Na-K)NO ₃	450	-400	1440
Fused silica/(Na-Li)NO ₃	600	-200	2

low alkali content. The lithium contents of the fused silica samples were, however, obtained by flame photometry.

The appropriate mesh sizes and equilibrating times for each system are summarized in Table I. Detailed information concerning the experimental procedure is found elsewhere.³

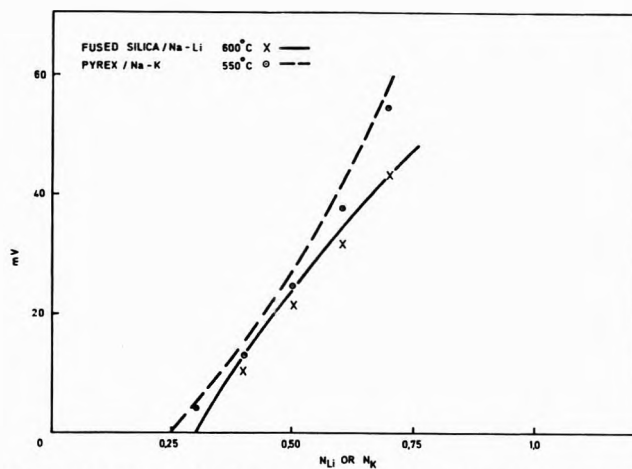


Figure 3. Emf vs. N_K for the system Pyrex/(Na-K)NO₃ at 550° (O) and emf vs. N_{Li} for the system fused silica/(Na-Li)NO₃ at 600° (X).

Using the experimental arrangement shown in Figure 1, several series of potential measurements were performed on the following systems: Pyrex/(Na-K)NO₃ at 550°, Pyrex/(Na-Li)NO₃ at 550°, Pyrex/(Na-Li)NO₃ at 450°, Pyrex/(Na-Li)NO₃ at 350°, and fused silica/(Na-Li)NO₃ at 600°.

In these experiments the ionic compositions of the membranes were left unaltered and were thus predominantly in the original sodium ion form. Potentials were measured for melt compositions which correspond with the range within which the mobility ratio has an almost linear dependence on ionic composition (see ref 1, Figures 4 and 6). The melt compositions used in the reference sides for the various experiments can be seen in Figures 2 and 3; *i.e.*, the compositions at zero potential values.

For the potential measurements at 350 and 450°, Ag|Ag⁺ electrodes were used as shown in Figure 1, while Na|Na⁺ electrodes were used at the higher temperatures. The Na|Na⁺ electrodes were prepared by electrolyzing sodium from molten sodium chloride to an amount of 8 atom % into molten lead metal at 820°. The Pb-Na bismetal was then kept in a 5-mm diameter glass tube under an inert gas atmosphere. Contact was made by means of a tungsten wire. This assembly was put into a 10-mm diameter glass tube containing 20 g of NaNO₃ and fitted with a glass frit near the bottom.

The experimental arrangement shown in Figure 1 allowed the direct measurement of membrane potentials. A nullpoint reading was obtained for each system with similar binary melts on both sides of the membrane. These null readings never exceeded 0.2 mV and were subtracted from the final potentials. During the series of measurements the composition of the reference leg remained unchanged. Additions were made through the addition and stirring tube shown in Figure 1, while a solid-state Keithley electrometer, Model 610C, was used for measuring the membrane potentials. Constant potential values were obtained within 15-30 min of each addition.

Results and Discussion

K_{Na_j} and n values for the various systems, as summarized in Table II, were obtained by plotting the results of the equilibrium sorption experiments according to eq 1, where j is either Li or K, and N and \bar{N} denote the mole fractions of the cationic species in the melt and glass

TABLE II: Experimental Values Obtained for K_{Na_j} , u_j/u_{Na} , and n^a

System	Temp. °C	K_{Na_j}	Mean u_j/u_{Na}	n	$k = K_{Na_j} \cdot (u_j/u_{Na})^n$
Pyrex/(Na-Li)NO ₃	550	5.37	0.225	0.62	2.13
Pyrex/(Na-Li)NO ₃	450	4.26	0.225	0.84	1.22
Pyrex/(Na-Li)NO ₃	350	3.0	0.225	1.17	0.52
Pyrex/(Na-K)NO ₃	550	1.41	0.075	1.07	0.09
Soda lime glass/ (Na-Li)NO ₃	450	11.24	0.025	1.37	0.07
Soda lime glass/ (Na-K)NO ₃	450	1.42		1.37	
Fused silica/ (Na-Li)NO ₃	600	2.30	2.70	1.02	4.90

^a Depending on the system, j represents either Li or K.

phases, respectively.³ A is the heat of mixing and was taken as -470 and -422 cal/mol for the (Na-Li)NO₃ and (Na-K)NO₃ systems, respectively.³ Plots of the left-hand side of eq 1 vs. $\log \bar{N}_j/\bar{N}_i$ resulted in excellent straight lines.

$$\log(N_j/N_i) - \frac{A}{2.303RT}(1 - 2N_i) = n \log(\bar{N}_j/\bar{N}_i) - \log K_{ij} \quad (1)$$

A study of Table II shows that, for Pyrex membranes, K_{NaLi} decreases while n increases with decreasing temperature. It is interesting to note that, in the presence of sodium and lithium ions, Pyrex membranes show either an ideal or nonideal behavior, depending on the working temperature. This may be explained by the change in glass structure and site affinities with temperature. Garfinkel³ reported n values varying from $n = 0.6$ to $n = 4$ for a variety of glasses between 300 and 500°. Eisenman⁵ even found n values as high as 6 for certain ordinary glass membranes at room temperatures.

Garfinkel⁶ used glasses similar in structure to Pyrex in molten sodium nitrate-potassium nitrate mixtures and calculated the mobility ratio u_{Na}/u_K from potential values. He concluded that the mobility ratio was primarily a function of temperature; u_{Na}/u_K increased sharply with increasing temperature. Direct mobility measurements on the system Pyrex/(Na-Li)Cl, using an electrolytic transport technique, showed no change in u_{Li}/u_{Na} over the temperature range 490–670°. The mobility ratio was found to be 0.225, in good agreement with the value reported in ref 1.

Doremus^{7,8} found the mobility ratio u_{Ag}/u_{Na} in Pyrex to be independent of temperature below 340°, while Thulin⁹ found that the transport numbers of Na⁺, K⁺, and Li⁺ were also temperature independent above 810°. It thus seems that the temperature dependence of the cationic mobility ratio varies from system to system and cannot be predicted from investigations conducted on similar systems.

It is a well-known fact that the electrical resistance of glass membranes decreases with increasing temperature. This implies that the applied electrolysis voltages should decrease with increasing temperature so as to maintain a

constant current density through the membrane. It thus seemed essential to investigate the dependence of the mobility ratio u_{Li}/u_{Na} through Pyrex membranes on the applied electrolysis voltage. During this investigation the composition of the salt bath was kept unchanged, and the temperature was maintained at 550°. The applied voltage was increased from 5 V, in steps of 5 V, to 50 V. It was found that the applied voltage had no effect on the mobility ratio.

Using the horizontal parts of the curves in the mobility ratio vs. membrane composition plots (see ref 1, Figures 4–6), mean mobility ratio values can be calculated for the various systems. These values are summarized in Table II.

Using the results of Table II, it is possible to calculate the selectivity constant k for each system from the definition

$$k = K_{ij}(u_j/u_i)^n \quad (2)$$

The right-hand column of Table II shows that k and not K_{ij} is a measure of the selectivity of ion-selective membranes. Ion-selective membranes with k values far from unity are important as far as the construction of ion-selective membrane electrodes is concerned.

Figures 2 and 3 show the experimental and theoretical potential values of this investigation for the systems Pyrex/(Na-Li)NO₃ at 550°, Pyrex/(Na-Li)NO₃ at 350°, Pyrex/(Na-K)NO₃ at 550°, and fused silica/(Na-Li)NO₃ at 600°.

The solid lines in Figures 2 and 3 represent the theoretical emf values, V_0 , calculated according to eq 3⁶ and 4 and the experimental values for the different parameters as summarized in Table II.

$$\log \gamma_i = (A/2.303RT)(N_i)^2 \quad (3)$$

γ_i is the activity coefficient of species i .

$$V_0 = \frac{nRT}{zF} \ln \frac{(a_i')^{1/n} + u_j/u_i(K_{ij}a_j')^{1/n}}{(a_i'')^{1/n} + u_j/u_i(K_{ij}a_j'')^{1/n}} \quad (4)$$

Good agreement with the theoretical values of eq 4 was obtained experimentally as shown by the crosses in Figures 2 and 3. Taking into account the independence of the mobility ratio on temperature, u_{Li}/u_{Na} was taken as 0.225 for the system Pyrex/(Na-Li) at 350°. From Figure 2 it is evident that this assumption was realistic as the experimentally obtained emf values agreed satisfactorily with the calculated values.

Conclusions

The results of this investigation show that eq 4 describes the potentials across glass membranes in molten salt systems adequately.

Acknowledgment. The authors are indebted to the South African Atomic Energy Board for permission to publish this paper.

- (5) G. Eisenman, *Biophys. J.*, **2**, 259 (1962).
- (6) H. M. Garfinkel, *J. Phys. Chem.*, **73**, 1766 (1969).
- (7) R. H. Doremus, *J. Electrochem. Soc.*, **115**, 924 (1968).
- (8) R. H. Doremus, *J. Phys. Chem.*, **72**, 2877 (1968).
- (9) L. U. Thulin, Ph.D. Thesis, University of Trondheim, 1970.

Heats of Mixing of Globular Molecules Differing in Size

D. D. Deshpande¹ and D. Patterson*

Chemistry Department, McGill University, Montreal 101, Canada (Received October 31, 1972)

Publication costs assisted by the National Research Council of Canada

The van der Waals combining rules, recently suggested by Rowlinson and collaborators, give a simple prediction for H^E in terms of differences between the components in intermolecular energies (θ) and molecular sizes (ϕ) and deviations from the Berthelot rule (ξ): $H^E \propto 2(1 - \xi) - \theta\phi/2$. Data for six new systems and six from the literature are in fair accord with this prediction.

Introduction

Interest in the thermodynamics of mixtures of quasi-spherical molecules has been renewed by theoretical² and experimental³ work. According to the older average potential or random mixture theory, a difference of molecular size should lead to very large positive contributions to the excess functions, G^E , H^E , and V^E . It is now agreed² that this prediction is incorrect, and Rowlinson and collaborators propose the use of new "van der Waals" combining rules. We wish to point out in this note that the new theory gives an extremely simple prediction for H^E . Data for systems containing globular molecules are in fair agreement, while Flory's theory⁴ seems to give poor results.

van der Waals Prediction for H^E

The systems selected for discussion, together with experimental values of H^E at equimolar concentration and 25°, are found in Table I. We calculate the equimolar H^E following Marsh, *i.e.*, using the one fluid approximation and the van der Waals combining rules together with the van der Waals equation of state. (Use of the two-fluid approximation or a more complicated equation of state would not affect the qualitative conclusions presented here (*cf.* ref 5 and 6)). Thus

$$H^E = -\langle a \rangle / \langle V \rangle + x_1 a_1 / V_1 + x_2 a_2 / V_2 \quad (1)$$

$$V_i = (a_i / 2RT) [1 - \{1 - 4b_i RT / a_i\}^{1/2}] \quad (2)$$

where a_i and b_i are the van der Waals constants and the averaged quantities are given by

$$\langle a \rangle = a_1 x_1^2 + 2a_{12} x_1 x_2 + a_2 x_2^2 \quad (3)$$

$$\langle b \rangle = b_1 x_1^2 + 2b_{12} x_1 x_2 + b_2 x_2^2$$

with

$$a_{12}/b_{12} = \xi(a_1/b_1)^{1/2}(a_2/b_2)^{1/2} \quad (4a)$$

$$b_{12} = (b_1^{1/3} + b_2^{1/3})^3 / 8 \quad (4b)$$

Here the a/b correspond to interaction energies, ϵ , and ξ is the empirical coefficient close to unity which takes into account any deviation from the geometric mean rule. The values of a and b were obtained from critical data.^{3,7} The energy and size difference parameters θ and ϕ are given by

$$1 + \theta = (a_2/b_2)/(a_1/b_1) = T_{c,2}/T_{c,1} \quad (5)$$

$$1 + \phi = b_2/b_1 = V_{c,2}/V_{c,1}$$

Figure 1 shows values of the equimolar H^E calculated for two values of ξ . Parallel smooth curves, almost straight

lines, are obtained when the H^E are plotted against the product $\theta\phi$. The explanation of this simple result follows from an approximate theoretical expression of Rowlinson and collaborators for G^E for a Lorentz-Berthelot mixture (eq 4.5 of ref 2a), valid for $\theta, \phi \ll 1$. Introducing the parameter ξ we have the following expression for H^E

$$H^E/x_1 x_2 = [2(1 - \xi)(1 + \theta/2) + \theta^2/4 - \theta\phi/2](-U + TC_p) \quad (6a)$$

$$\simeq [2(1 - \xi) - \theta\phi/2](-U + TC_p) \quad (6b)$$

Expression 6b for H^E differs from those for G^E and V^E in having no term in ϕ^2 . In eq 6, U and C_p are the configurational energy and heat capacity of component 1, taken as reference liquid. For a liquid following the van der Waals equation of state

$$-U + TC_p = (a/V)/(2 - V/b) \simeq a/V \quad (7)$$

The various components in the systems considered here have $a/V \simeq 15,000$ J mol⁻¹. This is the value of $-U + TC_p$ used in conjunction with eq 6b to draw the straight lines shown in Figure 1. It is clear that the equation gives a reasonable approximation to the values calculated using the van der Waals combining rules and equation of state, *i.e.*, eq 1-4. The value of $-U + TC_p$ calculated from eq 7 with a obtained from the critical constants is certainly too low. A value of a from the thermal pressure coefficient of the liquid would give a more realistic value of $\simeq 30,000$ J mol⁻¹. However, changing $-U + TC_p$ for the reference liquid by a factor of 2 would merely change the slopes in Figure 1 by this factor leaving the correlation unchanged. Equation 6b suggests, as confirmed by the calculation, that H^E at a given concentration is an approximately linear function of $\theta\phi$ even when θ and ϕ are large. Thus, a small weakly interacting component should give a negative contribution in H^E when mixed with a large, more strongly interacting component. The experimental values for the systems are shown in Figure 1. The agreement with theory seems poor, but this may mean that very different values of ξ must be used for the different systems.

- (1) On leave of absence from Department of Chemistry, Indian Institute of Technology, Powai, Bombay 76, India.
- (2) (a) T. W. Leland, J. S. Rowlinson, and G. A. Sather, *Trans. Faraday Soc.*, **64**, 1447 (1968); (b) T. W. Leland, J. S. Rowlinson, G. A. Sather, and I. D. Watson, *ibid.*, **65**, 2034 (1969).
- (3) K. N. Marsh, *J. Chem. Thermodyn.*, **3**, 355 (1971).
- (4) (a) P. J. Flory, *J. Amer. Chem. Soc.*, **87**, 1833 (1965); (b) A. Abe and P. J. Flory, *ibid.*, **87**, 1838 (1965).
- (5) M. L. McGlashan, *Trans. Faraday Soc.*, **66**, 18 (1970).
- (6) K. N. Marsh, M. L. McGlashan, and C. Warr, *Trans. Faraday Soc.*, **66**, 2453 (1970).
- (7) R. R. Dreisbach, *Advan. Chem. Ser.*, **No. 15** (1955).

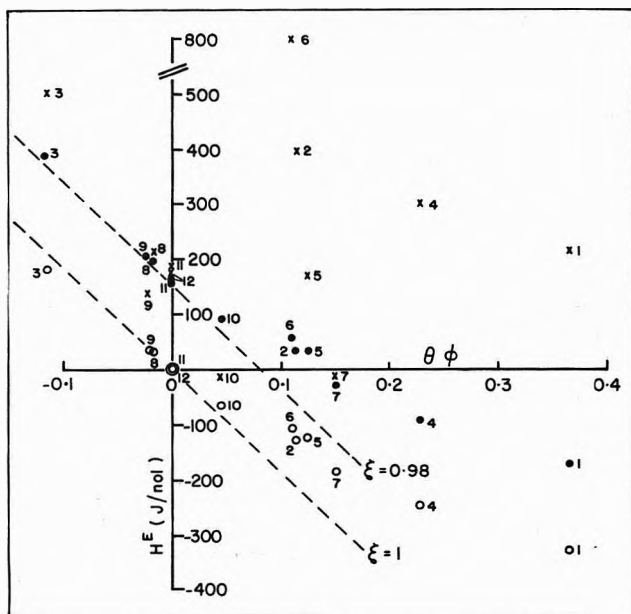


Figure 1. Heats of mixing H^E (J mol^{-1}) vs. $\theta\phi$, calculated H^E from van der Waals eq with $\xi = 1.0$; ●, calculated H^E from van der Waals eq with $\xi = 0.98$. Dotted lines corresponding to $\xi = 1.0$ and $\xi = 0.98$ are drawn for a value of $(-U + TC_p) = 15,000 \text{ J mol}^{-1}$. The crosses correspond to the experimental points.

Here, the series of systems OMCTS + *c*-C₅, + *c*-C₆, and + *c*-C₈ is of interest since the value of ξ might be considered to be the same throughout the series. The value of $\theta\phi$ changes from positive to negative in this series and the values of H^E do increase roughly as expected.

Marsh³ has measured all the excess functions for mixtures of OMCTS with cyclopentane, carbon tetrachloride, and benzene (systems 1, 5, and 6 of Table I). The van der Waals combining rules predict³ a striking consequence of the large size ratio, *viz.*, an extremely large contraction for each system, equimolar $V^E \approx -10 \text{ cm}^3/\text{mol}$. The experimental values, however, are respectively +0.046, -0.009, and -0.252 cm^3/mol . This discrepancy is clarified by recent Monte Carlo calculations⁸ which indicate that the van der Waals combining rules greatly overestimate the negative ϕ^2 term in V^E (see Table 9 of ref 8a). On the other hand, very good agreement⁸ is found with the single-fluid predictions of the other excess functions, and H^E is dominated by the $\theta\phi$ term.

Other Combining Rules

The new theory of Flory and collaborators⁴ introduces a parameter X_{12} corresponding to the combination of θ and ϕ in the Rowlinson theory. This parameter is energetic in origin. However, the combining rule for interaction energies is applied, not to the total interaction energies, ϵ_{11} and ϵ_{22} as in eq 4, but to these energies expressed per unit molecular surface (cf. eq 28 of ref 4a). The expression for X_{12} then becomes

$$\frac{X_{12}}{P_1^*} = 1 - 2\xi \left[\frac{P_2^*/s_2}{P_1^*/s_1} \right]^{1/2} + \frac{P_2^*/s_2}{P_1^*/s_1} = 2 \left[\frac{P_2^*/s_2}{P_1^*/s_1} \right] (1 - \xi) + \left\{ 1 - \left[\frac{P_2^*/s_2}{P_1^*/s_1} \right]^{1/2} \right\}^2 \quad (8)$$

The parameter P^* corresponds to a molecular interaction energy per unit molecular volume, and s to a molecular

TABLE I: Equimolar Heats and Molecular Parameters

System	$H^E, \text{J mol}^{-1}$	θ	ϕ	$10^2(X_{12}/P_1^*)$
1 cyclopentane + OMCTS	212 ^a	0.15	2.50	1.13
2 cyclohexane + OMCTS	397 ^b	0.06	1.94	0.08
3 cyclooctane + OMCTS	500 ^b	-0.09	1.23	0.25
4 <i>n</i> -hexane + OMCTS	300 ^b	0.16	1.47	1.46
5 carbon tetrachloride + OMCTS	163 ^a	0.05	2.29	0.02
6 benzene + OMCTS	790 ^a	0.04	2.51	0.05
7 cyclopentane + cyclooctane	-40 ^a	0.27	0.57	2.69
8 cyclohexane + <i>n</i> -hexane	218 ^c	-0.08	0.19	0.69
9 cyclohexane + neohexane	140 ^b	-0.12	0.16	1.51
10 neohexane + isooctane	-10 ^b	0.13	0.34	0.23
11 cyclohexane + isooctane	185 ^b	0.00	0.56	0.66
12 carbon tetrachloride + cyclohexane	166 ^d	0.00	0.12	0.02

^a See ref 3. ^b Unpublished results of V. T. Lam and P. Tancredi. ^c See S. Murakami and G. C. Benson, *J. Chem. Thermodyn.*, 1, 559 (1969). ^d See ref 11, p 136.

surface/volume ratio. Thus P^*/s corresponds to an energy/surface ratio and eq 8 shows X_{12} to have its origin in the relative weakness of this ratio for the contacts of unlike type. The Flory theory divides H^E into the "contact interaction" and "equation of state" terms. The X_{12} parameter appears explicitly in the first and implicitly (through T^* for the mixture) in the second of these terms. However, another division⁹ is possible where only the first term is due to X_{12} . The second term arises from a difference of thermal expansions between the components, and is usually negligible,⁹ except for polymer solutions or chain-molecule mixtures. Then (cf. eq 16 of ref 9)

$$H^E/x_1x_2 \approx (X_{12}/P_1^*)(-U + TC_p) \quad (9)$$

(The original equation contained a product of special concentration variables ψ_1X_2 which has been replaced here by x_1x_2 ; the configurational quantity $-U + TC_p$ is calculated for a single equivalent fluid using the properties of the pure components. For present purposes $-U + TC_p$ may be taken to refer to pure component 1.) The X_{12} parameter values listed in Table I were calculated using values of P^* obtained from equation of state data^{3,10} of the pure components and putting $\xi = 1$ in eq 8. There is no correlation between the experimental heats and the calculated X_{12}/P_1^* such as would be expected from eq 9. A value of ξ could be chosen for each system to fit eq 9 to H^E . Taking $-U + TC_p \approx 30,000 \text{ J mol}^{-1}$, a value of $\xi = 0.99$ instead of unity would raise H^E by 150 J mol^{-1} . The values of ξ required to fit the heats would thus not be unreasonably low. However, the variation of this parameter from system to system would be arbitrary, and several systems would have $\xi > 1$.

(8) (a) J. V. L. Singer and K. Singer, *Mol. Phys.*, 24, 357 (1972); (b) I. R. McDonald, *ibid.*, 24, 391 (1972).

(9) D. Patterson and G. De mas, *Disc. Faraday Soc.*, 49, 98 (1970).

(10) G. Allen, G. Gee, and G. J. Wilson, *Polymer*, 1, 456 (1960).

The parameter P^*/s through its significance as intermolecular energy/molecular surface may be related to the critical data and hence to θ and ϕ . We have

$$H^E/x_1x_2 = \{2(1 - \xi) + \theta^2/4 - \theta\phi/3 + \phi^2/9\}(-U + TC_p) \quad (10)$$

Here third powers of θ and ϕ and also products of θ and ϕ with $1 - \xi$ have been neglected. Also, Rowlinson¹¹ has pointed out that a similar expression may be obtained from the solubility parameter theory. For H^E

$$H^E/x_1x_2 = (\theta^2/4 - \theta\phi/2 + \phi^2/4)(-U + TC_p) \quad (11)$$

Equations 10 and 11 are similar to eq 6a except for the in-

clusion of a term in ϕ^2 . It is of interest that the Monte Carlo calculations^{8a} agree with the presence of a small ϕ^2 term. However, eq 10 and 11 gave poor correlations of the data in Table I. The van der Waals result, *i.e.*, the simple eq 6b seems more promising but further tests are desirable, particularly with mixtures containing a homologous series, *e.g.*, cycloalkanes + OMCTS.

Acknowledgment. We gratefully acknowledge the support of the National Research Council of Canada.

(11) J. S. Rowlinson, "Liquids and Liquid Mixtures," 2nd ed, Butterworths, London, 1969, p 339.

Ligand Field Theory of Metal Sandwich Complexes. Axial Field Spin-Orbit Perturbation Calculations for d^1 (d^9), d^2 (d^8), and d^3 (d^7) Configurations

Keith D. Warren

Department of Chemistry, University College, Cardiff, Wales, United Kingdom (Received October 12, 1972)

Complete ligand field perturbation calculations, including spin-orbit coupling, have been carried out for d^1 (d^9), d^2 (d^8), and d^3 (d^7) configurations in axial, $C_{\infty v}$, symmetry, using the strong field formalism. The application of the results to the interpretation of the d-d electronic spectra of metal sandwich complexes is discussed, with particular reference to the metallocenes of vanadium, cobalt, and nickel.

I. Introduction

The utility of the ligand field model for the assignment of the low-energy d-d transitions of metal sandwich complexes is now generally accepted,¹ and the approach has been used with some success for a number of the metallocenes. Thus, following the initial use of the method by Scott and Becker² for ferrocene, the spectra of both vanadocene and nickelocene were similarly interpreted by Prins and van Voorst.³ More recently Sohn, Hendrickson, and Gray⁴ have treated the spectra of ferrocene and ruthenocene, and of the ferrocenium and cobaltocenium ions on a ligand field basis, while nickelocene has been further treated by Scott and Matsen⁵ and by Pavlik, Cerny, and Maxova.⁶

It was shown by Scott and Matsen⁵ that metallocenes, bisarene metal compounds, and a number of related complexes, may all be treated on the basis of an effective axial ($C_{\infty v}$) symmetry, as long as only d^n configurations are involved, and currently full perturbation treatments, excluding spin-orbit effects, are available for d^2 (d^8) configurations in both the weak and the strong field schemes.^{5,6} Similar partial treatments for the d^3 configurations have been given by Prins and van Voorst³ in the strong field basis, and by Perumareddi⁷ and by DeKock and Gruen,⁸ in the weak field scheme, and for the d^6 and d^5 systems of ferrocene and the ferrocenium cation partial strong field matrices have also been calculated.⁴ However, only for

d^2 (d^8) systems is an axial field calculation including spin-orbit coupling available;⁹ this though is expressed in the weak field basis which is not very suitable for metallocenes and related species since the low nephelauxetic ratios found ($\beta \sim 0.5$) indicate that the eigenstates correspond to fairly well-defined strong field configurations.

Thus, in order to develop further the ligand field model for metal sandwich complexes the complete axial field energy matrices, including spin-orbit coupling, have been calculated in the strong field scheme for d^1 , d^2 , and d^3 (d^9 , d^8 , and d^7) configurations. Using these results the available data for the d-d spectra of the corresponding metallocenes have been analyzed, and general predictions made in those cases for which experimental spectra are lacking. In particular the present results permit a more detailed interpretation of the spin-forbidden transitions recently reported for nickelocene. In addition, relatively

- (1) C. J. Ballhausen and H. B. Gray, "Coordination Chemistry," Vol. 1, ACS Monograph No. 168, American Chemical Society Publications, Washington, D.C., 1971.
- (2) D. R. Scott and R. S. Becker, *J. Organometal. Chem.*, **4**, 409 (1965).
- (3) R. Prins and J. D. W. van Voorst, *J. Chem. Phys.*, **49**, 4665 (1968).
- (4) Y. S. Sohn, D. N. Hendrickson, and H. B. Gray, *J. Amer. Chem. Soc.*, **93**, 3603 (1971).
- (5) D. R. Scott and F. A. Matsen, *J. Phys. Chem.*, **72**, 16 (1968).
- (6) I. Pavlik, V. Cerny, and E. Maxova, *Collect. Czech. Chem. Commun.*, **35**, 3045 (1970).
- (7) J. R. Perumareddi, *J. Phys. Chem.*, **71**, 3144 (1971).
- (8) C. W. DeKock and D. M. Gruen, *J. Chem. Phys.*, **46**, 1096 (1967).
- (9) C. W. DeKock and D. M. Gruen, *J. Chem. Phys.*, **44**, 4387 (1966).

little work has been done on the magnetic susceptibilities and magnetic resonance phenomena of the above systems and their treatment by a complete spin-orbit perturbation method should serve to facilitate further progress.

II. Theory and Calculations

X-Ray diffraction studies have shown that the crystal-line metallocenes may occur either with the staggered, D_{5d} , conformation of the cyclopentadienyl rings, as in ferrocene and the other 3d complexes, or with the eclipsed, D_{5h} , arrangement found in ruthenocene and osmocene.¹⁰ For bisbenzenechromium, and probably for other bisbenzene complexes, a D_{6h} point group obtains,¹⁰ but it has been shown by Scott and Matsen⁵ that when only d^x configurations are considered all systems of C_n , C_{nh} , C_{nv} , D_{nd} , and D_{nh} symmetries may be treated in terms of a purely axial ($C_{\infty v}$) ligand field, as long as $n \geq 5$. The one-electron ligand field potential is then $V_{LF} = \lambda_1 V_0^0 + \lambda_2 V_0^2 + \lambda_3 V_0^4$ where the λ_i are expansion coefficients and the V_0^k spherical harmonics. The magnitudes of the λ_i are determined by the nature and geometrical arrangement of the ligands, but may be taken up into the axial parameters, D_s and D_t , thereby giving the same potential for all the symmetries considered.

In such a field the d orbitals split into three sets, $\sigma(d_{z^2}:d_0)$, $\pi(d_{xz}, d_{yz}:d_{\pm 1})$, and $\delta(d_{x^2-y^2}, d_{xy}:d_{\pm 2})$, with one-electron energies $E(\sigma) = 2D_s - 6Dt$, $E(\pi) = D_s + 4Dt$, and $E(\delta) = -2D_s - Dt$, following the definitions of Piper and Carlin.¹¹ Usually these one-electron core energies follow the order $\delta < \sigma \ll \pi$, and molecular orbital calculations¹² show the δ level to be strongly bonding, the σ level rather less so, and the π level appreciably antibonding. The gap between the δ and σ levels is though normally quite small (ca. 5 kK) and Hendrickson¹³ has recently shown that the SCF orbital energies may well follow the opposite order.

For the various d^x configurations the ligand field calculation reduces to the construction of the perturbation matrices of elements $H_{nm}' = \langle \Psi_n | H' | \Psi_m \rangle$ where

$$H' = \sum_{i < j} \frac{e^2}{r_{ij}} + \sum_i \xi(r_i) \vec{l}_i \cdot \vec{s}_i + \sum_i V_{LF}(r_i)$$

the sums over closed shells being excluded. Here the first term represents the interelectronic Coulombic repulsion, the second the spin-orbit interactions, and the last the axial ligand field, while the Ψ_n and Ψ_m are appropriate linear combinations of antisymmetrized determinantal functions. As explained in section I the strong field formalism appears the more useful for metallocenes and other sandwich complexes, and in this scheme the basis functions are the $C_{\infty v}$ ligand field orbital eigen functions d_z^2 ; d_{xz} , d_{yz} ; and $d_{x^2-y^2}$, d_{xy} . For the d^2 and d^3 cases the electrons occupy the one-electron d atomic orbitals in the configurations of a strong axial field, and appropriate symmetry adapted combinations are now constructed¹⁴ of antisymmetrized determinantal functions corresponding to the one-electron products. Spin is included only implicitly at this stage so as to distinguish between states of different multiplicity in the $C_{\infty v}$ field.

When spin-orbit coupling is introduced the symmetry states in the double group C_{∞}^* are found from the direct products of the orbital and spin components. Spin is now included explicitly and linear combinations of the $C_{\infty v}$ eigen functions taken which transform correctly in C_{∞}^* . The space-spin combinations are formed according to

Ballhausen¹⁴ and are constructed to be diagonal under C_{∞}^* ; for d^1 and d^3 the Kramers' doublets transform as $e^{\pm(n/2)\alpha}$, $n = 1, 3, 5, \dots$ and for d^2 as $e^{\pm n\alpha}$, $n = 1, 2, 3, \dots$. For d^1 of course the first term in H' vanishes and the orbital functions are at once invested with explicit spin to construct the C_{∞}^* functions.

The matrix elements of Coulombic repulsion for the d^2 and d^3 systems are listed in the Appendix¹⁵ in terms of the Racah parameters B and C ; the common terms in A are omitted from the diagonal elements. Also listed are the matrices of spin-orbit interaction for the d^1 , d^2 , and d^3 systems, in terms of the spin-orbit coupling constant, ξ , together with the matrix elements of the ligand field. These latter are entirely diagonal and are readily obtained as the sums of the appropriate one-electron core energies. The matrices of spin-orbit interaction and Coulombic repulsion are consistently phased and all have been checked by diagonalization in the weak field and jj limits. The matrices for the complementary configurations, d^9 , d^8 , and d^7 , are obtained from the d^1 , d^2 , and d^3 results, respectively, by reversing the signs of D_s , D_t , and ξ . In the Appendix are also included a correlation table between the groups C_{∞} and D_5 , tables of the splittings of the various weak field and strong field terms and configurations in $C_{\infty v}$ and C_{∞}^* , and the vector coupling coefficients for $C_{\infty v}$.

It is useful, finally, briefly to consider the types of sandwich complexes which possess effective axial ($C_{\infty v}$ or higher) symmetry, and which may therefore be treated on this ligand field model. These include bis- π -cyclopentadienyl complexes (metallocenes), bis- π -benzene compounds, mixed π -carbocyclic systems, such as π -C₅H₅ Cr π -C₇H₇ (C₇H₇ = cycloheptatrienyl), and a number of di- π -dicarbollyl, M(B₉C₂H₁₁) and mixed π -carbocyclic- π -dicarbollyl systems. In these examples the appropriate d^x configurations are deduced by assigning formal charges of -1, 0, +1, and -2 to the π -C₅H₅, π -C₆H₆, π -C₇H₇, and π -C₂B₉H₁₁ ligands, respectively.

III. Results and Discussion

$d^1(d^9)$ Configurations. The spin-orbit results for this simple case do not appear to have been given before. To the first order the ${}^2\Pi(\pi)$ and ${}^2\Delta(\delta)$ states are split by ξ and 2ξ , respectively, as shown in Figures 1 and 2; here the usual energetic order of levels, $\delta < \sigma \ll \pi$, is assumed. For a d^1 system therefore an unsplit low-energy transition, ${}^2\Delta \rightarrow {}^2\Sigma^+$, followed by an appreciably higher ${}^2\Delta \rightarrow {}^2\Pi$ excitation, split by ξ , would be expected. Known examples of d^1 systems include^{16,17} $(\pi$ -C₅H₅)₂Ti⁺ and $(\pi$ -C₅H₅)₂V²⁺, but no electronic spectra have been recorded. However, although ξ would be small, a study of these complexes would be of help in resolving the anomalies concerning their magnetic properties.

(10) G. E. Coates, M. L. H. Green, and K. Wade, "Organometallic Compounds," Vol. II, Methuen, London, 1968, Chapters 4 and 5 and references therein cited.

(11) T. S. Piper and R. L. Carlin, *J. Chem. Phys.*, **33**, 1208 (1960).

(12) M. F. Rettig and R. S. Drago, *J. Amer. Chem. Soc.*, **91**, 3432 (1969).

(13) D. N. Hendrickson, *Inorg. Chem.*, **11**, 1161 (1972).

(14) C. J. Ballhausen, "Introduction to Ligand Field Theory," McGraw-Hill, New York, N. Y., 1962.

(15) The Appendix will appear following these pages in the microfilm edition of this volume of the journal. Single copies may be obtained from the Business Operations Office, Books and Journals Division, American Chemical Society, 1155 Sixteenth St., N.W., Washington, D. C. 20036. Remit check or money order for \$4.00 for photocopy or \$2.00 for microfiche, referring to code number JPC-73-1681.

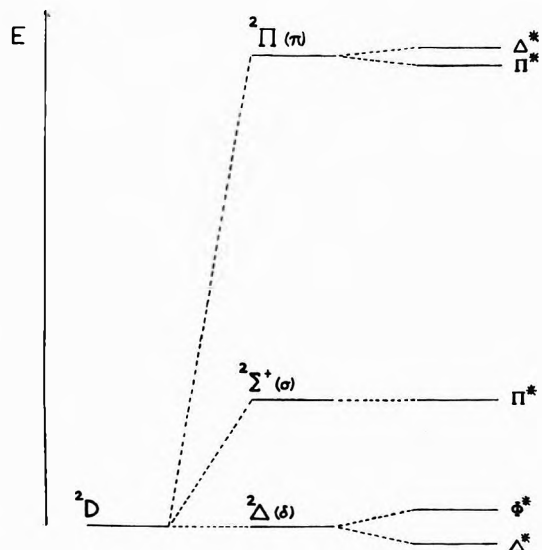


Figure 1. Energy level diagram for a d^1 system in C_{∞}^* symmetry. (In Figures 1–6 are shown the splittings of the free-atom terms due to a field of $C_{\infty v}$ symmetry, together with the first-order spin-orbit effects on these levels. In Figures 1 and 2 the energy scale assumes $Ds = 2Dt$, and the spin-orbit splittings are schematic only, and not to scale. In Figures 2, 4, and 6 the strong field configurations are expressed in terms of orbital vacancies.)

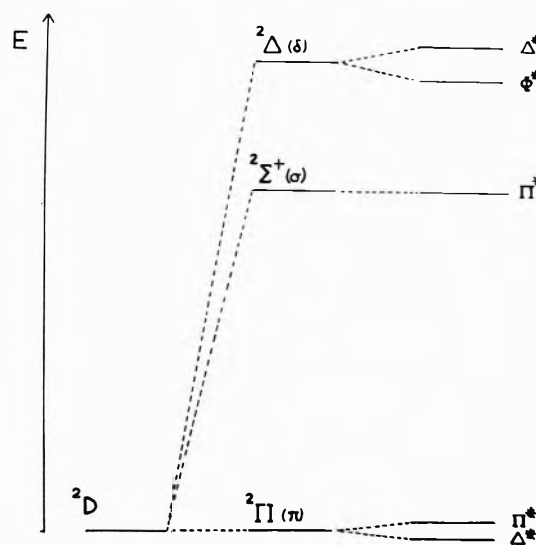


Figure 2. Energy level diagram for a d^9 system in C_{∞}^* symmetry.

is now only ξ as opposed to 2ξ for Ti(III) or V(IV), so that despite the larger spin-orbit coupling constant a Jahn-Teller effect could again be operative.

$d^2(d^8)$ Configurations. The discussion of results for these systems will be essentially restricted to considerations regarding spin-orbit effects since treatments excluding this feature have already been presented.^{5,6} For the d^2 configuration $(\pi-C_5H_5)_2Ti$, $(\pi-C_5H_5)_2Zr$, and $[(\pi-C_5H_5)_2V]^+$ are known,^{17,22,23} but no spectroscopic data are available and it is doubtful whether titanocene and zirconocene are true metal sandwich complexes; both are diamagnetic and dimeric and Brintzinger and Bartell²⁴ suggest that axial symmetry is not a stable arrangement for d^2 molecules, a bent structure being preferred. On the other hand, the magnetic moment of 2.86 BM, virtually the spin-only value, found for $[(\pi-C_5H_5)_2V]^+$ clearly indicates a linear structure with a $^3\Sigma^-(\delta^2)$ ground state. At low field strengths the $^3\Delta(\sigma\delta)$ level lies lowest, as shown in Figure 3, but for $Dt/B \sim 5$ the ground state becomes $^3\Sigma^-(\delta^2)$ as found for the vanadocinium ion.

For d^8 systems $(\pi-C_5H_5)_2Ni$, $(\pi-C_6(CH_3)_6)_2Fe$, and $[(\pi-C_6(CH_3)_6)_2Co]^+$ are known,^{25–27} all of which show magnetic moments close to the spin-only result (2.83 BM), thereby pointing to $^3\Sigma^-(\pi^2)$ ground states. (The d^8 and d^7 configurations are throughout represented in terms of the vacancies in the d shell.) Unfortunately, only for nickelocene have spectroscopic results been reported.

Thus the magnetic moments reported^{16,17} for $[(\pi-C_5H_5)_2Ti]^+$ [picrate]⁻ and for $[(\pi-C_5H_5)_2V]^{2+} 2Cl^-$, 2.29 and 1.85 BM, respectively, both exceed the spin-only value of 1.73 BM, and suggest an orbital contribution to the value. Nevertheless, for the vanadium compound (and for other $[(\pi-C_5H_5)_2Ti]^+$ species) an almost isotropic g value close to 2 has been found,¹⁸ which is readily shown to be inconsistent with a $^2\Delta$ ground state. Thus, using the space-spin adapted functions derived as in section II, the matrix elements of $\hat{l}_z + 2\hat{s}_z$ are found to act in a contrary sense, while those of $\hat{l}_x + 2\hat{s}_x$ and of $\hat{l}_y + 2\hat{s}_y$ both vanish. Consequently one obtains (cf. ref 19), assuming an orbital reduction factor, k , of unity, $g_{\parallel} = 2$ and $g_{\perp} = 0$. For many other $[(\pi-C_5H_5)_2Ti]^+$ salts though, nearly isotropic g values close to 2 are also found,¹⁸ and a magnetic moment of 1.68 BM, very close to the spin-only value, has been obtained²⁰ for $[(\pi-C_5H_5)_2Ti]^+ CNO^-$. It therefore seems that for most d^1 systems, the ground state is an orbital singlet, due either to a reversal of the usual one-electron energy level order (giving a $^2\Sigma^+$ ground state), or to the systems being distorted from axial symmetry to a bent C_{2v} structure. Such a distortion could conceivably be due to a Jahn-Teller, or pseudo-Jahn-Teller effect, since, although the lowest level for a $^2\Delta$ ground state would be the Δ^* Kramers' doublet, the small value of ξ would lead to it being only slightly separated from the Φ^* level.

Examples of d^9 systems are scarce, only $(\pi-C_6(CH_3)_6)_2Co$ being well established;²¹ no spectroscopic data are available but again two transitions would be expected, now quite close together, corresponding to the $^2\Pi \rightarrow ^2\Sigma^+$ and $^2\Pi \rightarrow ^2\Delta$ excitations. For Co the spin-orbit coupling constant is quite appreciable (ca. 600 cm^{-1}) so that the splitting of the $^2\Delta$ level could amount to 1 kK or so. The magnetic moment of 1.86 BM is somewhat above the spin-only value and consistent with the expected orbital contribution, but the nonzero dipole moment again suggests a bent C_{2v} structure. The ground-state splitting

- (16) G. Wilkinson and F. A. Cotton, *Progr. Inorg. Chem.*, **1**, 1 (1959).
- (17) G. Wilkinson and J. M. Birmingham, *J. Amer. Chem. Soc.*, **76**, 4281 (1954).
- (18) B. A. Goodman and J. B. Raynor, *Advan. Inorg. Chem. Radiochem.*, **13**, 136 (1970).
- (19) E. D. German and M. E. Dyatkina, *Zh. Strukt. Chim.*, **6**, 898 (1965).
- (20) R. Coultts and P. C. Wailes, *Inorg. Nucl. Chem. Lett.*, **3**, 1 (1967).
- (21) E. O. Fischer and H. H. Lindner, *J. Organometal. Chem.*, **2**, 222 (1964).
- (22) G. W. Watt, L. J. Baye, and F. O. Drummond, *J. Amer. Chem. Soc.*, **88**, 1138 (1966).
- (23) G. W. Watt and F. O. Drummond, *J. Amer. Chem. Soc.*, **88**, 5926 (1966).
- (24) H. H. Brintzinger and L. S. Bartell, *J. Amer. Chem. Soc.*, **92**, 1105 (1970).
- (25) G. Wilkinson, P. L. Pauson, and F. A. Cotton, *J. Amer. Chem. Soc.*, **76**, 1970 (1954).
- (26) E. O. Fischer and F. Rohrscheid, *Z. Naturforsch. B*, **17**, 483 (1962).
- (27) E. O. Fischer and H. H. Lindner, *J. Organometal. Chem.*, **1**, 307 (1964).

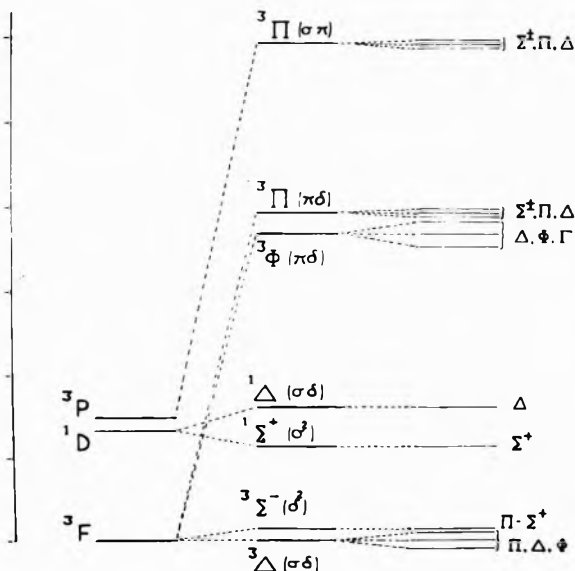


Figure 3. Energy level diagram for a d^2 system in C_{∞}^* symmetry; $Dt = 0.55Ds$, $Dt/B = 4.50$, $C/B = 4.19$. (In Figures 3–6 the energy scale is given in units of B , each division representing 10 units. The first-order spin-orbit effects are again shown in schematic form only, and are not to scale. Where energy levels are coincident this is indicated by hyphenating the levels involved, and the double group representations arising from the spin-orbit splittings of a given $C_{\infty v}$ level are listed, separated by commas, in order of ascending energy. The symbol Σ^{\pm} indicates a coincidence of the Σ^+ and Σ^- representations.)

For d^8 systems three spin-allowed d-d transitions corresponding to one-electron excitations would be expected, *viz.* ${}^3\Sigma^-(\pi^2) \rightarrow {}^3\Pi(\sigma\pi)$, ${}^3\Sigma^-(\pi^2) \rightarrow {}^3\Phi(\pi\delta)$, and ${}^3\Sigma^-(\pi^2) \rightarrow {}^3\Pi(\pi\delta)$. The ${}^3\Pi(\sigma\pi)$, ${}^3\Pi(\pi\delta)$, and ${}^3\Phi(\pi\delta)$ states are respectively split by ξ , ξ , and 3ξ in the first order, as shown in Figure 4, while the remaining triplet levels, ${}^3\Sigma^-(\pi^2)$, ${}^3\Sigma^-(\delta^2)$, and ${}^3\Delta(\sigma\delta)$, are respectively split by 0, 0, and 2ξ . The ${}^3\Sigma^-(\pi^2)$ ground state (an orbital singlet) is also Jahn-Teller resistant; spin-orbit coupling splits it into $\Sigma^+ + \Pi$ of which the former proves to lie slightly the lower.

The relative positions of the singlet levels depend strongly on the C/B values chosen and these are shown, together with the Ds/Dt ratios in the appropriate figure. The former parameter was taken according to the values of Tanabe and Sugano²⁸ and the latter was fixed so as to lie within the generally encountered range 0.5–0.6.

The electronic spectrum of nickelocene has been studied by several workers,^{5,6,11} and all agree in assigning three bands, at around 14.4, 16.8, and 23.0 kK, as the spin-allowed d-d transitions, ${}^3\Sigma^-(\pi^2) \rightarrow {}^3\Pi(\sigma\pi)$, ${}^3\Sigma^-(\pi^2) \rightarrow {}^3\Phi(\pi\delta)$, and ${}^3\Sigma^-(\pi^2) \rightarrow {}^3\Pi(\pi\delta)$, respectively. The two lowest lying transitions would be expected to lie fairly close together since the separation depends largely on the δ - σ energy gap implied by the Ds and Dt parameters, but in fact the bands overlap substantially and the positions of the maxima are difficult to determine. For nickelocene the free ion value of ξ is of the order of 600 cm^{-1} so that spin-orbit coupling may play an appreciable part in this situation since the ${}^3\Phi$ level might be split by as much as 1.5–2.0 kK, thereby contributing significantly to the overlapping of the two bands. The position of the band maximum for the ${}^3\Sigma^-(\pi^2) \rightarrow {}^3\Pi(\pi\delta)$ transition is also hard to ascertain because of its proximity to the charge-transfer region. In this case the inflection corresponding to the

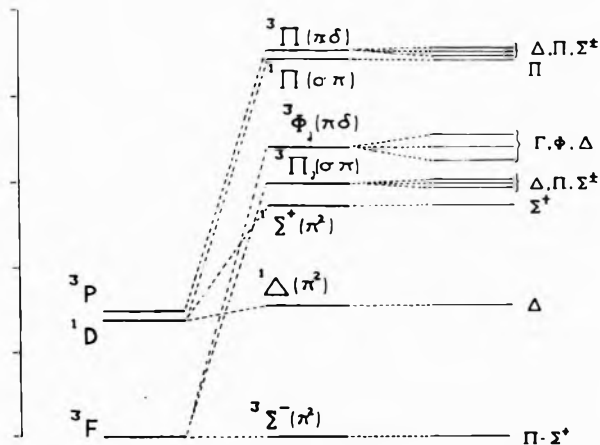


Figure 4. Energy level diagram for a d^8 system in C_{∞}^* symmetry; $Dt = 0.55Ds$, $Dt/B = 3.50$, $C/B = 4.71$.

transition is displaced to higher energy, thus giving misleadingly high values for B and β , and for all the d-d bands Gaussian analysis is necessary to establish the peak positions.

Consequently the identification of spin-forbidden transitions would be of particular help in obtaining fitting parameters, and Pavlik, *et al.*,⁶ have identified a small inflection at 11.7 kK, on the low-energy side of the 14.4-kK band, as the ${}^3\Sigma^-(\pi^2) \rightarrow {}^1\Delta(\pi^2)$ excitation. By Gaussian analysis they further deduced the presence of the ${}^3\Sigma^-(\pi^2) \rightarrow {}^1\Sigma^+(\pi^2)$ band at 19.2 kK, but their assignments for these two bands depend entirely upon the value of C/B adopted (a value close to 7 being adopted rather than the more usual $C/B \sim 4$ –5).

Moreover, both the ${}^3\Sigma^-(\pi^2) \rightarrow {}^1\Delta(\pi^2)$ and the ${}^3\Sigma^-(\pi^2) \rightarrow {}^1\Sigma^+(\pi^2)$ transitions represent intra-sub-shell excitations which should appear as rather sharp narrow bands. While the 11.7-kK inflection seems to represent quite a narrow peak the 19.2-kK band is calculated⁶ to have a half-height width of some 2 kK, which would be more consistent with a ${}^3\Sigma^-(\pi^2) \rightarrow {}^1\Pi(\sigma\pi)$ assignment. A C/B value of *ca.* 4–5 would permit this alternative interpretation, together with the attribution of the 11.7-kK band to the ${}^3\Sigma^-(\pi^2) \rightarrow {}^1\Sigma^+(\pi^2)$ excitation, and would predict the ${}^3\Sigma^-(\pi^2) \rightarrow {}^1\Delta(\pi^2)$ band to lie at still lower energies in the region of 7 kK. Thus the detection or otherwise of this lowest band would afford a strong indication of the appropriate C/B value.

The uncertainties concerning the positions of the band maxima of the spin-allowed transitions and the assignment of the 19.2-kK band render it difficult to select a definitive set of parameters to fit all the bands. The values $Ds = 3023 \text{ cm}^{-1}$, $Dt = 1663 \text{ cm}^{-1}$, $B = 475 \text{ cm}^{-1}$, and $C/B = 4.71$ provide a reasonable compromise. Assuming ξ to be reduced below the free ion value by the same factor as B yields a value of 301 cm^{-1} and the results obtained are given in Table I. Some improvement in the fit could be obtained using a lower C/B value but preference was given to adopting the Tanabe-Sugano figure.

From the eigenvectors the proportion of triplet character may be deduced for the ${}^1\Sigma^+(\pi^2)$ and ${}^1\Delta(\pi^2)$ levels. The former state shows about 1.1% triplet nature, mostly by interaction with the ${}^3\Pi(\sigma\pi)$ level, and the latter some 0.35% triplet nature, by mixing with both the ${}^3\Pi(\sigma\pi)$ and

(28) Y. Tanabe and S. Sugano, *J. Phys. Soc. Jap.*, **9**, 753, 766 (1954).

TABLE I: Fitting Parameters for $(\pi\text{-C}_5\text{H}_5)_2\text{Ni}^a$

Level	Calcd	Obsd	Level	Calcd	Obsd
$^3\Sigma^-(\pi^2)$			$^3\Phi(\pi\delta)$		
Σ^+	0.00		Γ	15.73	
Π	0.0 ⁻		Φ	16.18	16.8
$^1\Delta(\pi^2)$			Δ	16.64	
Δ	7.4 ^c		$^1\Pi(\sigma\pi)$		
$^1\Sigma^+(\pi^2)$			Π	21.22	19.2
Σ^+	13.05	11.7	$^3\Pi(\pi\delta)$		
$^3\Pi(\sigma\pi)$			Δ	21.39	
Δ	14.03		Σ^-	21.70	
Π	14.17	14.4	Σ^+	21.70	23.0
Σ^-	14.33		Π	21.73	
Σ^+	14.34				

^a $Dt = 1663 \text{ cm}^{-1}$, $Ds = 3023 \text{ cm}^{-1}$, $B = 475 \text{ cm}^{-1}$, $\xi = 301 \text{ cm}^{-1}$, $C/B = 4.71$.

$^3\Phi(\pi\delta)$ states. Making allowance for the much narrower band widths expected for the intra-sub-shell transitions, one would then estimate $\epsilon \sim 2\text{--}10$ for $^3\Sigma^-(\pi^2) \rightarrow ^1\Sigma^+(\pi^2)$, in good agreement with the experimental result, and $\epsilon \sim 0.5\text{--}4$ for $^3\Sigma^-(\pi^2) \rightarrow ^1\Delta(\pi^2)$. In the latter case therefore it is reasonable to expect direct optical detection of the transition should the proposed assignments be correct.

$d^3(d^7)$ Configurations. Examples of d^3 systems having axial symmetry include^{29,30} $(\pi\text{-C}_5\text{H}_5)_2\text{V}$, $[(\pi\text{-C}_5\text{H}_5)_2\text{Cr}]^+$, and $[(\pi\text{-C}_5(\text{C}_6\text{H}_5)_5)_2\text{Mo}]^+$, but only for the first two are spectra recorded. The d-d bands in vanadocene are well established, but for the chromocinium ion the extinction coefficients of the lowest energy transitions are rather high $\epsilon \sim 500$, and they may not therefore represent d-d transitions.

For all feasible ligand field strengths a $^4\Sigma^-(\sigma\delta^2)$ level is found to lie lowest, and this assignment for the ground state is confirmed by the observation of essentially the spin-only value of the magnetic moment (3.87 BM) for both $(\pi\text{-C}_5\text{H}_5)_2\text{V}$ and $[(\pi\text{-C}_5\text{H}_5)_2\text{Cr}]^+$. Three spin-allowed transitions corresponding to one-electron excitations should therefore be observed, namely, $^4\Sigma^-(\sigma\delta^2) \rightarrow ^4\Pi(\pi\delta^2)$, $^4\Sigma^-(\sigma\delta^2) \rightarrow ^4\Phi(\sigma\pi\delta)$, and $^4\Sigma^-(\sigma\delta^2) \rightarrow ^4\Pi(\sigma\pi\delta)$ (see Figure 5). Transitions to the higher lying $^4\Delta(\pi^2\delta)$ and $^4\Sigma^-(\sigma\pi^2)$ states, which represent two-electron jumps, should be weak and would in any case probably be obscured by charge-transfer bands.

The $^4\Pi(\pi\delta^2)$, $^4\Pi(\sigma\pi\delta)$, and $^4\Phi(\sigma\pi\delta)$ levels show first-order spin-orbit splittings of ξ , ξ , and 3ξ , respectively, while the $^4\Sigma^-(\sigma\pi^2)$ and $^4\Delta(\pi^2\delta)$ states are respectively unsplit and split by 2ξ . For the low-lying doublet levels, $^2\Gamma(\sigma\delta^2)$, $^2\Delta(\delta^3)$, $^2\Sigma^+(\sigma\delta^2)$, $^2\Sigma^-(\sigma\delta^2)$, and $^2\Delta(\sigma^2\delta)$, the corresponding splittings are 0, 2ξ , 0, 0, and 2ξ . As for d^8 systems the Φ state is split by 3ξ but here this will hardly contribute to any extensive band overlapping (e.g., in vanadocene) because of the small ξ value for V(II).

Prins and van Voorst³ fitted the d-d bands of vanadocene using the parameters $Ds = 3543 \text{ cm}^{-1}$, $Dt = 2074 \text{ cm}^{-1}$, and $B = 440 \text{ cm}^{-1}$. Assuming the same reduction of the free ion spin-orbit coupling constant as before one obtains $\xi = 99 \text{ cm}^{-1}$, which with the above parameters and a C/B value²⁷ of 4.31 yields the results shown in Table II. While the positions of the quartet states involve only the Racah parameter, B , (in addition to Ds , Dt , and ξ) the heights of the doublet states above the ground level also depend upon the C/B ratio. Using the Tanabe-Suga-

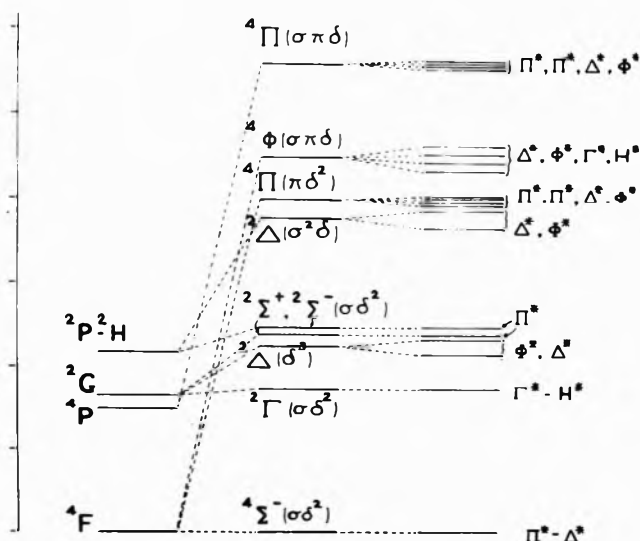


Figure 5. Energy level diagram for a d^3 system in C_∞^s symmetry; $Dt = 0.585Ds$, $Dt/B = 4.70$, $C/B = 4.31$.

TABLE II: Fitting Parameters for $(\pi\text{-C}_5\text{H}_5)_2\text{V}^a$

Level	Calcd	Obsd	Level	Calcd	Obsd
$^4\Sigma^-(\sigma\delta^2)$			$^4\Pi(\pi\delta^2)$		
Π^*	0.00		Π^*	17.67	
Δ^*	0.00		Π^*	17.70	
$^2\Gamma(\sigma\delta^2)$			Δ^*	17.73	17.7
H^*	7.57		Φ^*	17.77	
Γ^*	7.57		$^4\Phi(\sigma\pi\delta)$		
$^2\Delta(\delta^3)$			Δ^*	19.63	
Δ^*	10.04		Φ^*	19.73	19.7
Φ^*	10.06		Γ^*	19.83	
$^2\Sigma^+(\sigma\delta^2)$			H^*	19.93	
Π^*	10.54		$^4\Pi(\sigma\pi\delta)$		
$^2\Sigma^-(\sigma\delta^2)$			Π^*	24.59	
Π^*	10.91		Π^*	24.62	24.6
$^2\Delta(\sigma^2\delta)$			Δ^*	24.65	
Φ^*	16.59		Φ^*	24.69	
Δ^*	16.61				

^a $Dt = 2068 \text{ cm}^{-1}$, $Ds = 3535 \text{ cm}^{-1}$, $B = 440 \text{ cm}^{-1}$, $\xi = 99 \text{ cm}^{-1}$, $C/B = 4.31$.

no value for this the lowest doublet states arising from $(\sigma\delta^2)$ and (δ^3) comprise a closely spaced group which for all but rather weak ligand fields lie appreciably below the lowest excited quartet state. Consequently only the rather higher $^2\Delta(\sigma^2\delta)$ level will exhibit any significant quartet character; in fact this level does not interact directly with the lowest quartet, $^4\Pi(\pi\delta^2)$, but has matrix elements of $-\frac{1}{2}\sqrt{6}\xi$ and $\frac{1}{2}\sqrt{2}\xi$ with the $^4\Phi(\sigma\pi\delta)$ state in the Δ^* and Φ^* representations, respectively. Inspection of the eigenvalues obtained by diagonalization of the complete matrices shows the $^2\Delta(\sigma^2\delta)$ level to have about 0.05% quartet character. If the δ and σ levels lie close together a $^4\Sigma^-(\sigma\delta^2) \rightarrow ^2\Delta(\sigma^2\delta)$ excitation should represent an effectively intra-sub-shell transition, and should therefore show a much narrower band width than the spin-allowed excitations. These latter show extinction coefficients of the order of 10^2 so that one thus estimates $\epsilon \sim 0.1\text{--}1$ for the transition in question. This therefore is the only spin-

(29) E. O. Fischer and K. Ulm, *Chem. Ber.*, **95**, 692 (1962).

(30) W. Hubel and R. Merenyi, *J. Organometal. Chem.*, **2**, 213 (1964).

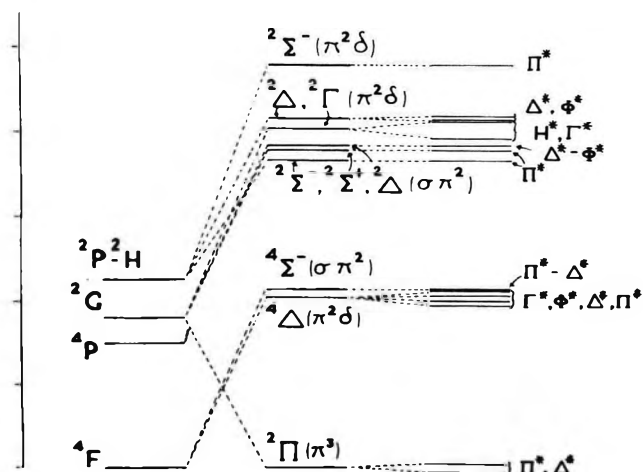


Figure 6. Energy level diagram for a d^7 system in C_{∞}^* symmetry; $Dt = 0.55Ds$, $Dt/B = 4.70$, $C/B = 4.63$.

forbidden band which is likely to be detected readily by optical means although some of the lower levels might be accessible by indirect (*e.g.*, photochemical) methods.

Known examples of d^7 systems include $(\pi-C_5H_5)_2Co$, $[(\pi-C_5H_5)_2Ni]^+$, $[(\pi-C_6(CH_3)_6)_2Fe]^+$, and $[(\pi-C_6(CH_3)_6)_2Co]^{2+}$, all of which show^{21,27,31,32} magnetic moments close to the spin-only value for one unpaired electron. In these cases therefore the ligand field is strong enough for the ground state to be the low-spin $^2\Pi(\pi^3)$ level, rather than the high-spin $^4\Delta(\pi^2\delta)$ state. In these circumstances the lowest spin-allowed d-d transitions take place from the $^2\Pi(\pi^3)$ state to a group of closely juxtaposed levels arising from the $(\sigma\pi^2)$ and $(\pi^2\delta)$ configurations, *viz.*, $^2\Sigma^-$, $^2\Sigma^+$, and $^2\Delta(\sigma\pi^2)$, followed by $^2\Gamma$ and $^2\Delta(\pi^2\delta)$; slightly above these lies the $^2\Sigma^-(\pi^2\delta)$ level, and rather higher again the $^2\Delta$ and $^2\Sigma^+(\pi^2\delta)$ states, as shown in Figure 6. Spin-orbit coupling will split these levels respectively by 0, 0, 0, 2ξ , $\frac{2}{3}\xi$, 0, 2ξ , and 0, but this would not readily be detected because of the proximity of these levels to each other. In the low-spin situation two low-lying quartet levels are also predicted, $^4\Sigma^-(\sigma\pi^2)$ and $^4\Delta(\pi^2\delta)$, split by 0 and 2ξ , respectively, whose heights above the ground state once more depend on the C/B ratio.

The only spectroscopic data available are those of Ammeter and Swalen³³ for cobaltocene; the recorded spectrum was not well resolved and assignments were made by averaging the fitting parameters for ferrocene and nickelocene and calculating a number of diagonal strong field

TABLE III: Fitting Parameters for $(\pi-C_5H_5)_2Co^0$

Level	Calcd	Obsd	Level	Calcd	Obsd
$^2\Pi(\pi^3)$			$^2\Sigma^+(\sigma\pi^2)$		
Π^*	0.00		Π^*	18.73	
Δ^*	0.26		$^2\Delta(\sigma\pi^2)$		
$^4\Delta(\pi^2\delta)$			Δ^*	18.76	
Γ^*	9.92		Φ^*	18.76	
Φ^*	10.09		$^2\Gamma(\pi^2\delta)$		
Δ^*	10.26		H^*	19.51	17.0, 18.3 (sh)
Π^*	10.44		Γ^*	20.03	
$^4\Sigma^-(\sigma\pi^2)$			$^2\Delta(\pi^2\delta)$		
Π^*	10.45		Φ^*	20.37	
Δ^*	10.45		Δ^*	20.47	
$^2\Sigma^-(\sigma\pi^2)$			$^2\Sigma^-(\pi^2\delta)$		
Π^*	17.83		Π^*	23.38	

$^a Dt = 2275 \text{ cm}^{-1}$, $Ds = 4180 \text{ cm}^{-1}$, $B = 484 \text{ cm}^{-1}$, $\xi = 257 \text{ cm}^{-1}$, $C/B = 4.63$.

energy differences. Adopting this approach here one obtains the parameters $Ds = 4180 \text{ cm}^{-1}$, $Dt = 2275 \text{ cm}^{-1}$, and $B = 484 \text{ cm}^{-1}$, which together with the values $C/B = 4.63$ and $\xi = 257 \text{ cm}^{-1}$ (derived on the same basis as before) yield the results shown in Table III. Thus the doublet states arising from the $(\sigma\pi^2)$ and $(\pi^2\delta)$ configurations mostly lie between 17 and 24 kK, *i.e.*, slightly higher than the experimental data indicate, but are in good agreement with the values calculated by Ammeter and Swalen and constitute a satisfactory fit in the absence of more precise spectroscopic results. The higher lying $^2\Delta$ and $^2\Sigma^+(\pi^2\delta)$ levels are not listed in the table since such transitions would probably lie in the charge-transfer region.

Below the doublet states the two quartet levels are predicted to lie at around 10 kK. The eigenvectors from the diagonalization of the complete matrices indicate that spin-orbit coupling introduces about 0.1% of doublet character into these states in some cases, most of this being due to mixing with the $^2\Pi(\pi^3)$ level. However, the spin-forbidden transitions $^2\Pi(\pi^3) \rightarrow ^4\Delta(\pi^2\delta)$ and $^2\Pi(\pi^3) \rightarrow ^4\Sigma^-(\sigma\pi^2)$ both correspond to a change of occupation of the strongly antibonding π level, and should therefore possess fairly large bandwidths. Consequently these two bands would be expected to be very weak with $\epsilon \sim 0.1$.

(31) E. O. Fischer and W. Hafner, *Z. Naturforsch. B*, **8**, 444 (1953).

(32) G. Wilkinson, *J. Amer. Chem. Soc.*, **74**, 6146 (1952).

(33) J. H. Ammeter and J. D. Swalen, *J. Chem. Phys.*, **57**, 678 (1972).

Revised Group Additivity Parameters for the Enthalpies of Formation of Oxygen-Containing Organic Compounds

H. K. Eigenmann,¹ D. M. Golden,* and S. W. Benson

Department of Thermochemistry and Chemical Kinetics, Stanford Research Institute, Menlo Park, California 94025
(Received December 4, 1972)

Data on ΔH_f° , the standard enthalpies of formation, in the gas phase for over 300 oxygen-containing compounds are critically examined. Internal consistencies within this set are scrutinized from the viewpoint of group additivity principles. New values for the contributions of groups to ΔH_f° , as well as higher order corrections, are obtained from multilinear regression analyses of the data. For alcohols and ethers observed values and group additivity values agree to within ± 1.0 kcal/mol, which is about the experimental precision. The data on these classes are very self-consistent. Very nearly the same is true of aldehydes and ketones. Major discrepancies exist in the classes of acids and esters and a few key compounds deviate seriously from other members of their class.

1. Introduction

In this report we wish to revise some of the group values for enthalpies of formation reported in our general review of group additivity² in order to take into account the increase in data in the past 4–5 years, and the appearance of two excellent reviews of thermochemical data of organic compounds.³ The report is focused on oxygen-containing groups because lack of thermochemical data about esters, acids, and anhydrides in 1968 produced some ambiguities in the related group values. Similar revisions for entropy and heat capacity for this class of compounds⁴ will hopefully be undertaken in the near future.

For a discussion of the basic concept of additivity rules for the estimation of thermochemical properties, the reader is referred to either the previous report or the original paper by Benson and Buss.⁵ Nomenclature and general presentation are maintained as in ref 2a.

2. General Discussion

Sources for enthalpies of formation are the two mentioned reviews of Stull, Westrum, and Sinke^{3a} and Pilcher and Cox,^{3b} and a systematic inspection of the Bulletins of Thermodynamics and Thermochemistry, No. 10–15 (1967–1972). For the search on more recent results (1971–1972), the appropriate journals have been surveyed. The results found in either source, although sometimes questionable, were included in the first calculation of group values. The procedure used to eliminate inaccurate values is described below. Estimates of enthalpies of vaporization were generally adopted from the original papers and the two reviews mentioned above.

In order to facilitate handling of the ~ 300 enthalpies of formation, these were grouped for the calculation: one set containing only alcohols and ethers (*i.e.*, no carbonyls), the other covering aldehydes, ketones, acids, anhydrides, and esters. In each set, the most frequently occurring groups were determined by a multilinear regression analysis (MLR). Adopting the group values obtained by MLR, the less common groups could be evaluated. For all calculations, group values for nonoxygen containing groups were taken from the previous report.^{2a}

Assuming group additivity to be correct, it was possible to use multilinear regression in the process of eliminating questionable data; all data producing large deviations in

the predicted value after regression were subject to critical examination and were possibly excluded, if either the enthalpy of vaporization is estimated or the measurement dates back before 1940. Then, without the excluded compounds, MLR was used to reevaluate the groups. This procedure was applied several times and resulted in the group values discussed in section 3.



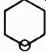
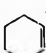
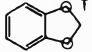
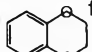
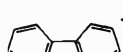
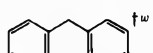




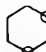


In our previous reports² several groups containing elements other than C, H, and O were assigned by analogy with oxygen group values (*i.e.*, $C_B-S \equiv C_B-O$). As long as these other classes of compounds are not revised separately, the values given in those reports must still be used.

3. Results

Tables I and II present the group values as obtained in this work. Table III-a–i⁶ compare measured and estimated values for the compounds used in the first calculation (including compounds eliminated by MLR). Compounds used in the final MLR are marked by an asterisk, those excluded by a dagger; compounds without a mark have been used for the calculation of the less frequently occurring groups. The original references for the measured data are given with the exception of those found in either review,³ which are marked as either 3a or 3b, respectively. In the following subsections these results are discussed with emphasis on chosen values for the groups and deviations from group additivity.

- (1) International Fellow supported by Ciba-Geigy AG, Basel, Switzerland.
- (2) (a) S. W. Benson, F. R. Cruickshank, D. M. Golden, G. R. Haugen, H. E. O'Neal, A. S. Rodgers, R. Shaw, and R. Walsh, *Chem. Rev.*, **69**, 279 (1969); (b) S. W. Benson, "Thermochemical Kinetics," Wiley, New York, N. Y., 1968.
- (3) (a) D. R. Stull, E. F. Westrum, Jr., and G. C. Sinke, "The Chemical Thermodynamics of Organic Compounds," Wiley, New York, N. Y., 1969; (b) J. D. Cox and G. Pilcher, "Thermochemistry of Organic and Organometallic Compounds," Academic Press, London, 1970.
- (4) The group values of peroxides and related compounds have recently been updated (S. W. Benson and R. Shaw, "Organic Peroxides," Vol. 1, D. Swern, Ed., Wiley, New York, N. Y., 1969, p 106) and are not included in this paper.
- (5) S. W. Benson and J. H. Buss, *J. Chem. Phys.*, **29**, 546 (1958).
- (6) Tables III a–i, "Comparison of Measured and Calculated Enthalpies of Formation," for all species considered, will appear following these pages in the microfilm edition of this volume of the journal. Single copies may be obtained from the Business Operations Office, Books and Journals Division, American Chemical Society, 1155 Sixteenth St., N.W., Washington, D. C. 20036. Remit check or money order for \$4.00 for photocopy or \$2.00 for microfiche, referring to code number JPC-73-1687.

TABLE I: Group Values for ΔH_f° 298 Noncarbonylic Groups (kcal/mol)^a

C-(H) ₃ (O) ^b	-10.1		4.7
C-(H) ₂ (C)(O)*	-8.1		
C-(H) ₂ (C _d)(O) ^g	-6.5		-5.8
C-(H) ₂ (C _t)(O) ^h	-6.5		
C-(H) ₂ (C _B)(O)†	-8.1		
C-(H)(C) ₂ (O)*	-7.2		
C-(C) ₃ (O)*	-6.6		0.5
C _d -(H)(O) ^c	8.6		
C _d -(CO) ^d	10.3		
C _d -(C _d)(O) ^e	8.9		1.2
C _B -(O)*	-0.9		
C-(H) ₂ (O) ₂ *	-16.1		
C-(H)(C)(O) ₂ *	-16.3		16.6
C-(C) ₂ (O) ₂ *	-18.6		
O-(H)(C)* ^f	-37.9		
O-(H)(C _d)* ^f	-37.9		
O-(H)(C _t)* ^f	-37.9		2.0
O-(H)(C _B)* ^f	-37.9		
O-(C) ₂ *	-23.2		6.5
O-(C _d)(C) ⁱ	-30.5		
O-(C _d) ₂ † ^j	-33.0		
O-(C _B)(C) ^k	-23.0		2.3
O-(C _B) ₂ † ^l	-21.1		
Strains			
Ether oxygen gauche*	0.5 (O gauche)		6.0
Di-tert-butyl ether† ^m	7.8		
Gauche ⁿ	0		
Ortho ^o	0		3.3
	26.8		
	25.2		0.2
	5.9		6.6

^a Determined by MLR. ^b C-(H)₃(O) ≡ C-(H)₃(C), assigned. ^c C_d-(H)(O) ≡ C_d-(H)(C), assigned. ^d C_d-(C)(O) ≡ C_d-(C)₂, assigned. ^e C_d-(C_d)(O) ≡ C_d-(C_d)(C), assigned. ^f O-(H)(C) ≡ O-(H)(C_d) ≡ O-(H)(C_t) ≡ O-(H)(C_B), assigned. ^g Based on methylallyl ether and allyl alcohol. ^h Based on 2-propyn-1-ol, rather than methyl 2-propynyl ether. The latter would imply an unexpectedly low group value. ⁱ Based on ethyl vinyl ether, 2-ethoxyprop-1-ene, 2-methoxy-*n*-but-2-ene. ^j Based on divinyl ether. ^k Based on methyl phenyl ether, ethyl phenyl ether, and 3-methoxy-1-methylbenzene. ^l Based on diphenyl ether. ^m Based on di-tert-butyl ether. ⁿ Based on ethylene oxide and propylene oxide. ^o Based on tetrahydrofuran and tetrahydrofurfuryl alcohol. ^p Based on furan and furfuryl alcohol. ^q Based on tetrahydropyran and 2-methoxytetrahydropyran. ^r Based on 1,3-dioxolane and the 2-methyl and 2,4-dimethyl derivatives. ^s See text. ^t Based on s-trioxane. See text. ^u No gauche correction is added for interactions of O with alkyl C or O along a C-C bond. ^v No ortho correction is added for O ortho to alkyl C or O. ^w Based on dibenzopyran using -7.2 for C-(H)₂(C_B)₂ (from diphenylmethane).^{3b}

3.1 Alcohols and Ethers. The following parameters (group values) have been subject to multilinear regression: C-(H)₂(C)(O), C-(H)(C)₂(O), C_B-(O), O-(C)(H), O-(C)₂, O-gauche, C-(H)₂(O)₂, C-(H)(CO)₂, C-(C)₂(O)₂. The remaining groups were determined by inspection from the rest of the available data. Twelve of 78 compounds were excluded from multilinear regression by the principles explained in section 2.

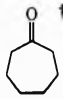
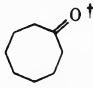
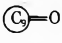
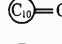
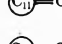

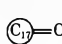
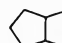

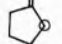


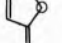
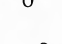
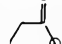


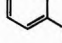
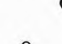
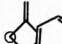
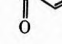
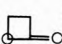
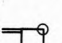
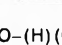
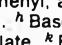
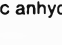
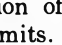
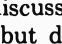
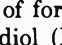
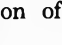

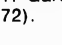



In the previous report^{2b} we used a value of +0.8 kcal/mol as the destabilization due to gauche interaction between O and alkyl carbon along C-C bonds in analogy to the value in hydrocarbons for gauche interactions between alkyl carbons. Some of the data on branched alcohols indicate that this value should be lowered. 0.3 kcal/mol would be in fair agreement with the reported conformational free energy of cyclohexanol.⁷ On the other hand, the differences in conformational free energies of 1-methylcyclohexanol, which are reported to be 0.1-0.3 kcal/mol,⁸ imply a similar, or the same value for either gauche interaction. On the basis of the polyols where this strain often occurs several times in one molecule (as oxygen-carbon or

oxygen-oxygen interaction), a stabilization, rather than a strain, would improve the agreement considerably. From a theoretical point of view, some hydrogen bonding may be responsible for this behavior. In this questionable situation we assigned 0 kcal/mol to this interaction. Although this is a compromise, it improves the general agreement, mainly with respect to the polyols. Similar arguments apply to the aromatic ortho interaction. The already fair agreement may even be improved by again assuming 0 kcal/mol as strain in the cases of O and C, or O and O, ortho to each other. The value of the ether oxygen gauche correction, where the alkyl carbons are gauche along a C-O bond, has been determined to be 0.5 kcal/mol from the MLR.

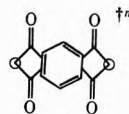
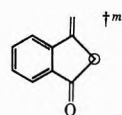
In Tables I and II, the best group values are summarized, and Tables III-a, III-b, and III-c cover alcohols, ethers, and cyclic ethers and present measured and calculated values for these compounds.

- (7) E. L. Eliel and S. H. Schroeter, *J. Amer. Chem. Soc.*, **87**, 5031 (1965).
 (8) J. J. Uebel and H. W. Goodwin, *J. Org. Chem.*, **33**, 3317 (1968).

TABLE II: Group Values for ΔH_f° Carbonylic Groups (kcal/mol)^a

C-(H) ₃ (CO) ^b	-10.1		
C-(H) ₂ (C)(CO)*	-5.2		2.3
C-(H) ₂ (C _d)(CO) ^d	-3.8		
C-(H) ₂ (C _t)(CO) [†]	-5.4		
C-(H) ₂ (C _B)(CO) ^e	-5.4		
C-(H)(C) ₂ (CO)*	-1.7		1.5
C-(C) ₃ (CO)*	1.4		
C _d -(H)(CO)*	5.0		
C _d -(C)(CO) [†]	7.5		4.7
C _d -(O)(CO) ^f	11.6		
C _B -(CO)*	3.7		3.6
C-(H) ₂ (CO) ₂ [†]	-7.6		4.4
C-(H)(C)(CO) ₂ [†]	-5.4		3.0
O-(H)(CO)*	-58.1		2.1
O-(C)(CO)*	-43.1		1.1
O-(C _d)(CO) [†]	-45.2		5.4
O-(C _B)(CO)*	-36.7		11.0
O-(CO) ₂ ^l	-46.5		4.5
(CO)-(H)(C)* ^c	-29.1		
(CO)-(H)(C _d)* ^c	-29.1		
(CO)-(H)(C _t)* ^c	-29.1		
(CO)-(H)(C _B)* ^c	-29.1		
(CO)-(C ₂)*	-31.4		
(CO)-(C _B)(C) ^g	-30.9		
(CO)-(C _B) ₂ [†]	-25.8		
(CO)-(H) ₂ [†]	-26.0		
(CO)-(H)(O) ⁿ	-32.1		3.6
(CO)-(C)(O)*	-35.1		
(CO)-(C _d)(O)*	-32.0		
(CO)-(C _B)(O)*	-36.6		
(CO)-(H)(CO) [†]	-25.3		
(CO)-(C)(CO) ^h	-29.2		0.8
(CO)-(C _B)(CO) [†]	-26.8		
(CO)-(O)(CO) ^j	-29.3		
(CO)-(O) ₂ [†]	-29.9		
			
			
			
			
			
			
			

Strains



^a See footnote a to Table I. ^b C-(H)₃(CO) ≡ C-(H)₃(C), assigned. ^c CO-(H)(C) ≡ CO-(H)(C_d) ≡ CO-(H)(C_t) ≡ CO-(H)(C_B), assigned. ^d Based on ethyl-, *n*- and isopropyl-, and *n*-butyl-3-pentenoate. ^e Based on benzyl methyl, benzyl phenyl, and dibenzyl ketone. ^f Based on furfuraldehyde and furoic acid. ^g Based on acetophenone, ethyl, *n*-propyl, and isopropyl phenyl ketone (see text). ^h Based on methyl glyoxal and diacetyl. ⁱ Based on acetic, propionic, and benzoic anhydride. ^j Based on oxalic acid, diethyl oxalate, and diphenyl oxalate. ^k Based on succinic anhydride (see text). ^l Based on maleic anhydride (see text). ^m The strain of pyromellitic anhydride is twice the strain of phthalic anhydride, as expected. ⁿ Based on formic acid and methyl formate.

a. Alcohols. Most of the calculated heats of formation are within 1.0 kcal/mol of the measured values. The aliphatic alcohols are in even better agreement (± 0.5 kcal/mol). Big discrepancies occur with 2-naphthol (A), thymol (B), 1,3-propanediol (C), 1,3-butanediol (D), 2,3-butanediol (E), glycerol (F), diethylene glycol (G), *l*-erythritol (H), pentaerythritol (I), and triethylene glycol (K). For compounds A, E, G, and K, either ΔH_f° or ΔH_{vap}^{298} were measured before 1940. Furthermore, most vicinal diols (E,F,H) show a stabilization of 2–5 kcal/mol, which might be due to hydrogen bonding. The estimated enthalpy of

formation of thymol (B) is almost within the reported error limits. In the report on 1,3-propanediol (C)⁹ the authors discuss the unexpectedly low value they have measured, but do not indicate any final arguments. The enthalpy of formation reported by the same authors for 1,3-butanediol (D) shows the same behavior. No obvious explanation of the discrepancy with *l*-erythritol could be found.

(9) P. T. Gardner and K. S. Hussain, *J. Chem. Thermodyn.*, **4**, 819 (1972).

An inconsistency exists between mono- and polyalcohols insofar as the predicted values for the former are mostly too negative, but too positive for the latter. This behavior is additionally accentuated by the fact that the polyalcohols have more statistical weight in the MLR due to the occurrence of more than one set of oxygen-containing groups in their molecules. In order to take into account the fact that enthalpies of formation of monoalcohols are generally much more reliable than those of polyols, we have chosen $O-(H)(C) \equiv O-(H)(C_d) \equiv O-(H)(C_t) \equiv O-(H)(C_B)$, -37.9 kcal/mol, instead of -38.3 , as calculated by MLR.

b. Ethers. With the exception of a few compounds, deviations no greater than ± 1.0 kcal/mol were observed. The difference for methoxybenzaldehyde is -2.3 kcal/mol, compared to a relatively big error of ± 1.4 kcal/mol for the measured value. Diallyl ether, burned in 1929, shows a deviation of $+7.3$ kcal/mol, that may only be assigned to the group $C-(H)_2(C_d)(O)$. However, this group value is well established by the excellent agreement for methylallyl ether and allyl alcohol. The group $C-(H)_2(C_t)(O)$ may be calculated from either methyl 2-propynyl ether or 2-propynyl-1-ol, leading to -1.9 or -6.5 kcal/mol, respectively. Although the enthalpies of formation of both compounds have the same source, we prefer -6.5 kcal/mol as calculated from the alcohol. This value is within the range suggested by the analogous groups $C-(H)_2(C)(O)$ (-8.1), $C-(H)_2(C_d)(O)$ (-6.5), and $C-(H)_2(C_B)(O)$ (-7.7).

c. Cyclic Ethers. This class of compounds mainly determines strain parameters for rings. Usually, only a few derivatives of each particular ring system have been measured. Therefore, most of the strain parameters are based on not more than three measured enthalpies of formation. No considerable deviations are observed, except for the families of 1,3-dioxanes and 1,3,5-trioxanes. In the former case, additional strain is observed with tri- and tetramethyl substituted derivatives which have been excluded from the calculation of the 1,3-dioxan strain. However, part of these discrepancies may be explained by taking into account the strain observed in the structurally similar diisopropyl and isopropyl *tert*-butyl ethers (0.7 and 0.4 kcal/mol, respectively). The enthalpy of formation of 5,5-dimethyl-1,3-dioxane should be remeasured in order to clarify its surprising extra stabilization of ~ 2.5 kcal/mol. In the latter case, enthalpies of formation of *s*-trioxane have been reported to be -111.32 (Monsson, *et al.*¹⁰), -116.1 (Busfield and Merigold¹¹), and -120.8 kcal/mol (Snelson and Skinner¹²). We have adopted -111.3 kcal/mol, a value that leads to a strain of 6.6 kcal for this compound. Furthermore, -111.3 kcal/mol is in agreement with the earlier measurement of Busfield and Merigold¹¹ if their value is corrected for the recently redetermined enthalpy of formation of formaldehyde¹³ (-26.0 instead of -27.7 kcal/mol). More experimental and theoretical knowledge are needed to explain the unexpected stabilization of the trimethyl derivative.¹⁴

3.2 Aldehydes, Ketones, Acids, Anhydrides, and Esters. In the calculation of groups of carboxylic compounds, the previously determined groups of alcohols and esters have been adopted as given in Table I. Of the remaining groups, the following were optimized using multilinear regression (MLR): $C-(H)_2(C)(CO)$, $C-(H)(C)_2(CO)$, $C-(C)_3(CO)$, $C_B-(CO)$, $C_d-(H)(CO)$, $CO-(H)(C) \equiv CO-(H)(C_B) \equiv CO-(H)(C_d)$, $CO-(O)(C)$, $CO-(O)(C_B)$, $CO-(O)(C_d)$, $O-(CO)(H)$, $O-(CO)(C)$, $O-(CO)(C_B)$. In order

to maintain linear independence between the groups, we had to modify some of the optional assignments of values to groups, mentioned in the previous report.^{2a} In analogy to $C-(H)_3(X)$, all groups, $CO-(H)(X)$ ($X = C, C_B, C_d$), were assumed to be equal. Furthermore, the previous assignment, $CO-(O)(C_B) \equiv CO-(O)(C_d)$, could be avoided.

Due to the higher numbers of compounds and parameters, the process of elimination of erroneous enthalpies of formation was more complicated than with alcohols and ethers. Finally, 97 to 123 compounds remained in the final set for multilinear regression. Twenty-six compounds were excluded on the basis outlined in section 2, and by some additional criteria that are explained in the context of Tables III-d-i. The resulting group values differ in part from the values reported earlier. The standard error of estimation, calculated on the basis of the 97 selected compounds, was lowered to 1.4 kcal/mol. On the basis of all 123 compounds, the improvement is 0.9 kcal/mol (4.4 kcal/mol using "old," 3.5 kcal/mol using "new" groups). The improved group values are listed in Table II. Those not calculated by MLR have been determined by inspection, using the groups already calculated. Tables III-d-i compare measured and calculated ΔH_f° values for all compounds used in this compilation.

a. Aldehydes. Except for 4-methoxybenzaldehyde and furfural, both measured 1940 or earlier, no severe deviations occur.

b. Ketones. Due to its obvious strain, di-*tert*-butyl ketone had to be excluded from the original data set for MLR. Its strain is surprisingly high (6.5 kcal/mol). By inspection, the enthalpies of formation of three ketones measured by Geisler, *et al.*,¹⁵ are too positive by $5-6$ kcal/mol. They have been rejected in the final MLR and should be remeasured in the future. Some minor strain is observed with sterically hindered species like methyl *tert*-butyl ketone (0.8), diisopropyl ketone (0.7), and isopropyl *tert*-butyl ketone (1.3 kcal/mol). Within the remaining compounds the trimethylacetophenones show large deviations. Their enthalpies of formation are based on measurements in 1941 and an estimate of ΔH_{vap} ²⁹⁸. The group $CO-(C)(C_B)$ has been calculated without these two values. Otherwise, calculated and measured values differ by less than 1.0 kcal/mol.

c. Cyclic Ketones. In this class of compounds, each strain parameter is based on one particular enthalpy of formation. Furthermore, the enthalpy of formation of bicyclo[3.3.0]octanone is calculated by the help of an estimated enthalpy of vaporization. Therefore, at present no discussion in terms of group additivity is possible with these compounds.

d. Acids. Within the acids more deviations from group additivity seem to occur than elsewhere. Therefore, a relatively high number of compounds had to be rejected before the final MLR. Beginning with tetradecanoic acid, all higher aliphatic acids were excluded in order to avoid influences of non-nearest-neighbor interactions onto the group values. Suberic, sebacic, and dodecandioic acid have not been used in the final fit. Their combustion

(10) M. Monsson, E. Morawetz, Y. Nakase, and S. Sunner, *Acta Chem. Scand.*, **23**, 56 (1969).

(11) W. K. Busfield and D. J. Merigold, *J. Chem. Soc. A*, 2975 (1969).

(12) A. Snelson and H. A. Skinner, *Trans. Faraday Soc.*, **57**, 2125 (1961).

(13) R. A. Fletcher and G. Pilcher, *Trans. Faraday Soc.*, **66**, 794 (1970).

(14) K. Pihlaja and M. L. Tuomi, *Suom. Kemistilehti B*, **43**, 224 (1970).

(15) Methyl phenyl, propyl butyl, and ethyl pentyl ketone [G. Geisler, N. Ratlevszh, K. Ebster, and I. Ziegel, *Ber. Bunsenges. Phys. Chem.*, **70**, 221 (1966)].

dates back to 1926, and all of them show an apparent high strain. Finally, the enthalpies of formation of maleic and fumaric acid cannot reasonably be fitted within the rest of carbonylic compounds. Their calculated enthalpies of formation are +7 to +9 kcal off the measured value. Both have been discarded.

Within the remaining set of compounds, most discrepancies occur in aromatic acids. They find their counterpart in aromatic anhydrides and esters, but benzoic acid is the most prominent disagreement. Excluding benzoic acid would considerably improve the consistency of the rest of the data. A redetermination of its heat of sublimation should be undertaken in order to establish a more reliable value for the important group, CO-(O)(C_B).

e. Anhydrides and Related Compounds. No MLR was carried out on these strained species. First, by using acetic, propionic, and benzoic anhydride, the group O-(CO)₂ was determined. The consistency of O-(CO)₂ within these three compounds is as bad as ±3 kcal/mol. Nevertheless, the averaged value of this group has been used to calculate strains of the intramolecular anhydrides. In the case of succinic and maleic anhydride, the methylated homologs have been neglected for the calculation of the respective strains. The available data indicate, for both molecules, extra stabilization of the methylated derivatives, although the enthalpies of formation are based on measurements earlier than 1942.

f. Esters. Although a considerable number of enthalpies of formation are reported, many enthalpies of vaporization are estimated and a lot of measurements date back before 1940. Therefore, we had to exclude from MLR a high number of compounds by the procedure described in section 2. Within the remaining major discrepancies, we eliminated all data leading to deviations too large to be corrected by a reasonable change of group values (*i.e.*, glycerol triacetate, $\Delta = -10.2$; alkyl esters of phthalic acid, $\Delta = -10$ to -15 kcal/mol). Although a critical review of these data is beyond the scope of this paper, some additional comments seem to be in order. The group CO-(H)(O) has been determined on the basis of the recently measured enthalpies of formation of formic acid and methyl formate, neglecting ethyl and allyl formate, both burned in 1929. The enthalpy of formation of ethyl propionate reported by Pilcher and Cox^{3b} should be corrected to -112.2 kcal/mol due to an arithmetical error. All isomeric butyl pentanoates show extra stabilization, probably due to a systematic error. The data reported by Hancock, *et al.*,¹⁶ (esters of α -methylbutyric, isovaleric, and

pivalic acid) lead to predictions positive by ~ 3 – 5 kcal/mol, again possibly a systematic error. (For methyl pivalate, a more recent value is in better agreement with group additivity.¹⁷) All enthalpies of formation of esters of the isomeric pentenoic and pentynoic acids are based on estimated enthalpies of vaporization. For methyl *cis*-9-octadecenoate and the diesters of phthalic acid, the reported error limits already account for ± 3 kcal/mol. All enthalpies of formation reported by Carson, *et al.*,¹⁸ produce deviations of the order of 3 kcal/mol (benzoic anhydride, diphenyl oxalate, and phenyl benzoate). However, for two of these compounds there exist previously reported values which are in better agreement with group additivity (benzoic anhydride = -79.9 ,¹⁹ and phenyl benzoate = -37.5 kcal/mol²⁰). Part of these discrepancies may furthermore be due to the general inconsistency of data on aromatic acids, anhydrides, and esters. Nevertheless, except for the compounds mentioned above, deviations generally remain within ± 1.5 kcal/mol, nearly as accurate as in the other classes of organic oxygen compounds.

4. Conclusions

The group values presented in this report are based on a considerably increased number of experimental data and predictions are mostly within ± 1.0 kcal/mol. We feel, therefore, that data leading to discrepancies of more than 2 kcal/mol should be reexamined carefully in each case. Either unexpected strain or stabilization may be the reason for this behavior, or the reported values are less accurate than is indicated by the precision listed by the authors. Typical examples are the aromatic acids, where the heats of formation of the alkyl esters are not compatible with that of the unsubstituted acid. A similar situation exists in the case of trioxane. The trimethyl derivative is far from the prediction based on trioxane itself.

It is our experience from dealing with a large amount of thermochemical data that the method of group additivity is not only useful for the prediction of thermochemical values, but also as a tool in estimating the internal consistency of data for homologous families of compounds.

(16) C. K. Hancock, G. M. Watson, and R. F. Gilby, *J. Phys. Chem.*, **58**, 127 (1954).

(17) H. K. Hall, Jr., and Z. F. Balducci, *J. Amer. Chem. Soc.*, **93**, 140 (1971).

(18) A. S. Carson, D. H. Fine, P. Gray, and P. G. Laye, *J. Chem. Soc. B*, 1611 (1971).

(19) J. W. Breitenbach and C. Derkosch, *Monatsh. Chem.*, **81**, 689 (1950).

(20) G. P. Adams, D. H. Fine, P. Gray, and P. G. Laye, *J. Chem. Soc. B*, 7, 720 (1967).

Film Bursting. V. The Effect of Various Atmospheres and the Anomaly of Newton Black Films

Karol J. Mysels*¹ and B. R. Vijayendran

Research Department, R. J. Reynolds Tobacco Company, Winston-Salem, North Carolina (Received February 8, 1973)

Publication costs assisted by the R. J. Reynolds Tobacco Company

The velocity of the rim of the growing hole in a bursting soap film is reduced due to the viscosity and density of the gas surrounding it. This windage effect increases as the film becomes thinner and as the calculated unobstructed rim velocity increases. Experiments in hydrogen, helium, air, and neon atmospheres indicate that windage is sufficient to account for the observed departures of rim velocities from the calculated one, even for the thinnest Newton black films where the actual rim velocity is reduced below that of somewhat thicker films. Although the experimental results can be fitted to an empirical relation, which involves only film thickness and the bulk properties of gas and liquid, an aerodynamic analysis would be very complicated since it has to involve the effect of the aureole preceding the rim.

A few years ago, McEntee and Mysels^{2a} gave a description, based on flash photographs, of the bursting of planar soap films, reported measurements of the rate at which the rim of the hole retracted under the influence of surface tension forces, and described the aureole, a thickening preceding this rim. The basic theory of the process has been given in an accompanying paper^{2b} and it has been used more recently along with improved measurement techniques to provide information about the interaction of surfactant molecules in monolayers compressed far beyond their equilibrium state³ and about the kinetics of very rapid desorption from such monolayers.⁴ An important improvement in the technique has been the use of a hydrogen atmosphere around the bursting film. For films thicker than some 2000 Å, this effectively eliminated the resistance offered by the atmosphere to the retracting film, as has been reported briefly earlier.³

Some features of the original observations remained unexplained, however, and thus seemed either to cast doubt on the validity of the basic theory or to provide unexplored clues to new phenomena. In particular, the rim velocity, which generally increases as the film becomes thinner, departed markedly from that expected on the basis of the theory for films thinner than some 1000 Å. In fact, the thinnest films, the Newton (second) black films, give actually slower rim velocities than the immediately thicker, common (first) black films.

The explanation originally suggested,^{2a} of an additional, very rapid shock wave absorbing the excess momentum, could not be confirmed despite much improved techniques used in looking for it. The discovery of the windage effect provided a more satisfactory explanation for the moderate deviations but left open the question whether it could account also for the reversal of the trend of velocity with thickness for the Newton films, a reversal which persists even in a hydrogen atmosphere. Experiments in various atmospheres now indicate that much, if not all, of this discrepancy can be explained as due to windage which becomes more pronounced as the velocity and area of the aureole increase.

Experimental Section

The apparatus used was designed in cooperation with Dr. G. Frens and is shown schematically in Figure 1. The

film was formed on a fixed rectangular frame about 3.5 cm wide and 5 cm high behind an optically flat window in vessel 2 which also held the electrodes for the burst-initiating spark. Washbottle 1 permitted the changing of level of the liquid studied in vessel 2 whereas washbottles 3 and 4 served to confine and manipulate the gas surrounding the film. Raising the liquid level in both 2 and 3 permitted expulsion of the gas through stopcock 5 and lowering these levels the introduction of another. As these liquid movements apparently generated sufficient static electricity to produce sparks, an inert gas was always used before and after hydrogen.

Bursting was followed by the method described previously.³ It consists essentially of recording with a double-beam oscilloscope the intensity of two beams of He-Ne laser light reflected from the film at two points, separated by between 0.67 and 1.16 cm along a horizontal line passing through the level of the spark and at least 0.3 cm away from it. The spark starts the burst and triggers the oscilloscope. Since varying film thickness corresponds to varying intensity of reflected light because of interference effects, the progress of the aureole and the appearance of the rim as they pass each of the two beams is shown in the oscilloscope screen. The velocities were obtained from the known separation of the two light beams and the relative delay of the oscilloscope traces as measured on their photographs.

The sodium dodecyl sulfate (NaLS) was a purified sample prepared from high purity dodecyl alcohol supplied by Applied Science Laboratory, State College, Pa. The gases were of commercial purity and salts were reagent grade. All experiments were conducted in an air conditioned room at 24°.

Results and Discussion

Figure 2 shows the rim velocity of films from the same solution having different thicknesses and bursting in four

- (1) Author to whom correspondence should be addressed at 8327 La Jolla Scenic Drive, La Jolla, Calif. 92037.
- (2) (a) W. R. McEntee and K. J. Mysels, *J. Phys. Chem.*, **73**, 3018 (1969); (b) S. P. Frankel and K. J. Mysels, *ibid.*, **73**, 3028 (1969).
- (3) G. Frens, K. J. Mysels, and B. R. Vijayendran, *Spec. Disc. Faraday Soc.*, **1**, 12 (1970).
- (4) A. T. Florence and G. Frens, *J. Phys. Chem.*, **76**, 3024 (1972).

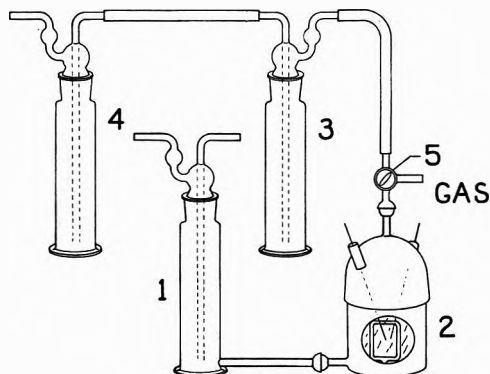


Figure 1. Apparatus for studying bursting in various atmospheres.

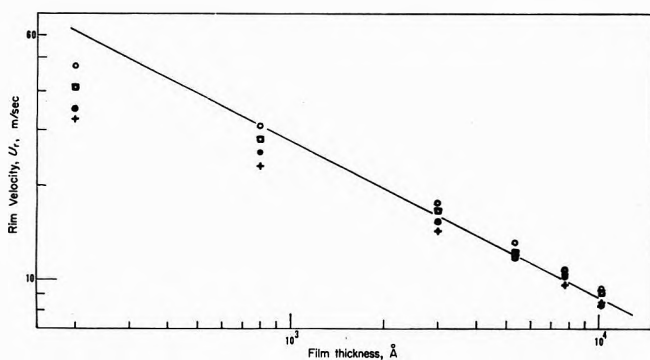


Figure 2. Rim velocities for several thicknesses of films of solution A (Table I) in different atmospheres: O, hydrogen; □, helium; ●, air; +, neon. The straight line shows Culick's velocity.

different atmospheres; namely, neon, air, helium, and hydrogen. To a first approximation the rim velocity is determined^{2b} by the balance of the surface tension, σ , forces which are always the same, and the inertia of the film which increases with its thickness, δ , and density, ρ_s . As the mass of the film which is accelerated in unit time increases with the velocity, the latter is inversely proportional to the square root of the thickness. This velocity, denoted by u_c , was derived by Culick⁵ and is strictly valid for the rim only in the absence of windage and when the aureole has zero width.^{2b} It is given by

$$u_c = (2\sigma/\delta\rho_s)^{1/2} \quad (1)$$

and corresponds to the straight line of Figure 2. Theory indicates that aureoles of moderate width cause only minor deviations from u_c ,^{2b} and that these can be in either direction for circular bursting such as studied here.⁶ Figure 2 shows, however, that deviations are in fact small only for the thickest films, that they increase rapidly as the film becomes thinner, and that they depend markedly on the nature of the gas present. Hydrogen produces the least reduction of rim velocity, followed by helium, air, and neon which has the largest effect. Helium has a slightly higher viscosity than air (198 vs. 185 μP) but a more than sevenfold lower density. Hence its lesser retardation of the rim shows that density plays an important role in the windage. On the other hand, air has a higher density than neon (1.20 vs. 0.84 g/l.) yet is less retarding, which indicates that viscosity, which is lower for air than for neon (185 vs. 314 μP), is also an important factor. Hydrogen which has the lowest density and lowest viscosity of all gases (0.083 g/l., 89 μP) affects least the rim velocity.

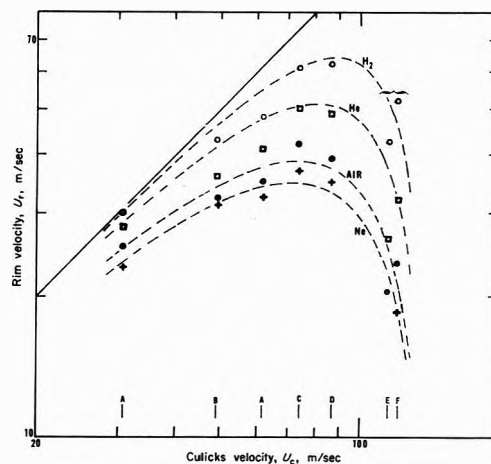


Figure 3. Rim velocities of films less than 1000 Å in thickness of solutions A-F (Table I) in several atmospheres. The full line shows Culick's velocity, the dashed lines eq 2. The bracket indicates Newton black films.

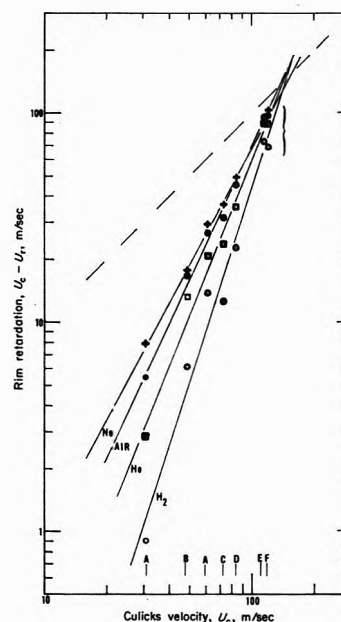


Figure 4. Rim retardation, $u_c - u_r$, vs. u_c for data of Figure 3. The solid lines are least-squares fitted, the dashed line shows $u_r = 0$, and the bracket indicates the Newton black films.

The same effect is shown in Figure 3 which represents the results of a series of rim velocity measurements on very thin and equilibrium films of a number of solutions of NaLS alone or with added salts. Their compositions are given in Table I along with some of their properties. Here windage effects were very pronounced but the surface tension varied from 29.5 to 38.3 so that their Culick velocities were not a smooth function of thickness. The results are therefore plotted in terms of the observed rim velocity u_r vs. u_c , the latter being of course close to proportional to the square root of the equilibrium thicknesses.

This figure shows clearly the effect mentioned in the introductory paragraph that the rim velocity of the thinnest films is definitely less than that of the intermediate ones, even in hydrogen. These thinnest films differ in some ways qualitatively from the thicker ones and have been already described as distinct by Newton.⁷ They form only

(5) F. E. C. Culick, *J. Appl. Phys.*, **31**, 1128 (1960).

(6) K. J. Mysels and B. R. Vijayendran, unpublished data.

(7) I. Newton, "Opticks," Book II, Part 1, London, 1704, observations 17-21.

TABLE I: Composition, Surface Tension, σ , and Equilibrium Film Thickness, δ_e , of Solutions Studied

Solution	NaLS, %	Salt	σ , dyn/cm	δ_e , Å
A	0.96		38.3	200
B	0.32		38.6	320
C	0.145	0.085 M LiCl	38.0	140
D	0.145	1.62 M LiCl	30.5	85
E	0.145	0.51 M NaCl	29.5	44
F	0.145	0.25 M NaCl	31.8	44

in the presence of certain salts such as NaCl (but not LiCl) and then only when the salt content exceeds a certain minimum, but their thickness (~ 50 Å) is essentially independent of the ionic strength of the solution, whereas for common black films equilibrium films are very sensitive to it.⁸ Their free energy is generally much lower than of the others.⁹ The aqueous core of these films is of the order of 15 Å which is less than the diameter of a micelle. Hence it was natural to attempt to explain the anomalies of their bursting in terms of these other differences. In contrast, the present results indicate that within experimental error the behavior of the Newton black films is due to the same effects which cause the much smaller deviations from Culick's velocity in the thicker common black films. This conclusion is indicated by Figure 4 which plots the same results as Figure 3 but in terms of the retardation of the rim; *i.e.*, $u_c - u_r$ vs. u_c on a log-log plot. The lines shown are least-squares fitted. Each corresponds to a different gas and it is apparent that the points for the Newton black films fit on each as well as those of the thicker films. In fact, lines fitted to the points of the common black films alone show, in each case, a larger standard deviation and a lower F value than lines which include the Newton black film points. Thus, to the extent that the windage effect can be represented by these straight lines, it accounts for all the films equally well.

This is further confirmed by the dashed lines drawn in Figure 3. They represent an attempt to account for the windage effect of all the gases on the basis of their density and viscosity. The equation developed is

$$u_r = u_c [1 - (u_c/144)^\beta] \quad (2)$$

with

$$\beta = 7.6/\eta^{0.24} \rho^{0.14} \quad (3)$$

where ρ is the density of the gas in g/l., η its viscosity in μ P, and the velocities are expressed in m/sec. This simple expression fits the experimental results relatively well and shows that indeed the properties of the gas and Culick's velocity are enough to account for the peculiarities of rim velocities. It should be noted, however, that this expression is purely empirical and serves only to represent the results obtained under our particular conditions. It is an idealization of Figure 3 in which all the lines intersect at 144 m/sec, clearly not a realistic condition. The problems of developing a meaningful aerodynamic theory of the complicated phenomena involved in bursting seems forbidding.

The reversal by windage of the trend of rim velocities with thickness for the Newton black films cannot be due to effects exerted upon the rim alone, since the rim moves slower and thus could not experience greater windage. The extra resistance must be accounted for by the aureole. As has been reported earlier^{2a} the aureole preceding the rim has an advancing edge, generally a shock wave,^{2b} whose velocity is substantially constant and of the order of $2u_c$. It could be represented by a line parallel to, and above, the u_c line in Figures 2 and 3. Although this front advances rapidly, the film material in it just begins to accelerate and thus moves relatively slowly and should be least affected by windage. Thus the aureole expands more rapidly for the thinner films and is further widened by windage for these. Both of these factors must contribute to cause the windage developed over the aureole surface to be largest for the thinnest films. In other words, if the rim velocities of two films of different thickness were otherwise equal, the aureole of the thinner ones would be more extended and moving faster. Hence the windage developed would be larger and this would in fact prevent the rim velocities from being equal by retarding more the one of the thinner film.

Acknowledgment. Mr. Henry S. Hazelton helped in preparing the figures.

(8) M. N. Jones, K. J. Mysels, and P. C. Scholten, *Trans. Faraday Soc.*, **62**, 1336 (1966).

(9) F. Huisman and K. J. Mysels, *J. Phys. Chem.*, **73**, 489 (1969).

Polymorphism in the Solid Solutions, Potassium Chloride–Sodium Chloride and Rubidium Chloride–Potassium Chloride, at High Pressure

Lin-gun Liu,* William A. Bassett,

Department of Geological Sciences, University of Rochester, Rochester, New York 14627

and Maria S. Liu

Department of Chemistry, University of Rochester, Rochester, New York 14627 (Received February 20, 1973)

Publication costs assisted by the Earth Sciences Section, National Science Foundation

The pressure-induced polymorphic transition in the metastable solid solution, KCl–NaCl, at $23 \pm 3^\circ$ was investigated by means of X-ray diffraction employing a diamond-anvil high-pressure cell. The transition is similar to the $F_{m3m} = P_{m3m}$ (B1 = B2) phase change of its end-member components. The technique used enables one to observe visually the phase change through the diamond anvils. The transition pressure was calculated on the basis of the lattice parameter of Ag, particles of which were imbedded in the solid solution. The transition pressure of the solid solution increases nonlinearly, but continuously with increasing NaCl content. Data for the transition pressure are generally in good agreement with those measured by Jamieson and by Bassett, but they differ significantly from those reported by Darnell and McCollum at elevated temperatures. Thermodynamic equations relating the transition pressure of an ideal binary solid solution to its mole fraction for both diffusion and diffusionless phase transformations were derived. The present observations of the phase transformation in the system of KCl–NaCl solid solution at $23 \pm 3^\circ$ are consistent with equations calculated on the basis of a diffusionless phase transformation. Room temperature observations on RbCl–KCl by Darnell and McCollum are consistent with the diffusionless equation while their observations at temperatures over 200° are consistent with the diffusion equations. The KCl–NaCl and RbCl–KCl solid solution series provide very useful pressure calibrants. By adjusting composition, a sample with a transition at any pressure between 5 and 300 kbars can be produced.

Introduction

Alkali halides crystallize in one of two structures, NaCl type (F_{m3m} , B1) and CsCl type (P_{m3m} , B2). At 25° and 1 bar 17 of the alkali halides have the B1 structure and three have the B2 structure. All but four of those with the B1 structure have been found to transform to the B2 structure at high pressure.¹⁻⁶ KCl transforms from B1 to B2 at about 19.5 kbars and NaCl transforms at about 300 kbars. Since the B1 phase of NaCl continues to coexist with the B2 phase to pressures higher than 300 kbars, there is some question about the equilibrium transition pressure.⁷

Some solid solutions of alkali halides have also been shown to undergo B1–B2 phase transformations as well. These occur at pressures intermediate between the transformation pressures of the end members. Darnell and McCollum⁸ demonstrated this for the series RbCl–KCl. NaCl and KCl are immiscible over most of the range of compositions at 25° and 1 bar, but are completely miscible at temperatures over 500° (Figure 1).⁹ Metastable solid solutions can be produced at 25° by rapid quenching from temperatures above 500° . These samples transform at pressures intermediate between the transformation pressures of KCl and NaCl just as if they were stable solid solutions.^{10,11}

Experimental Techniques

A. Samples. Granular salts of KCl (Fisher's Certified Reagent) and NaCl (Baker's Analyzed Reagent) were weighed in accordance with each desired molar ratio and

then mechanically mixed. The mixture was then melted in an alumina crucible. After air quenching, each sample was then annealed for more than 1 hr at 600° , a temperature at which all compositions in the series are miscible. After annealing, each sample was again air quenched to 25° . Samples thus produced are crystal clear and have perfect cubic cleavage. Due to exsolution, they lose both clarity and perfection of cleavage after sitting at room temperature for a few days.

B. Apparatus and Procedure. Studies of the phase transformation were carried out by means of the diamond anvil press.^{12,13} A small tabular single crystal of sample was placed on one of the diamond anvils, fine Ag powder was spread on it, and then another tabular single crystal was placed on top. Single crystals were used in order to

- (1) R. B. Jacobs, *Phys. Rev.*, **54**, 468 (1938).
- (2) J. C. Jamieson, *J. Geol.*, **65**, 334 (1957).
- (3) G. J. Piermarini and C. E. Weir, *J. Chem. Phys.*, **37**, 1887 (1962).
- (4) C. E. Weir and G. J. Piermarini, *J. Res. Natl. Bur. Std., Sect. A*, **68**, 105 (1964).
- (5) C. W. F. T. Pistorius and L. J. Admiraal, *Nature (London)*, **201**, 1321 (1964).
- (6) W. A. Bassett, T. Takahashi, H. Mao, and J. S. Weaver, *J. Appl. Phys.*, **39**, 319 (1968).
- (7) L. Liu and W. A. Bassett, *J. Appl. Phys.*, **44**, 1475 (1973).
- (8) A. J. Darnell and W. A. McCollum, *High Temp. Sci.*, **2**, 331 (1970).
- (9) E. Scheil and H. Stadelmaier in "Phase Diagrams for Ceramists," M. K. Reser, Ed., American Ceramic Society, Columbus, Ohio, 1964, p 376.
- (10) J. C. Jamieson in "Physics of Solids at High Pressures," C. T. Tomizuka and R. M. Emrick, Ed., Academic Press, New York, N. Y., 1965, pp 444–459.
- (11) J. C. Jamieson, personal communication.
- (12) W. A. Bassett and T. Takahashi, *Amer. Min.*, **50**, 1576 (1965).
- (13) L. Liu, *J. Appl. Phys.*, **42**, 3702 (1971).

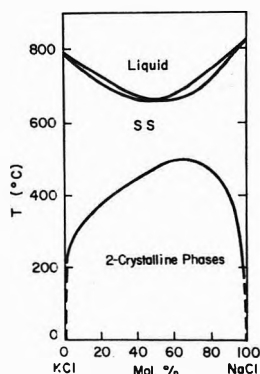


Figure 1. Temperature-composition phase diagram of KCl-NaCl at atmospheric pressure (Figure 1258 in ref 9).

prevent exsolution due to grinding and moisture absorbed on the surfaces of grains. Once the anvils were brought together and load was applied, the sample became a polycrystalline salt plate with Ag suspended in it. Visual observation of the sample permitted immediate detection of the phase transformation. Once the first sign of phase transformation was observed, application of load was halted, and the sample was left for at least 24 hr. If at the end of 24 hr the central portion of the sample was observed to consist of a mixture of the B1 and B2 phases, this was taken as an indication that the pressure had not surpassed the transition pressure. An X-ray diffraction pattern of the central portion of the sample where the B1-B2 mixture was observed was then made *in situ*. The average exposure time is about 400-500 hr. The pressure-volume relationship for silver reported by Liu and Bassett⁷ was then used to calculate the pressure from the lattice parameter of the silver mixed with the salt sample. When possible, the diffraction lines from the B1 and B2 phases of the KCl-NaCl solution were used to confirm the existence of both phases and to establish the volume change at the transition.

Results

Solid solutions with compositions of 0.1, 0.3, 0.5, 0.7, 0.85, and 0.9 mole fraction of NaCl were examined. Data for the transition pressure, P^t , of the binary solid solutions of KCl-NaCl at $23 \pm 3^\circ$ calculated from the lattice parameter of Ag are shown in Figure 2 along with those reported by Jamieson,^{10,11} Darnell and McCollum,¹⁴ and Bassett.¹⁵ The results are in reasonable agreement with those of Bassett and Jamieson. However, these low-temperature observations differ from those of Darnell and McCollum¹⁴ who concluded that the transition pressure remains essentially constant as a function of composition at 300° .

The total volume change, ΔV^t , which takes place during the transition was also measured when possible. We were not always successful in obtaining diffraction patterns that showed both B1 and B2 phases coexisting even though we saw them visually. When we did succeed, however, we used the information to calculate the ΔV^t . When these values are placed on a plot of ΔV^t vs. mole fraction, they seem to be consistent with a straight line between the published values (see Table I)^{16,17} for the pure end members (Figure 3). Our values were determined within an error of approximately ± 0.15 to ± 0.25 cm³/mol. The observations on the ΔV^t of the solid solution by us as well as the observations on the ΔV^t of pure NaCl by Bassett,

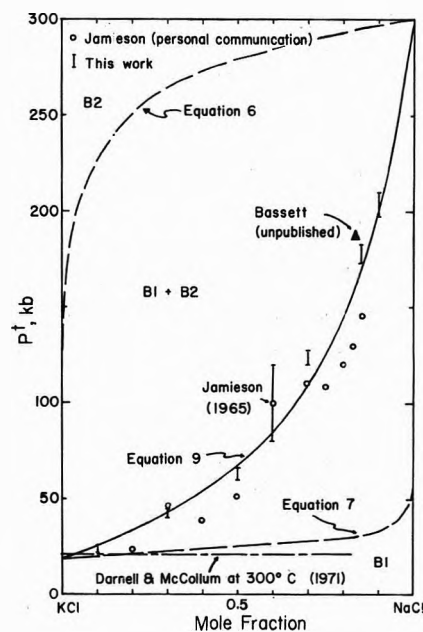


Figure 2. Experimental data for the transition pressure (P^t) of KCl-NaCl solid solution at room temperature determined in the present work along with those observed by Jamieson,^{10,11} Bassett,¹⁵ and Darnell and McCollum.¹⁴ The dashed curves were calculated on the basis of equations for phase transformations involving diffusion (eq 6 and 7). The solid curve was obtained from eq 9 for a diffusionless phase transformation.

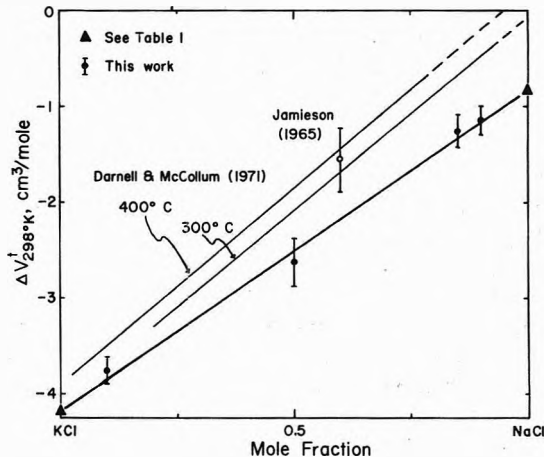


Figure 3. Experimental data for the volume change (ΔV^t) from B1 phase to B2 phase in the system of KCl-NaCl solid solution at room temperature. For comparison, data obtained by Jamieson¹⁰ and by Darnell and McCollum¹⁴ at elevated temperature have also been shown. A solid straight line was drawn between the published values for the pure end members.

et al.,⁶ and Liu and Bassett⁷ at room temperature are not consistent with those of Darnell and McCollum¹⁴ who found that a plot of ΔV^t vs. mole fraction at 300° indicates a value of zero when extrapolated to 100% NaCl (Figure 3).

Discussion

A. Theory. At a given pressure the theory of binary solid solutions with one common ion gives

$$xRT \ln [a_1(\text{I})/a_1(\text{II})] = \Delta F_1 \quad (1)$$

(14) A. J. Darnell and W. A. McCollum, *High Temp. Sci.*, **3**, 73 (1971).

(15) W. A. Bassett, unpublished results.

(16) P. W. Bridgman, *Proc. Amer. Acad. Arts Sci.*, **76**, 1 (1945).

(17) S. N. Vaidya and G. C. Kennedy, *J. Phys. Chem. Solids*, **31**, 2329 (1970).

TABLE I: Transition Pressure (P^t , kbar), Transition Volume ($-\Delta V^t$, cm^3/mol), and Differences of Free Energy of Formation (ΔF_{X-Y}^0 , kbar cm^3/mol) for the B1-B2 Phase Transformation in RbCl, KCl, and NaCl at 298°K

Salts		Ref 16	Ref 8	Ref 17	Ref 7	Av value
RbCl	P^t	4.9	5.68	5.2		5.26
	$-\Delta V^t$	6.00	6.95	6.24		6.40
	ΔF_{X-Y}^0					33.664
KCl	P^t	19.7	19.55	19.3		19.52
	$-\Delta V^t$	4.20	4.11	4.21		4.17
	ΔF_{X-Y}^0					81.398
NaCl	P^t				300 ^a	300
	$-\Delta V^t$				0.83	0.83
	ΔF_{X-Y}^0					249

^a It has been pointed out by Liu and Bassett⁷ that the transition pressure of NaCl cannot be exactly located at present. Hence, we have tentatively used the value reported by Bassett, *et al.*⁶

$$xRT \ln [a_2(\text{I})/a_2(\text{II})] = \Delta F_2 \quad (2)$$

where one molecule of salt gives x noncommon ions, R is the gas constant, T the temperature, a the activity, ΔF the molar free energy difference of the two phases, I and II, at the specified pressure and temperature and is a function of P and T only, and the subscripts 1 and 2 denote two end-member components. The free energy difference, ΔF , is related to pressure P as follows

$$\Delta F_i = - \int_P^{P_i^t} [V_i(\text{I}) - V_i(\text{II})] dP \quad (3)$$

where V is the molar volume, P^t is the equilibrium transition pressure of the two phases and is a function of T only, and $i = 1$ or 2. For an ideal solution, the activity equals the mole fraction N . Hence

$$\ln \frac{N_1(\text{I})}{N_1(\text{II})} = \Delta V_1^t (P_1^t - P) / xRT \quad (4)$$

$$\ln \frac{1 - N_1(\text{I})}{1 - N_1(\text{II})} = \Delta V_2^t (P_2^t - P) / xRT \quad (5)$$

where $\Delta V_i^t = V_i(\text{I}) - V_i(\text{II})$ is the volume change during the phase change and has been assumed to be constant with pressure.

Equations 4 and 5 may be combined and rearranged to obtain $N_1(\text{I})$ and $N_1(\text{II})$ as a function of pressure

$$N_1(\text{I}) = N_1(\text{II}) k_1 e^{-\Delta V_1^t P / xRT} \quad (6)$$

$$N_1(\text{II}) = (1 - k_2 e^{-\Delta V_2^t P / xRT}) / (k_1 e^{-\Delta V_1^t P / xRT} - k_2 e^{-\Delta V_2^t P / xRT}) \quad (7)$$

where $k_1 = \exp(\Delta V_1^t P_1^t / xRT)$ and $k_2 = \exp(\Delta V_2^t P_2^t / xRT)$. Equations 6 and 7 require that diffusion take place during the phase change of the solid solution. For phase transformations of solid solution occurring at room temperature, however, the diffusion rate is almost certainly too slow to allow the separation of phases with two different compositions. Hence, for a diffusionless phase transformation we proposed the following approaches.

Integrating eq 3 from 0 to the transition pressure yields

$$P^t = -\Delta F^0(\text{II} - \text{I}) / \Delta V(\text{II} - \text{I}) \quad (8)$$

for a pure component. Replacing $\Delta F^0(\text{II} - \text{I})$ and $\Delta V(\text{II} - \text{I})$ by the following relationships

$$\Delta F^0(\text{II} - \text{I}) = N_1 \Delta F_1^0(\text{II} - \text{I}) + N_2 \Delta F_2^0(\text{II} - \text{I})$$

$$\Delta V(\text{II} - \text{I}) = N_1 \Delta V_1(\text{II} - \text{I}) + N_2 \Delta V_2(\text{II} - \text{I})$$

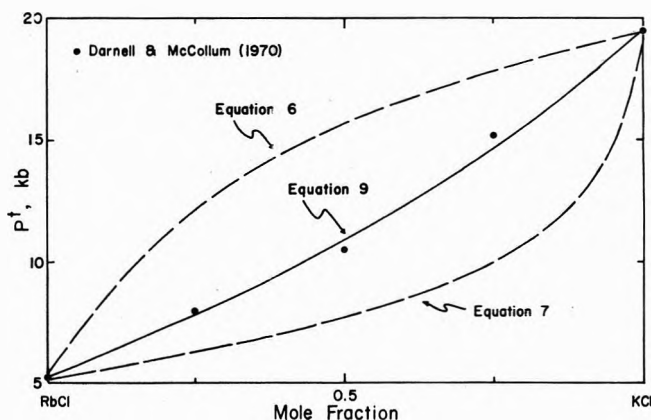


Figure 4. The circles show the experimentally determined transition pressures for the system of RbCl-KCl at 25° published by Darnell and McCollum.⁸ They are compared with the upper and lower subsolidus curves calculated from eq 6 and 7, and the diffusionless transition curve calculated from eq 9.

for a binary solution, where $\Delta F_i^0(\text{II} - \text{I}) = \mu_i^0(\text{II}) - \mu_i^0(\text{I})$, $\Delta V_i(\text{II} - \text{I}) = V_i(\text{II}) - V_i(\text{I})$, $i = 1$ or 2, and μ the chemical potential. Hence, the transition pressure for a diffusionless phase transformation in a binary solid solution may be expressed by

$$P^t = - \frac{\Delta F_2^0(\text{II} - \text{I}) + N_1 [\Delta F_1^0(\text{II} - \text{I}) - \Delta F_2^0(\text{II} - \text{I})]}{\Delta V_2(\text{II} - \text{I}) + N_1 [\Delta V_1(\text{II} - \text{I}) - \Delta V_2(\text{II} - \text{I})]} \quad (9)$$

This relationship is based on the assumption that volume change and free energy change associated with a diffusionless transition in a binary solid solution are linear functions of atomic fraction. Figure 3 seems to indicate that the first assumption is valid within experimental error for the volume change.

B. The RbCl-KCl System. Darnell and McCollum⁸ studied this system at temperatures ranging from 25 to 800° by dilatometry. At 25° their results for the transition pressure as a function of mole fraction seem to be completely consistent with eq 9, calculated on the basis of the values listed in Table I, for the diffusionless case (Figure 4). On both loading and unloading cycles they found that the phase transition took place over a range of pressures. That is, the phase transition would start at one pressure, progress as the pressure was changed, and finally go to completion at another pressure. When they averaged the pressure ranges for the up and down cycles, a pattern

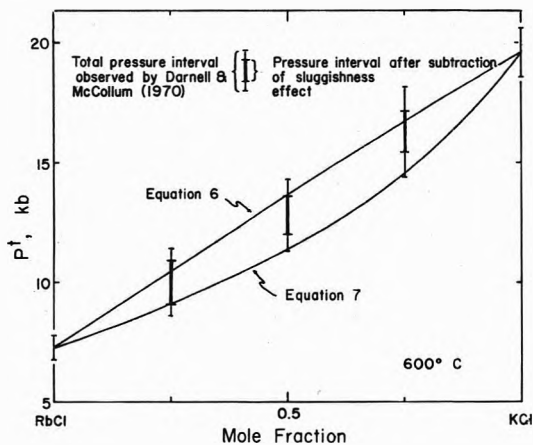


Figure 5. Transition pressures in the RbCl-KCl system at 600°. The bars show the pressure intervals during which the transitions ran observed by Darnell and McCollum.⁸ The heavy portion of each bar represents the interval after subtraction of the interval found for each end member and attributed by us to sluggishness. These are compared with the subsolidus curves based on eq 6 and 7 for transition involving diffusion.

emerged for the runs made at the higher temperatures. The pressure range over which the transition occurred was smaller for the end-member compositions than for the three intermediate compositions, 25, 50, and 75%. They acknowledge that this pattern might result from the two subsolidus curves analogous to the solidus-liquidus curves found in constant pressure $T-x$ diagrams. In such a case the pressure range observed for the end members would be attributed to sluggishness and the pressure range for the intermediate members would be attributed to sluggishness plus the separation of the subsolidus curves. However, Darnell and McCollum do not favor this explanation. Instead, they attribute the pattern to differences in hysteresis. It is our feeling that for temperatures of 200° and above, the transition would no longer be diffusionless. Note the agreement between their data at 600°, after subtracting the effect due to sluggishness, and the curves calculated on the basis of eq 6 and 7 (Figure 5).

If our interpretation is correct, then the B1 and B2 phases that coexist during the transition should have different compositions. There is no information on this aspect. Such information would be the surest indication of whether diffusion is involved in the transition.

C. The KCl-NaCl System. In the KCl-NaCl system at 25° and 1 bar, the diffusion rates are sufficiently slow so that solid solutions quenched from 600° continue to behave like solid solutions for days in spite of the fact that they exist in a two-phase region (Figure 1). Phase transitions in this system at 25° should, therefore, be of the diffusionless type. A plot of the transition pressure *vs.* mole fraction at 25° is given in Figure 2 and compared with a curve calculated on the basis of eq 9 for diffusionless transitions. The good agreement seems to bear out the expectation that these samples undergo diffusionless transitions.

At high temperatures (200° and over) diffusion probably takes place rapidly with one of two results.

(1) If the two-phase region shown in Figure 1 continues to exist or expands at high pressure, then samples cease to be solid solutions at higher temperatures and separate into K-rich and Na-rich phases. Thus, measurements will be on mixtures and not solid solutions.

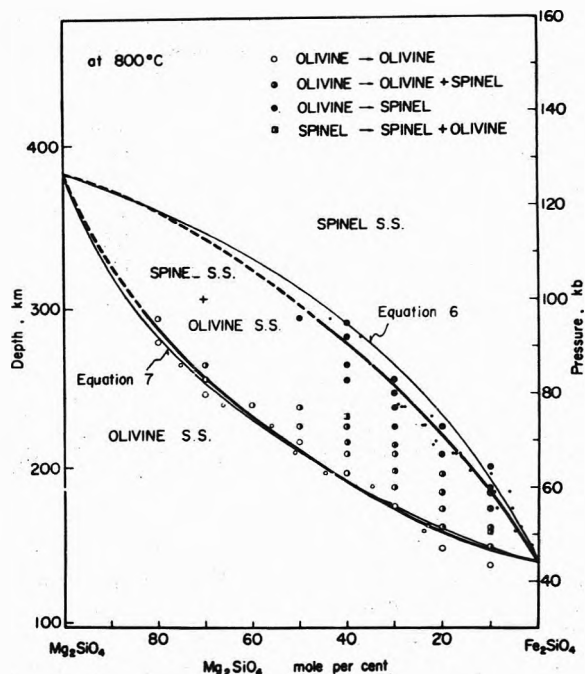


Figure 6. Comparison of the transition pressures for the system of Mg_2SiO_4 - Fe_2SiO_4 from the olivine phase to the spinel phase determined by Akimoto and Fujisawa¹⁸ at 800° with those calculated from eq 6 and 7. Scale on the left indicates depth within the earth's interior.

(2) If the two-phase region shrinks or disappears at high pressures, then the samples would behave like solid solutions and should undergo the B1-B2 phase transition in accordance with eq 6 and 7 for diffusion type transitions. Curves calculated on the basis of these equations (Figure 2) show an exceptionally large open loop. It is interesting to note that in either of the above cases, the first indication of a phase transition with increasing pressure would appear to be somewhat above 20 kbars and almost independent of mole fraction. In the first case a definite volume change would be observed whereas in the second case only the initiation of a volume change would be observed. Darnell and McCollum¹⁴ observed a phase transition at a pressure just over 20 kbars with a definite volume change (Figure 3). The transition pressure they observed was independent of composition but the volume change decreased steadily as the composition was shifted from the KCl end to the NaCl end. Thus, their results seem to be completely consistent with the first case described above, namely, the compression of a mixture of K-rich and Na-rich phases which exsolved due to immiscibility. If the sample is a mixture, the transition pressure should be that of the K-rich phase no matter how much of the Na-rich phase is present and the volume change should vary with composition according to the equation

$$\Delta V_m = \Delta V_K(1 - N_2) \quad (10)$$

where ΔV_m is the volume change in the mixture, ΔV_K is the volume change in pure KCl, and N_2 the mole fraction of pure NaCl. The results of Darnell and McCollum shown in Figure 3 are completely consistent with this equation.

In the room temperature experiments, however, there is good evidence that the phase transition proceeds in a diffusionless manner. The composition dependence of the transition pressure for the room temperature diffusionless

transition from B1 to B2 in the present study is in good agreement with measurements made by Jamieson^{10,11} and by Bassett.¹⁵

D. Fe₂SiO₄-Mg₂SiO₄ System. Besides the alkali halides the only other solid solution series studied in detail as a function of pressure is the Fe₂SiO₄-Mg₂SiO₄ system. Except for compositions of more than 80% Mg₂SiO₄, members of this series undergo a phase transition from the olivine structure to the spinel structure. Experimental data of Akimoto and Fujisawa¹⁸ showed the separation of the subsolidus curves (Figure 6). The volume change, ΔV^t , at room temperature for pure Fe₂SiO₄ is approximately 4.4 cm³/mol and for Mg₂SiO₄ it is estimated to be approximately 4 cm³/mol. At 800°, the transition pressure, P^t , for Fe₂SiO₄ is approximately 44 kbars and for Mg₂SiO₄ it is estimated to be approximately 127 kbars (Akimoto and Fujisawa¹⁸). Using these data and ignoring the fact that olivine transforms to a different structure at greater than 80% Mg₂SiO₄ we calculated the subsolidus curves on the basis of eq 6 and 7. These are compared with the experimental data of Akimoto and Fujisawa in Figure 6. Considering the uncertainties in assumed ΔV^t and P^t , the agreement is remarkable.

Conclusions

There is a striking paucity of experimental data for subsolidus relationships in P - x diagrams such as we have discussed in this paper. The fact that the equations we have proposed are in reasonable agreement with the data that are available leads us to believe that these equations should prove useful in interpreting subsolidus relationships when experimental data are lacking or insufficient.

The RbCl-KCl and KCl-NaCl series are potentially useful for pressure calibration. It is possible to produce solid solutions in these systems which have a transition at any desired pressure between 5 and 300 kbars simply by preparing the correct mole fraction. We have followed this procedure in our laboratory and found it to be successful when visual observations of the transition are possible.

Acknowledgments. This research was partially supported by NSF Grants GA-31902 and GA-38056X.

(18) S. Akimoto and H. Fujisawa, *J. Geophys. Res.*, **73**, 1467 (1968).

Thermodynamic Properties of the Reciprocal System (K⁺, Ag⁺ || NO₃⁻, SO₄²⁻) from Its Phase Diagram

M. L. Saboungi,^{1a} C. Vallet,^{*1b} and Y. Doucet

Laboratoire de Thermodynamique des Sels Fondus, associé au C.N.R.S., Centre St. Jérôme, 13013 Marseille, France
(Received May 15, 1972)

Publication costs assisted by the University of Provence, Marseille, France

The liquidus curves calculated from two solution theories are compared with the values obtained from our new phase diagram data on the (K⁺, Ag⁺ || NO₃⁻, SO₄²⁻) reciprocal salt system. Calculations from a random mixing model and a nonrandom mixing quasichemical model are given. In dilute solution of K₂SO₄ in AgNO₃, the pair formation energy ΔA_1 is determined by comparison between the expressions resulting from the generalized quasilattice theory and the quasichemical model. The value obtained is in accordance with the determination of Watt and Blander. In more concentrated solutions, the nonrandom mixing assumption leads to results which are close to our experimental data on both diagonals.

I. Introduction

The thermodynamic study of the molten salt reciprocal mixture (Ag⁺, K⁺ || NO₃⁻, SO₄²⁻) has been carried out from its liquidus curves, corresponding to both pairs Ag-NO₃(solvent)-K₂SO₄ and KNO₃(solvent)-Ag₂SO₄.

The departure from ideality, as expressed in terms of the mole fraction activity coefficients relative to pure solvent, is small, but not negligible. It is, however, greater for the solution of silver sulfate in potassium nitrate than for the solution of potassium sulfate in silver nitrate.²

This work is an attempt at calculating those deviations from ideality by taking into account short-range interactions.

II. Theories of Reciprocal Molten Salt Systems

In this section, we will give a short review of two principal theories: the Flood, Førland, and Grjøtheim theory³ (FFG) based on the hypothesis of a random mixing, and the quasichemical theory where a nonrandom mixing is considered. Both theories are extended to asymmetrical mixtures and put into a useful form for our calculations.

- (1) (a) Research Fellow C.N.R.S., Lebanon, (b) Reactor Chemistry Division, Oak Ridge Laboratory, Oak Ridge, Tn. 37830.
- (a) C. Vallet and M. L. Saboungi, *C. R. Acad. Sci., Ser. C*, **272**, 146 (1971); (b) M. L. Saboungi, *These de Specialite Aix-Marseille*, 1971.
- H. Flood, T. Førland, and K. Grjøtheim, *Z. Anorg. Allg. Chem.*, **276**, 289 (1954).

Random Mixing. The Flood, Førlund, and Grjøtheim theory has been applied to reciprocal mixtures of the general type ($W^+, X^+ || Y^-, Z^{2-}$) with the following basic assumptions.

(a) The configurational entropy of the solution is supposed to be the same as in an ideal mixture. The cations are randomly distributed on cation sites and the anions on anion sites.⁴ If the system contains w mol of W^+ , x mol of X^+ , y mol of Y^- , and z mol of Z^{2-} , the configurational entropy is

$$\Delta S^\circ = R(w \ln (w+x)/w + x \ln (w+x)/x + y \ln (y+z)/y + z \ln (y+z)/z) \quad (1)$$

(b) Long-range interactions are neglected. Only interactions between nearest and next nearest neighbors of both different charge sign and the same charge sign are taken into account. The former are due to the W^+Y^- , X^+Y^- , $W^+Z_{0.5}^-$, $X^+Z_{0.5}^-$ contacts. The two last types of contact are such that the pairs in question are neutral. In order to find the total number of contacts, the method used by Guggenheim⁵ for mixtures of neutral molecules has been followed, so that the relative numbers corresponding the various contacts are respectively

$$\begin{aligned} & wy/(w+x) \\ & xy/(w+x) \\ & 2wz/(w+x) \\ & 2xz/(w+x) \end{aligned}$$

To represent the enthalpy of the solution, one must include interactions such as $W^+Y^-X^+$; $Y^-W^+Z_{0.5}^-$; $W^+Z_{0.5}^-X^+$; $Y^-X^+Z_{0.5}^-$. The corresponding relative numbers of bonds may be calculated in the same manner.

$$\begin{aligned} & wxy/(w+x)^2 \\ & 2wzy/(w+x)^2 \\ & 2xwz/(w+x)^2 \\ & 2yxz/(w+x)^2 \end{aligned}$$

The interaction parameter which has been experimentally determined previously in the case of common ion systems⁶ may be interpreted in terms of the variation of energy corresponding to the formation of the above associations. It can be defined as the partial molal enthalpy of mixing of the solute at infinite dilution; in the case of a regular mixture, it is also the interaction parameter found from the Gibbs free energy of mixing. The Gibbs free energy of mixing can be written as follows

$$\begin{aligned} G^M = & \frac{wy}{w+x} G_{WY}^\circ + \frac{2wz}{w+x} G_{WZ_{0.5}}^\circ + \frac{xy}{w+x} G_{XY}^\circ + \\ & \frac{2xz}{w+x} G_{XZ_{0.5}}^\circ + \frac{wxy}{(w+x)^2} \lambda_Y + \frac{2wxz}{(w+x)^2} \lambda_Z + \\ & \frac{2wyz}{(w+x)^2} \lambda_W + \frac{2xyz}{(w+x)^2} \lambda_X - T\Delta S^\circ \quad (2) \end{aligned}$$

where ΔS° is given by eq 1, the G_{ij}° terms are relative to the pure components ij and the λ_i 's represent the interaction constants for the binary systems with a common ion, the single subscript indicating the common ion. The chemical potential of a component, WY, for instance is

$$\bar{G}_{WY} = \left[\frac{\partial G^M}{\partial w} \right]_{x,y,z} + \left[\frac{\partial G^M}{\partial y} \right]_{x,w,z} \quad (3)$$

whence

$$\begin{aligned} RT \ln a_{WY} = & \bar{G}_{WY} - G_{WY}^\circ = RT \ln \frac{wy}{(w+x)(y+z)} + \\ & \frac{2xz}{(w+x)^2} (G_{WZ_{0.5}}^\circ + G_{XY}^\circ - G_{XZ_{0.5}}^\circ - G_{WY}^\circ) + \\ & \frac{2z(xy+2wz)}{(w+x)^3} \lambda_W + \frac{2xz(2z-y)}{(w+x)^3} \lambda_X + \\ & \frac{x(xy+2wz)}{(w+x)^3} \lambda_Y + \frac{2xz(x-w)}{(w+x)^3} \lambda_Z \quad (4) \end{aligned}$$

By definition the activity coefficient f_{WY} is

$$G_{WY} = f_{WY} X_W X_Y \quad (5)$$

where X_W and X_Y are the Temkin ionic fractions and a_{WY} is the activity of WY.

$$\begin{aligned} X_W &= w/(w+x) \\ X_Y &= y/(y+z) \\ X_X &= x/(w+x) \\ X_Z &= z/(y+z) \end{aligned} \quad (6)$$

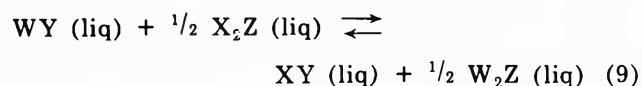
the neutrality condition being $w+x = y+2z$. From eq 4 and 5, the excess free energy of WY in the WY- X_2Z mixture is

$$\begin{aligned} T \ln f_{WY} = & X_X' X_Z' [\Delta G^\circ + \lambda_X (X_Z' - X_Y')] + \\ & \lambda_Z (X_X' - X_W') + (\lambda_W X_Z' + \lambda_Y X_X') (X_W' X_Z' + X_X' X_Y') \end{aligned} \quad (7)$$

The X_i' being the equivalent ionic fractions

$$\begin{aligned} X_X' &= x/(w+x) \\ X_Y' &= y/(y+2z) \\ X_W' &= w/(w+x) \\ X_Z' &= 2z/(y+2z) \end{aligned} \quad (8)$$

and ΔG° the free energy change for the exchange reaction

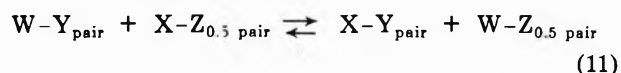


For the cases of interest here $w = y$ and $x = 2z$. Consequently we may write in terms of X_X'

$$\begin{aligned} RT \ln f_{WY} = & X_X'^2 (\Delta G^\circ + 2\lambda_W + 2\lambda_Y - \lambda_X - \lambda_Z) + \\ & 2X_X'^3 (\lambda_X + \lambda_Z - \lambda_W - \lambda_Y) \quad (10) \end{aligned}$$

Nonrandom Mixing. In a second approach, the dissimilarities between the properties of the ions have been taken into account; a nonrandom mixing has therefore been assumed. If y^* is the departure from random mixing, the number of X-Y bonds is $[xy/(w+x)^2] + y^*$, by counting only nearest neighbors pairs.

The energy change for the reaction



is denoted by $\Delta E^\circ/Z$, Z being the mean coordination number of the ions in the molten salt. Applying the mass-

(4) M. Temkin, *Acta. Phys. Chim. USSR*, **20**, 411 (1945).

(5) E. A. Guggenheim, "Mixtures," Oxford University Press, London, 1952.

(6) C. Vallet, These Aix-Marseille, 1970.

action law to the above reaction as in the quasichemical theory we obtain

$$\frac{\left[\frac{2wz}{(w+x)^2} + y^* \right] \left[\frac{xy}{(w+x)^2} + y^* \right]}{\left[\frac{wy}{(w+x)^2} - y^* \right] \left[\frac{2xz}{(w+x)^2} - y^* \right]} = K = \exp\left(\frac{-\Delta E^\circ}{ZRT}\right) \quad (12)$$

Using the equivalent ionic fractions given by eq 6, we may write

$$\frac{-\Delta E^\circ}{ZRT} = \ln \left[1 + \frac{y^*}{X_W'X_Z'} \right] + \ln \left[1 + \frac{y^*}{X_X'X_Y'} \right] - \ln \left[1 - \frac{y^*}{X_W'X_Y'} \right] - \ln \left[1 - \frac{y^*}{X_X'X_Z'} \right] \quad (13)$$

If y^* is smaller than any of the products of an anionic and cationic equivalent fraction, the logarithmic terms may be expanded in powers of y^* . Hence neglecting the square terms

$$y^* = -X_W'X_X'X_Y'X_Z' (\Delta E^\circ/ZRT) \quad (14)$$

The excess energy of mixing due to the nonrandom distribution is

$$\Delta E^* = y^* \Delta E^\circ = -X_X'X_W'X_Z'X_Y' [(\Delta E^\circ)^2/ZRT] \quad (15)$$

and the corresponding free excess energy of mixing is

$$\Delta G^* = T \int_0^{1/T} \Delta E^* d(1/T) = -X_X'X_W'X_Z'X_Y' [(\Delta E^\circ)^2/2ZRT] \quad (16)$$

The total free energy of the solution, which takes into account the departure from a random distribution, is

$$G^{*M} = G^M + (w+x) \Delta G^* \quad (17)$$

where G^M is given by eq 2 and $(w+x)$ is the number of moles present in the solution.

By following the same derivations as in eq 3 and 5 we obtain

$$RT \ln f_{WY} = X_X'^2 (\Delta G^\circ + 2\lambda_W + 2\lambda_Y - \lambda_X - \lambda_Z - \Lambda) + 2X_X'^3 (\lambda_X + \lambda_Z - \lambda_W - \lambda_Y + 2\Lambda) - 3X_X'^4 \Lambda \quad (18)$$

where Λ is given by

$$\Lambda = -(\Delta E^\circ)^2/2ZRT \sim -(\Delta G^\circ)^2/2ZRT \quad (19)$$

A different statistical mechanical treatment of the mixture ($W^+, X^+ || Y^-, Z^{2-}$) may be used by applying the conformational ionic solution (CIS) theory proposed by Blander and Yosim.⁷ Depending on the order of the approximation in the power expansion, one can derive easily either eq 10 (first-order approximation) or 18 (second-order approximation). The nonrandom mixing term Λ , however, cannot be obtained readily from theory but is proportional to $(\Delta G^\circ)^2$. It is introduced by comparison with the corresponding term in the quasilattice theory.⁸

III. Experimental Section

In order to study the reciprocal diagram of the system ($K^+, Ag^+ || NO_3^-, SO_4^{2-}$), we determined the liquidus curves on both ($AgNO_3-K_2SO_4$) and ($KNO_3-Ag_2SO_4$) diagonals.

Merck reagent grade chemicals were used. The salts were finely ground (except in the case of $AgNO_3$) and heat dried. The relative error on the determination of solute masses did not exceed 10^{-4} .

Each run was begun by a measurement of the melting point of the pure solvent. The solute was then added in three or four successive portions in each crucible and the liquidus temperature determined from the thermal halt. The quantities added were increasingly significant in determining the composition, so that the final composition was known with the same relative precision.

The temperature was recorded with a Pt-Pt-10% Rh thermocouple. The hot junction, sealed in a thin-walled Pyrex tube, was introduced along the axis of the cylindrical crucible and the cold junction was in a water triple point cell. The composition and temperature in the sample were kept homogeneous by efficient stirring.

The major fraction of the thermocouple emf was compensated by means of a P 12 manual potentiometer and the remainder, less than 1 mV, was amplified with a Leeds and Northrup voltage amplifier and recorded on a MECI potentiometer.

The cooling rate being less than 1 K min^{-1} , the cooling curves recorded for the liquid and the liquid + solid were nearly two straight lines of different slopes. The temperature at which solid forms is given by their intersection.⁹ Each recording was performed in triplicate and the reproducibility was better than 0.02 K.

IV. Results

The activity coefficients of the solvent on both diagonals were calculated, under the assumption of no formation of solid solution from the liquidus temperatures of the phase diagram^{2b} utilizing the Schroder van Laar equation.

$$R \ln a = -\Delta H_0 \left(\frac{1}{T} - \frac{1}{T_0} \right) + \Delta C_p \left(\frac{T_0}{T} - 1 - \ln \frac{T_0}{T} \right) \quad (20)$$

ΔH_0 is the heat of fusion of the solvent at the melting temperature T_0 and ΔC_p , the heat capacity change upon melting, is defined by

$$\Delta C_p = C_p(\text{liq}) - C_p(\text{sol})$$

The parameters used in eq 20 were obtained from standard literature values.^{10,11} Activity coefficients were calculated for each solvent from the expressions

$$a_{KNO_3} = X_K X_{NO_3} f_{KNO_3}$$

and

$$a_{AgNO_3} = X_{Ag} X_{NO_3} f_{AgNO_3} \quad (21)$$

where the X_i 's are the ionic fractions defined in the eq 6. The values of $RT \ln f_{KNO_3}$ and $RT \ln f_{AgNO_3}$ are plotted in Figures 1 and 2, respectively.

Calculations in Concentrated Solutions. We will make two sets of calculation from theory for both diagonals for comparison with the experimental data. The first calculation is based upon the FFG theory and consists of applying eq 10. The second calculation is based upon the

(7) M. Blander and S. J. Yosim, *J. Chem. Phys.*, **39**, 2610 (1963).

(8) M. Blander, *J. Chem. Phys.*, **34**, 432 (1961); M. Blander and J. Braunstein, *Ann. N. Y. Acad. Sci.*, **79**, 838 (1960).

(9) C. Vallet, *J. Chim. Phys.*, **69**, 311 (1972).

(10) K. K. Kelley, Bureau of Mines, Bulletin No. 584, 393, 477.

(11) F. D. Rossini, *Nat. Bur. Stand. U. S. Circ.*, 500 (1952).

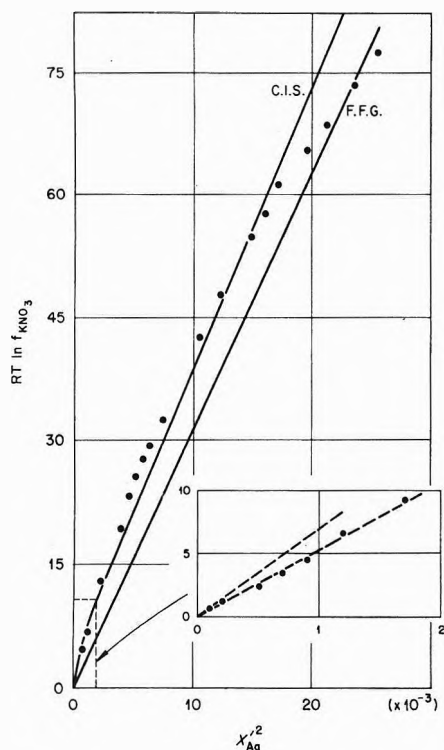
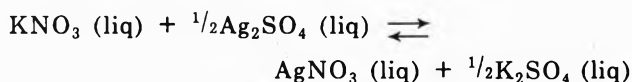


Figure 1. Experimental and calculated values at the liquidus temperatures of excess chemical potential of KNO_3 vs. X_{Ag}^2 in the KNO_3 - Ag_2SO_4 quasibinary mixture: (circle) our experimental results; F.F.G., Flood, Førland, and Griøtheim theory (random mixing); CIS, conformal ionic solution theory (nonrandom mixing). Inset shows our results in the dilute solution range and the corresponding limiting slopes.

quasichemical theory or the CIS theory using eq 18. A comparison of these calculations with our experimental data will enable us to evaluate the importance of the nonrandom mixing term.

The Gibbs free energy exchange, ΔG° , corresponding to the equilibrium



has been calculated from tabulated data on pure molten salts¹¹ by taking into account the heats of fusion, formation, and transition. The specific heats of the reactants and the products are assumed to be equal.¹² The value obtained is 4 kcal/mol. The variation of ΔG° with temperature along the liquidus is negligible.

We reported in Table I the values of the interaction parameters. These were estimated from phase diagrams or calorimetric data when the latter were available. By applying eq 20 to phase diagram data on the AgNO_3 - Ag_2SO_4 ¹³ and KNO_3 - K_2SO_4 ¹⁴ systems, average values for λ_{Ag} and λ_{K} were then estimated by assuming a regular behavior of the solutions. The λ_{NO_3} coefficient was determined by comparison with the calorimetric data of Kleppa¹⁵ and the results of Franzosini.¹⁶ The K_2SO_4 - Ag_2SO_4 ¹⁷ system forms solid solutions; the λ_{SO_4} parameter is consequently small and might be assumed equal to zero.¹⁸

A mean value of the quasilattice "coordination number" Z has been taken equal to 5 as it varies generally from 4 to 6 in some molten salts.¹⁹

As discussed above, values of ΔG° , λ_i , and Z were utilized in conjunction with eq 10, 18, and 19 to calculate the

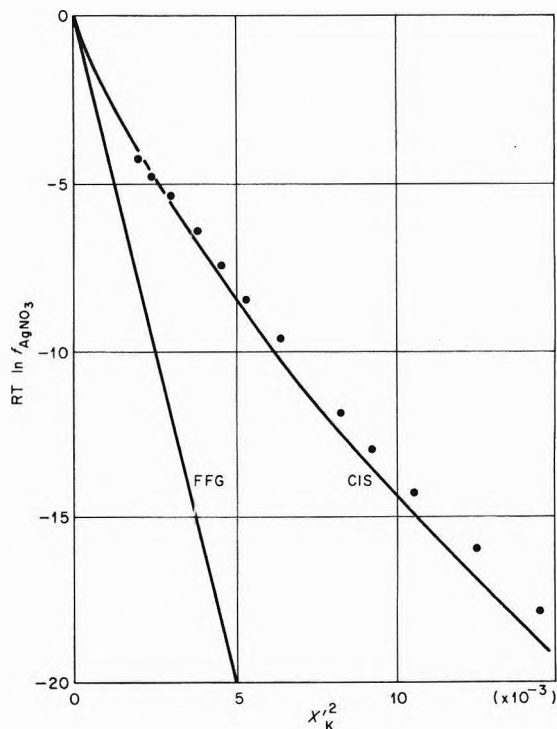


Figure 2. Experimental and calculated values at the liquidus temperatures of excess chemical potential of AgNO_3 vs. X_{K}^2 in the AgNO_3 - K_2SO_4 quasibinary mixture: symbols, same as in Figure 1.

TABLE I: Values of λ_i for Binary Mixtures

Mixture	λ_i , cal/mol
AgNO_3 - KNO_3^a	-500
AgNO_3 - Ag_2SO_4^b	700
KNO_3 - K_2SO_4^c	300
K_2SO_4 - Ag_2SO_4^d	0

^a From ref 15 and 16. ^b From ref 13. ^c From ref 14. ^d From ref 17.

two sets of values of $RT \ln f_{\text{sol}i}$ along each diagonal. These values are reported in Tables II and III.

In Figure 1, experimental values of $RT \ln f_{\text{KNO}_3}$ have been plotted vs. X_{Ag}^2 and compared to those calculated from both theories. At the dilute end, the CIS theory is in very good agreement with the experimental data. In fact, if the parameters were adjusted within their known uncertainties, an exact fit could be obtained along the curve.

In the case of the AgNO_3 - K_2SO_4 quasibinary mixture, the three sets of values of $RT \ln f_{\text{AgNO}_3}$ have been plotted vs. X_{K}^2 . A striking agreement is obtained between our experimental values and those calculated from the CIS theory, while a large departure from the values calculated from the F.F.G. theory is evident.

- (12) M. Blander and L. E. Töpol, *Inorg. Chem.*, **5**, 1641 (1966).
 (13) E. Kordes, *Z. Elektrochem.*, **55**, 600 (1951).
 (14) E. Ph. Perman and W. J. Howells, *J. Chem. Soc.*, **123**, 2128 (1923).
 (15) O. J. Kleppa, R. B. Clarke, and L. S. Hersh, *J. Chem. Phys.*, **35**, 175 (1961).
 (16) P. Franzosini and C. Sinistri, *Ric. Sci.*, 439 (1963).
 (17) R. Nacken, *Neues Jahrb. Mineral. Geol. Palaontol. Beil. Band.*, **24**, 1 (1907).
 (18) M. Blander and L. E. Topol, *Electrochim. Acta*, **10**, 1161 (1965).
 (19) H. A. Levy, P. A. Agron, M. A. Bredig, and H. D. Danford *Ann. N. Y. Acad. Sci.*, **79**, 762 (1960).

TABLE II: Excess Chemical Potentials of KNO₃, along the Liquidus, in the KNO₃-Ag₂SO₄ Quasibinary

10 ⁴ X _{Ag} ^{1/2}	RT ln f _{KNO₃}		
	Measured	Random mixing (FFG)	Nonrandom mixing (CIS)
22	12.929	6.470	11.770
40	19.243	12.050	16.920
46	23.275	13.880	18.758
51	25.558	15.420	20.626
58	27.641	17.630	23.336
63	29.470	19.170	25.104
73	32.302	22.250	29.012
103	42.618	31.760	40.300
122	47.877	37.810	47.330
147	54.848	45.870	56.370
160	57.750	50.000	61.010
171	61.368	53.640	64.360
195	65.617	61.410	75.590
212	68.700	67.060	79.480
235	73.040	74.630	87.370
254	77.263	80.950	93.070

TABLE III: Excess Chemical Potentials of AgNO₃, along the Liquidus, in the AgNO₃-K₂SO₄ Quasibinary

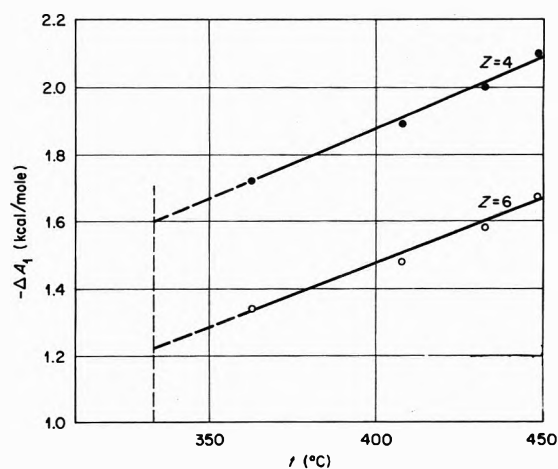
10 ⁴ X _K ^{1/2}	RT ln f _{AgNO₃}		
	Measured	Random mixing (FFG)	Nonrandom mixing (CIS)
20.5	-4.201	-8.180	-3.984
24.5	-4.657	-9.340	-4.496
29.6	-5.293	-11.670	-5.086
37.9	-6.470	-14.770	-6.466
45.7	-7.462	-17.880	-7.846
53.6	-8.446	-20.980	-8.870
65	-9.595	-25.250	-10.205
83.9	-11.798	-32.610	-12.068
94.1	-12.932	-36.480	-13.470
106.2	-14.232	-41.120	-14.570
125.6	-15.943	-48.860	-16.646
144.7	-17.814	-56.200	-18.773

Consequently, at intermediate concentrations, a non-random mixing hypothesis is necessary for describing solution behavior.

Calculations in Dilute Solutions. The AgSO₄⁻ Pair Formation Energy

Although phase diagram measurements are not among the most sensitive for the study of association of dilute solutes and although such a study was not the original aim of our investigation, we felt that it would be worthwhile to estimate the pair formation energy of AgSO₄ from our lowest concentration measurements. This seemed of particular interest because of a discrepancy in reported results for the temperature dependence of the AgSO₄⁻ pair formation energy in KNO₃.

The very dilute solution range has been investigated by Watt and Blander²⁰ and by Sacchetto, *et al.*,²¹ by means of emf measurement. These authors discussed the properties of very dilute solution of K₂SO₄ and AgNO₃ in the solvent KNO₃ in terms of the quasilattice model. According to the quasilattice calculations^{22,23} in both the symmetric and asymmetric approximations the conven-

**Figure 3.** Extrapolation of the energy of ion pair formation ΔA_1 from results of Watt and Blander.²⁰

tional association constant K_1 is given by

$$K_1 = Z[\exp(-\Delta A_1/RT) - 1] \quad (22)$$

where Z is the mean coordination number in the quasilattice and ΔA_1 is a pair formation energy.

If the y_i are Temkin ionic fractions of species, considering AgSO₄⁻ pair formation, the association constant is defined as

$$K_1 = y_{\text{AgSO}_4} / y_{\text{Ag}} y_{\text{SO}_4} \quad (23)$$

The part of the KNO₃ activity coefficient arising from the nearest neighbor interactions which lead to nonrandom mixing can be written as

$$f_{\text{KNO}_3}' = y_{\text{K}} y_{\text{NO}_3} / (1 - X_{\text{Ag}})(1 - X_{\text{SO}_4}) \quad (24)$$

By expanding $\ln f_{\text{KNO}_3}'$, one obtains easily the limiting equation

$$\lim_{X_{\text{Ag}} \rightarrow 0} [d(\ln f_{\text{KNO}_3}') / d(X_{\text{Ag}}'^2)] = K_1/2 \quad (25)$$

which may be applied to the data in very dilute solutions. In order to account for the influence of longer range interactions on the excess chemical potential of KNO₃, we have added the binary terms included in eq 10 as suggested by Blander and Topol.¹⁸ The association constant, K_1 , can then be calculated from the limiting slope [ls] of the plot of excess chemical potential of KNO₃ plotted *vs.* the square of the ionic mole fraction of silver, X_{Ag}'

$$[\text{ls}] = (RT/2)K_1 + (2\lambda_{\text{K}} + 2\lambda_{\text{NO}_3} - \lambda_{\text{Ag}} - \lambda_{\text{SO}_4}) \quad (26)$$

From the results given in Table IV and represented in inset of Figure 1, the estimated value of the limiting slope is in the range 7300-5500. Our resultant value for the pair formation energy, ΔA_1 , at 607 K²⁴ has an estimated uncertainty of 150 cal. It should be noted that this accuracy is better than might be expected for data obtained from phase diagram measurements at such low concentrations.

(20) W. J. Watt and M. Blander, *J. Phys. Chem.*, **64**, 729 (1960).

(21) G. A. Sacchetto, C. Macca, and G. G. Bombi, *J. Electroanal. Chem.*, **36**, 319 (1972).

(22) M. Blander, *J. Phys. Chem.*, **63**, 1262 (1959).

(23) J. Braunstein, "Ionic Interactions," Vol. 1, Academic Press, New York, N. Y., 1971, p 232.

(24) We notice that the ΔA_1 variation along the liquidus branch (the freezing point depression being of the order of 5 K) is negligible. We assume consequently that our ΔA_1 determination has been obtained at the melting temperature of pure KNO₃ (607 K).

TABLE IV: Excess Chemical Potential of KNO_3 , along the Liquidus, in the Dilute End of $\text{KNO}_3\text{-Ag}_2\text{SO}_4$

$10^4 X_{\text{Ag}}'^2$	1	2	5	7	9	12	17
$RT \ln f_{\text{KNO}_3}$	0.714	1.245	2.452	3.527	4.566	6.617	9.372

TABLE V: Comparison of Values of AgSO_4^- Pair Formation Energy in Molten KNO_3

	Z		
	4	5	6
$-\Delta A_1,^a$ kcal	1.51 \mp 0.15	1.35	0.15
$-\Delta A_1,^b$ kcal	1.6		1.19 \mp 0.15
$-\Delta A_1,^c$ kcal		1.58	0.05

^a This work. ^b Values extrapolated at 607 K from ref 20 assuming a linear temperature dependence. ^c Average value from ref 21 in the temperature range 622–715 K assuming no temperature dependence.

Comparison of our results for $Z = 4, 5,$ and 6 with those previously reported,^{20,21} is given in Table V. Our value of ΔA_1 is in better agreement with a value extrapolated (Figure 3) from the reported results of Watt and Blan-

der²⁰ than with the temperature independent value reported by Sacchetto, *et al.*²¹ Nevertheless, a more specific investigation with a more sensitive experimental method is required to provide an unequivocal evaluation of the temperature dependence of the association energy.

Conclusion

Experimental data have been presented for the system ($\text{K}^+, \text{Ag}^+ | | \text{NO}_3^-, \text{SO}_4^{2-}$) and have been interpreted theoretically. In dilute solutions, our estimation of the $(\text{AgSO}_4)^-$ pair formation energy is in the same range of order as previous determinations. (The nonrandom mixing hypothesis was found to give better agreement with the experimental results than the random mixing hypothesis, the fit being most striking at high concentrations.)

Acknowledgments. The authors wish to thank Dr. M. Blander (Argonne National Laboratory) and Dr. J. Braustein (Oak Ridge National Laboratory) for their interest and for many helpful suggestions. Financial assistance from the National Research Council of Lebanon to one of us (M. L. S.) is gratefully acknowledged.

Kinetics and Mechanism of the Reaction between Hydroxyapatite and Fluoride in Aqueous Acidic Media^{1,2}

Zao-Shon Liang and William I. Higuchi*

College of Pharmacy, The University of Michigan, Ann Arbor, Michigan 48104 (Received March 24, 1972)

Publication costs assisted by the National Institute of Dental Research

The physical model of the reaction was investigated both experimentally and theoretically over a wide range of conditions. The theoretical rates were calculated as a function of pH, fluoride concentration, and phosphate concentration of the reaction solution. Experimental rate data obtained under a wide variety of conditions were compared to these model predictions. The agreement of the model predictions with the experiments was found to be essentially quantitative under all conditions with the adjustment of a single parameter, the apatite-calcium fluoride "equilibrium" constant. The magnitude of this constant was found to be consistent with the interpretation that the apatite-calcium fluoride interface was significantly supersaturated with respect to calcium fluoride during the reaction. A calcium fluoride activity product of about 10^{-8} was deduced from this analysis. This is greater than the solubility product of calcium fluoride by a factor of about 10^3 . Supersaturations of this same order of magnitude were found in the calcium fluoride precipitation studies.

Introduction

There is overwhelming evidence today that the topical application of relatively concentrated fluoride solutions to teeth results in the significant reduction in the tendency for dental caries formation.³ While certain aspects of the chemistry of the fluoride-enamel (the mineral of which is principally hydroxyapatite) reactions have been investigated, these studies have not considered the kinetics and mechanisms of the reaction.⁴

When hydroxyapatite is exposed to high concentrations of fluoride, calcium fluoride is precipitated while the

- (1) Presented at 49th Meeting of International Association for Dental Research, Chicago, Ill., March 1971.
- (2) Portions of this paper are derived from the Ph.D. dissertation of Z. Liang, The University of Michigan, 1971.
- (3) F. Brudevold, A. Savory, D. E. Gardner, M. Spinelli, and R. Speirs, *Arch. Oral Biol.*, **8**, 167 (1963); J. R. Mellberg, *J. Dent. Res.*, **45**, 303 (1966).
- (4) H. G. McCann, *Arch. Oral Biol.*, **13**, 987 (1968); A. Malaowalla and H. M. Myers, *J. Dent. Res.*, **41**, 413 (1962).

phosphate is released to the solution.⁵ The application of physical chemical principles to elucidate the mechanism of this reaction involving fluoride and hydroxyapatite was proposed by Nelson and Higuchi.⁶ They presented a model based on the simultaneous diffusion and chemical equilibria of the reactants and products⁷ and an equilibrium chemical reaction at the moving interface between hydroxyapatite and the precipitating layer of calcium fluoride.

The purpose of the present study was to examine the applicability and the validity of the model under various experimental conditions. The quantitative determinations of fluoride uptake in experiments were to be carried out over a wide range of reactant concentrations and at various solution pH and buffer conditions where the model predicts dramatic changes in the reaction rate.

Theory

The proposed model⁶ (Figure 1) assumes that steady-state diffusion exists in the layer of calcium fluoride which forms during the reaction of hydroxyapatite with buffered fluoride solutions. It is assumed that transport through the CaF_2 layer occurs by diffusion in the aqueous solution filling the pores of the layer which is characterized by a porosity and tortuosity. It is also assumed that the transport resistance of the CaF_2 layer is in series with a fluid film resistance characterized by a thickness, h . Recalling Fick's first law of diffusion, taking the concentration gradients to represent the driving forces, and neglecting the influences of the electric diffusion potential,⁸ we may write

$$-J_{\text{TB}} = \sum_{i=1}^2 D_{\text{Bi}} \frac{dC_{\text{Bi}}}{dx} \quad (1)$$

$$-J_{\text{TP}} = \sum_{i=1}^4 D_{\text{Pi}} \frac{dC_{\text{Pi}}}{dx} \quad (2)$$

$$-J_{\text{TH}} = \sum_{i=1}^3 i D_{\text{Pi}} \frac{dC_{\text{Pi}}}{dx} + \sum_{i=1}^2 D_{\text{Fi}} \frac{dC_{\text{Fi}}}{dx} + D_{\text{H1}} \frac{dC_{\text{H1}}}{dx} + D_{\text{B1}} \frac{dC_{\text{B1}}}{dx} \quad (3)$$

$$-J_{\text{TF}} = \sum_{i=1}^2 i D_{\text{Fi}} \frac{dC_{\text{Fi}}}{dx} + D_{\text{F3}} \frac{dC_{\text{F3}}}{dx} \quad (4)$$

where the subindices are chosen so that TB, TP, TH, and TF are the total buffer, total phosphate, total acid, and total fluoride, respectively. The subindex B1 represents HB, B2 represents B^- , P1 represents HPO_4^{2-} , P2 represents H_2PO_4^- , P3 represents H_3PO_4 , P4 represents PO_4^{3-} , F1 represents HF, F2 represents HF_2^- , H1 represents H^+ , F3 represents F^- , the C 's are the concentrations, the J 's are the fluxes, and the D 's are the effective diffusivities for the species indicated by the subindices. Equations 1-4 assume that a given ionic species is diffusing without interacting with the other species present. The effective diffusivity D for a given species is related to the diffusivity of the species in the aqueous phase, D_{aq} , by

$$D = D_{\text{aq}}(\epsilon/\tau)$$

where ϵ = porosity and τ = tortuosity of the CaF_2 layer.

According to the stoichiometry of the net reaction

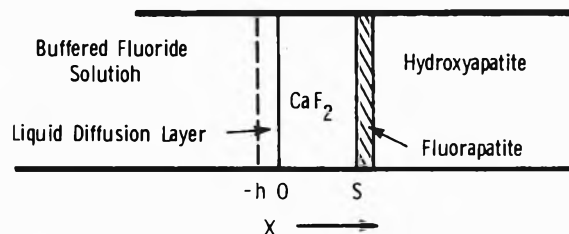
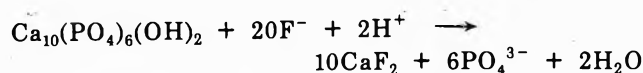


Figure 1. Physical model of apatite to calcium fluoride reaction.

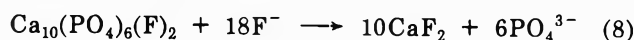
we have

$$J_{\text{TB}} = 0 \quad (5)$$

$$20J_{\text{TP}} = -6J_{\text{TF}} \quad (6)$$

$$20J_{\text{TH}} = 2J_{\text{TF}} \quad (7)$$

When hydroxyapatite is in contact with a fluoride solution, it simulates^{6,9} a "fluoroapatite phase" which may govern the reaction conditions at $x = s$. This fluoroapatite phase may be characterized⁶ by an activity product, K_{FAP} . Therefore a constant, K_{eq} , may be written for the reaction



$$K_{\text{eq}} = (\text{PO}_4^{3-})^6 / (\text{F}^-)^{18} = K_{\text{FAP}} / K_{\text{CaF}_2}^{10}$$

solving the above equations, we get

$$(\text{F}^-)_s = \frac{(OU - MV) + \sqrt{(MV - OU)^2 - 4(LV - PU)(NV - RU)}}{2(LV - PU)} \quad (9)$$

$$K(\text{F}^-)_s^3(\text{H}^+)_s^2V - P(\text{F}^-)_s^2 - (\text{F}^-)_s - R = 0 \quad (10)$$

where

$$K = K_{\text{eq}}^{1/6} / K_{3p}K_{2p}$$

$$K_p = (\text{H}^+)(\text{H}_2\text{PO}_4^-) / (\text{H}_3\text{PO}_4)$$

$$K_{2p} = (\text{H}^+)(\text{HPO}_4^{2-}) / (\text{H}_2\text{PO}_4^-)$$

$$K_{3p} = (\text{H}^+)(\text{PO}_4^{3-}) / (\text{HPO}_4^{2-})$$

$$K_{\text{HF}} = (\text{H}^+)(\text{F}^-) / (\text{HF})$$

$$K_{\text{HF}_2} = (\text{HF}_2^-) / (\text{HF})(\text{F}^-)$$

$$K_{\text{HB}} = (\text{H}^+)(\text{B}^-) / (\text{HB})$$

$$K_{\text{CaF}_2} = (\text{Ca}^{2+})(\text{F}^-)^2$$

$$K_{\text{FAP}} = (\text{Ca}^{2+})^{10}(\text{PO}_4^{3-})^6(\text{F}^-)^2$$

$$L = -\frac{16}{20}D_{\text{HF}}(K_{\text{HF}_2}/K_{\text{HF}})(\text{H}^+)_s$$

$$M = \frac{2}{20}D_{\text{F}} - \frac{18}{20}D_{\text{HF}}[(\text{H}^+)_s/K_{\text{HF}}]$$

(5) J. R. Blayney and I. N. Hill, *J. Amer. Dent. Ass.*, **74**, 233 (1967).

(6) K. G. Nelson and W. I. Higuchi, *J. Dent. Res.*, **49**, 154 (1970).

(7) D. R. Olander, *AIChE J.*, **6**, 233 (1960).

(8) Z. Liang, doctoral dissertation, Appendix IV, The University of Michigan, 1971.

(9) N. A. Mir, W. I. Higuchi, and J. J. Hefferren, *Arch. Oral Biol.*, **14**, 901 (1969).

$$\begin{aligned}
 N &= -\frac{2}{20}D_F(F^-)_0 + \frac{18}{20}D_{HF}(HF)_0 + \frac{16}{20}D_{HF_2}(HF_2^-)_0 - \\
 &D_H(H^+)_s + D_H(H^+)_0 - D_{HB}\frac{D_{HB}(HB)_0 + D_B(B^-)_0}{D_{HB} + [D_B K_{HB}/(H^+)_s]} + \\
 &D_{HB}(HB)_0 + D_{HPO_4}(HPO_4^{2-})_0 + 2D_{H_2PO_4}(H_2PO_4^-)_0 + \\
 &\quad 3D_{H_3PO_4}(H_3PO_4)_0 \\
 P &= -\frac{12}{20}D_{HF_2}(K_{HF_2}/K_{HF})(H^+)_s \\
 Q &= -\frac{6}{20}D_F - \frac{6}{20}D_{HF}[(H^+)_s/K_{HF}] \\
 R &= \frac{6}{20}D_F(F^-)_0 + \frac{6}{20}D_{HF}(HF)_0 + \frac{12}{20}D_{HF_2}(HF_2^-)_0 + \\
 &D_{H_3PO_4}(H_3PO_4)_0 + D_{H_2PO_4}(H_2PO_4^-)_0 + \\
 &\quad D_{HPO_4}(HPO_4^{2-})_0 + D_{PO_4}(PO_4^{3-})_0 \\
 U &= \frac{D_{HPO_4}}{(H^+)_s}K_{2p} + 2D_{H_2PO_4} + 3D_{HPO_4}\frac{(H^+)_s}{K_p} \\
 V &= D_{H_3PO_4}\frac{(H^+)_s}{K_p} + D_{H_2PO_4} + D_{HPO_4}\frac{K_{2p}}{(H^+)_s} + \\
 &\quad D_{PO_4}\frac{K_{3p}K_{2p}}{(H^+)_s^2}
 \end{aligned}$$

and the parentheses indicate the concentrations of the enclosed species.

The concentration terms with subscripts 0 correspond to the conditions in the bulk solution and s to that at the CaF₂-hydroxyapatite interface.

The total fluoride flux may now be related to the time change in concentration of total fluoride in the bulk solution by

$$V\frac{d(TF)}{dt} = AD_{TF}\frac{(TF)_s - (TF)}{S + (h\epsilon/\tau)} \quad (11)$$

where A is the area exposed to the solution in cm², V is the volume of the solution, S is the thickness of CaF₂ layer, and $D_{TF} [= (D_{TF})_{aq} (\epsilon/\tau)]$ is the *apparent* effective diffusivity for total fluoride. The use of D_{TF} is essentially the same as equating the diffusion coefficients for all of the fluoride species.

It can be shown that eq 11 may be integrated holding $(TF)_s$ constant when $[(TF) - (TF)_s] \gg \Delta(TF)_s$ where $\Delta(TF)_s$ is the maximum change in $(TF)_s$ during an experiment. Integration of eq 11 and substitution⁶ of the density of fluoride, Δ , into the equation then yield

$$\begin{aligned}
 &\frac{19V^2}{A^2\Delta(1-\epsilon)D_{TF}} \left((TF) - (TF)_i + \right. \\
 &(TF)_s \ln \frac{(TF) - (TF)_s}{(TF)_i - (TF)_s} \left. - \left(\frac{19(TF)_i V^2}{A^2\Delta(1-\epsilon)D_{TF}} + \right. \right. \\
 &\quad \left. \left. \frac{Vh\epsilon}{\tau AD_{TF}} \right) \ln \frac{(TF) - (TF)_s}{(TF)_i - (TF)_s} = t
 \end{aligned}$$

The (TF) is implicitly a function of time. For any specific (TF) or for the corresponding amount of phosphate released to the solution, the time can be calculated.

All the numerical calculations with the model could be carried out on an IBM 360 digital computer. For solving $(F^-)_s$ and $(H^+)_s$ a numerical successive iteration method based upon eq 9 and 10 may be used.

Experimental Section

General Considerations. The basic approach was to carry out those experiments which were expected to provide independent tests of the different aspects of the model. Thus it was decided to investigate first the influences of the fluoride concentration, the buffer concentration for two buffer types, the pH, and the phosphate concentration upon the rate of reaction of hydroxyapatite disks with fluoride in buffered solution to form calcium fluoride.

In order to separate the driving force factors expressed by eq 11 from the permeability characteristics of the calcium fluoride layer, experiments were planned that involved placing an inert porous silver membrane in series with the reacting hydroxyapatite disk. As will be seen these experiments permit the separation of the K_{eq} from the τ/ϵ factor in the model when the diffusivities are known.

Although an independent determination of the *apparent* effective diffusivity, D , (see eq 11) for the reaction could not be conceived, it was decided to measure the apparent diffusivity for total fluoride under the conditions similar to those in the reaction rate experiments.

Preparation of Hydroxyapatite Disks. A sample of hydroxyapatite was prepared by the method developed at the Fundamental Research Branch of Tennessee Valley Authority.¹⁰ The hydroxyapatite was prepared by heating a stoichiometric mixture of monocalcium phosphate monohydrate and calcium carbonate in an atmosphere of steam and nitrogen. The pure monocalcium phosphate monohydrate and calcium carbonate were each ground to pass a 200-mesh sieve and then mixed thoroughly in the ratio of 3 mol of monocalcium phosphate to 7 mol of calcium carbonate. The mixture in a platinum boat was heated in a tube furnace at 1200° for 3 hr in an atmosphere of equal volumes steam and nitrogen. The product was then dried at 110° for 24 hr, and ground to pass a 200-mesh sieve. It was then divided into 10-g portions, each of which was extracted with 100 ml of neutral ammonium citrate solution at 55° for 1 hr and repeated to remove any calcium salts other than apatite. The hydroxyapatite was washed thoroughly with distilled water and dried at 100°. It was examined by infrared spectroscopic analysis, X-ray diffraction analysis, and components analysis with Ca:P mole ratio of 1.67. The sample was well mixed with 12.5% polyethylene powder and about 200 mg of the mixture was compressed at 51,000 psi in a 0.5-in. die with flat faced punches. The disk was then mounted in a glass tube, 1.6 cm inside diameter and 11 cm long, by white beeswax in a manner that one surface of the disk was exposed and was flush with the end of the tube. For the preparation of the disks with the attached porous silver membrane, the disk was placed on a piece of silver membrane filter (FM-3.7-1.2 μ)¹¹ and white molten beeswax was dripped around and on it. After the wax had solidified a cork borer was centered and depressed over the wax-covered disk. The disk with the membrane was then mounted in the glass tube. Benzoic acid disks were also prepared in the same manner.

Apparatus. The apparatus for the reaction rate studies is shown in Figure 2. The inlet tube and outlet tube of

(10) Tennessee Valley Authority, Report No. 678, Nov. 6, Wilson Dam, Ala. (1956).

(11) Selas Flotronics, Spring House, Pa. 19477.

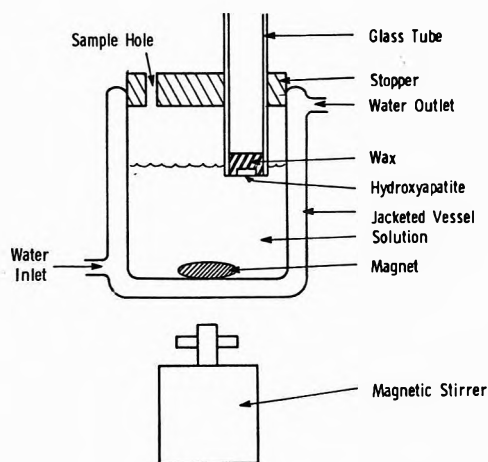


Figure 2. Schematic diagram of the apparatus for reaction rate studies.

this 250-ml jacketed vessel provided a circulation of constant temperature water at 30°. For each experiment, 100 ml of buffered fluoride solution was used. The magnetic stirrer consisted of a magnet attached to the shaft of a 150-rpm constant-speed motor.¹² The glass tube was adjusted so that the apatite disk surface would be about 4 mm below the surface of the solution. The samples withdrawn from the fluoride solution at scheduled times were analyzed for phosphate by a modified method of Gee, Domingues, and Deitz.¹³

Procedure for Phosphate Common Ion Experiments. A modified procedure was used for experiments in which phosphate was initially present in the buffered fluoride solution. At each scheduled time, a disk was removed from the reacting solution and apatite was soaked in 1 *N* acetic acid for 24 hr. The apatite disk was removed again and soaked repeatedly in acetic acid until all of the calcium fluoride had dissolved as was shown by analysis of each extraction on fluoride content.

Preparation of Buffered Fluoride Solutions. Acetate and pyridine buffers were employed. A reagent grade of sodium fluoride¹⁴ was used as the source of fluoride. The quantities of the acid and salt forms for the buffer systems were calculated using the Henderson-Hasselbach equation. All solutions were adjusted to an ionic strength of 0.5 mol by addition of sodium chloride. The pH of the solutions was measured with a Beckman Model G pH meter¹⁵ and adjusted to within ± 0.02 of the desired value.

Determination of the Mass Transfer Coefficients. The amount of solute released by diffusion to the solution may be quantitatively expressed by the integrated form of the Noyes-Whitney equation¹⁶

$$\log \frac{C_s}{C_s - C} = \frac{D}{h} \frac{At}{2.303V}$$

where D/h is mass transfer coefficient of the solute, D is the diffusivity of the solute, h is the effective diffusion layer, A is the exposed area of the solute, V is the volume of the solution, C_s is the solubility of the solute, and C is the concentration of solute at time, t . An experiment was carried out in the apparatus with a benzoic acid disk and 0.12 *N* hydrochloric acid as the solvent. The samples were analyzed spectrophotometrically at 276 μ .¹⁷ The $\log C_s/(C_s - C)$ obtained were then plotted against time in minutes. The slope obtained from the plot was used to calculate the mass transfer coefficient of the solute as well

as the diffusion layer thickness using the diffusivity value for benzoic acid of 1.11×10^{-5} cm²/sec.

Determination of the Apparent Diffusivity, $(D_{TF})_{aq}$, for Fluoride. In order to have an estimate of $(D_{TF})_{aq}$, a two-chambered diffusion cell described by Goldberg was used.¹⁸ A 0.01 *M* benzoic acid solution was used to calibrate the cell. The buffered fluoride solution was diffused into a buffered solution not containing fluoride.¹⁹ The concentration of fluoride in the receptor chamber was determined by a colorimetric analysis procedure based on the use of Amadac-F²⁰ developed by Burdick and Jackson Laboratories Inc.

Studies on the Calcium Fluoride Supersaturation in the Reaction. Because it was suspected that appreciable supersaturation existed at the reaction interface, experiments on the nucleation of calcium fluoride in buffered fluoride solutions were conducted. This was done by adding 10 ml of calcium chloride solutions to 10 ml of buffered fluoride solutions in polyethylene bottles which were kept at 30° in a water bath. Teflon-coated magnetic stirring bars were used to agitate the solutions. At different times samples were pipetted and transferred to a 10-ml syringe which had a Swinney filter adapter with a 0.22- μ millipore filter. The filtrate was then analyzed for calcium by the method of Gatehouse and Willis²¹ with an atomic absorption spectrophotometer.²²

Results

Typical results²³ of the various experiments on the rate of reaction of hydroxyapatite disks exposed to acidic fluoride solutions are summarized in Figures 3-6. All of these experiments were run in, at least, duplicate. The precision of the results was found to be generally quite good with an experimental error of around $\pm 2\%$.

The mass transfer coefficients for the disks without and with the silver membrane were determined using the benzoic acid dissolution rate data. These experiments yielded mass transfer coefficients of 3.7×10^{-3} and 4.0×10^{-4} cm/sec for the two cases, respectively, which correspond to effective h values of 32.4 and 270 μ .

The apparent diffusivity, $(D_{TF})_{aq}$, for fluoride was found to be $9.3 \pm 0.4 \times 10^{-6}$ cm²/sec on the average from the buffered fluoride solutions of pH value from 4 to 5.5.

The results of the calcium fluoride supersaturation and precipitation studies are summarized in Table I. Activity products for calcium fluoride were calculated from the data employing activity coefficients of 0.36 and 0.63 for the calcium and the fluoride ion, respectively. As can be

(12) Bodine Motors, Chicago, Ill.

(13) G. Gee, L. P. Domingues, and V. R. Deitz, *Anal. Chem.*, **26**, 1487 (1954).

(14) J. T. Baker Chemical Co., Phillipsburg, N. J.

(15) Beckman Instruments, Inc., South Pasadena, Calif.

(16) A. A. Noyes and W. R. Whitney, *J. Amer. Chem. Soc.*, **19**, 930 (1897).

(17) Hitachi Model 139 spectrophotometer, Coleman Instruments Corp., Maywood, Ill.

(18) A. H. Goldberg and W. I. Higuchi, *J. Pharm. Sci.*, **57**, 1583 (1968).

(19) Inert silver membrane filter (FM-37-1.2 μ), Selas Flotronics, Spring House, Pa. 19477.

(20) Amadac-F is a carefully blended solid mixture of partially hydrated sodium acetate, acetic acid, stabilizer, lanthanum nitrate, and alizarin complexan, the lanthanum and complexan being equimolar, which is developed by Burdick and Jackson Laboratories Inc., Muskegon, Mich. 49442.

(21) B. M. Gatehouse and J. B. Willis, *Spectrochim. Acta*, **17**, 710 (1961).

(22) Perkin-Elmer Corp., Norwalk, Conn.

(23) Additional data may be found in Z. Liang's doctoral dissertation, The University of Michigan, 1971.

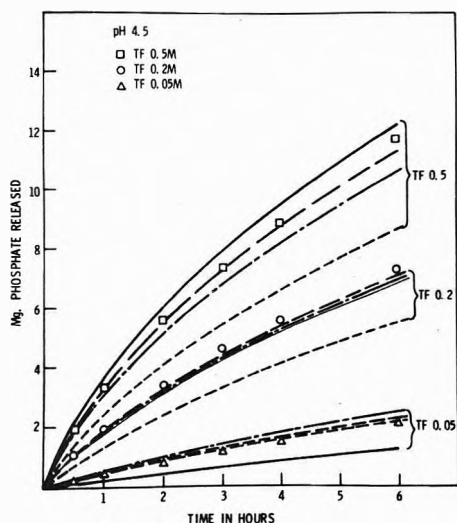


Figure 3. Comparisons of theoretical computations with experimental results for the amount of phosphate released with time showing the influence of K_{eq} and diffusion coefficients on the rates of reaction at pH 4.5 of 0.1 M pyridine buffered fluoride solution. The values used in theoretical computation are as follows.

D , cm ² /sec	K_{FAP} (in K_{eq})
-----	1.5×10^{-5} 10^{-158} (10^{-54})
-----	0.9×10^{-5} 10^{-152} (10^{-48})
-----	0.7×10^{-5} 10^{-148} (10^{-44})
-----	0.3×10^{-5} 10^{-131} (10^{-27})

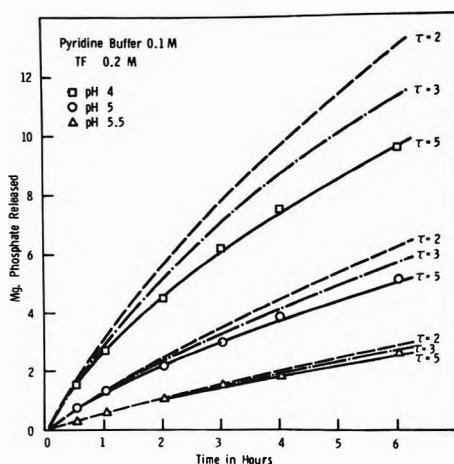


Figure 4. Comparisons of theoretical calculations (curves) using different tortuosity (τ) values with the experimental data (symbols): $h = 270 \mu$, $D = 0.9 \times 10^{-5}$ cm²/sec, and $K_{FAP} = 10^{-152}$.

seen significantly large supersaturations were found at early times. It can be seen that, for initial activity products less than about $K = 2 \sim 3 \times 10^{-9}$, the supersaturation was sustainable for long periods of time. However, when $K \approx 5 \times 10^{-9} \sim 1.0 \times 10^{-8}$ the precipitation rates became very rapid.

The theoretical calculations were carried out for determining the initial reaction rates and the time dependence. All calculations were done employing an IBM 360 digital computer. The constants used in the calculations are tabulated in Table II. The average porosity of CaF_2 layer formed in the reaction was calculated to be 0.367.

It was anticipated that, in the experiments involving the silver membrane, the initial rates of reaction would be relatively insensitive to $S(\tau/\epsilon)$ of the calcium fluoride

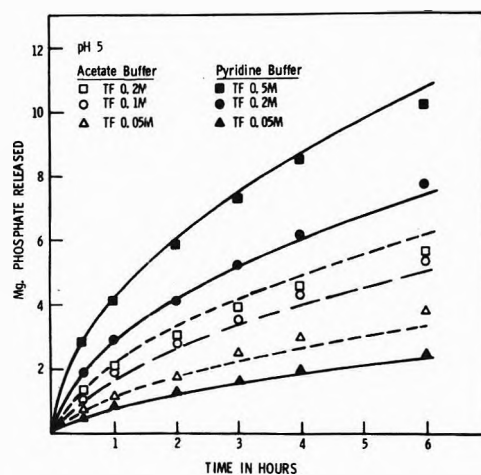


Figure 5. Rates of reaction in the amount of phosphate released with time compared to theoretical computations with the model for pH 5 and 0.1 M buffered fluoride solution: (-----) acetate buffered fluoride solution; (—) pyridine buffered fluoride solution.

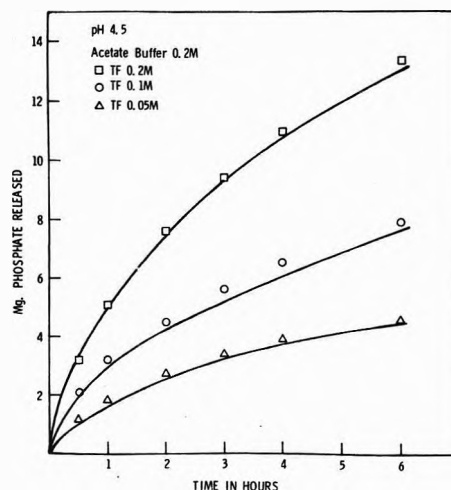


Figure 6. Rates of reaction in the amount of phosphate released with time compared to theoretical computations with the model.

TABLE I: Calcium Fluoride Precipitation Experiments Showing CaF_2 Activity Products Changes with Time^a

t , min	(Ca^{2+}) , M	K_{CaF_2}	(Ca^{2+}) , M	K_{CaF_2}
<1	2.5×10^{-5}	2.2×10^{-9}	3.0×10^{-5}	2.6×10^{-9}
5	2.5×10^{-5}	2.2×10^{-9}	3.0×10^{-5}	2.6×10^{-9}
20	2.5×10^{-5}	2.2×10^{-9}	3.0×10^{-5}	2.6×10^{-9}
60	2.5×10^{-5}	2.2×10^{-9}	2.5×10^{-5}	2.2×10^{-9}
240	2.5×10^{-5}	2.2×10^{-9}	2.4×10^{-5}	2.1×10^{-9}
<1	5.0×10^{-5}	4.4×10^{-9}	1.1×10^{-4}	9.6×10^{-9}
5	4.0×10^{-5}	3.5×10^{-9}	1.5×10^{-5}	1.3×10^{-9}
20	2.8×10^{-5}	2.4×10^{-9}	1.5×10^{-5}	1.3×10^{-9}
60	2.2×10^{-5}	1.9×10^{-9}	1.5×10^{-5}	1.3×10^{-9}
240	2.2×10^{-5}	1.9×10^{-9}	1.5×10^{-5}	1.3×10^{-9}

^a Initial fluoride concentration = 2.5×10^{-2} M, ionic strength = 0.5 M. The results of CaF_2 activity products for other combinations of calcium and fluoride concentrations are presented in Z. Liang's doctoral dissertation, The University of Michigan, 1971.

layer. Therefore these experiments were expected to provide situations in which only K_{eq} and D are the main parameters. Thus theoretical computations were carried out

TABLE II: Summary of Constants Used in Computation^a

Thermodynamic Constants	
$K_D = 6.98 \times 10^{-3}$	$K_{HF} = 3.53 \times 10^{-4}$
$K_{DP} = 6.40 \times 10^{-8}$	$K_{HF_2} = 4.0$
$K_{3P} = 4.73 \times 10^{-12}$	
$K_{HB} = 1.75 \times 10^{-5}$ (acetate buffer)	
$K_{HB} = 6.46 \times 10^{-6}$ (pyridine buffer)	

Activity Coefficients	
$r_{F^-} = 0.632$	$r_{H_2PO_4^-} = 0.55$
$r_{Ac^-} = 0.735$	$r_{HPO_4^{2-}} = 0.23$
$r_{H^+} = 0.8$	$r_{PO_4^{3-}} = 0.095$
$r_{OH^-} = 0.7$	$r_{Ca^{2+}} = 0.36$
$r_{Py} = 0.7$	

^a Density of calcium fluoride = 3.18 g/ml; diffusion layer thickness $h = 32.4 \mu$ (without membrane); diffusion layer thickness $h = 270 \mu$ (with membrane).

and compared to the experimental results employing these two quantities as the "adjustable" parameters. Figure 3 gives four combinations of D and K_{eq} used in the theoretical calculations. A τ value of 5 was used in all of these computations. The comparisons between experiment and theory in Figure 3 show that, except for the last combination, *i.e.*, $D = 0.3 \times 10^{-5}$ and $K_{eq} = 10^{-27}$, the theoretical predictions correlate reasonably well with the experimental results. It appears, however, that the best fit combination is that for which $K_{eq} = 10^{-48}$ and $D = 0.9 \times 10^{-5}$. This pair consistently provided good agreement between theory and experiment over the entire pH and fluoride concentration ranges encountered with the two buffer systems.

In Figure 4, the influence of τ upon the theoretical calculations is shown for $K_{eq} = 10^{-48}$ and $D = 0.9 \times 10^{-5}$. As was stated earlier, for initial rates the choice of τ is rather unimportant when $h = 270 \mu$. The D value determined by the fitting process described above is in reasonably good agreement with the experimentally measured apparent diffusion coefficient for fluoride. This lends support to the likelihood that the model is basically sound from the physical point of view.

Figure 5 shows the comparisons of the experimental results obtained without the silver membrane with the model predictions based upon $D = 0.9 \times 10^{-5}$, $K_{eq} = 1 \times 10^{-48}$, $\tau = 5$, and $h = 32.4 \mu$. It can be seen that the agreement between the experiments and theory is essentially quantitative over the ranges of pH and fluoride concentration for the two buffer systems.

The Meaning of $K_{eq} = 1.0 \times 10^{-48}$. Let us now consider the physical meaning of K_{eq} and D values. Referring to eq 8 and taking the literature value for the solubility product of calcium fluoride, K_{CaF_2} ,²⁴ one finds that $K_{eq} = 1.0 \times 10^{-48}$ would correspond to a K_{FAP} value of 1.0×10^{-152} . This is an extremely small value²⁵ and suggests the following possibilities. Either the conditions prevailing during the reaction are such that the calcium fluoride-fluoroapatite interface is highly undersaturated with respect to the fluoroapatite phase or highly supersaturated with respect to calcium fluoride or possibly both.

In order to explore this question, the hydroxyapatite dissolution reaction rate data for the low fluoride situation (see Figure 7) were first compared to the theoretical rates. In this situation calcium fluoride does not form. The theoretical rates were calculated from the equations proposed by Mir and Higuchi⁹ using K_{FAP} as the adjustable param-

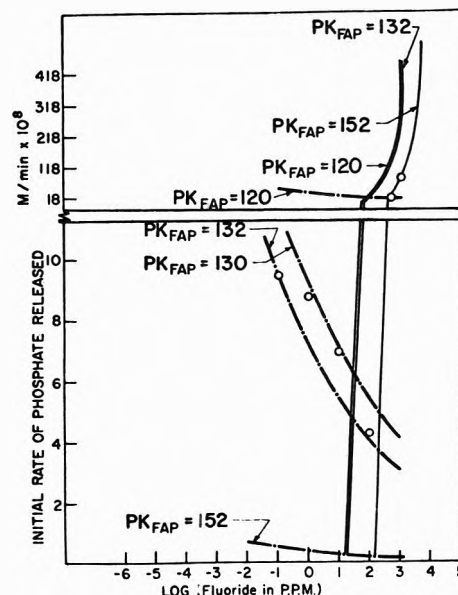


Figure 7. Comparisons of theoretical computations with experimental results for the initial rate of the reactions involving low and high concentrations of fluoride: TVA hydroxyapatite disks, pH 4.5, (TB) = 0.1 M (pyridine); (—) theory for the formation of CaF_2 ; (---) theory for fluoroapatite model. Circles are experimental results.

eter. Figure 7 shows that at low fluoride concentration, a K_{FAP} value of 10^{-130} – 10^{-132} is in agreement with the experimental data. This range of values was essentially what Mir and Higuchi found in similar studies.

In contrast to this, if calcium fluoride is assumed to be in equilibrium, the experimental data at high fluoride concentrations are found to be in agreement with a K_{FAP} value of 1.0×10^{-152} . Because the apparent abrupt change of the K_{FAP} value at the point where calcium fluoride begins to form would seem to be unlikely, it was reasoned that the discrepancy is mainly caused by the supersaturation of the interface with respect to calcium fluoride. Thus, if a K_{FAP} value of 10^{-131} is used, one finds that an activity product for calcium fluoride of $10^{-8.3}$ is required to give $K_{eq} = 1.0 \times 10^{-48}$. It can be seen from Table I that, indeed, the calcium fluoride precipitation rate becomes very rapid when $K_{CaF_2} \lesssim 10^{-8}$ which is consistent with the above analysis. Based upon the actual rates of reaction of the hydroxyapatite disks, one can easily show that the rates of precipitation of CaF_2 per cc in the apatite disk situation is several orders of magnitude greater than those found in the precipitation experiments. Thus it is likely that, in the apatite-fluoride reaction conditions, the precipitation of CaF_2 is far into the three-dimensional nucleation-controlled region rather than crystal growth controlled. The proposed large supersaturations would be consistent with this view. An alternate interpretation of the large supersaturation is that a relatively short-lived intermediate polymorphic phase of CaF_2 may first precipitate and that it is the activity product of this phase that is involved in the $K_{eq} = 1 \times 10^{-48}$ value.

An independent test of calcium fluoride supersaturation hypothesis was carried out by studying, both experimentally and theoretically, the rate of reaction of dicalcium phosphate dihydrate with fluoride to form calcium fluo-

(24) L. G. Sillen and A. E. Martell, "Stability Constant," Chemical Society, London, 1964, p 258.

(25) T. C. Farr, G. Tarbuton, and H. T. Lewis, *J. Phys. Chem.*, **66**, 318 (1962).

ride.²⁶ Based upon the assumption that dicalcium phosphate dihydrate was in equilibrium at the $\text{CaHPO}_4 \cdot 2\text{H}_2\text{O}$ – CaF_2 interface, the fit of the experimental data yielded an activity product for CaF_2 of about 4×10^{-8} .

An Interpretation of the K_{FAP} and the "Fluoroapatite Phase." The fluoroapatite phase referred to above might be described⁹ as hydroxyapatite crystals which have undergone surface exchange of the hydroxide ions by the fluoride ions. This confers upon the hydroxyapatite crystals the apparent dissolution kinetics characteristics of fluoroapatite as Mir and Higuchi⁹ have shown. Their kinetics data for the TVA hydroxyapatite crystals in low (5×10^{-6} – 5×10^{-4} M) fluoride solutions over a wide range of conditions (pH, phosphate ion, and calcium ion concentrations) showed that an activity product, $K_{\text{FAP}} = (\text{Ca})^{10}(\text{PO}_4)^6(\text{F})^2$ with $K_{\text{FAP}} \approx 10^{-130}$ – 10^{-132} , governs the rate of dissolution. Thus the fluoroapatite phase may be equated to a surface fluoroapatite phase or to an activated complex for dissolution rather than to a true thermodynamic phase.

Comments of Choice of $D = 0.9 \times 10^{-5}$ cm²/sec. There are some questions related to the use of a single diffusivity value to represent the diffusivities of all species in the system under all conditions encountered in the studies. The first of these relate to the possible error arising because the "intrinsic" diffusivities (see eq 1–10) for the species are not the same and the electrolyte solutes in multicomponent systems (buffered fluoride solutions) do not diffuse independently.²⁷ Since the ions and molecules which comprise the present system have a high ionic strength the estimates of all volume-fixed diffusion coefficients may introduce more error than the use of Fick's law for each solute.^{27b} A reasonable estimate of the spread of the intrinsic diffusivities which depending upon the conditions, e.g., pH, the different diffusivities are weighted differently in the calculation, would be about ± 20 to 25% about a mean. This spread would generally be expected to be somewhat smaller when electric diffusion potential effects are considered.

An estimate of the influence of such a spread in diffusivities upon the reaction rate and upon the magnitude of the deduced K_{eq} value was made by using eq 9 and 10 with $D_{\text{H}} = D_{\text{HF}} = D_{\text{HF}_2} = D_{\text{F}} = 0.9 \times 10^{-5}$ cm²/sec, $D_{\text{HB}} = D_{\text{B}} = 0.7 \times 10^{-5}$ cm²/sec, $D_{\text{H}_3\text{PO}_4} = D_{\text{H}_2\text{PO}_4^-} = D_{\text{HPO}_4^{2-}} = D_{\text{PO}_4^{3-}} = 0.6 \times 10^{-5}$ cm²/sec, and $K_{\text{eq}} = 1.0 \times 10^{-48}$. The results were that at pH 5.5 the $\Delta(\text{TF}) = (\text{TF}) - (\text{TF})_s$ value was 30% larger than when all D values were set equal to 0.9×10^{-5} cm²/sec. At pH 4.0, the corre-

sponding error was about 14%. This essentially means that, considering eq 11, a choice of a $D = 8.1 \times 10^{-6}$ cm²/sec $\pm 10\%$ assigned to all species can account for the results obtained in the above calculations. The corresponding K_{eq} values would be about 1×10^{-46} instead of 1×10^{-48} . These differences are comparable to the uncertainties in the experiments and in the method for fitting the data to deduce the K_{eq} values. Therefore, with regard to the first question $D = 0.9 \times 10^{-5}$ cm²/sec and $K_{\text{eq}} = 1.0 \times 10^{-48 \pm 2}$ should be considered as a reasonable choice as the best fit values. The second question is related to that of the influence of the electrical diffusion potential upon the effective diffusivities of the various ionic species in the system. Calculations have been carried out⁸ which appear to show that the influence of the diffusion potential upon the fluoride ion diffusivity is at most the order of $\pm 5\%$. It would be reasonable to expect similar effects for the other ions under similar conditions. Thus the assumption that, over a wide range of conditions, the effective diffusivities remain essentially constant should be a good one.

Conclusions

This study has shown that over a wide range of conditions the model proposed by Nelson and Higuchi is quantitatively in agreement with the experimental results provided that an activity product for calcium fluoride of the form $K_{\text{CaF}_2} = (\text{Ca})(\text{F})^2$ and much larger than the solubility product is assumed to prevail at the reacting interface, $x = s$. The high supersaturation is consistent with other experiments which show that the precipitation of calcium fluoride should require comparably high supersaturations.

The permeability characteristics of the depositing calcium fluoride layer are defined by the porosity and tortuosity values that are reasonable from the physical viewpoint.

Acknowledgment. This research was supported by the National Institute of Dental Research through U.S.P.H.S. Grant No. DE-01830. We wish to thank the Lederle Company for the fellowship support received by Z. Liang.

(26) Z. Liang, doctoral dissertation, Appendix II, The University of Michigan, 1971.

(27) Reference for diffusion in multicomponent systems see the following: (a) V. Vitagliano and R. Sartori, *J. Phys. Chem.*, **74**, 2949 (1970); (b) R. P. Wendt and M. Shamim, *ibid.*, **74**, 2770 (1970); (c) P. R. Patel, E. C. Moreno, and T. M. Gregory, *J. Res. Nat. Bur. Stand. U. S., Sect. A*, **73**, No. 1, 43 (1969); (d) D. G. Miller, *J. Phys. Chem.*, **71**, 616 (1967).

Effect of the Dielectric Constant on the Reactivity of the Solvated Electron

F. Barat, L. Gilles, B. Hickel,* and B. Lesigne

Departement de Recherche et Analyse, SRIRMa, CEN-Saclay, B.P. n° 2, 91190, Gif-sur-Yvette, France
(Received February 12, 1973)

Publication costs assisted by Commissariat à l'Energie Atomique

The effect of the dielectric constant of the solvent on the reactivity of the solvated electron formed by pulse radiolysis has been studied in water-ethanol mixtures. It was found that the rate constant $k(e_s^- + NO_3^-)$ diminishes with decreasing water concentration whereas $k(e_s^- + Zn^{2+})$ increases in going from pure water to 60% by weight ethanol. On the other hand, $k(e_s^- + H^+)$ is almost invariant with the solvent composition, from pure water to 99% by weight ethanol. From measurements of the rate constant of the very fast reaction $e_s^- + C_6H_5NO_2$ we have estimated the diffusion coefficient of the solvated electron in water-ethanol mixtures. Using the appropriate equations with the values of the diffusion coefficient of e_s^- thus determined we have shown that it is possible to correlate the rate constants of the reactions between solvated electrons and ions with the macroscopic dielectric constant of the medium. The distance at which reaction takes place is, in each case, approximately equal to the sum of the individual ionic radii.

Introduction

Previous studies have shown that the reactivity of the solvated electron is nearly the same in water and in alcohols.^{1,2} The only exception in our knowledge was the work of Janovsky,³ who made independently a study of the reactivity of e_s^- in methanol and methanol-water mixtures and found in some cases a decrease of the rate constant of e_s^- with negative ion when the concentration of methanol increases.

According to the Brønsted-Christiansen-Scatchard equation,⁴ the rate constant, k , of the reaction between two ions at zero ionic strength is given by the relation

$$\log k = \log k_\infty - \frac{NZ_A Z_B e^2}{2.3\epsilon dRT} \quad (I)$$

where Z_A and Z_B are the valences of the ions, e is the electronic charge, N is Avogadro's number, ϵ is the static dielectric constant of the medium, d is the distance between the ions when the reaction takes place, and k_∞ represents the rate constant in the absence of coulombic interaction, i.e., in a medium of infinite dielectric constant. Similar equations have been derived by Laidler and Eyring⁵ and Logan.⁶ Although derivation of eq 1 implies some simplification, it has been successful in explaining in many cases the effect of the dielectric constant on the rate of ionic reactions. It would be interesting to test the applicability of eq 1 to the reactions of solvated electrons and we have therefore investigated the rate constants of this species with ions and neutral molecules in water-ethanol mixtures. We have also included preliminary measurements in water-dioxane mixtures. Table I gives some properties of these solvent mixtures at room temperature. In water-ethanol media the position and the intensity of the absorption spectra of the solvated electron remain approximately independent of the composition.⁷ In water-dioxane mixtures, the absorption spectra of the solvated electron, down to a mole fraction of 53% water, is the same as in pure water.⁸ This interesting feature has been interpreted as a selective solvation of the electron by water molecules.

Experimental Section

Solvated electrons were produced by pulse radiolysis of the solutions using a modified Febetron 707 delivering 1.8-MeV electrons in a 5-nsec (half-width) pulse.⁹ The doses used throughout this work varied from 5 to 15 krad. The cells of high purity silica were rectangular and the optical path was 2.2 cm. Experimental details on the spectrophotometric detection system are given elsewhere;¹⁰ perchloric acid Suprapur, acetone, nitrobenzene, ethanol, and *p*-dioxane "pro analysis" were supplied by Merck. Lithium nitrate from Baker and Adamson and zinc perchlorate from Frederic Smith were reagent grade products. All of them were used without additional purification. The water was tridistilled and solutions were deaerated by bubbling with high purity argon supplied by Air Liquide.

The rate constants were determined from the decay of the absorption of the solvated electron at 600 nm in solutions containing various concentrations of solutes after subtracting the decay found in the pure solvent mixture.

Results and Discussion

Corrections for ionic strength were made according to the Debye-Hückel theory as applied to ionic reaction rates by Brønsted, Bjerrum, and Christiansen.⁴

$$\log k_{\text{exp}} = \log k + \frac{2B\sqrt{\mu}}{1 + ag\sqrt{\mu}} Z_A Z_B \quad (II)$$

where k_{exp} is the experimental rate constant in a medium

- (1) E. J. Hart and M. Anbar, "The Hydrated Electron," Wiley-Interscience, New York, N. Y., 1970, p 173.
- (2) G. R. Freeman in "Action chimiques et biologiques des radiations," Vol. 14, Masson, Paris, 1970, p 73.
- (3) I. Janovsky, Thesis, University of Leeds, 1969.
- (4) G. Scatchard, *Chem. Rev.*, **10**, 229 (1932).
- (5) K. J. Laidler and H. Eyring, *Ann. N. Y. Acad. Sci.*, **39**, 303 (1940).
- (6) S. R. Logan, *Trans. Faraday Soc.*, **63**, 3004 (1967).
- (7) S. Arai and M. C. Sauer, *J. Chem. Phys.*, **44**, 2297 (1966).
- (8) M. A. J. Rodgers in "Pulse Radiolysis," M. Ebert, Ed., Academic Press, London, 1965, p 291.
- (9) R. Sauneuf and B. Lesigne, to be published.
- (10) F. Barat, L. Gilles, B. Hickel, and B. Lesigne, *J. Phys. Chem.*, **76**, 302 (1972).

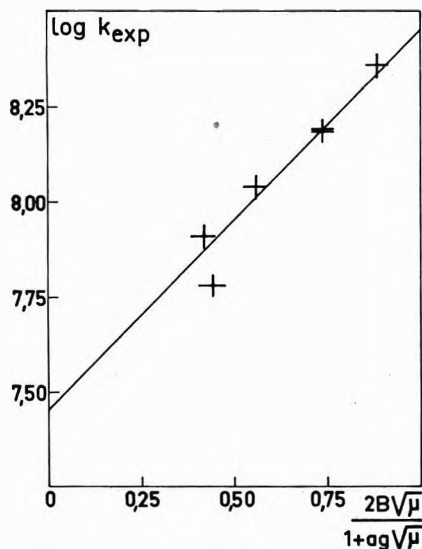


Figure 1. Plot of $\log k(e_s^- + \text{NO}_3^-)$ in 99% ethanol vs. $2B\sqrt{\mu}/1 + ag\sqrt{\mu}$ with $2B = 5.9$, $g = 5.9$, and $a = 6 \text{ \AA}$; μ was varied by adding LiNO_3 .

TABLE I: Dielectric Constant and Viscosity of the Solvent Mixtures at 25°

	Wt % $\text{C}_2\text{H}_5\text{OH}$					
	0	20	40	60	80	100
ϵ	78.5	67	55	43.4	32.8	24.3
η , cP	0.89	1.8	2.37	2.23	1.74	1.1

	Wt % $\rho\text{-C}_6\text{H}_{10}\text{O}_2$				
	0	10	20	30	40
ϵ	78.5	69.7	60.8	51.9	43
η , cP	0.89	1.08	1.29	1.51	1.74

of ionic strength μ , a is the distance of closest approach of the ions, and B and g are functions of the dielectric constant and temperature.

$$B = \frac{1824 \times 10^6}{(\epsilon T)^{3/2}}; \quad g = \frac{50.29}{(\epsilon T)^{1/2}}$$

If a is expressed in angstrom units,¹¹ Figure 1 gives a plot of $\log k_{\text{exp}}$ vs. $2B\sqrt{\mu}/(1 + ag\sqrt{\mu})$ for the reaction of e_s^- with NO_3^- in ethanol. The best line with the slope of +1 predicted by eq II is obtained for $a = 6 \text{ \AA}$. For the same reaction in water Anbar and Hart found $a = 4 \text{ \AA}$.¹² The extrapolated rate constants are not very sensitive to the value of a and under the conditions of our experiments, changing this value by 1 \AA would give, in the most unfavorable case, a variation of 1% in the logarithm of k ($\mu = 0$). For this reason we have used a mean value of 5 \AA for a throughout this work.

Conductivity measurements show that LiNO_3 is entirely dissociated in water-ethanol mixtures.^{13,14} In pure ethanol Campbell and Debus¹³ found no evidence for the formation of ion pairs whereas Parfitt and Smith¹⁴ reported an association constant of 18.7. As the question remains open and in the worst case 90% of LiNO_3 is dissociated, we have made no correction for incomplete dissociation. From pure water up to 50% by weight of ethanol Davies and Thomas¹⁵ had shown that $\text{Zn}(\text{ClO}_4)_2$ is entirely dissociated.

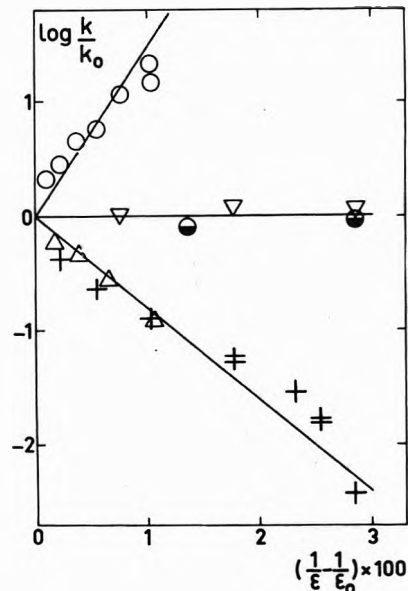


Figure 2. Variations of the reaction rate constants of solvated electrons with the static dielectric constant of the medium: Δ , NO_3^- in H_2O dioxane; $+$, NO_3^- ; \bullet , acetone; ∇ , H^+ ; \circ , Zn^{2+} in H_2O - $\text{C}_2\text{H}_5\text{OH}$.

Comparison of Experimental Data with Eq I. To test the applicability of eq I to solvated electron reaction rates, we have plotted in Figure 2 $\log(k/k_0)$ against $(1/\epsilon - 1/\epsilon_0)$ where k_0 and k are, respectively, the values of the rate constant at zero ionic strength in media of dielectric constant ϵ_0 and ϵ . Water was taken as reference medium ($\epsilon_0 = 78.5$ at 25°). Although the values of k_0 are generally known, for the sake of internal consistency we have redetermined them. Table II gives these values of k_0 , which were used throughout this work, and also previously published values.

Acetone: $Z_A Z_B = 0$. As expected there is no effect of the dielectric constant on the reaction rate. The small decrease of $\log(k/k_0)$ in 70% by weight ethanol mixture ($\epsilon = 38$) may be due to the increase of the viscosity.

Nitrate Ion: $Z_A Z_B = 1$. Equation I predicts a linear decrease of $\log k(e_s^- + \text{NO}_3^-)$ with $1/\epsilon$. This is approximately true and water-ethanol and water-dioxane mixtures give similar results. From the slope of the line equal to $-NZ_A Z_B e^2/2.3dRT$ we get $d = 3 \text{ \AA} \pm 0.4$.

The radius of solvated electron is approximately the same in water and in ethanol and various estimations give $r(e_s^-) = 2.6 \text{ \AA} \pm 0.4$.¹ In water a recent determination gave $r(\text{NO}_3^-) = 1.96 \text{ \AA} \pm 0.03$.¹⁶ Although there is some doubt about the radius of e_s^- , the reaction distance is lower than the sum of the individual radii; the reason for this will be discussed later.

Zinc Ion: $Z_A Z_B = -2$ and the rate constant, as expected, increases with $1/\epsilon$. The slope of the line gives $d = 3.3 \text{ \AA} \pm 0.4$. Taking $r(\text{Zn}^{2+}) = 0.74 \text{ \AA}$,¹⁷ $r(e_s^-) + r(\text{Zn}^{2+}) = 3.24 \text{ \AA}$ which is approximately equal to the reaction distance.

- (11) G. Kortüm, "Treatise on Electrochemistry," Elsevier, Amsterdam, 1965, p 183.
- (12) M. Anbar and E. J. Hart, *Advan. Chem. Ser.*, **No. 81**, 79 (1969).
- (13) A. N. Campbell and G. H. Debus, *Can. J. Chem.*, **34**, 1232 (1956).
- (14) G. D. Parfitt and A. L. Smith, *Trans. Faraday Soc.*, **59**, 257 (1963).
- (15) C. W. Davies and G. O. Thomas, *J. Chem. Soc.*, 1392 (1958).
- (16) W. L. Masterton, D. Bolocofsky, and T. P. Lee, *J. Phys. Chem.*, **75**, 2809 (1971).
- (17) L. Pauling, "The Nature of the Chemical Bond," 3rd ed, Cornell University Press, Ithaca, N. Y., 1960.

TABLE II: Reaction Rate Constants of the Solvated Electron with Some Scavengers in Water at 25°

$k_{\text{u} = \text{o.}}$ $M^{-1} \text{sec}^{-1}$	NO_3^-	CH_3COCH_3	$\text{C}_6\text{H}_5\text{NO}_2$	H^+	Zn^{2+}
This work	8.6×10^9	6.5×10^9	4.2×10^{10}	2.4×10^{10}	10^9
Ref 1	8.5×10^9	5.6×10^9	3×10^{10}	2.2×10^{10}	1.2×10^9

Hydrogen ion. The reaction $e_s^- + \text{H}^+$ seems an exception. From water to ethanol the rate constant changes by less than 20% although eq I predicts a relative increase of 10 to 100, depending on the value of d .

Diffusion-Controlled Reactions. This feature seems not to be restricted to H^+ . Dainton and coworkers have reported that Ag^+ reacts no faster with solvated electrons in methanol ($\epsilon = 32.6$) than in water.¹⁸ This reflects the limitation of the Brønsted-Christiansen-Scatchard equation which was implicitly derived for comparatively slow reactions. For diffusion-controlled reactions the rate constant between two ions is given by the Debye equation.¹⁹

$$k_{\text{diff}} = \frac{4N(r_A + r_B)(D_A + D_B)}{1000} \times \frac{Q}{(\exp Q) - 1} \quad (\text{III})$$

where r_A and r_B are the radii in centimeters of the reacting species A and B, D_A and D_B are their diffusion coefficients in $\text{cm}^2 \text{sec}^{-1}$, and k_{diff} is the rate constant in $\text{mol}^{-1} \text{sec}^{-1}$ at zero ionic strength.

$$Q = \frac{NZ_A Z_B e^2}{\epsilon(r_A + r_B)RT}$$

The first part of Debye equation gives the rate constant in the absence of coulombic interactions and may be compared with k_{∞} of eq I. The second part is a correction factor for reactions between ions. For $Z_A Z_B$ positive $e^Q \gg 1$ and eq III becomes

$$\log k_{\text{diff}} = \log \frac{4N(r_A + r_B)(D_A + D_B)}{1000} - \frac{Q}{2.3} + \log Q \quad (\text{III}')$$

Equation III' differs from eq I only by the term $\log Q$ and thus predicts an almost similar dependence of the rate constant on the dielectric constant, but for $Z_A Z_B$ negative $e^Q \ll 1$ and eq III becomes

$$\log k_{\text{diff}} = \log \frac{4N(r_A + r_B)(D_A + D_B)}{1000} + \log(-Q) \quad (\text{III}'')$$

which gives a much smaller dependence of the rate on the dielectric constant. As the diffusion coefficient of the solvated electron is not known in the water-ethanol mixture, it would be impossible to test eq III' quantitatively. By comparing the rate constants for $\text{OH}^- + \text{H}^+$ and $e_s^- + \text{H}^+$ in water and in alcohols, Fowles²⁰ concluded that the mobility of e_s^- like that of OH^- is not anomalously high in alcohols and that the reaction $e_s^- + \text{H}^+$ is diffusion controlled in alcohols, but not in water. However, if the diffusion coefficient of the solvated electron is much lower in alcohol than in water it is difficult to explain why the rate constant of the reaction $e_s^- + \text{O}_2$ which is nearly diffusion controlled in water has the same value in methanol and ethanol.²¹ To try to decide between the two hypotheses we have measured the rate constant of the reaction of solvated electrons with nitrobenzene in water-ethanol mixtures (Figure 3). This reaction is abnormally fast in water and is certainly diffusion-controlled.¹² If we make the basic assumption that the cross section of the reaction

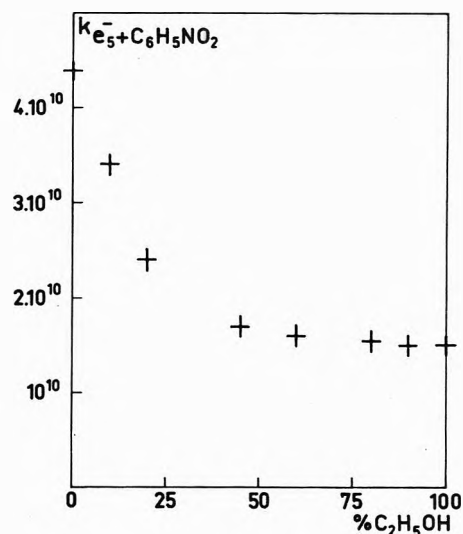


Figure 3. Reaction rate constants of solvated electrons with nitrobenzene in ethanol-water mixtures.

remains constant, it is possible, using eq III, to estimate the diffusion coefficient of the solvated electron in water-ethanol mixtures, the diffusion coefficient in pure water being known.²² Values of the diffusion coefficient of $\text{C}_6\text{H}_5\text{NO}_2$ in water and ethanol are not available and so were calculated according to the semiempirical correlation of Wilke²³ and in the water-ethanol mixtures using the interpolation method of Tang and Himmelblau.²⁴ The calculated coefficients are probably in error by no more than 10%. Table III gives $D(e_s^-)$ calculated from eq III taking $D(e_s^-) = 4.9 \times 10^{-5} \text{cm}^2 \text{sec}^{-1}$ in pure water.²² Examination of Table III shows that $D(e_s^-)$ decreases in going from water to ethanol and the product $D(e_s^-) \times \eta$ is not constant as it would be if the solvated electron obeyed the Stokes-Einstein equation. In 99% ethanol we found $D(e_s^-) = 1.14 \times 10^{-5} \text{cm}^2 \text{sec}^{-1}$ compared to $0.8 \times 10^{-5} \text{cm}^2 \text{sec}^{-1}$ deduced from the conductivity work of Fowles in pure ethanol.²⁰ In methanol preliminary experiments with the same method give $D(e_s^-) = 1.64 \times 10^{-5} \text{cm}^2 \text{sec}^{-1}$ which is close to $1.55 \times 10^{-5} \text{cm}^2 \text{sec}^{-1}$ calculated from Fowles' data.

Inserting these values of $D(e_s^-)$ in eq III it is possible now to calculate $k(e_s^- + \text{NO}_3^-)$. $D(\text{NO}_3^-)$ is calculated from the limiting conductivity of LiNO_3 ^{14,25} and the ionic mobility of Li^+ ²⁶ in water-ethanol mixtures using the

- (18) G. V. Buxton, F. S. Dainton, and M. Hammerli, *Trans. Faraday Soc.*, **63**, 1191 (1967).
 (19) P. Debye, *Trans. Electrochem. Soc.*, **82**, 265 (1942).
 (20) P. Fowles, *Trans. Faraday Soc.*, **67**, 428 (1971).
 (21) I. A. Taub, D. A. Harter, M. C. Sauer, and L. M. Dorfman, *J. Chem. Phys.*, **41**, 979 (1964).
 (22) K. H. Schmidt and S. M. Ander, *J. Phys. Chem.*, **73**, 2846 (1969).
 (23) C. R. Wilke and P. Chang, *A.I.Ch.E. J.*, **1**, 164 (1955).
 (24) Y. P. Tang and D. M. Himmelblau, *A.I.Ch.E. J.*, **11**, 54 (1965).
 (25) J. L. Whitman and D. M. Hurt, *J. Amer. Chem. Soc.*, **52**, 4762 (1930).
 (26) G. Kortum and A. Weller, *Z. Naturforsch.*, **5a**, 590 (1950).

TABLE III: Diffusion Coefficients of Solvated Electrons and Nitrobenzene in Ethanol–Water Mixtures

	Wt % C ₂ H ₅ OH							
	0	10	20	40	60	80	90	99
$D(\text{C}_6\text{H}_5\text{NO}_2)$, $10^{-5} \text{ cm}^2 \text{ sec}^{-1}$	0.94	0.81	0.70	0.60	0.63	0.71	0.81	0.94
$D(e_s^-)$, 10^{-5} $\text{cm}^2 \text{ sec}^{-1}$	4.9 ^a	3.92	2.64	1.76	1.59	1.45	1.27	1.14
$D(e_s^-) \times \eta$	4.4	5.2	4.75	4.15	3.7	2.5	1.8	1.25

^a From ref 22.

TABLE IV: Calculation of Diffusion-Controlled Reaction Rate Constants of e_s^- with NO_3^- in Ethanol–Water Mixtures

	Wt % C ₂ H ₅ OH						
	0	20	40	60	80	90	99
$D(\text{NO}_3^-)$, ^a 10^{-5} $\text{cm}^2 \text{ sec}^{-1}$	1.9	1.18	0.79	0.59	0.58	0.56	0.69
k_{diff} , ^b 10^9 $M^{-1} \text{ sec}^{-1}$	8.65	4	2	1.1	0.51	0.27	0.15
$k_{\text{exp}} (\mu = 0)$ $10^9 M^{-1} \text{ sec}^{-1}$	8.75	3.6	2	1.1	0.49	0.28	0.03

^a Calculated from data of ref 14, 25, and 26. ^b $r(e_s^-) + r(\text{NO}_3^-) = 4.3 \text{ \AA}$.

Nernst equation.²⁷ Table IV gives the results of these calculations using $r(e_s^-) + r(\text{NO}_3^-) = 4.3 \text{ \AA}$.

From pure water to 90% by weight of ethanol the agreement between experimental and calculated values is very good, but in 99% ethanol the experimental rate constant is five times smaller than the calculated value. Errors in the value of the diffusion coefficient of the solvated electron cannot explain the discrepancy, and using the value found by Fowles would decrease the calculated rate constant in ethanol by only 20%. As mentioned above, at least 90% of LiNO_3 is dissociated in ethanol, so formation of ion pairs cannot account for the low rate constant. Moreover, on the basis of purely electrostatic considerations ion pairing is expected in this case to increase the rate of the reaction.²⁸

It is possible to fit the experimental value in ethanol with eq III by using $r(e_s^-) + r(\text{NO}_3^-) = 3.3 \text{ \AA}$, but the reason why the reaction distance would decrease by 1 \AA from 90% to 99% in weight of ethanol is not clear. Moreover, the same effect was found in methanol (3) where $k(e_s^- + \text{NO}_3^-) = 4 \times 10^7 M^{-1} \text{ sec}^{-1}$. Taking $\epsilon = 32.7$, $D(e_s^-) = 1.6 \times 10^{-5} \text{ cm}^2 \text{ sec}^{-1}$ in methanol, eq III gives $r(e_s^-) + r(\text{NO}_3^-) = 2.25 \text{ \AA}$, which has no physical meaning. It seems from these results that the reduction of NO_3^- by e_s^- takes place less easily when the concentration of water is low and is no longer a diffusion-controlled process in methanol and ethanol.

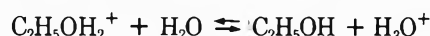
Intermediate Case. $D(\text{H}^+)$ values are available from the conductivity data for water–ethanol mixtures.^{29,30} If we attempt the same calculation for the reaction $e_s^- + \text{H}^+$ with $r(e_s^-) + r(\text{H}^+) = 4.3 \text{ \AA}$, we find that k_{diff} from eq III is always larger than the corresponding experimental value but the difference becomes smaller at low dielectric constant (Table V). It is not possible to fit the experimental data by adjusting the reaction distance because, for $Z_A Z_B$ negative, eq III is rather insensitive to this parameter.

Recently, Logan³¹ derived expression IV, which has more general boundary conditions than the Debye equation

which is strictly valid only for reactions taking place at the first encounter

$$\frac{Z}{k} = \left(\frac{1}{p} - \frac{1}{2} \right) e^Q + \frac{Z}{k_{\text{diff}}} \quad (\text{IV})$$

where k is the rate constant at zero ionic strength, Z is the collision factor in the liquid, p is the probability that the reaction takes place in an encounter, and k_{diff} is given by eq III. For $p = 1$ (diffusion-controlled reactions) eq IV differs from Debye equation only by the term $\frac{1}{2} e^Q$, which is generally negligible compared with Z/k_{diff} . For $p \ll 1$ (slow reactions) eq IV reduces to eq I. pZe^{-Q} is the rate of the chemical reaction which would apply if the rate were not restricted by diffusion. Taking for Z in water the plausible value of 10^{11} ,³² the value of p which fits the experimental data for the reaction $e_s^- + \text{H}^+$ in water is $p = 0.06$. Inserting these two values in eq IV, we have calculated the rate constants in water–ethanol mixtures (Table V). Comparison between eq III and IV and experimental data supports the hypothesis that the reaction $e_s^- + \text{H}^+$ is not truly diffusion controlled from water to ethanol, but as the difference between eq III and IV vanishes for $Z_A Z_B$ negative when the dielectric constant decreases the rate constant seems to obey to the Debye equation in alcohol, but not in water.²⁰ Because the equilibrium



lies far to the right ($K \approx 3 \times 10^2$)³⁰ from water to 99% by weight ethanol, the proton is principally present in the form of H_3O^+ and the assumption that p is constant is reasonable. However, in dry ethanol the proton gives

(27) Reference 11, p 199.

(28) C. W. Davies, "Ion Association," Butterworths, London, 1962, p 136.

(29) H. O. Spivey and T. H. Shedlovsky, *J. Phys. Chem.*, **71**, 2165 (1967).

(30) I. I. Bezman and F. H. Verhoek, *J. Amer. Chem. Soc.*, **67**, 1330 (1945).

(31) S. R. Logan, *Trans. Faraday Soc.*, 1712 (1967).

(32) A. A. Frost and G. R. Pearson, "Kinetics and Mechanisms," 2nd ed, Wiley, New York, N. Y., 1965, p 130.

TABLE V: Comparison between Experimental and Calculated Rate Constants for the Reaction $e_s^- + H^+$ in Ethanol-Water Mixtures

	Wt % C ₂ H ₅ OH				
	0	50	80	99	100
$D(H^+),^a 10^{-5}$ $cm^2 sec^{-1}$	9.4	2.7	1.15	0.61	1.6
k_{diff} (eq III) ^b in $10^{10} M^{-1} sec^{-1}$	9.5	4	3.4	3.1	4.75 ^c
k (eq IV) in $10^{10} M^{-1}$ sec^{-1} ($\rho = 0.06$)	2.4	2.8	3.05	3	4.6 ^c
k_{exp} in 10^{10} $M^{-1} sec^{-1}$	2.4	2.5	2.9	2.8	4.6 ^d

^a Calculated from the data of ref 29 and 30. ^b $r(e_s^-) + r(H^+) = 4.3 \text{ \AA}$. ^c Assuming that $D(e_s^-)$ is the same as in 99% ethanol. ^d Reference 20.

$C_2H_5OH_2^+$ and we cannot rule out the possibility that p changes. This would not be reflected in the rate constant because for $Z_A Z_B$ negative and values of p not too small, the first term in eq IV becomes negligible at low dielectric constant. The same reasoning holds for Z and if we suppose, for example, that Z changes from 10^{11} in water to 3×10^{10} in ethanol, the rate constant in ethanol calculated by eq IV would decrease only by 5%.

The sharp increase in the rate constant $k(e_s^- + H^+)$ from 99% to 100% ethanol as observed for the first time by Fowles²⁰ may be quantitatively accounted by the change in proton mobility (Table V) and by assuming that the mobility of solvated electron is low ($r(e_s^-) \approx 10^{-5} cm^2 sec^{-1}$) and remains the same in this narrow composition range. If the mobility of e_s^- was the same in ethanol and in water the change in the rate constant due to the increase of the mobility of H^+ would be only one-third of the observed value.

Conclusion

This work shows that it is possible to correlate the reactivity of solvated electrons with the static dielectric con-

stant of the solvent by using the appropriate equations. For reactions which are comparatively slow in water, $k < 10^9 M^{-1} sec^{-1}$, the variation of the diffusion coefficients with the composition of the solvent can be ignored, but not for faster reactions. The tentative determination of the diffusion coefficient of the solvated electron by kinetics measurements gives coherent values which need to be checked by other methods. The reaction distances for the ions are approximately equal to the sum of individual radii if the correct equation is used. However, because equations I, II, and IV do not take into consideration either noncoulombic interactions or the dielectric saturation in the vicinity of the ions,³³ the real reaction distances may be different.

Acknowledgments. The authors wish to thank Dr. J. Sutton and Dr. S. O. Nielsen for their comments during the completion of the manuscript and Mr. J. Lemoine for skillful assistance in electronics.

(33) K. J. Laidler, *Can. J. Chem.*, **37**, 138 (1959).

An Electron Paramagnetic Resonance Study of π System Interaction in Dithiin Derivatives

Dolan H. Eargle, Jr.,*¹ and Maria de Conceição Ramos de Carvalho

Centro de Estudos de Química Nuclear e Radioquímica do Laboratório Químico, Universidade de Coimbra, Coimbra, Portugal
(Received July 28, 1972)

The anion radical of tetracyanodithiin (I) is shown to be a divalent sulfur system in which d-orbital participation in conjugation is negligible. The g value (2.0024) indicates that spin-orbit coupling is very small, and a molecular model shows that direct π - π overlap of the ethylene moieties is probable. Other S-containing cation and anion systems are compared, including 2,5-diphenyldithiin (IV) and tetracyanothiophene (VI). Large cation g value deviations and small anion deviations of S heterocycles are contrasted with hydrocarbons.

Recent attempts to obtain a radical anion of a dithiin system, specifically thianthrene, in which the sulfur is in the divalent state have proven unsuccessful^{2,3} due to either decomposition of the material upon reduction or insufficient electron affinity (EA) of the compound under conditions of metal reduction. We wish to report a system that overcomes the previous difficulties, 2,3,5,6-tetracyanodithiin (I), and suggest some implications of the importance of its anion.

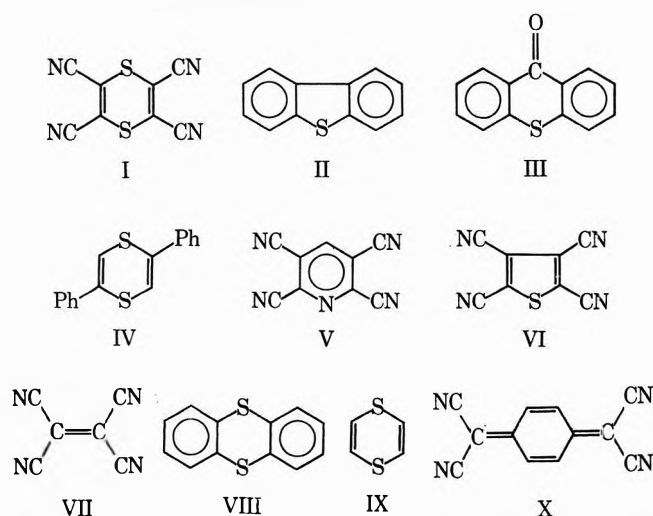
Two other anion radical systems involving electron conjugation through the sulfide system have been explored, dibenzothiophene (II)^{4,5} and thioxanthone (III),^{2,6} but these systems have the obvious drawbacks of containing other types of bonds linking the π systems. In our search for a compound which could demonstrate conjugation of π systems through a purely sulfide linkage we found that I possesses an EA sufficiently high for the required stability. Another compound, 2,5-diphenyldithiin, IV, was found to possess an insufficient EA for reduction; however, its cation radical was readily obtainable.

unsuccessful. Oxidation of IV was accomplished both in fuming H_2SO_4 and in the AlCl_3 - CH_3NO_2 mixture. Oxidation of VI was successful only in fuming H_2SO_4 . Spectra were obtained on a Varian V-4502 spectrometer of the Universidade de Coimbra and a JEOLCO JESME instrument of the Universidad de Los Andes.

Results and Discussion

The esr spectra of I consisted of nine lines with approximately the appropriate intensity distribution for four equivalent nitrogen atoms. Although considerable evidence has been gathered concerning the ability of sulfide to transmit conjugative effects,⁷ this is the first instance in which an odd electron has been observed to be easily transmitted between π -electron moieties of an anion radical containing purely divalent sulfur linkages.⁸

The matter of which sulfur orbitals should be considered is of considerable interest. Several of the studies of the cations of dithiins point to the predominance of the involvement of p orbitals, with a small contribution of the sulfur d orbital.^{9,10} Likewise, anions of sulfides (and sulfones) containing aromatic systems indicate some inclusion of the d as well as p orbitals (ref 7 and other pages therein). However, in nearly all these systems some deviation of the g value from that of free spin ($g = 2.0023$) has been detected. This is probably due to some spin-orbit interaction of the electron with the sulfur nucleus. However, in this case (I), as in that of thianthrene disulfone,¹¹ there is almost no deviation of the g value of the anion from that of the free-spin value.¹² This observation indicates that the spin-orbit interaction is very small indeed, and



Experimental Section

Reductions of I and VI were by potassium metal in tetrahydrofuran at a temperature of -80° . Dimethoxyethane proved an unsatisfactory solvent for I, but serves well for VI⁻. Attempted oxidations of I in H_2SO_4 (96% or fuming) and in a mixture of AlCl_3 in nitromethane were

- (1) Present address, Departamento de Química, Universidad de los Andes, Mérida, Venezuela.
- (2) E. T. Kaiser and D. H. Eargle, Jr., *J. Amer. Chem. Soc.*, **85**, 1821 (1963).
- (3) E. T. Kaiser and D. H. Eargle, Jr., *J. Chem. Phys.*, **39**, 1353 (1963).
- (4) R. Gerdil and E. A. C. Lucken, *Proc. Chem. Soc.*, 144 (1963).
- (5) D. H. Eargle, Jr., and E. T. Kaiser, *Proc. Chem. Soc.*, 22 (1964).
- (6) M. M. Urberg and E. T. Kaiser, *J. Amer. Chem. Soc.*, **89**, 1937 (1967).
- (7) M. M. Urberg and E. T. Kaiser in "Radical Ions," E. T. Kaiser and L. Kevan, Ed., Interscience, New York, N. Y., 1968, pp 302-306.
- (8) This observation does not apply to radical cations. See G. Vincow in ref 7, pp 190-193.
- (9) E. A. C. Lucken, *Theor. Chim. Acta*, **1**, 397 (1963).
- (10) P. D. Sullivan, *J. Amer. Chem. Soc.*, **90**, 3618 (1968).
- (11) D. H. Eargle, Jr., *J. Phys. Chem.*, **73**, 1854 (1969).
- (12) Using biphenyl⁻ as a standard.

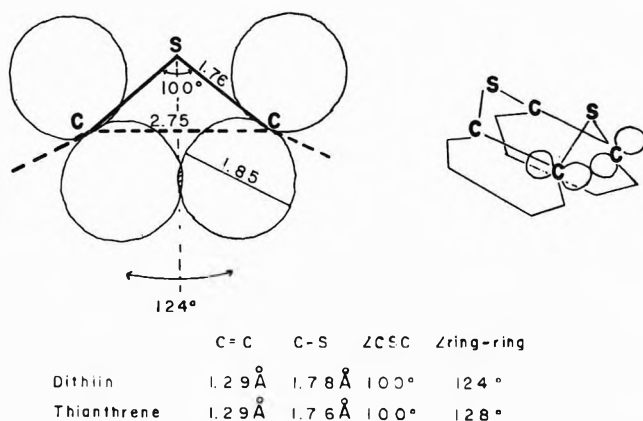


Figure 1. Models of dithiin and thianthrene drawn to scale using the molecular parameters of ref 16 and 17. The Slater orbitals of the benzene rings are from Pauling.¹³ The ring carbon-ringing carbon distance of 2.75 Å may be compared, for example, to the distance of 2.83 Å (between the 1 and 1' carbons) found quite sufficient for ring-ring exchange of the odd electron in [2.2]paracyclophanes.¹⁴ Even with [3.3]paracyclophanes in which this distance is somewhat greater, direct π - π overlap and rapid electron exchanges have been observed.¹⁵

on consideration of the HMO, there is theoretically no spin density on the sulfur atoms (in the nodal plant). (See Table I.)

Taking into account, then, this apparent lack of spin of the odd electron on the sulfur atoms and the facile spin exchange between the two dicyanoethylene moieties, we are led to the conclusion that electron transfer may be based on direct π - π overlap of the two ethylene systems. This possibility has been advanced in the case of some sulfones by Urberg (ref 7, pp 315 and 319).

Consider now the models in Figure 1.¹³⁻¹⁵ The crystal structures of both thianthrene (VIII) and dithiin (IX) have been obtained,^{16,17} and constructing the model for these two molecules we find that the carbon-carbon π orbitals of both systems have considerable direct overlap (as a matter of fact, quite sufficient to enable neglect of any contribution of sulfide orbitals). From this evidence we suggest that any "assistance" to conjugation in anions through the sulfur itself must be small, as is its contribution to the stability of the anion radical.

In addition, we should assume that the anion radicals of both these molecules do not assume planarity or even rapid conformational "flapping." In the thianthrene disulfone case this is not likely, considering the conformational stability of the anions of the *cis*- and *trans*-thianthrene disulfone isomers.³ The line widths observed for the anion of I (0.25 G) should be much larger, too, if conformational interconversion were occurring.

The observation of Urberg and Kaiser (ref 7, p 303) that bis(*p*-nitrophenyl)sulfide anion preserves its electron on only one-half of the molecule also contributes valuable information to this problem. In this system, even though direct π - π overlap is possible, it is not nearly as likely to furnish a good conjugative route for the electron, due to the free rotation of both aromatic rings.

We also attempted reduction of the disulfide, 2,5-diphenyldithiin (IV), in the hope that its two styryl groups might furnish sufficient stability (EA) along with the two S atoms for the odd electron. However, this experiment failed to realize a stable anion, no doubt due to the rotatability of the phenyl rings out of the planarity necessary for conjugation (Figure 2).

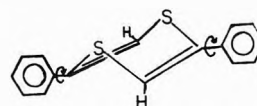


Figure 2.

TABLE I: Epr Spectral Data

Compd	Radical	Hfs, G	Spectral width, G	g value
I	Anion	$a_N = 1.6$	15.1	2.0024
IV	Cation	$a_{H(3,6)} = 2.94$ $a_{H(Ar)} = 3.2$	9.8	2.0048
VI	Cation	(Unresolvable)	10.5 ± 0.5	2.0123
VI	Anion	$a_N = 1.10 \pm 0.02^a$	10.8	2.0020

^a This hfs was measured at -40° . Further cooling gave more hyperfine lines whose origins were not easily interpretable; however, they are probably from a slight variation of the ^{14}N and ^{13}C couplings in the nitrile groups.

TABLE II

Radical anion		$a^{14}\text{N}(\text{C}\equiv\text{N}), \text{G}$	Spectral width, G	Ref
Tetracyano-dithiin	I	1.6	15.1	This work
Tetracyano-ethylene	VII	1.56	12.5 (excluding ^{13}C)	a
Tetracyano-pyridine	V	1.1	15.4	b
Tetracyanoquino-dimethane	X	1.01 ($a_H = 1.42$)	13.9 (excluding ^{13}C)	c
Tetracyano-thiophene	VI	1.1	10.5	This work

^a W. D. Phillips and J. C. Rowell, *J. Chem. Phys.*, **33**, 626 (1960). ^b M. T. Jones, *J. Amer. Chem. Soc.*, **88**, 5060 (1966). ^c P. H. H. Fischer and C. A. McDowell, *ibid.*, **85**, 2694 (1963); M. T. Jones and W. R. Hertler, *ibid.*, **86**, 1881 (1964).

We did succeed, however, in obtaining the cation radical, which produced a very strong signal of only three lines, and although rather broad (1.57 G), they showed only a slight tendency to split.¹⁸ This indicates that the odd electron density in the phenyl rings is small, and consequently would add little to the stability of an anion.

Several other observations were made in the spectra of I and IV.

(1) In the spectrum of I⁻ were observed several lines of low intensity between the major ^{14}N splittings. These can be attributed to ^{13}C splittings, especially in light of the expected high electron density on the cyano groups. No attempt was made at further interpretation.

(2) The *g* value of IV⁻ was measured at 2.0048 and is not unlike those of other S-containing cations bearing large *g* value deviations from 2.0023 (e.g., thianthrene-, *g* = 2.0081).¹⁹ We are thus confronted with a situation in

- (13) L. Pauling, "Nature of the Chemical Bond," 2nd ed, Cornell University Press, Ithaca, N. Y., 1945, pp 164-189.
- (14) A. Ishitani and S. Nagakura, *Mol. Phys.*, **12**, 1 (1967).
- (15) F. Gerson and W. B. Martin, Jr., *J. Amer. Chem. Soc.*, **91**, 1883 (1969).
- (16) P. A. Howell, R. M. Curtis, and W. N. Lipscomb, *Acta Crystallogr.*, **7**, 498 (1954).
- (17) H. Lynton and E. G. Cox, *J. Chem. Soc.*, 4886 (1956).
- (18) See Table I. Two or three small lines or shoulders were detectable in each of the strong 3,6 proton lines. These are attributable to splittings from protons of the 2,5-phenyl groups.
- (19) See G. Vincow in ref 7, p 190.

which there are rather large g value deviations in S heterocyclic cations, and very small deviations in the anions. This suggests very strongly that there is considerably more odd electron density on S in the cations than in the anions, and, therefore, different molecular orbitals are being utilized, or at least participation of S orbitals is different and more pronounced in the cations (see ref 19, p 197).

In anions, we are utilizing a higher energy antibonding orbital in which, in our symmetrical molecules, the odd electron experiences a node at the S atom, while in cations we are robbing a *bonding* orbital, an orbital which "sees" the S nucleus strongly. Stone proposed²⁰ (also see ref 7, p 164) that two effects are operative: one, that the filled orbitals of cation radicals are close in energy to those of the MO of the unpaired electron, giving rise to large cation g values, and two, that the antibonding orbitals of anions generally possess MO coefficients of opposite signs on adjacent atoms, causing coupling with the filled orbitals and thus large anion g values. In hydrocarbons, the second effect prevails, resulting in large g values for the anions. However, it appears that in sulfur-containing heterocycles, the first effect appears to predominate, resulting in larger *cation* g values.

Findings of g values of 2.0020 and 2.0026 for the anions of tetracyanothiophene (VI) and tetracyanoquinodimethane (X) (Table II, ref c), respectively, and a large g value of 2.0123 for the cation of VI lend considerable support to this theory.

(3) Two rather strong lines of equal intensity were observed at 8.84- and 11.96-G downfield from the center of the spectrum of IV⁻ when oxidized in fuming H₂SO₄ (the upfield lines were broadened). They were not present, however, in the AlCl₃-CH₃NO₂ medium, and therefore must be attributable to a decomposition product in H₂SO₄. ³³S lines could not be detected.

At this point it should be of interest to compare the ¹⁴N hyperfine splitting (hfs) of I⁻ with those molecules of somewhat similar structures. A comparison of the ¹⁴N hfs constants should not be made without first considering the structures of these systems, although the splitting constants are rather similar. First, as pointed out by Jones (Table II, ref b), the proper MO picture of V should not be considered as possessing a node of zero spin density through the center, since the molecule is both planar and somewhat asymmetric. Nevertheless, we do find the hy-

perfine splitting constant similar to that of I. Considering our model (Figure I) of the structure of I, and comments made earlier, we may, however, consider the anion radical of I somewhat similar to that of VII, if we neglect the S atom contributions. Thus, each half of the tetracyanodithiin would be considered as a half-TCNE.²¹ The similarity of the ¹⁴N hfs lends credence to this notion. Actually, it appears that slightly more electron density may be located on the nitrile groups of I than VII, judging from its greater hfs (Table II, ref a).²²

The ¹⁴N hfs of X is, of course, somewhat diminished in comparison because of the electron density on the central benzene ring.

For this work we found it of interest to compare the anion of VI with that of I, since they are of rather different symmetry, although differing in composition by only one S atom. The anion of VI is planar, and considering that the total spectral width is almost 5 G less than that of I⁻, a large amount of spin density is located within the thiophene ring.

Both the cation and anion spectra of this compound contained a small amount of an impurity which caused in the anion some distortion of a spectral wing. Its g value was sufficiently different from that of VI, however, that interference was minimal.

We have, then, in conclusion, observed that the tetracyanodithiin system can serve as a conjugative path for the odd electron in the anion radical, whether by use of divalent sulfur orbitals, or by direct π - π overlap. We have also observed that the cation g values of S heterocycles are considerably higher than those of corresponding or similar anions.

Acknowledgments. D. H. Eargle wishes to thank the Fundação Gulbenkian and the Instituto de Alta Cultura of Portugal for considerable support in this research.

(20) A. J. Stone, *Mol. Phys.*, **6**, 509 (1963); **7**, 311 (1964).

(21) This observation is, of course, valid only if there is small spin density on the ethylene carbons, otherwise we might have only a fortitious resultant of C-C \equiv N spin polarization. However, spin density on each ethylene carbon is <0.10.

(22) We have not attempted MO calculations of I⁻ because of the indeterminacy of including S atom p and d orbital involvement and simultaneous π - π overlap. Indeed, it does not appear to be necessary to do so, in light of the similarity of the hyperfine splittings of I⁻ and VII⁻ and the adequacy of the structural model shown in Figure 1.

Influence of Annealing on the Catalytic Activity of Cold-Worked Metals for the Decomposition of Formic Acid

Shozo Kishimoto

Department of Chemistry, Faculty of Science, Kobe University, Rckkodai, Nada-ku, Kobe, Japan (Received July 17, 1972)

Changes in the catalytic activity of cold-worked metals due to annealing were studied for the decomposition of formic acid vapor. On platinum, palladium, and nickel, the simultaneous changes in the catalytic activity and the activation energy occurred in the range of disappearance temperature of dislocations during annealing at 300–900°. These results indicate that the presence of dislocations at the surface of catalysts plays an important role in governing the activity. In the case of gold and silver, the catalytic activity and the activation energy were not influenced by annealing at 300–600°. It can be considered that dislocations produced by cold-working are already annealed out at 300° before the catalytic measurements are made. From a comparison of the relative activities of these metals, it is found that the huge change in the activity of an element during annealing overwhelms the differences between the activities of different metals. It can be concluded that Sachtler's proposal to the problem concerning the activity sequence of metals is not a complete answer.

Introduction

The catalytic decomposition of formic acid has been investigated in detail for a long time by many workers because of the simplicity of the reacting system.¹ However, many problems still remain for the correlation between the physical properties of catalyst and the catalytic activity. Study of the activity sequence of metals is one of the current problems in heterogeneous catalysis. Various attacks on the problem have been made since Beeck first reported the study on evaporated metal films.² There are very few reports about the relative activities of various metals for the decomposition of formic acid. It is well known that the activity of metal catalysts depends in many respects on the different physical forms of catalysts, such as evaporated films, powder, and massive crystals. Sachtler and Fahrenfort³ reported that the catalytic activities of supported metals for the decomposition of formic acid can be related to the heat of formation of metal formates. Furthermore, it has been generally accepted that the activity of metal in the same physical form is influenced by the pretreatment, such as cold-working, ion-bombardment, quenching, and annealing. With respect to this problem, the present author and coworkers⁴ have already proposed that lattice defects at the surface of metal catalysts play the main part of active sites for various reactions, from the experimental fact that the temperature range of the disappearance of lattice defects agrees with the range of decrease in the catalytic activity of cold-worked metals during annealing. Using a similar method, the present study proves that the meaning of comparison of the activity between different elements is doubtful.

Experimental Section

The formic acid employed was purified by repeated distillation at room temperature, after removal of water with anhydrous boric acid. In order to remove the oxide layer and other impurities, metal wires (99.9% or higher purity) were annealed at 900° (Pt, Pd, and Ni) and 600° (Au and Ag) in flowing hydrogen (50 cm³/min) for 2 hr and then were compressed to a constant degree (80% compression)

at room temperature. After being washed with *n*-hexane and acetone, these specimens were dried in the reaction vessel under high vacuum. The apparent surface area of samples used as catalyst was about 30 cm². The annealing of specimens was carried out in the reaction vessel in 100 Torr of hydrogen for 1 hr at various temperatures between 300 and 900°. Any poisons generated during annealing were removed by a liquid nitrogen trap which is connected to the reaction vessel. In particular, Ni catalysts were annealed at 250° in hydrogen for at least 2 hr before experiments were begun. This treatment was sufficient to obtain reproducible results. The hydrogen used was purified using a palladium thimble. The rate of decomposition of formic acid was obtained by measuring the pressure increase in a closed vessel at temperatures of 180–260° and in the pressure range 30–40 Torr. The poisoning of the catalyst by mercury vapor was avoided by using a gold foil trap between the reaction vessel and a mercury manometer. The acid decomposed to CO₂ and H₂ exclusively on each of the metals. The rate was calculated by using a pressure-time plot in the range of zero-order reaction. The catalytic activity (*A*) was expressed as molecules of formic acid decomposed per second per square centimeter of catalyst. The activation energy (ΔE) was derived from the data at 180–260°. To determine the temperature range (*T_d*) in which the disappearance of dislocations occurs during annealing, the measurements of thermoelectric force and hardness using the same specimens as used for the rate measurements were carried out by the method previously described.⁵

- (1) P. Mars, J. J. F. Scholten, and P. Zwietering, *Advan. Catal.*, **14**, 35 (1963).
- (2) O. Beeck, *Discuss. Faraday Soc.*, **8**, 118 (1950); M. Boudart, *J. Amer. Chem. Soc.*, **72**, 1040 (1950); G. C. A. Schuit and L. L. van Reijen, *Advan. Catal.*, **10**, 242 (1958); J. H. Sinfelt, *Catal. Rev.*, **3**, 175 (1970).
- (3) W. M. H. Sachtler and J. Fahrenfort, *Proc. Int. Congr. Catal. 2nd, Paris*, **1**, 831 (1961).
- (4) I. Uhara, S. Yanagimoto, K. Tani, G. Adachi, and S. Teratani, *J. Phys. Chem.*, **66**, 2691 (1962); I. Uhara, S. Kishimoto, T. Hikino, Y. Kageyama, H. Hamada and Y. Numata, *ibid.*, **67**, 996 (1963); I. Uhara, S. Kishimoto, Y. Yoshida, and T. Hikino, *ibid.*, **69**, 880 (1965).
- (5) S. Kishimoto, *J. Phys. Chem.*, **66**, 2694 (1962); **67**, 1161 (1963).

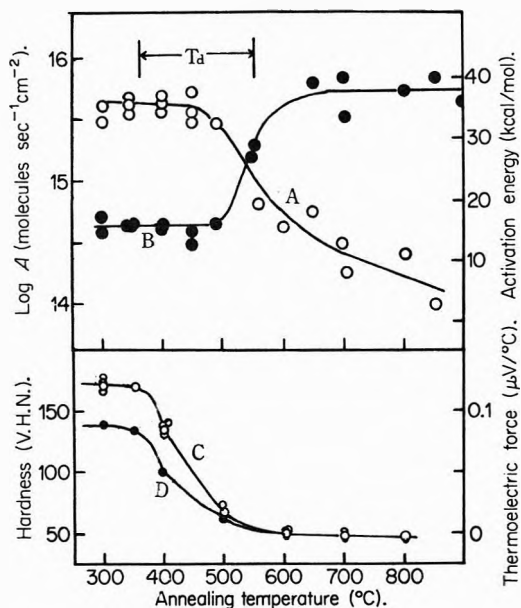


Figure 1. Changes in catalytic activity (A), activation energy (B), hardness (C), and thermoelectric force (D) during annealing of cold-worked Pt (reaction temperature 200°).

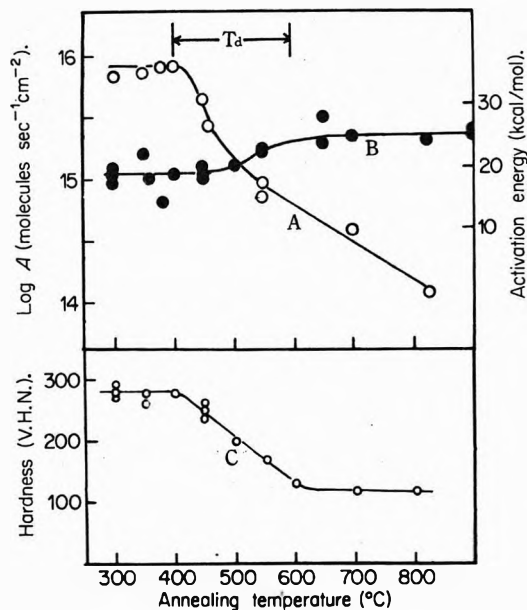


Figure 3. Changes in catalytic activity (A), activation energy (B), and hardness (C) during annealing of cold-worked Ni (reaction temperature 200°).

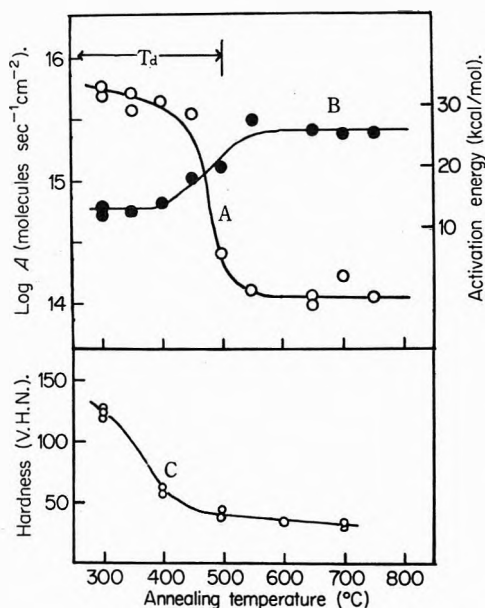


Figure 2. Changes in catalytic activity (A), activation energy (B), and hardness (C) during annealing of cold-worked Pd (reaction temperature 200°).

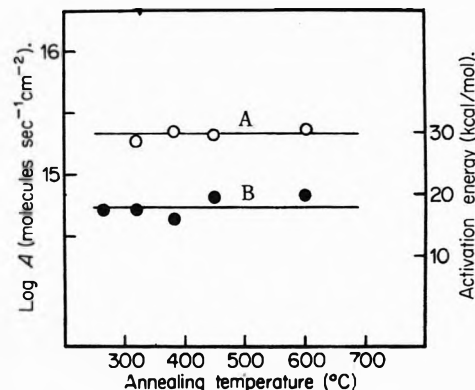


Figure 4. Catalytic activity (A) and activation energy (B) of cold-worked Au as a function of annealing temperature (reaction temperature 230°).

Results and Discussion

The dependence of A and ΔE of cold-worked Pt at a reaction temperature of 200° on annealing temperature is given in Figure 1. The sudden changes in the range 400–550° correspond to T_d . Figure 2 shows the effect of annealing on a Pd catalyst. At a reaction temperature of 200°, the simultaneous changes in A and ΔE are considerable in the range 300–500°, which approximately corresponds to T_d of cold-worked Pd. As Figure 3 shows, the behavior of Ni catalysts is almost the same as in the case of Pt and Pd except for a small change in ΔE in the range 400–700°.

Rienäcker⁶ found an increase in catalytic activity of Ni on cold-working for the decomposition of formic acid, although ΔE of cold-worked samples were 3–5 kcal higher contrary to the present results. This conflict is difficult to

explain, but it may presumably result from the difference in the nature and the degree of cold-working. It is well known that the number of dislocations of cold-worked metals decreases by a factor of about 10^4 after high-temperature annealing. We may conclude that the presence of dislocations at the surface plays an important role in determining the catalytic property of these metals.

From another view point, two possible reasons for accounting the decrease in A by annealing may be considered as follows: (a) decrease in the surface area of catalysts and (b) decrease in active lattice planes at the surface. Kabe, Mizuno, and Yasumori⁷ found that Pd foils have a roughness factor of less than 2 in the range of annealing, 150–800°. According to the results of the decomposition of formic acid on definite crystal planes, generally, different crystal planes exhibit different catalytic behavior.⁸ In certain cases, however, it was found that the values of frequency factor and activation energy for the

(6) G. Rienäcker, *Z. Elektrochem.*, **46**, 369 (1940).

(7) T. Kabe, T. Mizuno, and I. Yasumori, *Bull. Chem. Soc. Jap.*, **40**, 2047 (1967).

(8) H. M. C. Sosnovsky, *J. Chem. Phys.*, **23**, 1486 (1955); G. Rienäcker and J. Völter, *Z. Anorg. Allg. Chem.*, **302**, 292 (1959).

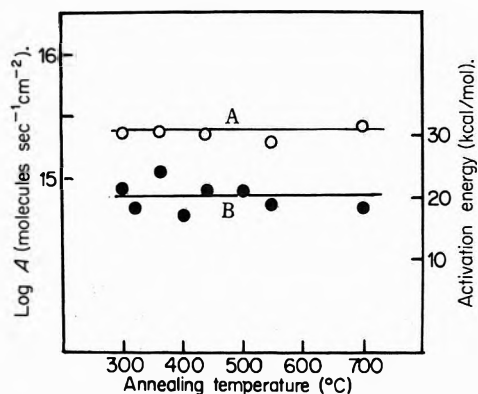


Figure 5. Changes in catalytic activity (A) and activation energy (B) of cold-worked Ag as a function of annealing temperature (reaction temperature 255°).

TABLE I: The Relative Activities of Metals for Formic Acid Decomposition^a

Metal	Au	Ag	Pd	Pt	Ni
Sachtler and Fahrenfort ³	1.91	2.09	2.51	2.88	2.14
Present work					
(300° annealing)	2.11	2.01	2.36	2.31	2.29
(600° annealing)	2.11	2.01	2.11	2.14	2.15

^a The figures are $10^3/T_r(^{\circ}\text{K})$, where T_r is the temperature which gives a log rate of $14.2 \text{ molecules cm}^{-2} \text{ sec}^{-1}$.

reaction depend upon structural details of the surface and these change together to give an almost constant rate.⁹ Even if both (a) and (b) have some influence on the catalytic activity, these factors do not seem to account for the sudden decrease in the activity in the restricted range of annealing temperatures.

Figure 4 shows that A and ΔE of Au at a reaction temperature of 230° are not influenced by annealing in the range 300–600°. The changes in thermoelectric force and hardness take place in the annealing range 100–200° (T_d).¹⁰ Figure 5 shows that Ag catalysts give results approximately similar to the case of Au at a reaction temperature of 255°. The T_d of cold-worked Ag used in this experiment was in the range of 70–250°. In these cases, dislocations produced by cold-working cannot be responsible for the active sites, since each of the specimens is already annealed at 300° before the catalytic measurements are made. Furthermore, it is considered that the annealing at temperatures above 300° has direct effects upon a length of crystallite boundaries, crystal edges, and angular points at the surface. However, the results indicate that these factors have almost no influence on the activity.

Figure 6 shows a comparison of the relative activities of various metals at a reaction temperature of 200°. It is clear

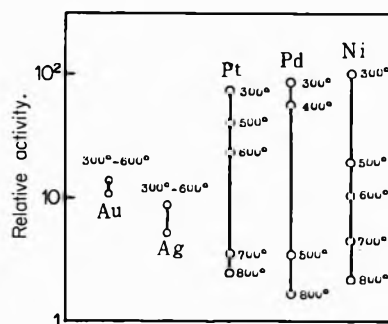


Figure 6. Comparison of activities of different metals. The solid lines represent the range of the change in the activity obtained at 200° during annealing. The figures designate the annealing temperature.

that the values of relative activities of Pt, Pd, and Ni are about 10 times those of Au and Ag at an annealing temperature of 300°. However, this difference disappears after annealing at temperatures above T_d . That is to say, the huge change in the activity of an element during annealing overwhelms the differences between the activities of different metals. It was shown by Sachtler and Fahrenfort³ that the relative activities of supported metals are as follows: $\text{Au} < \text{Ag} < \text{Pd} < \text{Pt} > \text{Ni} > \text{Fe}$ as a function of the heat of formation of their formates. Therefore, they claimed that a metal such as Au or Ag is a poor catalyst but the metals Pt and Pd are good catalysts. Hinshelwood and his coworkers¹¹ found that under the conditions of their experiments the ratio of relative activities is $\text{Pt}:(\text{Au,Ag}) = 50:1$. A detailed comparison between the results of Sachtler and of the present study is given in Table I, and the differences in the activities between supported and cold-worked metals are made sufficiently clear. We have no complete explanation for these facts; however, it is considered that the role of lattice defects in catalysis appeared sensitively. From the above mentioned point of view, so far as cold-worked and annealed metals are concerned, it is concluded that attempts to correlate bulk property and catalytic activity are largely unsuccessful and do not have a significant meaning. For this purpose, it is considered desirable to employ perfect crystal planes, which are free from lattice defects and impurities.

Acknowledgment. The author wishes to express his gratitude to Professor I. Umeta for reading the manuscript and for helpful discussions.

- (9) J. Bagg, H. Jager, and J. V. Sanders, *J. Catal.*, **2**, 449 (1963); H. Jager, *ibid.*, **9**, 237 (1967).
 (10) S. Kishimoto and M. Nishioka, *J. Phys. Chem.*, **76**, 1907 (1972).
 (11) C. N. Hinshelwood, "The Kinetics of Chemical Change," Oxford University Press, 1940.

Electron Transfer Interactions between Superoxide Ion and Organic Compounds

R. Poupko and I. Rosenthal*

*Isotope Department and Department of Organic Chemistry, The Weizmann Institute of Science, Rehovot, Israel
(Received February 16, 1973)*

The superoxide radical anion, O_2^- , readily reacts with electron acceptors, such as quinones, nitro-substituted aromatic hydrocarbons, etc., to yield the corresponding radical anions. With electron donors, such as amines, the superoxide anion reacts as an oxidant to give nitric oxides. No experimental support could be provided to the suggested use of superoxide ion as a source of singlet molecular oxygen, $O_2(^1\Sigma_g^+)$.

Introduction

In recent years, convincing evidence that a free-radical form of molecular oxygen, the superoxide ion O_2^- , is formed in a substantial amount by the univalent reduction of molecular oxygen in biological systems has been provided by direct esr measurements using a rapid-freezing technique.¹ Thus, the generation of superoxide ion has been reported in several enzymatic systems such as xanthine oxidase and the ability of reduced flavines and a variety of flavoproteins to produce superoxide anion radicals was described. Furthermore, regarding the subsequent processes undergone by superoxide ion in biological systems, it has been suggested that it can mediate the flow of electrons from enzymes to electron acceptors such as cytochrome C, or could be involved in chemical reactions catalyzed by oxygenases.²

However, there is a paucity of data on primary chemical processes which involve superoxide ion, particularly regarding the basic interactions of this species with organic substrates. In view of the paramagnetic character of the superoxide ion, it is expected that its interaction with organic compounds should yield as a first product, paramagnetic species. Since electron spin resonance provides a powerful and unambiguous technique for searching for such species, we undertook a study of initial interactions of superoxide ion with several groups of organic compounds using this technique.

Experimental Section

The organic compounds were from commercial sources and were carefully purified before use. Potassium superoxide (Research Organic/Inorganic Chemical Corp.) was used as supplied. Dimethyl sulfoxide was freshly distilled over CaH_2 . The tetrabutylammonium superoxide was synthesized in a preparative scale by electrochemical one-electron reduction of molecular oxygen on a mercury-pool cathode following the experimental procedure described by McCord and Fridovich.³ The mixing of the superoxide ion containing solution and the solution of organic substrate was carried out in a vacuum apparatus, although in most cases flushing of the solution containing the mixed reagents with helium, turned out to be satisfactory.

Esr spectra were recorded with a Varian E12 esr spectrometer. The spectra were examined at room temperature at X-band frequency.

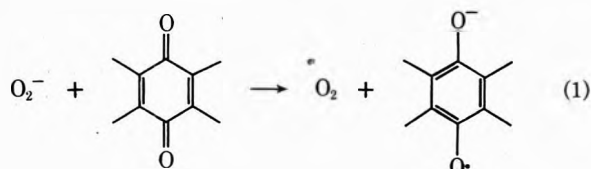
Results and Discussion

Since the redox potentials of $O_2|O_2^-$ and $O_2^-|H_2O_2$ are -0.7 and 1.3 V, respectively, at pH 7,⁴ an expected

feature of this superoxide anion is the ability of acting as a reductant in the presence of electron acceptors and an oxidant in the presence of electron donors. For the purposes of providing data against which theoretical prediction can be tested, it is of interest to study the interaction of O_2^- with suspected organic scavengers.

Inorganic superoxides can provide a direct and convenient source of superoxide ion. Thus potassium superoxide, KO_2 , was used preferentially as the source of superoxide ion in this work.⁵ The presence of O_2^- in a dimethyl sulfoxide solution of KO_2 was easily detected by esr at -196° due to the asymmetric main g_{\perp} line at 2.00 and g_{\parallel} component of low amplitude at 2.10. Occasionally, certain reactions were repeated with tetrabutylammonium superoxide, $(C_4H_9)_4N^+O_2^-$, in dimethylformamide or acetonitrile with similar results.

The importance of quinones and related structures in metabolism and biological oxidations prompted us to undertake a close examination of the reaction of superoxide ion with these compounds. We found that quinones are spontaneously reduced by KO_2 in dimethyl sulfoxide solution to give fairly stable semiquinone anion radicals. Thus the mode of electron transfer may be formulated as follows



The esr spectra of the semiquinone radical anions generated by reaction 1 were identified and compared with the spectra of the corresponding radicals prepared by alternative methods as indicated in the Table I.^{6,7}

With certain quinones, particularly benzoquinones, the effect of the presence of the counter cation, K^+ , in close proximity to the radical anion molecule was observed. In these cases the spectrum was complex,⁸ the main effect being the appearance of an additional radical with an

- (1) R. Nilsson, F. M. Pick, and R. C. Bray, *Biochim. Biophys. Acta.*, **192**, 145 (1969).
- (2) I. Fridovich, *Accounts Chem. Res.*, **5**, 321 (1972).
- (3) J. M. McCord and I. Fridovich, *J. Biol. Chem.*, **244**, 6049 (1969).
- (4) W. M. Latimer, "Oxidation Potentials," 2nd ed, Prentice Hall, New York, N. Y., 1952. The values have been recomputed for pH 7.
- (5) J. E. Bennett, D. J. E. Ingram, M. C. R. Symons, P. George, and J. S. Griffith, *Phil. Mag.*, **46**, 443 (1955).
- (6) A. Fisher in Landolt-Bornstein, New Series, Vol. 1, K. H. Hellwege and A. M. Hellwege, Ed., Springer Verlag, Heidelberg, 1965.
- (7) L. M. Stock and J. Suzuki, *Proc. Chem. Soc.*, 136 (1962).
- (8) Cf. E. A. C. Lucken, *J. Chem. Soc.*, 4234 (1964).

TABLE I

Parent quinone	Hyperfine splitting constants (present work), G	Ref
<i>p</i> -Benzoquinone	$a^H = 2.35$	6
2,5-Dichlorobenzoquinone	$a^H = 2.15$	6
2,6-Dichlorobenzoquinone	$a^H = 2.35$	6
2,5-Di- <i>tert</i> -butylbenzoquinone	$a^H = 2.20$	7
2,5-Dimethylbenzoquinone	$a_{Me}^H = 2.12, a^H = 1.92$	6
<i>p</i> -Fluoranil	$a^F = 4.0$	6
2,3-Dichloro-5,6-dicyanobenzoquinone	$a^N = 0.62$	
1,4-Naphthoquinone	$a_{5,6}^H = 0.31, a_{6,7}^H = 0.62,$ $a_{2,3}^F = 3.25$	6
Anthraquinone	$a_1^H = 0.30, a_2^H = 0.97$	6
5,8-Dihydroxynaphthoquinone	$a^H = 2.35, a_{OH}^H = 0.50$	6
9,10-Phenanthrenequinone	$a_{2,7}^H = 0.22, a_{4,5}^H = 0.42,$ $a_{1,8}^F = 1.37, a_{3,6}^H = 1.65$	6

asymmetric electron spin density distribution. This results in different hyperfine splitting of hydrogens which are equivalent in the uncomplexed radical anion. However, the addition of a small quantity of water displaced the metal from the semiquinone and restored the spectrum to that usually observed.

Several hydroxy-substituted benzoquinones and anthraquinones reacted spontaneously with potassium superoxide as witnessed by the sudden change in color and release of oxygen on mixing with a solution of KO_2 under vacuum. However, no paramagnetic species could be detected by esr. These observations can be explained by the formation of the corresponding colored potassium phenolates, whose electron-accepting capabilities were not sufficient to promote the electron transfer from the superoxide ion. Furthermore, the perhydroxyl radical HO_2 formed by replacement of K^+ by the phenolic proton would easily disproportionate with release of molecular oxygen



Similar to quinones, we found that nitro-substituted aromatic hydrocarbons are easily reduced to the corresponding radical anions, according to the reaction

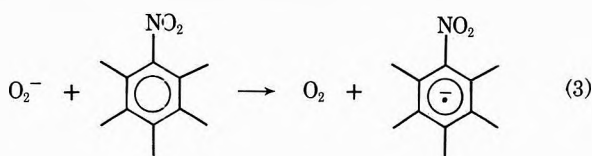


Table II^{9,10} summarizes our work with these compounds and the hyperfine coupling constants derived from it.

In this case, also, the radicals generated by the reaction with superoxide ion compare very well with the same radicals generated by alternative methods. It is noteworthy that the lines corresponding to nuclear spin states of the nitrogen atom $M_1 = \pm 1$ of the 3,5-dinitrobenzoic acid radical anion were slightly broadened. This effect was explained¹¹ as resulting from fluctuations in spin density at a rate comparable with the reciprocal hyperfine interval. Nevertheless, the measured splitting parameters of this radical were found to be in very good agreement with those of the electrochemically generated radical in a dimethyl sulfoxide solution using tetrabutylammonium perchlorate as supporting electrolyte.

An unusual reaction occurred between *p*-nitrotoluene and KO_2 . The esr spectrum obtained by mixing these compounds was identical with the *p*-nitrobenzaldehyde

TABLE II

Parent compound	Hyperfine splitting constants (present work), G	Ref
Nitrobenzene	$a^N = 9.90, a_{2,6}^H = 3.35,$ $a_{3,5}^H = 1.07, a_4^H = 4.00$	6
<i>p</i> -Formylnitrobenzene	$a^N = 5.40, a_{2(6)}^H = 2.30,$ $a_{6(2)}^H = 2.95, a_{3(5)}^H = 0.30,$ $a_{5(3)}^H = 0.42, a_{CHO}^H = 1.30$	6
<i>p</i> -Cyanonitrobenzene	$a^N = 6.55, a_{2,6}^H = 3.05,$ $a_{3,5}^H = 0.75, a_{CN}^N = 0.75$	6
<i>m</i> -Methoxynitrobenzene	$a^N = 9.75, a_{2(6)}^H = 3.22,$ $a_{6(2)}^H = 3.32, a_4^H = 3.70,$ $a_5^H = 1.0$	9
<i>m</i> -Chloronitrobenzene	$a^N = 9.0, a_{2,6}^H = 3.30,$ $a_4^H = 4.20, a_5^H = 1.0$	10
3,5-Dinitrobenzoic acid	$a^N = 4.50, a_{2,6}^H = 3.92,$ $a_4^H = 3.20$	

radical anion suggesting the oxidation of the *p*-methyl group to aldehyde during the process.

It could be expected that superoxide ion reacts also with other electron acceptors to yield the corresponding radical anions. Thus 7,7,8,8-tetracyanoquinodimethane (TCNQ) gave a multiline spectrum identical with the one described in literature for its radical anion⁶ with the hyperfine coupling constants $a^H = 1.43$ and $a^H = 1.00$.

Similarly, anthrone reacts instantaneously with KO_2 to give a radical spectrum composed of two quintets with a binomial distribution 1:4:6:4:1 and hyperfine splitting constants 0.97 and 0.30 G. This spectrum is peculiar in that no splitting due to the $-CH_2-$ group at position 9 is apparent, as would be expected on the basis of a hyperconjugation mechanism. Furthermore, this esr spectrum is identical with that of the radical anion of 9,10-anthraquinone generated by the same procedure. Since extreme care was taken to prepare a pure sample of anthrone for this reaction, the formation of anthraquinone radical anion could be due to an oxidation process with molecular oxygen produced from superoxide ion.¹² The facile conversion of anthrone to 9,10-anthraquinone radical anion during the reduction process has been suggested.¹³ In most of the other reactions, however, the esr spectra of the primary radical anions generated by reduction with superoxide ion could still be obtained after hours at room temperature without any special precaution being taken to increase the lifetime of the radicals.

Since it was expected that superoxide ion would react as an oxidant with electron donors, this possibility was checked by treating it with amines. We found that secondary amines are instantaneously oxidized to dialkyl nitroxides by KO_2 in dimethyl sulfoxide solution. The nuclear hyperfine coupling constants of the nitric oxides generated by this procedure are listed in Table III.^{14,15}

It should be mentioned that while the dialkyl nitroxides were generated in a pure form without any interference

(9) T. Fujinaga, Y. Deguchi, and K. Umemoto, *Bull. Chem. Soc. Jap.*, **37**, 822 (1964).

(10) A. R. Metcalfe and W. A. Waters, *J. Chem. Soc. B*, 918 (1969).

(11) P. B. Ayscough, "Electron Spin Resonance in Chemistry," Methuen, London, 1967, p 272.

(12) Nevertheless, the electrolytic reduction of anthrone in a carefully degassed solution of dimethyl sulfoxide or dimethylformamide with tetrabutylammonium perchlorate as supporting electrolyte generated the same radical anion.

(13) B. J. Tabner and J. R. Zdysiewicz, *J. Chem. Soc. B*, 1659 (1971).

(14) A. Hudson and H. A. Hussain, *J. Chem. Soc. B*, 1299 (1967).

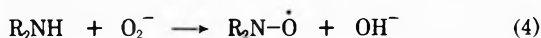
(15) A. Mackor, Th. A. J. W. Wajer, Th. J. de Boer, and J. D. van Voorst, *Tetrahedron Lett.*, 2115 (1966).

TABLE III

Parent amine	Hyperfine splitting constants (present work), G	Ref
Diisopropylamine	$a^N = 15.0, a^H = 4.30$	14
Dicyclohexylamine	$a^N = 14.75, a_\beta^H = 4.25, a_\gamma^H = 0.65$	15
Diphenylamine	$a^N = 10.1, a_{o,p}^H = 1.85, a_m^H = 0.82$	6

from other radicals, as primary reaction products, the diphenylnitric oxide was produced after the solution of amine and KO_2 in dimethyl sulfoxide was diluted with water. The initial esr spectrum of the mixture of diphenylamine and KO_2 appeared to be a superimposition of several radicals; the addition of water to this mixture removed the primary radicals, yielding diphenylnitric oxide as the exclusive paramagnetic species.

Two observations shed light on the mechanism of formation of nitric oxide in this reaction: (a) no stable radical products have been observed from tertiary amines like triphenylamine and (b) the reaction occurs in the absence of atmospheric oxygen. These observations suggest that the production of disubstituted nitric oxides is according to the following equation



A final aspect of electron transfer reaction of O_2^- concerns the use of a dimethyl sulfoxide solution of KO_2 as a source of superoxide ion. In 1970 it was reported¹⁶ that the superoxide anion, O_2^- , from potassium superoxide, generates singlet molecular oxygen in dimethyl sulfoxide solution. The presence of singlet oxygen was detected by chemical means, using 2,5-dimethylfuran as scavenger, as well as by fluorescence sensitization techniques. The quenching effect of water as well as the energetic requirements in the luminescence sensitization experiment led to the conclusion that $O_2(^1\Sigma_g^+)$ was preferentially generated.¹⁷ However, several observations led us to doubt the correctness of this interesting suggestion. Thus in the event that KO_2 releases singlet molecular oxygen in dimethyl sulfoxide, the concentration of superoxide ion in such a solution should rapidly decrease in time. However, the periodical check of this solution by esr at -196° hardly showed any change in the superoxide ion signal intensity after several hours at room temperature. In fact the stability of the superoxide ion in nonprotic solvents has also been noticed by other groups. Thus, Poever and White¹⁸ reported that superoxide ion generated by electrolytic one-electron reduction of oxygen in several nonprotic solvents including dimethyl sulfoxide has considerable stability. According to McCord and Fridovich,³ tetrabutylammonium superoxide produced by a similar procedure in *N,N*-dimethylformamide was stable for hours at room temperature. Thus a rapid chemical reaction be-

tween KO_2 and dimethyl sulfoxide can be excluded. In addition we carried out several chemical tests for singlet oxygen using a dimethyl sulfoxide solution of KO_2 . Thus 2,3-dimethyl-2-butene, 2-methyl-2-pentene, and cyclohexene, compounds known to be chemical scavengers of singlet molecular oxygen of a wide range of reactivities,¹⁹ turned out to be practically unaffected by a dimethyl sulfoxide solution of KO_2 after 24 hr at room temperature as shown by gas-liquid chromatography analyses. Tetraphenylcyclopentadienone (tetracyclone) reacted rapidly in a dimethyl sulfoxide solution of KO_2 , to give, after water hydrolyses of the reaction mixture and extraction with chloroform, a major product of mp $190-192^\circ$, γ_{max} 1696 cm^{-1} , λ_{max} 245 nm ($\log \epsilon$ 4), 320 nm ($\log \epsilon$ 3), and m/e 328. However, no *cis*-dibenzoylstilbene, the reaction product of tetracyclone with singlet oxygen, could be detected.²⁰

Although these chemical tests have been developed for $O_2(^1\Delta_g)$, similar reactions can be expected for $O_2(^1\Sigma_g^+)$ in view of the easy deactivation to $O_2(^1\Delta_g)$ by intermolecular collision.²¹

Finally, we wish to point out our disagreement with a view which has appeared in the literature. The one-electron transfer reaction $O_2^- = O_2 + e$ is not likely to generate molecular oxygen in an excited singlet state, mainly because such a reaction does not provide sufficient energy to do so. The electronic levels of singlet oxygen have been accurately determined as being 22.5 and 37.5 kcal above the ground state of $O_2(^3\Sigma_g^-)$ for $O_2(^1\Delta_g)$ and $O_2(^1\Sigma_g^+)$, respectively.¹⁹ Since the attachment of an electron to an oxygen molecule is an exothermic process, the ground state of O_2^- lies below $O_2(^3\Sigma_g^-)$ with an amount of energy equal to the electron affinity of molecular oxygen. A recent measurement of the electron affinity of oxygen by charge exchange of cesium and molecular oxygen yielded a lower limit of $0.46 \pm 0.05\text{ eV}$.²² It results that the "bare" conversion of superoxide ion to singlet oxygen is endothermic and in the absence of an additional source of energy such a process cannot take place. In this respect, it is interesting to mention that the standard free energy available from the reaction $2O_2^- + 2H^+ \rightarrow O_2 + H_2O_2$ of 37.5 kcal⁴ provides sufficient energy for the generation of excited molecular oxygen. However, this suggestion²³ has not yet been experimentally substantiated.

(16) A. U. Khan, *Science*, **168**, 476 (1970).

(17) The possibility of alternative explanations for these experimental observations has been suggested. D. R. Kearns, *Chem. Rev.* **71**, 395 (1971).

(18) M. E. Poever and B. S. White, *Electrochim. Acta*, **11**, 1061 (1966).

(19) C. S. Foote, *Accounts Chem. Res.*, **1**, 104 (1968).

(20) C. S. Foote, S. Wexler, W. Ando, and R. Higgins, *J. Amer. Chem. Soc.*, **90**, 975 (1968).

(21) R. P. Wayne, *Advan. Photochem.*, **7**, 400 (1969).

(22) S. J. Nalley and R. N. Compton, *Chem. Phys. Lett.*, **9**, 529 (1971).

(23) R. h. Steele and L. C. Cusachs, *Nature (London)*, **213**, 800 (1967).

Look no further for original research dealing with factors influencing properties and performance.

In **PRODUCT R & D** you'll find the papers quarterly, and the data on:

- preparation of new or improved chemical products
- improved methods for the preparation of existing products
- new uses for existing products
- the modification of materials to satisfy the requirements of specific end uses

SPECIAL FEATURES: PLENARY ACCOUNTS helps you probe advances in "the other man's discipline"—with both the newest data and the relevant background . . . plus technical and/or Product Reviews, Special Topics and the new Signals of Science. To begin your self-development program as soon as possible, just complete the form and mail it to us.



... another ACS service

**I&EC—R & D
American Chemical Society**

1155 Sixteenth Street, N.W.
Washington, D.C. 20036

Yes, I would like to receive **I&EC PRODUCT R & D** at the one-year rate checked below:

	<i>U.S.</i>	<i>Canada</i>	<i>Latin America</i>	<i>Other Nations</i>
ACS Member Personal-Use				
One-Year Rate	<input type="checkbox"/> \$ 7.00	<input type="checkbox"/> \$10.00	<input type="checkbox"/> \$10.00	<input type="checkbox"/> \$10.50
Nonmember	<input type="checkbox"/> \$21.00	<input type="checkbox"/> \$24.00	<input type="checkbox"/> \$24.00	<input type="checkbox"/> \$24.50

Bill me Bill company Payment enclosed

Name _____

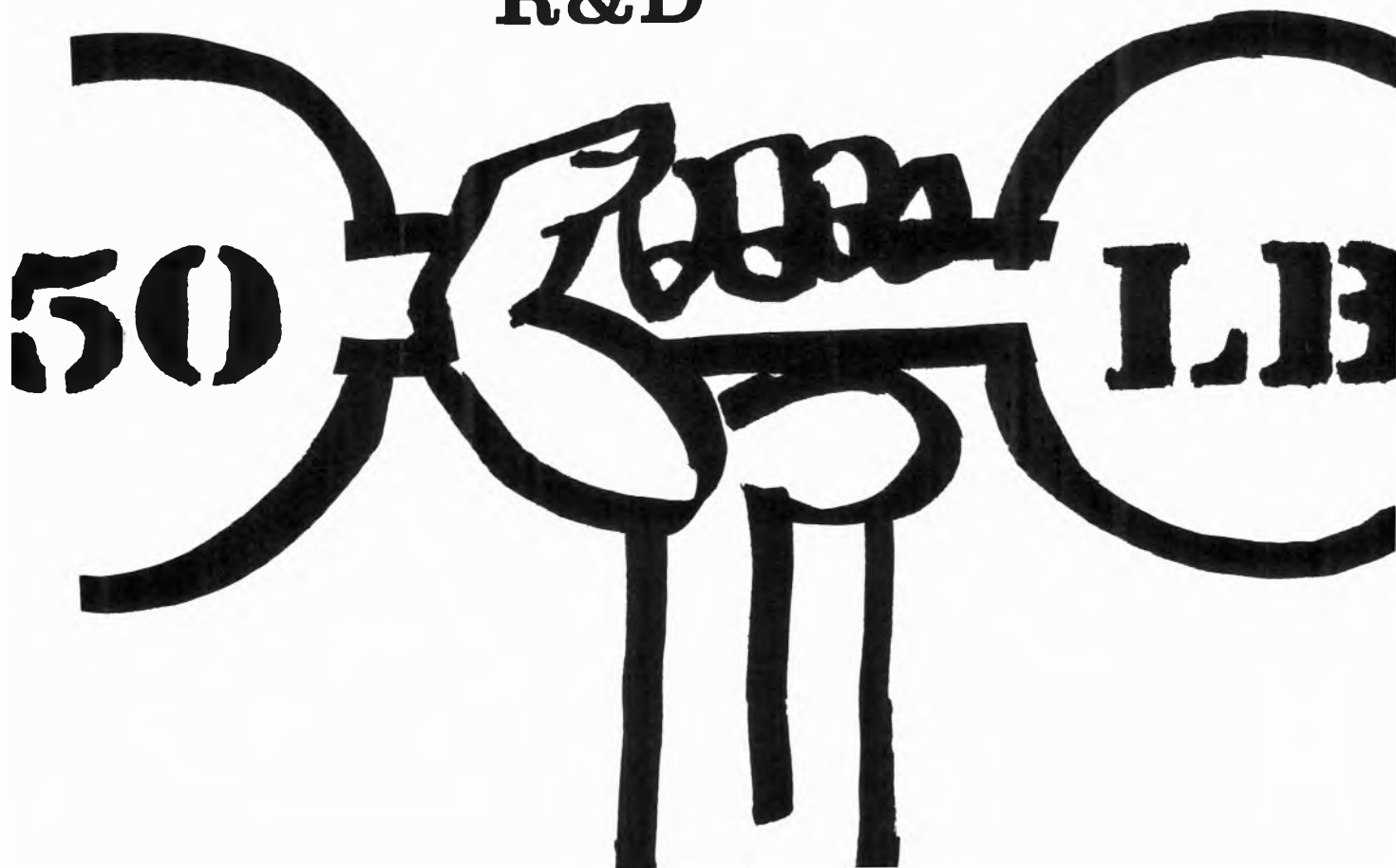
Street _____ Home
Business

City _____ State _____ Zip _____

V-73

Research for your own Development

I&EC PRODUCT R&D



American Chemical Society

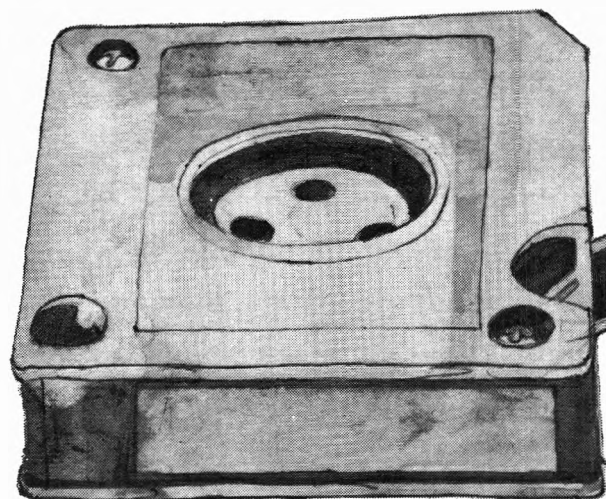
"Primary Publications on Microfilm"

Your Key to—

■ Dramatic savings in archival space and dollars . . . over 1,000,000 pages of chemical literature contained in a carousel measuring only 17" x 17" x 39".

■ Faster access to needed data. Slash costly search and retrieval time required of your scientists and librarians.

■ Unlimited distribution of copyrighted scientific data. "ACS Primary Publications on Microfilm" are available under a unique licensing agreement permitting you to make as many enlarged photocopies per page as desired . . . for distribution throughout your company.



American Chemical Society Primary Publications included in this microfilm program:

JOURNAL OF THE AMERICAN CHEMICAL SOCIETY
INDUSTRIAL & ENGINEERING CHEMISTRY
CHEMICAL TECHNOLOGY
CHEMICAL & ENGINEERING NEWS
CHEMICAL & ENGINEERING NEWS ANNUAL INDEXES
ANALYTICAL CHEMISTRY
JOURNAL OF PHYSICAL CHEMISTRY
JOURNAL OF AGRICULTURAL AND FOOD CHEMISTRY
JOURNAL OF ORGANIC CHEMISTRY
JOURNAL OF CHEMICAL AND ENGINEERING DATA
CHEMICAL REVIEWS
JOURNAL OF CHEMICAL DOCUMENTATION
I&EC FUNDAMENTALS
I&EC PROCESS DESIGN AND DEVELOPMENT
I&EC PRODUCT RESEARCH AND DEVELOPMENT
BIOCHEMISTRY
INORGANIC CHEMISTRY
JOURNAL OF MEDICINAL CHEMISTRY
CHEMISTRY
ENVIRONMENTAL SCIENCE & TECHNOLOGY
ACCOUNTS OF CHEMICAL RESEARCH
MACROMOLECULES

For information on "ACS Primary Publications on Microfilm", write or call:

Special Issues Sales
American Chemical Society
1155 16th Street, N.W.
Washington, D.C. 20036
(202-872-4364)